University of Southampton

Faculty of Engineering and Physical Sciences

School of Chemistry

Understanding the Mechanochemical Synthesis of Manganite Perovskites and their Catalytic Behaviour

by

Rachel Hazel Blackmore

Thesis for the degree of Doctor of Philosophy

March 2021

University of Southampton

Abstract

Faculty of Engineering and Physical Sciences

School of Chemistry

Thesis for the degree of Doctor of Philosophy

Understanding the Mechanochemical Synthesis of Manganite Perovskites and their Catalytic Behaviour

by

Rachel Hazel Blackmore

The tightening of emission regulations and increasing prices of precious metals for existing commercial catalysts drives the need to develop of new sustainable catalysts at lower performance costs. Mechanochemistry offers a solventless, 'one-step' route to preparing metal oxide catalysts, however, there is limited information on the chemical steps involved. The use of multiple advanced characterisation techniques, such as HERFD, XES and NAP-XPS, has been applied in this work to understand the structure of the highly disordered and heterogeneous materials produced by ball milling. This thesis has provided further insights to begin to form generalised rules for the mechanochemical synthesis of mixed metal oxides, such as perovskites. In doing so, it can start to aid the rational design of new catalyst technologies.

A predominant part of the work within this thesis has focused on the mechanochemical synthesis of $LaMnO_3$. Preforming XAS on *ex situ* 'time slices' during the milling procedure was successful in providing insights into the underlying chemistry; not previously possible by lab-based XRD. The XAS data showed the La precursor to disperse readily over Mn_2O_3 at the early stages of milling. On increasing the milling time it allowed for mechanical activation of both precursors and the formation of powdered $LaMnO_3$, with no calcination step required. Applying the same milling conditions as for $LaMnO_3$ to the synthesis of other manganite perovskites, $ErMnO_3$ and $YMnO_3$, did not result in the desired phase, with a highly amorphous material produced. This highlights the intrinsic difficulties with regards to the mechanochemical syntheses; often each individual system requires specific optimisation to reach the desired material properties. However, exploring the effect of La dispersion at low mechanical energies was shown to be effective in another system, Au/Al_2O_3.

Challenges regarding the *in situ* monitoring of mechanochemistry have been addressed within this work. Difficulties in the dynamic set-up of commercial milling equipment has meant *in situ* monitoring of planetary ball milling is not possible. However, the work here attempted a modified *in situ* mill and *in situ* high pressure experiments to mimic those

experienced during mechanochemistry. It was able to show the challenges in (1) monitoring mixed metal oxide systems in real-time and (2) mimicking impact forces occurring as a result of mechanical action.

Surface sensitive studies, such as XPS, have been crucial in determining improved catalytic activity towards deN_2O for the ball milled $LaMnO_3$. Following the reaction under working conditions *via* NAP-XPS, the increased activity at lower reaction temperatures was accredited, not to changes in the catalytic active site Mn, but to increased surface oxygen vacancies, and the presence -OH within the La 3d XPS region.

This research demonstrates by collating a large variety of complementary characterisation techniques it has produced new insights into the mechanochemical synthesis of manganite perovskites. However, it also highlights the continued innovation and development required for the analysis of highly complex materials and equipment set-ups.

Table of Contents

Table of Tables

Table of Figures

List of Accompanying Materials

Thesis dataset: https://doi.org/10.5258/SOTON/D1798

Research Thesis: Declaration of Authorship

Print name: Rachel Hazel Blackmore

Title of thesis: Understanding the Mechanochemical Synthesis of Manganite Perovskites and their Catalytic Behaviour

I declare that this thesis and the work presented in it are my own and has been generated by me as the result of my own original research.

I confirm that:

1. This work was done wholly or mainly while in candidature for a research degree at this University;
2. Where any part of this thesis has previously been submitted for a degree or any other qualification at this University or any other institution, this has been clearly stated;
3. Where I have consulted the published work of others, this is always clearly attributed;
4. Where I have quoted from the work of others, the source is always given. With the exception of such quotations, this thesis is entirely my own work;
5. I have acknowledged all main sources of help;
6. Where the thesis is based on work done by myself jointly with others, I have made clear exactly what was done by others and what I have contributed myself;
7. Parts of this work have been published as:-

R. H. Blackmore, M. E. Rivas and T. E. Erden, Trung Dung Tran, Huw R. Marchbank, Dogan Ozkaya, Martha Briceno de Gutierrez, Alison Wagland, Paul Collier and Peter P. Wells. Understanding the Mechanochemical Synthesis of $LaMnO_3$ and its Catalytic Behaviour. *Dalt. Trans*., 2020, **49**, 232–240.

R. H. Blackmore, M. E. Rivas, G. F. Tierney, K. M. H. Mohammed, D. Decarolis, S. Hayama, F. Venturini, G. Held, R. Arrigo, M. Amboage, P. Hellier, E. Lynch, M. Amri, M. Casavola, T. Eralp Erden, P. Collier and P. P. Wells. The electronic structure, surface properties, and *in situ* N_2O decomposition of mechanochemically synthesised $LaMnO_3$. *Phys. Chem. Chem. Phys.*, 2020, **22**, 18774–18787

Conferences

Oral Presentations: UK Catalysis Conference 2020, Loughborough; Johnson Matthey Academic Conference 2021, virtual.
Poster Presentations: Johnson Matthey Academic Conference 2018, 2019, 2020, Loughborough / Warwick; UK Catalysis Conference 2019, Loughborough; 14th European Congress on Catalysis, EuropaCAT, 2019, Aachen, Germany; 17th International Congress on X-ray Absorption Spectroscopy 2018, Krakow, Poland.

Signature: ..... Date: 13/04/2021

Acknowledgements

I would like to first like to thank my academic supervisor, Dr Peter Wells. His constant support, encouragement and patience has enabled me to gain and improve not only my research skills but also personal development. Working closely with other members of the Wells research group throughout this project has allowed the opportunity for travel and broadening my scientific knowledge and skills. Specific thanks to George, Donnie, Evan, Ellie and Pip for their support throughout my PhD, and further help through multiple beamtimes. With specific thanks to Dr Khaled M. H. Mohammed for his analysis of Mn Kβ XES data and Monik Panchal for the Au/Al_2O_3 TEM images.

This PhD was funded by the UK Research and Innovation though an iCASE award, for which I am very grateful.

This project was further funded by Johnson Matthey and collaborated closely with the work within the New Applications Department. I would like to express many thanks towards my industrial supervisor, Dr Maria-Elena Rivas. Her consistent help and support has allowed for me to transition and work confidently within an industrial environment. Through her keen involvement it has allowed my projected to continuously grow and flourish. The resources and expertise have also been widely accessible to me throughout my research and further thanks are extended many members of the Johnson Matthey Analytical Department; particularly Dr Edd Bible, Dr Huw Marchbank, Dr Mahrez Amri for all their help towards numerous XRD measurements, to Dr Trung Dung Tran for performing TEM with STEM-EELS and Dr Tugce Eralp Erden for her analysis of XPS data. Their vast knowledge and skills on specific characterisation techniques has been extremely beneficial. Thank you to Dr Nicoleta Muresan for the synthesis of Au/Al_2O_3. Particular thanks are also given to Dr Paul Collier for the continued collaboration between academia and industry.

I owe significant proportion of this work towards the access of synchrotron radiation facilities, specifically at the Diamond Light Source (DLS) and the European Synchrotron Facility (ESRF). Further thanks are extended to the staff at these facilities which made the experiments possible; Dr Shusaku Hayama at I20-Scanning, Dr Monica Amboage at I20-EDE and Dr Federica Venturini and Dr Georg Held on B07-C, VerSoX. Furthermore, I would like to acknowledge the UK Catalysis, especially Dr June Callison, for her organisation and running of X-ray absorption spectroscopy measurements as part of the catalysis BAG time. Many thanks are also extended the B18 beamline and all their staff.

I would also like to thank the UK Catalysis Hub for the incredibly supportive and friendly environment. The combination of different research groups centred on catalysis offers a rare and fortunate base for the collaboration of ideas and support. Specific thanks

are again given to Dr June Callison for her constant technical support and Dr Josie Goodall for ensuring the smooth running of the Catalysis Hub. To the students that I have learnt alongside with, I am forever thankful for not only providing significant support through the struggles but for all the enjoyment and fun, practically to Andrea, Emma and Alex who I started this journey with.

For the never fading support and love provided by my parents and brother I am extremely grateful. Thanks to my closest friends, Alex and Cariss who kept me sane and motivated throughout the writing process during multiple lockdowns due to COVID. For their support through the highs and lows, I am forever grateful. Finally, thanks to my boyfriend Tom for his consistent patience, love and unwavering belief in me.

Definitions and Abbreviations

at% ..... Atomic percentage
BET ..... Brunauer-Emmett-Teller
BF ..... Bright field
CCD ..... Charge coupled device
.cif ..... Crystallographic information files
DAC ..... Diamond anvil cell
DC ..... Direct current
deN2O ..... Decomposition of nitrous oxide
DFT ..... Density functional theory
DLS ..... Diamond light source
E_a ..... Activation energy
EDE ..... Energy-dispersive EXAFS
EDS ..... X-ray energy dispersive spectroscopy
EELS ..... Electron energy loss spectroscopy
ESRF ..... European Synchrotron Radiation Facility
EXAFS ..... Extended X-ray absorption fine structure
FCC ..... Face centred cubic
GHSV ..... Gas hour space velocity
GWP ..... Global warming potential
HAADF ..... High angle annular dark field
HERFD ..... High energy resolution fluorescence detection
HOMO ..... Highest occupied molecular orbital
ICP-OES ..... Inductively coupled plasma optical emission spectroscopy
ILAG ..... Ion and liquid assisted grinding
IR ..... Infrared
LCF ..... Linear combination fit
LINAC ..... Linear accelerator
LUMO ..... Lowest unoccupied molecular orbital
LVol-IB ..... Length diffraction column volume breathe
MCR ..... Multivariant curve resolution
MFC ..... Mass flow controller
MO ..... Molecular orbital
MOF ..... Metal organic framework
NAP-XPS ..... Near ambient pressure X-ray photoelectron spectroscopy

NP ..... Nanoparticle
PDF ..... Powder diffraction files
PGM ..... Platinum group metals
PID ..... Proportional integral derivative
PMMA ..... Polymethyl methacrylate
PVC ..... Polyvinyl chloride
QEXAFS ..... Quick extended X-ray absorption fine structure
QGA ..... Quantitative gas analysis
QIC ..... Quick inlet capillary
RF ..... Radio frequency
RIXS ..... Resonant inelastic X-ray scattering
RT ..... Room temperature
SE ..... Scanning electron
SEM ..... Scanning electron multiplier
STEM ..... Scanning transmission electron microscopy
TEM ..... Transmission electron microscopy
UHV ..... Ultra high vacuum
VCM ..... Vinyl chloride monomer
VTC ..... Valence-to-core
wt% ..... Weight percentage
XANES ..... X-ray absorption near edge spectroscopy
XAS ..... X-ray absorption spectroscopy
XES ..... X-ray emission spectroscopy
XPS ..... X-ray photoelectron spectroscopy
XRD ..... X-ray diffraction
YTZ ..... Yttria-stabilised zirconia

Chapter 1

Introduction

It is extremely important in today's world that we must continually seek for sustainable solutions for future generations. Whilst current catalysts begin to address this, the increasing drain on finite sources drives the need for continuous scientific advancement within this field that are both environmentally and economically viable. Though catalysts seek for 'greener' opportunities, their synthesis and composition of materials should also be considered. The topics discussed here highlight the importance of developing new catalysts from sustainable reactants, how the preparation method can affect the final material properties and catalytic activity of materials, outlines the scope of the project.

1.1 Sustainability in catalysis

Chemists face the challenge of developing novel products and processes that are also societally, economically and environmentally beneficial.[1] In general, they must combine continuous innovation and improvement of technologies by using less, or more sustainable materials, along with minimising the production of pollutants and of harmful waste.[2] Not only should the supply of energy become more renewable, but the processes themselves must be energy efficient. The ever increasing population, demand on resources and tightening of environmental regulations, such as emissions and waste management, drive the advancement of new technologies that are still competitive with existing processes.[3,4]

Catalysis plays a significant role towards achieving more sustainable processes. It provides an alternative pathway that lowers the required energy input, improving reaction efficiency, along with greater product selectivity.[4] These advantages result in catalysts being used in over 90% of all industrial chemical processes today, with one third of them focussed towards the reduction of pollutents.[5] The use of catalysts has been crucial for the transport industry, allowing for the efficient cracking of long-chained hydrocarbons to be used as fuel sources. However, in turn this has resulted in the increase of atmospheric pollutants and emissions, which are detrimental to human health and the environment.[6] WHO predicts

around 91% of the worlds pollution lives in areas of poor air quality, estimating it results 7 million deaths per year.[7]

Since the 1960s the catalysis sector has grown rapidly with development of catalysts for applications such as the removal of sulfur from fossil fuels, automobile emission treatment to remove CO, NO_x and unburnt hydrocarbons (three-way catalysts) and the selective reduction of NO_x from power plants.[5,8,9] However, in 2007 WHO still recorded an average of 4.2 million premature deaths a year worldwide as a result of exposure to particulate matter.[7] Even though the National UK statistics show the long term decrease in pollutants such as sulfur dioxide, nitrogen oxides and particulate matter since 1970, emission regulations will continue to push for lower targets.[10] This cannot be achieved by simply increasing catalyst concentrations as they themselves often contain rare, unsustainable platinum group metals (PGM) such as platinum, palladium and rhodium. As PGM prices continue to rise, coupled alongside tightening of emission control regulations the need to develop new sustainable alternatives at lower performance costs has never been so prevalent.[11] Rare earth metals are emerging as a suitable sustainable material resource, possessing the highest level of any other industrially used metal in the earth's crust. However, issues surrounding their extraction are challenging and expensive due to their combination with many other materials. Work still remains to maintain the correct balance between supply and demand, alongside recyclability of the most in demand rare earth metals.[12]

1.2 Catalysis

A catalyst is a material that enhances and accelerates the rate of a thermodynamically feasible reaction, without changing the position of its equilibrium.[13] A catalyst provides an alternative pathway (Figure 1.2.1) at a lower activation energy for a chemical reaction to occur, with the total free energy of the reaction remaining unchanged.[14] Figure 1.2.1 shows a simplified schematic comparing the energies and pathway for a catalysed and un-catalysed reaction. The catalyst offers a more complicated, yet alternative route that is more energetically favourable to speed up the approach to equilibrium.[15] Though a catalyst is not consumed in the reaction itself, side reactions and structural changes can lead to the deactivation of the catalyst material. Reducing the activation energy via a catalytic processes can have a huge impact on the overall reaction conditions, with the potential to dramatically reduce operating temperatures and pressures.[16] Without the application of catalysts to industrial processes it would result in uneconomical and unsustainable reactions.[17]

Catalysis can be classified as either homogeneous or heterogeneous. Homogeneous catalysis occurs when both the catalysts and reactants have the same physical state e.g. liquid-liquid, whereas heterogeneous catalysis occurs within separate physical states, such

as solid-gas. Homogeneous catalysts can benefit from high selectivity with increased contact between its active sites and the reactants, however, they often have low thermal stability whist being extremely difficult to separate the final material product from the catalyst. Heterogeneous catalysts generally have a higher thermal stability with easy product separation yet tend to have a lower concentration of active sites, which are often only exposed at the surface.[17]

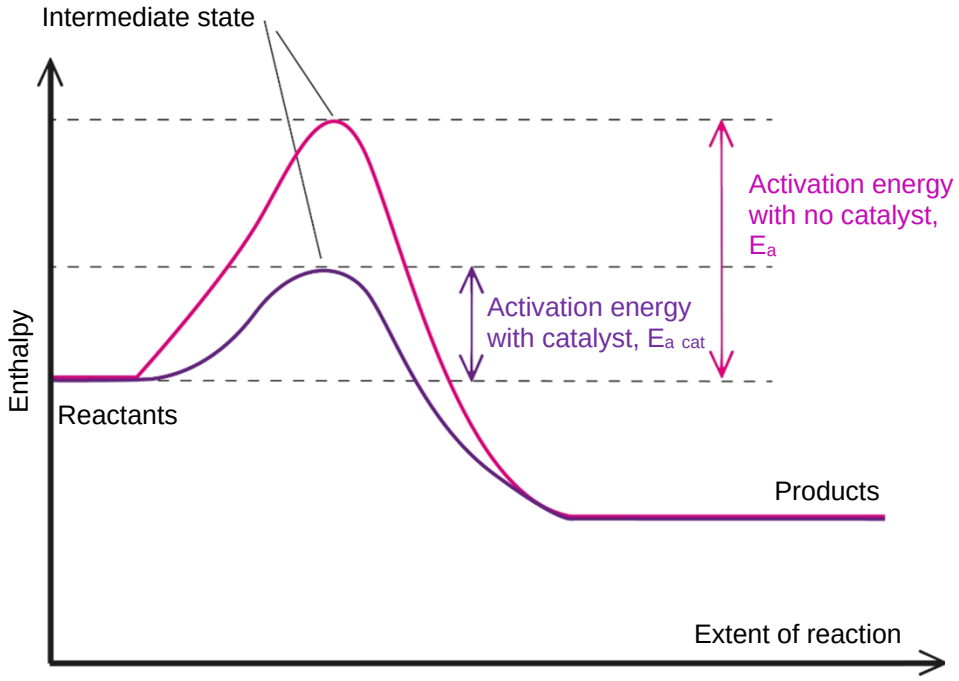

Figure 1.2.1: *A simplified schematic of the energies associated for a reaction with and without a catalyst present*

1.2.1 Heterogeneous catalysis

A heterogeneous catalyst is often solid with either gas or liquid reactants adsorbed onto its surface. Therefore, the surface is often be considered the crucial interface when determining its reactivity.[14] They commonly operate by providing active sites at the surface, which anchor reactants and stabilise intermediate species during the reaction, before being desorbed. The ability of a reactant gaseous species to adsorb onto a catalyst depends on the availability and type of active sites at the surface.[13] As a result, the surface area, composition and structure all affect the ability of reactants to bind to the catalyst and therefore its activity.

Gas molecules adsorb onto a catalyst surface by either physisorption (~10 kJ mol^{-1}) with long range, weak van der Waals forces or by stronger chemisorption (~200 kJ mol^{-1}) interactions. Physisorbed species associatively bind at the surface for a short lifetime, whereas chemisorbed species often dissociate, as a result of forming a chemical bond with the surface weakening the bonding within the adsorbed species. Once the substrate has absorbed onto the catalyst surface its interaction is also important in determining activity. It must possess a balance between being strong enough to allow enough time for a reaction

to take place, but also weak enough to allow for interactions with neighbouring species for the formation of products, to then desorb. The study of the stability of these intermediate species with different transition metal catalysts is known as Sabatier's principle. This relates the temperature of the rate of decomposition of absorbates with respect to the fixed heat of formation of the products.[13]

Further understanding of how gases absorb and react on the surface of a transition metal catalyst can be characterised into three commonly encountered mechanisms; Langmuir-Hinshelwood, Eley-Rideal or Mars-van Krevelen (Figure 1.2.2):

(1) The Langmuir-Hinshelwood is often the most commonly observed mechanism, whereby two species, already bound at the catalyst surface, react to form a product which consequently desorbs from the surface.

(2) Alternatively the Eley-Rideal mechanism describes an incoming gas molecule directly reacting with an absorbed gas species on the surface with the product either desorbing or remaining absorbed on the surface.[18]

(3) Finally, the Mars-van Krevelen mechanism is an example whereby a reactant species absorbs on the surface, combining with an atom from the catalyst surface. After the product desorbs a vacancy is then left at the surface of the catalyst which is either filled by another reactant molecule or from a sub-layer of the catalyst.[19]

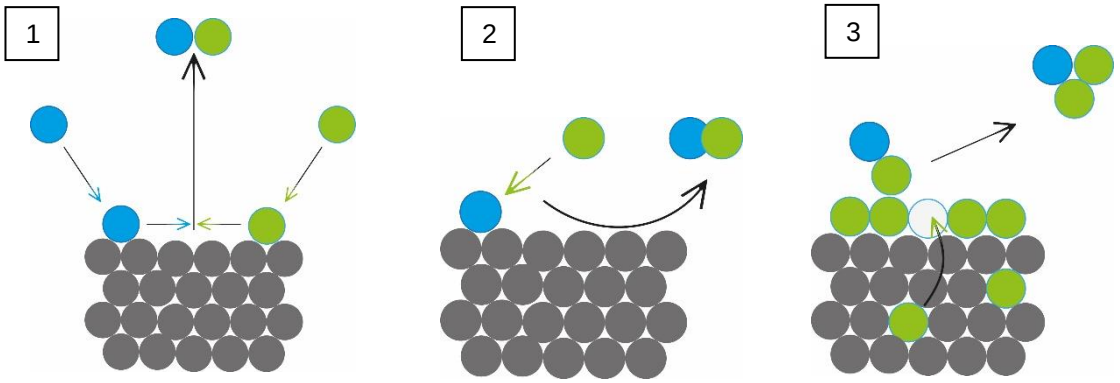

***Figure 1.2.2**: A schematic representing 3 general catalytic mechanisms **(1)** Langmuir-Hinshelwood, **(2)** Eley-Rideal and **(3)** Mars-van Krevelen*

1.3 Perovskites

Perovskite-type mixed metal oxides attract a great deal of interest due to their relative low cost, oxidation activity and thermal stability. Coupled alongside their flexible structural tailoring possibilities, it results in their use towards applications such as catalysis, fuel cells and batteries.[20–22] They are represented by the general formula ABX_3 (A = large sized cation, B = medium sized cation, X = anion, often oxygen) with an ideal cubic structure and space group $Pm\bar{3}m$ (Figure 1.3.1).[23] In this geometry the perovskite is expected to have

the larger cation A-site with a 12-fold coordination to the X, oxygen, atoms and the smaller cation at the B-site having a 6-fold coordination.[24]

By choosing different A and B-site cations it affects the overall electronic structure. For example, when using a first row transmission metal the electronic configuration is determined by the 3*d* electrons in the antibonding levels from O 2*p* orbitals and B ion *d* orbitals to form σ and π bonding orbitals.[25] On selecting these different cations at both the a huge variety of distortion can be induced into the perovskite structure. Further complexity can be added through partial substitution of A and/or B sites, controlling their valence state and oxygen content.

The stability of the resulting perovskite phase can then be determined using the Goldschmidt tolerance factor, t, (Equation 1.3.1) where the value must range from 0.75 to 1.00 in order obtain a perovskite structure.[9] This Goldschmidt tolerance factor is derived from the ideal perovskite structure where by the B – O bond distance is equal to $\frac{a}{2}$ (a is the length of a unit cell) and the A – O bond distance is equal to $\frac{a}{\sqrt{2}}$, giving raise to the relationship between the ionic radii (Equation 1.3.2).[24]

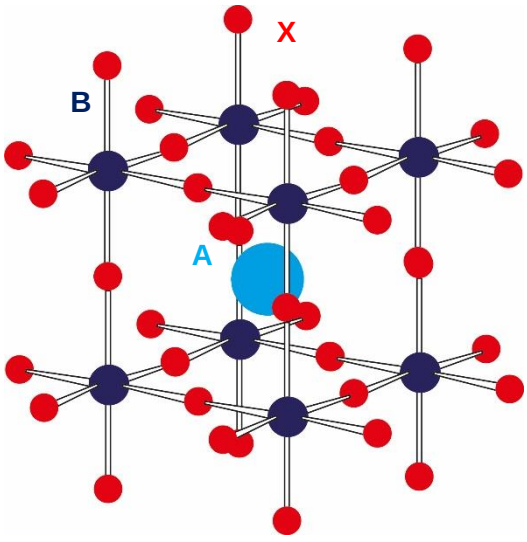

Figure 1.3.1: *A diagram representing ideal perovskite structure, with A representing the larger cation and B a smaller cation. Oxygen atoms bond in an octahedral around the B cation, with BO_6 forming an octahedral around the A cation*

$$t = \frac{(r_A + r_O)}{\sqrt{2}(r_B + r_O)}$$

Equation 1.3.1: *Goldschmidt tolerance factor describing stability of perovskites, where r_A, r_B and r_O are the ionic radii of A, B & O ions, respectively*

$$(r_A + r_O) = \sqrt{2(r_B + r_O)}$$

Equation 1.3.2: *Describing the relationship between ionic radii in an ideal perovskite structure*

Distortion can also be introduced into the perovskite structure via the Jahn Teller effect. In a metal complex with octahedral symmetry the *d* orbitals within the central metal ion split into two levels, t_{2g} (d_{xy}, d_{xz}, d_{yz}) and e_g ($d_{x^2-y^2}$ and d_{z^2}) (Figure 1.3.2). Their energy difference is known as the octahedral crystal field splitting, Δ_o (Figure 1.3.3). Within the perovskite structure the e_g orbitals overlap with the 2*p* atomic orbitals of the oxygen, forming σ bonds, and the t_{2g} orbitals face in between the oxygen orbitals to form a π orbitals.[26] If the B cation site has partially filled *d* orbitals the electronic structure will seek to minimise the degeneracy and lower the energy of the system, causing a Jahn Teller distortion. For example, in a high spin octahedral complex with d^4 electrons, a vacancy occurs in one of the e_g orbitals causing it to be electronically unstable. The ligands along the *z* axis are more screened from the metal ion electrons, as their electron density is concentrated on the d_{z^2} orbital, compared to the ligands in *x* and *y* planes.

Therefore, along the *z* axis there is a lower electronic repulsion, forming elongated bonds in that direction. The d_{z^2} orbital becomes more stable, lowing in energy to below that of the antibonding $d_{x^2-y^2}$ orbital. The t_{2g} energy level then splits to further stabilise. Opposingly, Jahn teller compression in the *z* axis can be observed for complexes, such as d^9, which increases electron repulsion and steric hindrance to cause the orbitals in the *z* axis to destabilise and increase in energy.[27]

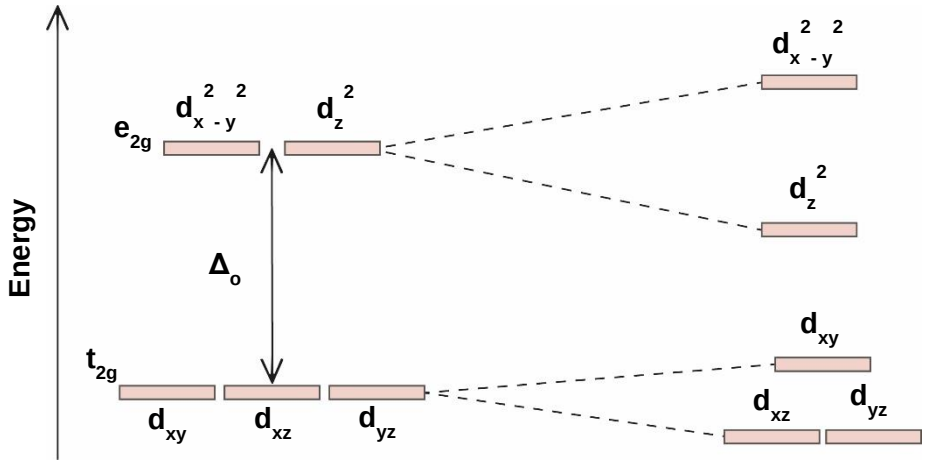

Figure 1.3.2: *Illustration of Jahn-Teller elongation distortion of an octahedral complex*

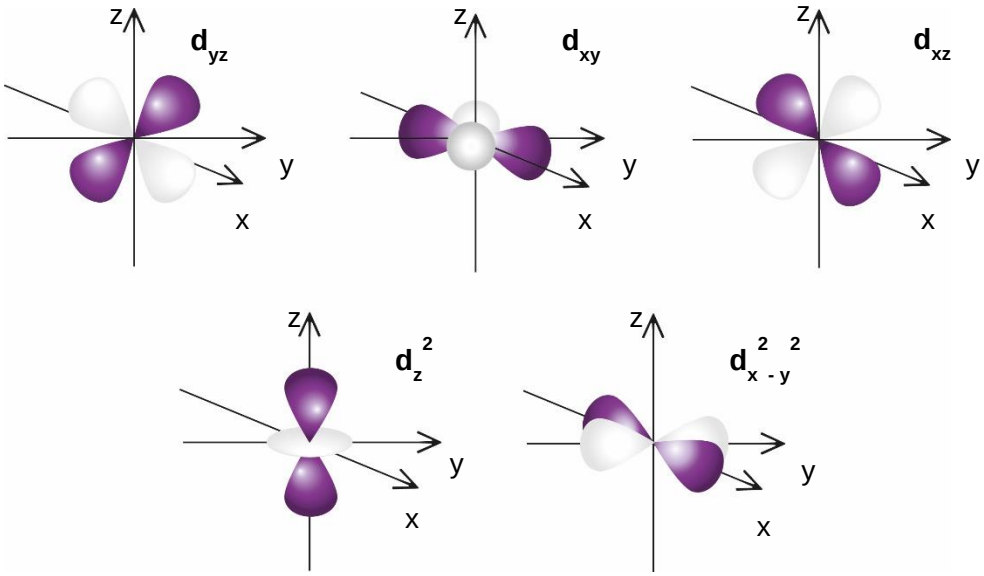

Figure 1.3.3: *Illustration depicting the different d orbitals*

1.3.1 Synthesis of perovskites

One of the oldest synthetic routes known today for the preparation of mixed metal oxide perovskites is the ceramic method, where the single metal oxide precursors, such as hydroxides or carbonates, are calcined together at 1000˚C for several hours. This synthetic route commonly produces highly aggregated, low purity perovskites with surface areas of less than 5 $m^2 g^{-1}$.[28,29] In order to prepare powders that are free of agglomeration, with a narrow particle size distribution, and higher surface areas methods such as spray/freeze-drying, co-precipitation and sol-gel can be performed. These often routes involve dissolving the precursor materials in a suitable solvent, to be homogeneously mixed and then followed by drying and calcination steps.

Spray drying is performed to produce materials with a narrow particle size distribution. Here, a solution of metal salt cations is dispersed by controlling the droplet size from a spray nozzle onto a heated surface. This causes the solvent to instantaneously evaporate and the remaining solid reacts and decomposes to leave spherical or hollow particles.[28] In co-precipitation the precursor materials, commonly metal nitrate salts, are dissolved in water, with a precipitation agent, such as NaOH, under pH control. The resulting precipitate formed is then filtered, dried and calcined. The sol-gel synthesis of perovskites can also start with metal nitrate salt precursors, however, they are then mixed with citrate acid, which on heating eventually forms a ‘gel’. The presence of an organic matrix, such as citric acid, ensures an even dispersion of nucleation sites in initial stages of heating for small crystallite sizes. On further heating of the gel the following stages occur: (1) combustion of citric acid at ~ 300 – 400 ˚C and (2) crystallisation of the perovskite phase up to ~800 ˚C.[30] Continued modifications of this preparation route lead to the development of the Pechini method.[31]

This route benefits from its ability to dispersed two or more metals more homogeneously. The method differs to traditional sol-gel synthesis by producing a covalent polymer network by transesterification of the citrate acid and ethylene glycol to entrap the metal ions (Figure 1.3.4).[30]

The physical properties of perovskites are highly dependent on their synthetic route, which is often considered for their desired application. For catalysis high surface areas are highly desirable, yet they are notoriously low for perovskites.[32] The use of elevated temperatures causes sintering of the particles, increasing grain growth and particle sizes.[33] Attempts to disperse the perovskites onto supports has resulted in higher surface areas and improved catalytic activity. Yet, this comes with limitations as once again high temperatures are required to fix the perovskite to the support alongside the need to consider support compatibility and mass transfer.[28]

Mixed metal oxides with perovskite-like structures, ABO_3, are known to readily form via mechanochemical grinding from their single metal oxide precursors, such as $LaMnO_3$ from La_2O_3 and Mn_2O_3.[33–35] The mechanochemical synthesis allows for the absence of a high temperature calcination step, limiting the sintering of particles, providing a high surface concentration of –OH, high levels of distortion, and a significant volume of intergrain amorphous phase with high oxygen mobility and therefore produce improved catalytically active materials.[28] Mechanochemistry is discussed further in section 1.4.

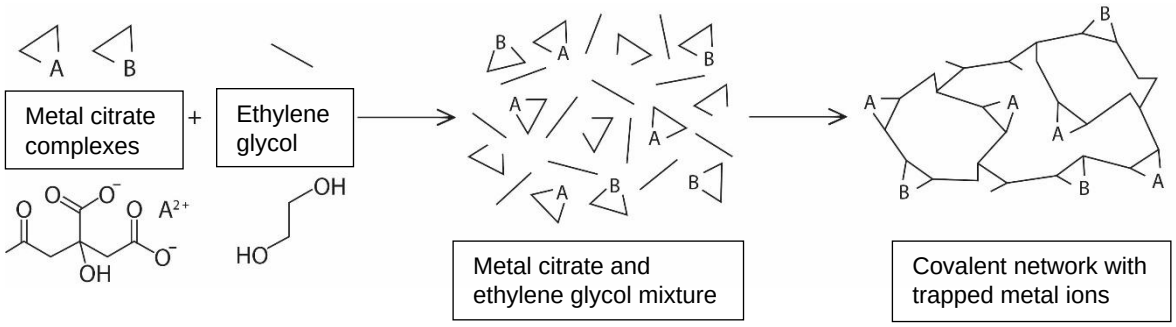

Figure 1.3.4: *Schematic of the stages involved during the Pechini sol-gel method*

1.3.2 Catalysis

In 1971 it was first observed that perovskite-type oxides, such as $LaCoO_3$, have the potential to become viable economic rivals to platinum gas phase catalysts for auto exhaust clean air technologies.[36] However, at low concentrations of CO the percentage conversion was significantly lower than for Pt based catalysts, along with their high susceptibility to SO_2 poisoning.[37] Perovskites are commonly used as catalysts due the incorporation of transition metals at the B site within their structure. Transition metals are known to show good catalytic activity as a result of their redox capabilities whereby the electronic structure readily changes oxidation state to allowing species to adsorb and desorb from their surface. The

huge versatility of the perovskite composition and structure allows for tailoring of the oxygen and cation stoichiometry to promote their catalytic properties further. Perovskites benefit from a higher thermal stability compared to that of single metal oxides, which easily oxidise at high reaction temperatures.[24]

With the B-site cation surrounded by an octahedron of oxygen ligands in its bulk perovskite state, at the surface it can be suggested to have a 5-fold coordination, BO_5; this leaves an available site for absorbates. For example, when the vertical oxygen is absent at the terminating surface, the orientation of the e_g orbitals favours a strong overlap with absorbing species at the surface. The nature of this e_g energy states is, as previously discussed, dependent on the choice of B cation and its number of *d* electrons.[26] This corresponds to Sabatier's principle (introduced in section 1.2.1) which describes the how the interaction between the transition metal and the substrate effects the catalyst activity. Performing CO oxidation over La A-site perovskites indicated that with decreasing e_g occupancy came increased activity, leading to subsequent perovskite research with Mn and Co B-sites.[25]

A mechanism in which perovskites performed oxidation catalysis was proposed by Voorhoeve *et al.;* where it was said to be either suprafacial or intrafacial, at low or high reaction temperatures, respectively.[38] Weakly bound oxygen present at the surface of perovskites is assigned as α-oxygen, with lattice oxygen ascribed as β-oxygen. During a catalytic reaction α-oxygens are likely to desorb at lower temperatures from the surface of the perovskite catalyst (Figure 1.3.5a). This oxygen vacancy can then either be filled by an oxygen species from the catalytic reaction or from diffusion of oxygen from sub lattice layers (Figure 1.3.5b) and bulk perovskite (Figure 1.3.5c). Elevated temperatures can result in high oxygen mobility and improved catalytic activity, but also the reduction of the B-site, causing

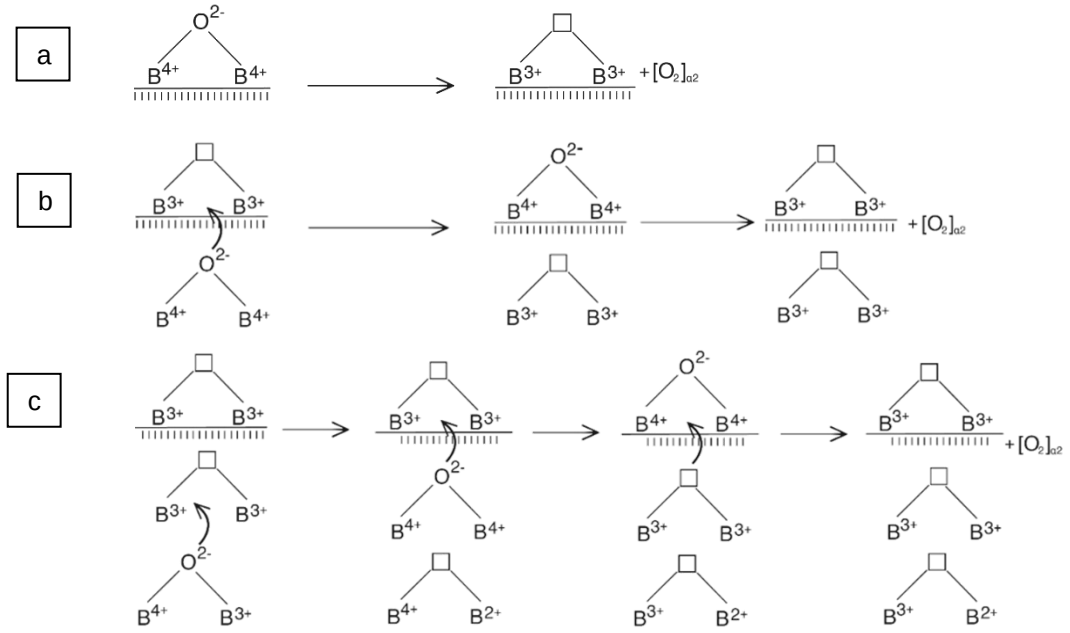

Figure 1.3.5: *Schematic to demonstrate redox capabilities of the B cation site as oxygen is* ***(a)*** *desorbed from the surface,* ***(b)*** *sub-lattice layers and* ***(c)*** *oxygen mobility from bulk perovskite*

deactivation of the perovskite catalyst.[39] Therefore, the mechanism that takes place is highly dependent on structure, *i.e.* selection of A and B sites, and reaction temperatures.

1.4 Mechanochemistry

Solid-state chemical transformations, induced by the mechanical energy of milling and grinding, for the formation of new solid phases is known as mechanochemistry. This alternative synthetic route has rapidly grown in interest due to its compliance cleaner and more sustainable process.[40] Mechanochemistry benefits from reduced process steps, removal of pH control, filtration and washing, which predominantly result from the absence of solvent.[3,41] However, the rapid movement of milling jars and constant impact of the milling media have limited the research and understanding into this preparation route. Furthermore, milling parameters often require a high level of optimisation for each individual material, as controlling the final material properties is commonly difficult in mechanochemistry. Here, a brief overview of the mechanochemical synthesis, specifically for inorganic materials, has now been discussed along with its advantages and challenges in becoming a viable industrial technique.

1.4.1 A brief history

Heinicke that established mechanochemistry as a branch of chemistry which deals with the chemical and physio-chemical transformations of materials produced by the effect of mechanical energy.[42] The term mechanochemistry was first published back in 1894, yet the initial description of this process can be traced back as far as 300 BC in the preparation of mercury from HgS.[41,42] Further examples of mechanochemical reactions are recorded from 300 BC all the way through to the 19th Century, however, it was *Ostwald* in 1887 that gave the name "*mechanochemistry"* to the process in the Textbook of General Chemistry.[43] Though it has been widely known and used for hundreds of years it has not been until the last few decades that its science and understanding has been properly investigated, with the number of publications increasing dramatically within the last 30 years.[44]

In the early stages mechanochemical action was primarily used for the size reduction or dispersion of particles; *Huttig* suggested that mechanochemistry only results in the deformation of lattice bonds without the formation of new substances, assuming a purely physical affect.[28,41,45] However, *Spring* studied how mechanical action resulted in a chemical reaction, observing the crystallisation of new amorphous phases under compression stress.[46] This was closely followed by *Carey Lea* who observed $MgCl_2$ and AgCl to both decompose under the grinding action of a pestle and mortar yet sublime or melt undecomposed, respectively, when heated.[46] *Carey Lea* showed that mechanical action did

not only bring about a chemical change but that the kinetics of the reaction and properties of the final product were remarkably different to those synthesised by thermochemical reactions.[28] This and the combination of numerous other researchers led to the classification of mechanochemistry as a branch of chemistry in 1919.[46]

1.4.2 Background

The rapid growth in interest and development of mechanochemistry over recent years has been driven largely by the need for more environmentally and economically solutions within chemical industries.[40] This preparation route provides a 'one-step' synthesis to produce materials with enhanced properties for applications in pharmaceuticals, waste management, metal alloying and catalysis.[28,47,48] It offers a rapid and solvent-less route for the efficient mixing, particle size reduction and formation of new powered materials.[49] Recent research has focused on not only extending the use of this synthetic route to a wider range of nanomaterials but also on understanding and monitoring the mechanochemical mechanism.

The mechanical action of a mill first allows for improved mixing and particle size reduction, thus improving contact between the reagents. This mechanical action then transfers energy in the form of compression, shear or friction, due to collisions between the wall of the jars and milling media, to form new interfaces and surfaces on the powdered precursors to induce chemical transformations (Figure 1.4.1).[46] Mechanochemical action can vary depending on the design of mill used, for example it can be constant, such as hydrostatic compression, or supplied in continuous short pulses (section 1.4.3). These different mechanochemical treatments greatly affect the outcome much be considered when selecting the application of mechanochemistry. For example, relaxation of the

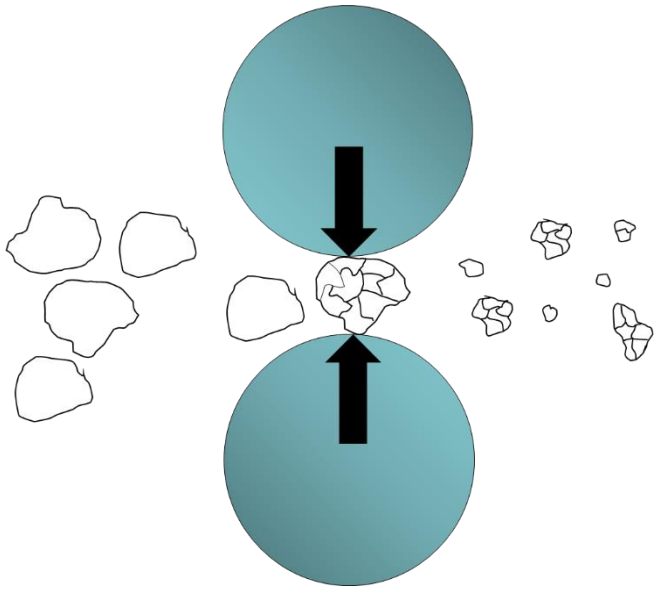

Figure 1.4.1: *Illustration of milling media under mechanochemical action results in the crushing and chemical transformation of precursor materials*

mechanical stress after a short pulse mechanical action event can proceed via multiple different channels, which in turn effects the chemical changes in the system.[50]

A mechanochemical reaction is said to be governed by kinetics, as during milling there is limited time and equilibrium products often cannot form. The formation of these metastable products indicates the differences compared to traditional thermally induced processes.[51] The species originate from the mechanical action inducing dislocations and defects to produce a high level of local strain into the structure of a precursor material, e.g. when a linear bond angle becomes bent. This is said to decrease the energy gap between the highest occupied molecular orbital (HOMO) and the lowest unoccupied molecular orbital (LUMO) energy levels, thus decreasing the bond stability (Figure 1.4.2). This now provides a greater opportunity for chemical reactions to take place.[52] This highlights the clear differences between mechanical energy and thermal induced processes, with the former being under non-equilibrium conditions, forming metastable intermediates as a consequence of mechanical deformation.[28]

A generalised theoretical explanation of mechanochemical reactions is extremely difficult to achieve as often reactions are specific to the individual system whilst involving a variety of different length and time scales.[46] Therefore numerous theories and models exist for the hypothesis of mechanical activation of chemical reactions. Some examples of these are the *hot-spot theory* that suggests friction causes temperatures of up to 1000 K near the tip of a crack, or the *magma-plasma model* which suggests that a large amount of energy is released during the contact of colliding particles leading to the emission of excited fragments.[41] The reaction will then take place in the plasma at the surface of particles in the excited state. Countless more theories exist, including the rapid induction of defects followed by propagation, and it has therefore been concluded that mechanically activated reactions do not obey a single mechanism. Differences arise between each particular system, not only due to starting precursors but also the huge amount of variables such as,

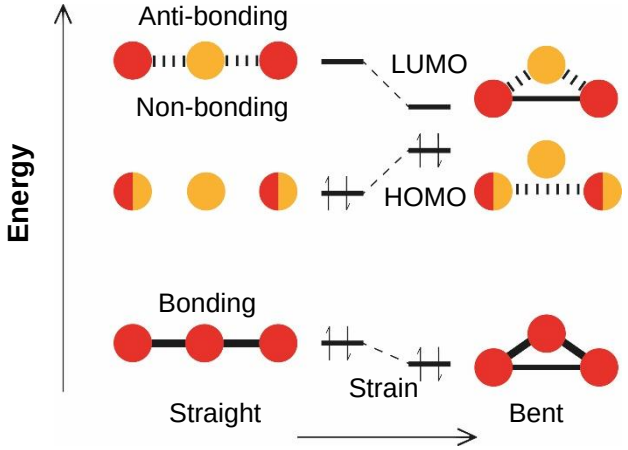

Figure 1.4.2: *Schematic showing a Walsh energy-level diagram for H_3 for the effect of sheer on a LUMO-HOMO gap*

milling material, milling media, speed, reagent ratios, type of mill and milling atmosphere.[41,45]

1.4.3 Mill design

Milling technologies have continued to develop alongside the growing interest within mechanochemistry. With unique mill designs comes different mechanical action, which in turn can lead to a change in the final material structure and properties. The outlining principles of high energy mills will now be discussed.

The most commonly used mills to perform mechanochemical reactions is reported in literature as either vibrational, planetary and attrition mill designs.[40,41,53] These all perform a combination of shear and impact mechanochemical treatment, however, with varying degrees and ratios.[50] A vibrational mill (Figure 1.4.3A, E) uses a circular or elliptic trajectory motion with a combination of factors, such as the speed of vibration, horizontal & vertical amplitude and phase angle. They are often applied during the preparation of fine materials, requiring much longer milling times due to their lower energy output.[54]

Attrition milling, first invented in 1922, was initially only used to homogeneously disperse particles and it was not until 1970 that the first high energy attrition mill was applied to the mechanochemistry of metal alloying. Attrition mills (Figure 1.4.3B) have a rotating central drive shaft with multiple impellers alongside milling media within the grinding chamber. This mill is commonly used for large quantities and benefits from its energy input being directly transferred to the media, rather than being applied to rotating or vibrating the milling chamber.[55]

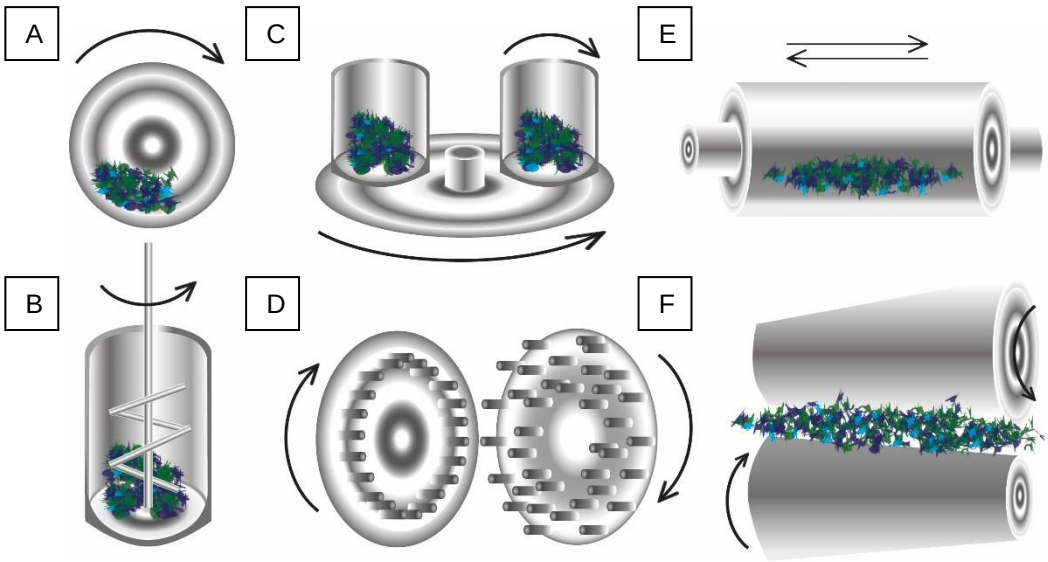

Figure 1.4.3: *Types of high energy mills:* ***(A)*** *Roll mill* ***(B)*** *attritor ball mill* ***(C)*** *planetary ball mill* ***(D)*** *pin mill* ***(E)*** *vibrational mill* ***(F)*** *rolling mill*

Planetary ball mills (Figure 1.4.3C) benefit from high energy density alongside and simple set-up, handling and cleanability, however, they are often limited to small scale reactions, 5 – 50 g.[41] Here, the grinding jars rotate in a planet-like movement around a central axis at both the centre of the mill and about the grinding jar (Figure 1.4.4). These two rotations acting in opposite directions form a centrifugal force, causing the milling media to run down the grinding jar wall, lift and then travel through the central chamber to collide against the opposite wall.[56] These mills exploit the principle of centrifugal acceleration rather than gravitational acceleration used by vibrational or attrition mills, resulting in a higher mechanical activation after shorter milling times. Other mill designs exist, such as pin and rolling mills, performing impact or sheer mechanochemical action, respectively (Figure 1.4.3D, F).

Limited research has been focused around industrial approaches from lab-scale experiments. Of the large array of milling equipment and technologies attrition mills represent the most suitable for linear scale-up for industrial applications, with vibrational and planetary ball mills being challenging due their high volume of moving parts. Though *Blair et al.* were able to show successful scalability, highlighting the importance of impact forces and macroscopic mixing, vastly more research is required into a variety of different systems for specific applications.[53]

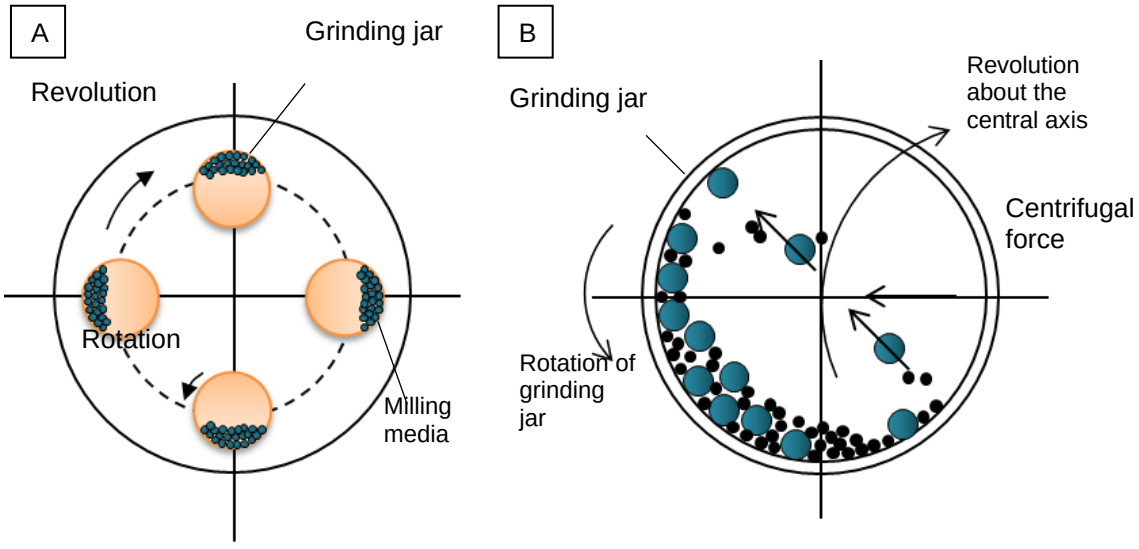

Figure 1.4.4: (A) *A schematic of a 4-station high energy planetary ball mill* ***(B)*** *Movement of milling media and material within a one rotating grinding jar of a planetary ball mill*

1.5 Aims and objectives

Developing sustainable synthetic routes to produce 'earth-abundant' catalysts can help towards finding alternatives to the commercial PGMs currently used.[24] Furthermore, despite the extensive possible uses, commercial success for perovskite-type materials is challenging to achieve. This presents a clear opportunity to progress the mechanochemical synthesis of perovskites and optimize the performance in renewable energy conversion technologies and emission control strategies.[24,57] However, there are significant challenges in mechanochemical reactions; controlling uniform stoichiometry and structure of the resultant materials has proved difficult.[41] This is further complicated by the dynamic nature of the milling equipment and use of grinding media, alongside the formation of amorphous structures during milling.[58] To develop the technology an improved understanding of the underlying chemical steps is required. Therefore, advanced characterisation techniques, such as X-ray absorption spectroscopy (XAS), high energy resolution fluorescence detection (HERFD) and X-ray emission spectroscopy (XES), have been utilised in order to understand the chemical transformations occurring within ball-milling. XAS is highly sensitive to the local structure of materials without the need for periodic ordering; it is ideally suited to studying samples prepared through ball-milling as it provides information on both amorphous and crystalline phases.[59] In addition these materials have shown promising catalytic activity at low temperatures towards deN_2O, which has been detected by using transmission electron microscopy (TEM) and X-ray photoelectron spectroscopy (XPS).

Herein, the mechanochemical synthesis of the perovskite $LaMnO_3$, from La_2O_3 and Mn_2O_3 has been undertaken, and a reaction pathway has been proposed for its formation. Moreover, the performance of these materials has been demonstrated towards deN_2O and highlights how mechanochemical routes introduce active sites for catalysis. The understanding gained from the $LaMnO_3$ system has then been combined with other A-site manganate perovskites to begin to set out generalised rules for the mechanochemical synthesis of mixed metal oxide materials.

1.6 References

1 J. H. Clark, *Green Chem.*, 1999, 1–8.

2 J. F. Jenck, F. Agterberg and M. J. Droescher, *Green Chem.*, 2004, **6**, 544.

3 X. Guo, D. Xiang, G. Duan and P. Mou, *Waste Manag.*, 2010, **30**, 4–10.

4 P. Anastas and N. Eghbali, *Chem. Soc. Rev.*, 2010, **39**, 301–312.

5 J. N. Armor, *Catal. Today*, 2011, **163**, 3–9.

6 S. M. George, *Chem. Rev.*, 1995, **95**, 475–476.

7 A. Prüss-Üstün and C. Corvalän, *World Heal. Organ.*, 2007, **12**, 115–116.

8 R. Sheldon, I. Arends and U. Hanefeld, *Introduction: Green Chemistry and Catalysis*, Wiley-VCH, 2007.

9 S. Keav, S. Matam, D. Ferri and A. Weidenkaff, *Catalysts*, 2014, **4**, 226–255.

10 K. Kanemoto, D. Moran and M. Lenzen, *Glob. Environ. Chang.*, 2014, **24**, 52–59.

11 P. Seegopaul, M. Bassir, H. Alamdari and A. Van Neste, *Cleantech 2007*, 2007, 274.

12 T. Dutta, K. H. Kim, M. Uchimiya, E. E. Kwon, B. H. Jeon, A. Deep and S. T. Yun, *Environ. Res.*, 2016, **150**, 182–190.

13 O. Deutschmann, H. Knözinger, K. Kochloefl and T. Turek, *Heterogeneous catalysis and solid catalysts*, Wiley-VCH, 2009.

14 M. Bowker, *The Basis and Applications of Heterogeneous Catalysis*, Oxford University Press, 1998.

15 J. R. Anderson and M. Boudart, Eds., *Catalysis: Science and Technology*, Springer Berlin Heidelberg, 1983.

16 I. P. Silverwood, S. F. Parker and C. R. A. Catlow, *Phys. Chem. Chem. Phys.*, 2016, **18**, 17140–17140.

17 I. Chorkendorff and J. W. Niemantsverdriet, in *Concepts of Modern Catalysis and Kinetics*, WILEY-VCH Verlag, 2007.

18 W. H. Weinberg, *Acc. Chem. Res.*, 1996, **29**, 479–487.

19 J. R. H. Ross, 'The Kinetics and Mechanisms of Catalytic Reactions' in *Contemporary Catalysis*, Elsevier B.V., 2019, pp. 161–186.

20 H. Aono, M. Tsuzaki, A. Kawaura, M. Sakamoto, E. Traversa and Y. Sadaoka, *J. Am. Ceram. Soc.*, 2001, **75**, 969–975.

21 J. Suntivich, H. A. Gasteiger, N. Yabuuchi, H. Nakanishi, J. B. Goodenough and Y. Shao-Horn, *Nat. Chem.*, 2011, **3**, 546–550.

22 M. Shaterian, M. Enhessari, D. Rabbani, M. Asghari and M. Salavati-Niasari, *Appl. Surf. Sci.*, 2014, **318**, 213–217.

23 M. N. Iliev and M. V. Abrashev, *J. Raman Spectrosc.*, 2001, **32**, 805.

24 N. Labhasetwar, G. Saravanan, S. K. Megarajan, N. Manwar, R. Khobragade, P. Doggali and F. Grasset, *Sci. Technol. Adv. Mater*, 2015, **16**, 1–13.

25 R. J. H. Voorhoeve, J. P. Remeika and L. E. Trimble, *Ann. N.Y. Acad. Sci.*, 1976, **2**, 272.

26 J. Hwang, R. R. Rao, L. Giordano, Y. Katayama, Y. Yu and Y. Shao-Horn, *Science*, 2017, **358**, 751–756.

27 R. Freitag and J. Conradie, *J. Chem. Educ.*, 2013, **90**, 1692–1696.

28 P. Granger, V. I. Parvulescu, S. Kaliaguine and W. Prellier, in *Perovskites and Related Mixed Oxides Concepts and Applications*, eds. P. Granger, V. Parvulescu, S. Kaliaguine and W. Prellier, Wiley-VCH, 2015, pp. 3–23.

29 M. A. Pena and J. L. G. Fierro, *Chem. Rev.*, 2001, **101**, 1981–2017.

30 A. E. Danks, S. R. Hall and Z. Schnepp, *Mater. Horizons*, 2016, **3**, 91–112.

31 *US Pat. 3,330,697*, 1967, 2. – 'Method of preparing lead and alkaline earth titanates and niobates and coating method using the same to form a capacitor'

32 A. E. Giannakas, A. K. Ladavos and P. J. Pomonis, *Appl. Catal. B Environ.*, 2004, **49**, 147–148.

33 S. Kaliaguine, A. Van Neste, V. Szabo, J. E. Gallot, M. Bassir and R. Muzychuk, *Appl. Catal. A Gen.*, 2001, **209**, 345–358.

34 Q. Zhang and F. Saito, *J. Alloys Compd.*, 2000, **297**, 99–103.

35 B. D. Stojanovic, *J. Mater. Process. Technol.*, 2003, **143**–**144**, 78–81.

36 W. F. Libby, *Science*, 1971, **171**, 499–500.

37 R. J. H. Voorhoeve, D. W. Johnson, J. P. Remeika and P. K. Gallagher, *Science,* 1977, **195**, 827–834.

38 M. Misono, *Stud. Surf. Sci. Catal.*, 2013, **176**, 67–95.

39 H. Najjar, J. F. Lamonier, O. Mentré, J. M. Giraudon and H. Batis, *Appl. Catal. B Environ.*, 2011, **106**, 149–159.

40 J. L. Do and T. Friščić, *ACS Cent. Sci.*, 2017, **3**, 13–19.

41 P. Baláž, M. Achimovičová and M. Baláž, *Chem. Soc. Rev.*, 2013, **42**, 7571–7637.

42 G. Heinicke, *J. Synth. Lubr.*, 1985, **3**, 55–56.

43 V. V. Boldyrev, *Russ. Chem. Rev.*, 2006, **75**, 177–189.

44 C. Suryanarayana, E. Ivanov and V. . Boldyrev, *Mater. Sci. Eng. A*, 2001, **304**, 151–158.

45 F. J. Gotor, M. Achimovicova, C. Real and P. Balaz, *Powder Technol.*, 2013, **233**, 1–7.

46 L. Takacs, *Chem. Soc. Rev.*, 2013, **42**, 7649–7659.

47 Q. Zhang and F. Saito, *Adv. Powder Technol.*, 2012, **23**, 523–531.

48 T. Frišči, I. Halasz, P. J. Beldon and A. M. Belenguer, *Nat. Chem.*, 2012, **5**, 66–73.

49 C. Xu, S. De, A. M. Balu, M. Ojeda and R. Luque, *Chem. Commun.*, 2015, **51**, 6698–6713.

50 E. Boldyreva, *Chem. Soc. Rev.*, 2013, **42**, 7719–7738.

51 T. D. Hatchard, A. Genkin and M. N. Obrovac, *AIP Adv.*, 20107, **7**, 1–12.

52 J. J. Gilman, *Science.*, 1996, **274**, 65.

53 R. G. Blair, K. Chagoya, S. Biltek, S. Jackson, A. Sinclair, A. Taraboletti and D. T. Restrepo, *Faraday Discuss.*, 2014, **170**, 223–233.

54 P. Balaz, *Mechanochemistry in Nanoscience and Minerals Engineering*, Springer Berlin Heidelberg, 2008.

55 R. W. Rydin, D. Maurice and T. H. Courtney, *Metall. Trans. A*, 1993, **24**, 175–185.

56 C. F. Burmeister and A. Kwade, *Chem. Soc. Rev.*, 2013, **42**, 7660.

57 M. Konsolakis, *ACS Catal.*, 2015, **5**, 6397–6421.

58 V. Šepelák, S. Bégin-Colin and G. Le Caër, *Dalt. Trans.*, 2012, **41**, 11927.

59 F. Ali, A. V. Chadwick and M. E. Smith, *J. Mater. Chem.*, 1997, **7**, 285–2

Chapter 2

Experimental methods

This section details the background and theory of experimental methods used throughout this thesis. A variety of lab-based techniques, along with a significant proportion of the synchrotron-based methods, has been performed to achieve advanced characterisation and understanding of complex materials. An emphasis has been placed on X-ray absorption and emission spectroscopy techniques, which have been detailed along with complementary lab-based characterisation. Specific experimental conditions, catalyst synthesis and activity testing have been detailed in the appropriate chapter material and methods section.

2.1 X-ray diffraction

Powder X-ray diffraction (XRD) is a common lab-based technique used to identify and analyse crystalline bulk structures. The resulting diffraction pattern can be used to determine not only the composition of crystal structures but also to refine lattice parameters and particle size.

2.1.1 Theory

Crystalline materials are considered to consist of atoms with long range order. Here the electron density from the atoms acts as a lattice plane within the structure. When an incident X-ray beam interacts with these lattice planes of periodically spaced atoms in a material, the light can diffract with either constructive or destructive interference. In order to predict whether diffraction will take place, Bragg's Law must be satisfied (Equation 2.1.1). For example, when an X-ray beam is diffracted by two lattice planes (n = 2) that are in-phase constructive interference occurs and a peak appears on the diffraction pattern (Figure 2.1.1). Therefore, using a fixed incident wavelength, Bragg's Law provides information on interatomic distances and dimensions of a crystal unit cell. Powder XRD uses this basis of single crystal theory, however, can measure multiple crystals/poly-crystalline systems, at

different orientations within one sample. XRD of powdered samples compresses the diffraction occurring in all directions into one dimension, known as 2θ.[1]

$$n\lambda = 2d_{hkl} \sin\theta$$

Equation 2.1.1: *Where n is an integer, λ is the incident X-ray wavelength, θ incident angle of the incident X-ray beam, also known as the Bragg angle and d_{hkl} is the interatomic distance between lattice planes.*

Each lattice plane can be further defined by using the Miller indices, hkl, where each d_{hkl} is associated with a Bragg peak on the diffraction pattern. d_{hkl} is defined as a vector, which is draw from the origin of the unit cell to intersect the crystallographic plane (hkl) at a 90 ° angle. The position of this diffraction peak will result from an average of the atomic distance in the crystal. Therefore, any changes in average bond distances will change the diffraction peak position.

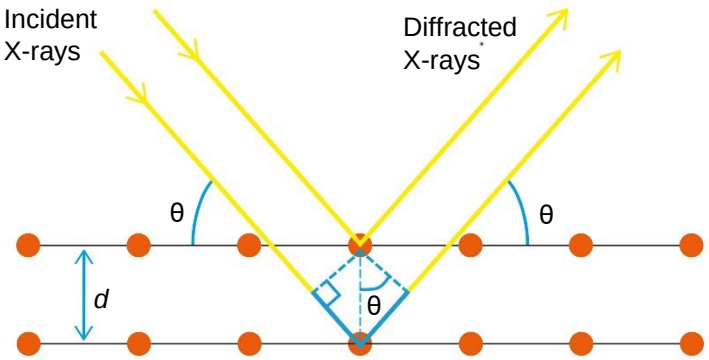

Figure 2.1.1: *A diagram representing Brag's Law of reflection and a* ***(B)*** *schematic of an X-ray diffractometer*

2.1.2 Instrument set-up

The monochromatic X-ray radiation is typically generated within a sealed tube. Here, high energy electrons, generated by a tungsten filament, are accelerated towards a Cu anode. This results in the ejection of a core electron, which is then filled by an electron from an out shell, releasing Cu Kα radiation (1.54 eV). This X-ray radiation next passes to a single crystal monochromator, to narrow the wavelength distribution and collimate the beam. A monochromator also uses Bragg's Law to diffract only specific wavelengths due its fixed *d* spacings within the crystal. Mirrors are used to focus the beam onto the sample, where only wavelengths that satisfy Bragg's Law are diffracted. These are detected using a goniometer circle set-up (Figure 2.1.2), where the sample is in a fixed sample position and both the source and detector move by either -θ or θ, respectively. Coherent diffraction leads to the observation of diffraction peaks, to make up a diffraction pattern of intensity with respect to 2θ. The 2θ position of each peak accesses the interlayer distance of atoms of the structure,

with the intensity corresponding to the percentage that refection is contributing to the pattern.

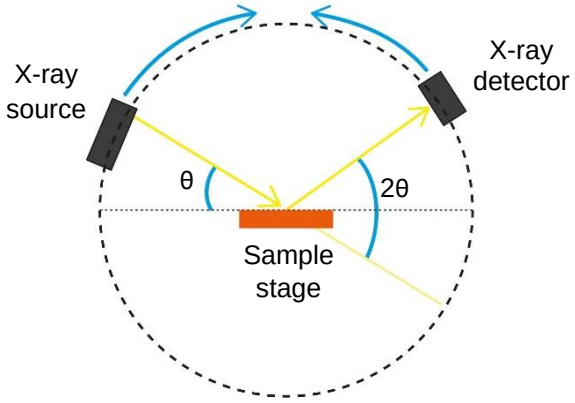

Figure 2.1.2: *Schematic of an X-ray diffractometer*

2.1.3 Data Analysis

After data collection, the Bruker DIFFRAC software package was used for phase identification, composition weight percentage analysis and calculating crystallite size. Initial phase identification was performed after background subtraction in DIFFRAC.EVA, whereby the most appropriate match was chosen from the Johnson Matthey crystallographic database. DIFFRAC.TOPAS was then used to perform Rietveld refinement to the chosen crystallographic information files (.cif). The Rietveld method of analysis allows for the assessment of powdered materials, using a step-scanned intensity of the data and least squares procedure to optimised and refine the fit.[2] This method accounts for the peak overlap that commonly occurs in powdered samples, which effect the Bragg peak intensities. Within DIFFRAC.TOPAS an optimised instrument file is loaded and the appropriate .cif and data files were then imported. Following a background subtraction, individual refinement of the different crystalline species was performed. Additional peaks were added to account for trace species, amorphous areas or for the inert sample holder.

2.2 X-ray photoelectron spectroscopy

X-ray photoelectron spectroscopy (XPS) is a near surface-sensitive analytical technique, where X-rays are used to probe only the first few nanometers of a surface. It can provide quantitative analysis of the surface elemental composition, oxidation states and, with catalytic materials, information about the nature of active sites. It has been used consistently throughout this work for understanding how the mechanochemical synthesis affects the surface composition and properties, and in turn the effect this has on the catalytic performance.

2.2.1 Theory

In XPS the sample is exposed to low energy monochromatic X-rays where the energy is absorbed by an atom, causing photoelectrons to be ejected and creating a core hole (Figure 2.2.1). The ejected photoelectrons are measured for their kinetic energy, producing a photoelectron spectrum.[3] By applying Einstein's photoelectric equation (Equation 2.2.1) with a known incident X-ray energy and measured kinetic energy, the binding energy can be calculated (Equation 2.2.2). These binding energies are characteristic of specific elements, as well as their chemical environment. Assessing the position and intensity of the binding energies can provide information on the chemical state and the proportion of material at the surface, respectively.[4]

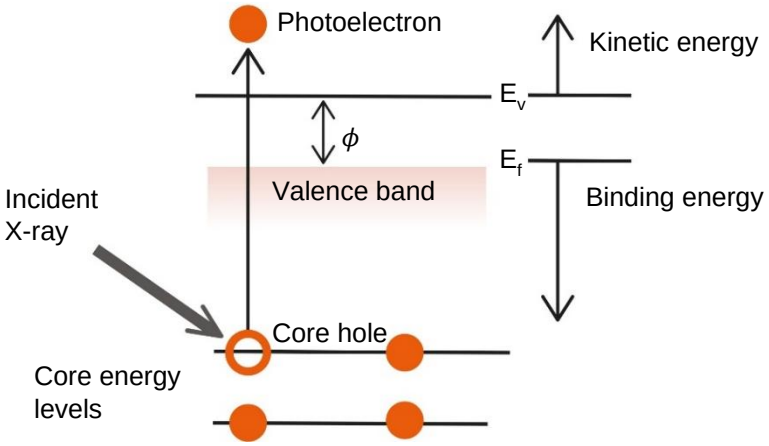

Figure 2.2.1: *Schematic of an incoming photon exciting an outer shell electron whereby the kinetic energy is measured*

$$E = h\,v$$

Equation 2.2.1: *Where E is the energy of the incident photon, h is Planck's constant, 6.62 x 10^{-34} J s, and v is the frequency, Hz*

$$BE = hv - (KE + \phi_{sample})$$

Equation 2.2.2: *Where BE is the binding energy, KE is the kinetic energy of the ejected photoelectron and φ is spectrometer work function which corresponds to the energy required to travel the detector, constant for each instrument.*

Additional peaks can also observed within the XPS spectrum. These occur when electrons from higher energy orbitals relax to fill the core hole the relaxation energy can be transferred to another electron. This electron is then ejected, with a specific kinetic energy, known as an Auger electron. Though the Auger process is not as chemical specific as the

main binding energy peaks in XPS, the kinetic energy of these electrons is still characteristic of the sample and can help distinguish between metals oxides and metal nitrides.[5]

XPS is often thought as a purely surface sensitive technique, yet it detects ejected electrons from a few nanometres below the surface. The kinetic energy of the electron is an indication of depth within the sample from which orbital it has been eject from. It is important to remember when performing XPS experiments with lab-based equipment they have a fixed incident X-ray energy source. Therefore, solving Equation 2.2.2 for the kinetic energy, whereby the binding energies and incident energy are static, results in varying kinetic energies and thus different penetration depths for each XPS elemental region.

2.2.2 Instrument set-up

A typical X-ray photoelectron spectrometer comprises of an X-ray source, sample stage, electron energy analyser and a detector, all contained within an ultra-high vacuum (UHV), 10^{-8}–10^{-10} mbar (Figure 2.2.2). X-rays are generated by bombarding an anode, commonly Al or Mg, with electrons to produce Al Kα or Mg Kα radiation at photoenergies of either 1486.6 eV or 1253.6 eV, respectively. The X-ray beam is then focused onto the sample using a crystal monochromator. After photoelectrons are emitted from the sample, they are transferred to the electron energy analyser, which ensures only electrons with given energies, known as the pass energy, reach the detector. Due to the low energy signals produced by XPS, detection requires the use of an electron multiplier to amplify this signal. Here, photoelectrons collide with the walls, emitting secondary electrons, which in turn cause a cascade of electrons to reach the anode, where the voltage is measured. XPS experiments traditionally require an UHV as low energy electrons are easily scattered by residual gas molecules, reducing signal and increasing the signal-to-noise-ratio. Furthermore, these residual gas molecules can also form a monolayer on the surface of the sample at a much quicker rate than a typical scan time.[6]

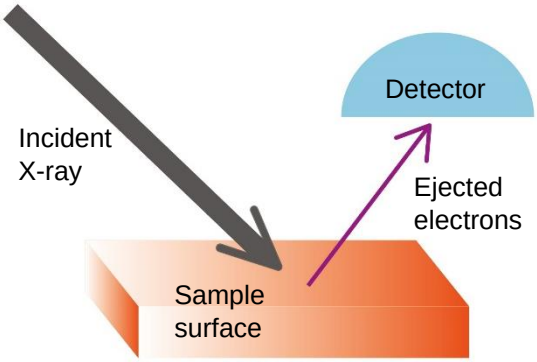

Figure 2.2.2: *A simplified XPS experimental set up*

2.2.3 Near ambient pressure X-ray photoelectron spectroscopy

Performing *ex situ* XPS under vacuum can produce a good fingerprint of the surface properties and composition, however, materials often present vastly different properties when performing under working conditions. In recent years significant developments have been made towards performing XPS experiments under near ambient pressures (NAP). Within this work NAP-XPS has been coupled with the use of synchrotron radiation by performing *in situ* catalytic experiments at the B07-C (VerSoX) soft energy beamline, at the Diamond Light Source, Didcot, UK. Using synchrotron radiation allows for a tuneable incident beam for depth profiling, and quick acquisition times, vital when under ambient gas conditions.

The B07-C beamline utilised synchrotron radiation produced by a bending magnet, to produce soft energy X-rays, 250 – 2800 eV. The X-ray radiation is specifically optimised using a configuration of toroidal, plane, cylinder and elliptical mirrors before reaching the exit slits and then the sample (Figure 2.2.3). An UHV it kept continuously between the synchrotron ring and the analysis chamber to maintain optical reflectively of the soft X-rays and to avoid contamination, such as carbon, from entering the system.[7] For NAP-XPS to be possible the optics and experimental end station, including sample stage, analyser and detector, are connected to different pumping stages.[8] Synchrotron radiation is discussed later in section 2.10.

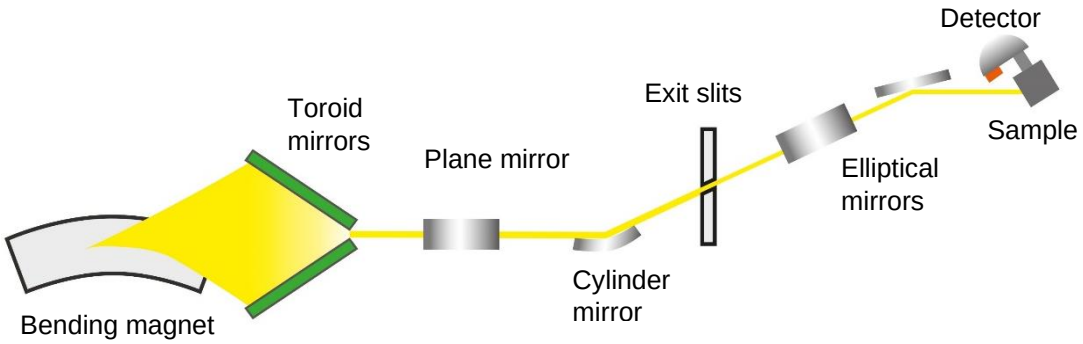

Figure 2.2.3: *Schematic of the B07-C VerSoX beamline configuration*

2.3 Transmission electron microscopy

Transmission electron microscopy (TEM) is useful tool in obtaining microstructural and electronic information of materials. Along with allowing for the visualisation of morphology and particle size, TEMs can also perform elemental analysis and distribution, with some even able to provide spatial resolution to the atomic level.

2.3.1 Theory

The resolution of an optical microscope is limited by the wavelength of visible light. Here, however, when electrons are considered to behave as a wave, the de Broglie equation can be applied (Equation 2.3.1). The resulting de Broglie wavelength of the electron is considerably shorter than that of visible light. Furthermore, the electron beam is accelerated to greater than 400 kV voltages (Equation 2.3.2), results in a resolution that far surpasses that of optical microscopes.

$$\lambda = h/p$$

Equation 2.3.1: *Where h is Plank's constant and p is related to the electron's momentum*

$$\lambda = h\sqrt{(2m_eV)}$$

Equation 2.3.2: *Where m_e is the mass of an electron and V is the velocity*

For successful TEM measurements, the sample must be extremely thin (< 100 nm) to allow for the transmission of the electron beam through the material. Images are produced when the electron beam interacts with the electron density of the sample. How the sample interacts with these electrons depends on the material composition and/or thickness to produce a contrast image. For example, when the electron beam interacts with the sample some electrons are then scattered or disperse, depending on the density of the material. If an area of the sample is composed of a high mass density, then the electrons scatter more and thus produce a darker region. Unscattered electrons hit the fluorescent viewing screen behind the specimen, to result in brighter areas within the image.[9]

2.3.2 Instrument set-up

A TEM is comprised of five parts; (1) the electron source, (2) a condenser lens, (3) an objective lens (4) the sample and (5) magnifying lens/eye piece (Figure 2.3.1). Though the proportion of lenses may change between microscopes these basic components make up most TEMs. A vacuum system throughout the TEM is vital due to the large instrument path length (1 – 2 m) required of the electron. A typical vacuum required is ~10^{-4} Pa, however, for higher voltage and resolution systems a range of at least 10^{-7} – 10^{-10} Pa is required.

First, the sample is loaded in the vacuum chamber, onto the illumination stage. Electrons are commonly generated by supplying a high current to LaB_6 or a tungsten filament at the source. When sufficient current has been applied to the filament, electrons are emitted and are accelerated to at least 400 kV, before travelling down the microscope. These high energy electrons are then guided using a variety of magnetic or electrostatic lenses, to focus the electron beam towards the optical axis. The image of the sample is then

magnified and focused to be viewed from an eye piece or imaging device, such as a charge coupled device (CCD) digital image sensor. Different TEM instrumental models have been developed and produced to fit the different experimental requirements and can be applied alongside a variety of other techniques.[10]

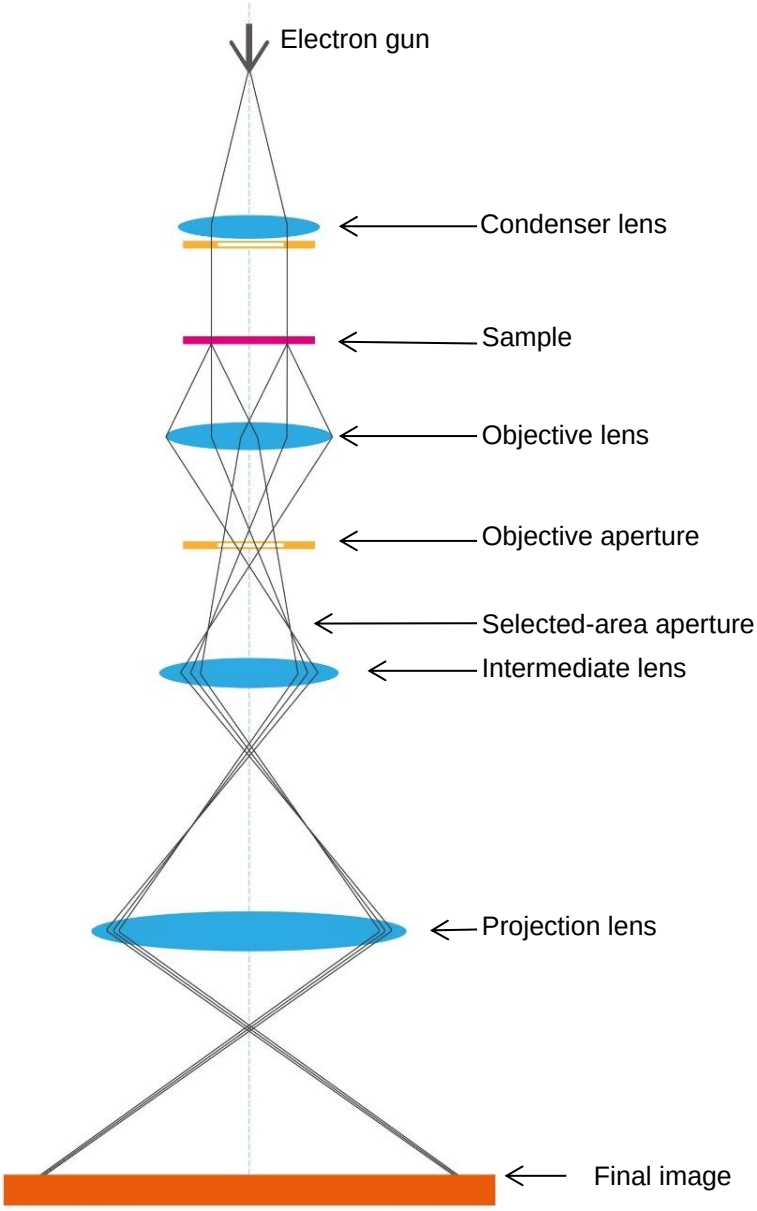

Figure 2.3.1: *Diagram representing the path of an electron beam through a transmission electron microscope*

2.3.3 Scanning transmission electron microscopy

To acquire images via TEM, a scanning transmission electron microscopy mode (STEM) is commonly selected and has been used throughout this project. Within this mode the high energy electron beam is confined to an extremely fine spot, which then scans over an area of the sample. The signal is collected after transmission through the sample underneath the

specimen by a detector, such as a high-angle annular dark-field (HAADF) detector. A HAADF detector is commonly installed due to its capabilities of being able to collect signals at high semiangles of $\theta_3 > 50$ mrad.[11]

By performing characterisation in this STEM mode, a contrast image of the composition *Z* character is produced. The high energy electron beam is focused on a very fine spot and scanning over the sample it limits the exposure time, removing full illumination of the sample by TEM mode and possible beam damaging effects. STEM further overcomes the limitations of TEM mode, whereby it does not suffer from the chromatic aberration effect, which can lead to blurry and indistinct images at larger sample thicknesses. It also allows for the elemental analysis, such as X-ray energy dispersive spectroscopy (EDS) or electron energy loss spectroscopy (EELS), to be performed alongside STEM imagining.[11]

2.3.4 Elemental Analysis

Providing complimentary information to imaging of the morphology and crystalline structure, the collection of elemental analysis, EDS and EELS, in tandem to imaging is a vital tool in materials characterisation.

Both EDS and EELS techniques are based on the same underlying principles, whereby the electron beam excites an electron from a core shell of the sample, creating a hole. In EDS, an electron from an outer shell then relaxes, and the emitted X-ray radiation is measured. This X-ray emission is element specific and therefore provides information on the elemental composition.

Within EELS an electron spectrometer records the energy lost from the incident electron beam due to inelastic interactions with the sample to produce structural and electronic information.[12] At the valence region of an EELS spectrum, <50 eV, dominant features arise from collective resonant plasmon oscillations of the valence electrons and interbank transitions from valence to conduction bands.[13] However, at energy losses of above 50 eV the spectrum shows characteristic features called ‘ionisation edges’. These edges are equivalent to those from X-ray absorption spectroscopy (XAS) (see section 2.9.1) and arise by the same process whereby an inner-shell electron absorbed enough energy to be excited into the continuum.[12] These edges are element specific and by applying elemental mapping with a high spatial resolution through EELS the material composition can be derived.

2.4 Surface area analysis

With the surface of a catalyst often considered crucial in determining reactivity, measuring the total surface area can often correlate to the catalytic capabilities of a material. Brunauer-Emmett-Teller (BET) theory is well established as a viable way to assess the surface area of heterogenous catalysts.[14] BET has been utilised within this project to understand the

effect of the mechanochemical synthesis on the material surface area with respect to their catalytic performance.

2.4.1 BET Theory

BET analysis applies an adsorption isotherm, whereby an inert gaseous species, such as N_2 or Kr, adsorb onto a surface at varying pressures. Based on the gas adsorption isotherm proposed by Langmuir, the BET model allows more than one layer of adsorbate molecules to form (Figure 2.4.1A). Therefore, two phases must now be considered; (1) the first monolayer interacting with the surface and (2) adsorbates interacting with subsequent layers. The later phase records a heat of adsorption comparable to the heat of vaporisation for the adsorbate. There are, however, limitations to this BET model due to the following assumptions:[14]

1. The surface is completely homogeneous.
2. All sites are equivalent, with the energy of an adsorbed molecule being independent to the presence of other molecules.
3. The surface only has a specific number of sights, which can only adsorb one molecule. Once all these sites are full no more adsorption can occur.

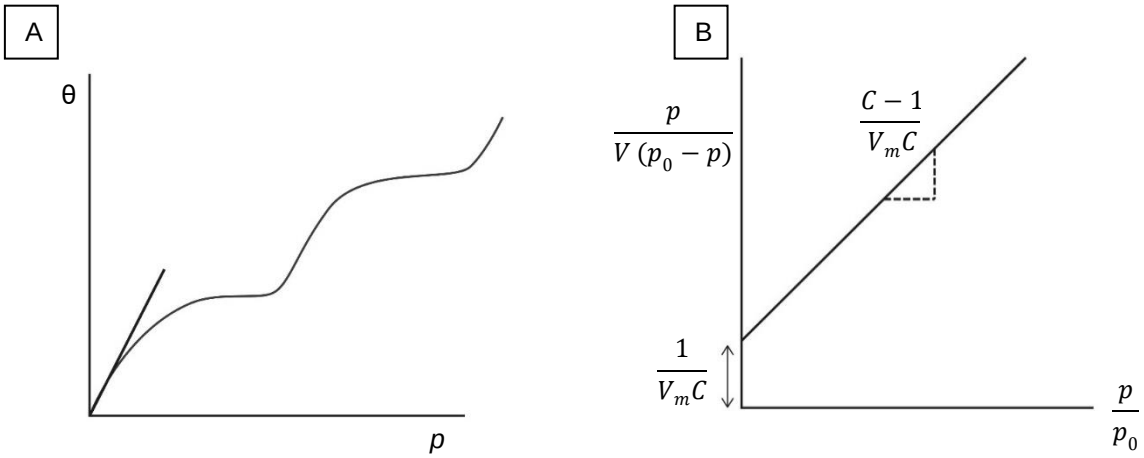

Figure 2.4.1: (A) *multilayer isotherm and* ***(B)*** *plot of equation 2.5.1.3 where* $\frac{p}{V(p_0-p)}$ *vs* $\frac{p}{p_0}$ *gives a straight line with a* $\frac{1}{V_mC}$ *intercept and a gradient of* $\frac{C-1}{V_mC}$

In order to calculate the specific surface area ***Equation 2.4.1*** is applied to understand how varying partial pressures can affect gas adsorption at the surface.

$$\frac{p}{\theta(p_0-p)} = \frac{1}{C} + \frac{C-1}{C} \times \frac{p}{p_0}$$

Equation 2.4.1: *Where* p_o *is the initial pressure,* p *is pressure and C is given in* Equation 2.4.2

$$C \approx e^{\frac{(\Delta H_D - \Delta H_{vap})}{RT}}$$

Equation 2.4.2: *Where ΔH_D is the enthalpy of desorption of the first layer, ΔH_{vap} is the enthalpy of vaporisation of the subsequent layers, R is the gas constant (8.314 J K^{-1} mol^{-1}) and T is temperature*

Rearranging Equation 2.4.1 into the form y = c + mx (Equation 2.4.3) allows for the data to then be plotted as a straight line (Figure 2.4.1B).

$$\frac{p}{V\,(p_0 - p)} = \frac{1}{V_m C} + \frac{C-1}{V_m C} \times \frac{p}{p_0}$$

Equation 2.4.3

Solving for the volume of the gas adsorbed, V_m, the specific surface area of the material, *S*, can be calculated by Equation 2.4.4.

$$S = \frac{V_m N_a a_m}{m}$$

Equation 2.4.4: *Where N_a is Avogadro's number ($6.022 \times 10^{23}\ mol^{-1}$), a_m is the effective cross-section area of one adsorbate molecule (0.162 nm^2 for N_2 and 0.195 nm^2 for Kr) and m is the mass of material (g).*

2.5 Inductively coupled plasma optical emission spectroscopy

Inductively coupled plasma optical emission spectroscopy (ICP-OES) is an elemental analysis technique. It allows for the identification and quantification of the composition of elements present within a sample.

This is achieved by passing the sample though an argon plasma, generated by accelerating electrons, to collide with an argon gas. As the atoms enter the plasma, they become ionised, due to a core electron being excited to a higher energy level. On relaxation of this excited state to fill the core hole an X-ray is emitted, characteristic of a specific element. Often an element has many excited and relaxed states, which ICP-OES can then these assign multiple wavelengths for identification of an element.

2.6 Testing Catalytic Performance

Within this work, the evaluation and characterisation of catalyst activity has been performed on a fixed bed, continuous flow Hiden CATLAB microreactor. This set-up is integrated with a Hiden Analytical QGA dynamic sampling mass spectrometer to allow for the *in situ* monitoring of resulting gas / vapour during catalytic reactions. Microreactors are commonly used in laboratories to mimic the conditions experienced in industrial set-ups, whilst benefiting from quick, versatile and accurate analysis during the development stages of new

catalytic materials. In this thesis the CATLAB microreactor has been predominantly used for understanding the link between the catalyst material properties and their activity towards the decomposition of environmental pollutant N_2O. The set-up consisting of a microreactor, mass flow controllers (MFCs) and a quadrupole mass spectrometer (Figure 2.6.1) has now been discussed.

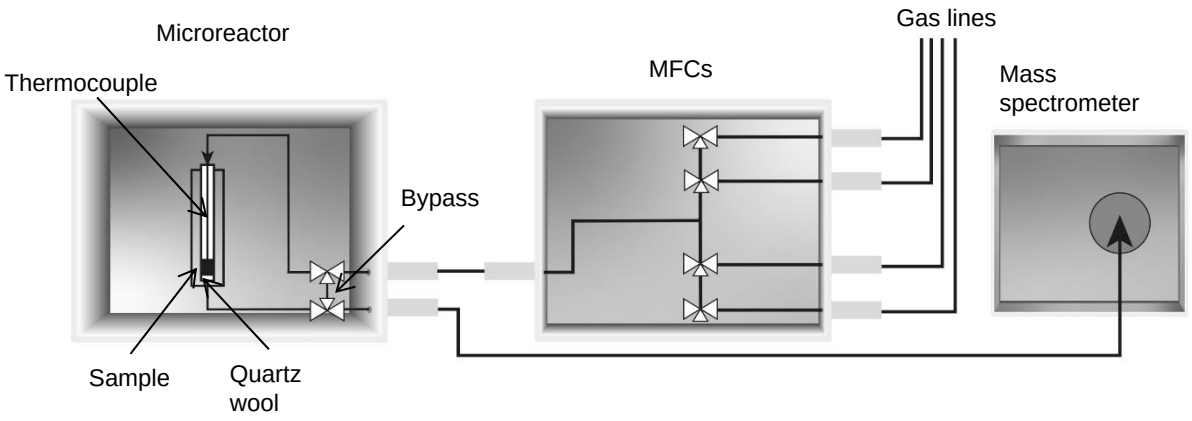

Figure 2.6.1: *Schematic drawing of the set-up for a Hiden CATLAB microreactor, including MFCs and Hiden Analytical QGA dynamic sampling mass spectrometer*

2.6.1 CATLAB Microreactor

The CATLAB is a fixed bed, continuous flow microreactor with its schematic shown in Figure 2.6.1. The specific instrument used within this work comprises of a standard gas manifold with two banks of four gas streams (only one bank drawn for simplicity), each with independent mass flow control. Of the 8 gas streams, 7 have standard MFCs with a flow range of 3 – 100 ml min^{-1} with a minimum pressure of 3 bar required. The remaining MFC has a maximum mass flow of up to 200 ml min^{-1}. Furthermore, one standard flow MFC has been tailored with Kalrez corrosive resistant fittings, along with the manifold, to allow for the use of corrosive gases, such as NH_3. An inert carrier gas, such as helium or argon, is constantly connected to flow through the system when experiments are not being performed.

Within the microreactor, after exiting the MFC unit, the gas flows up and then down over the fixed bed of the catalyst, forming an overall positive gas flow over the sample. The catalyst is pre-prepared into specific sieve fractions, and loaded into a quartz capillary, to ensure an even gas velocity and consistent tortuosity between different materials. This is extremely important as changes in velocity or pressure affect the contact time between the gas and sample. To quantify the gas flow rate with respect to catalyst volume the gas hour space velocity (GHSV) is often reported. A thermocouple placed in the catalyst bed to produce information on the sample temperature and feedback to the furnace, which surrounds the quartz capillary. Here, the furnace is capable of temperatures up to 1000 ˚C

with a ramp rate range of 0.1 – 20 ˚C min^{-1} and used a large proportional integral derivative (PID) controller for accurate temperature control and quick response time. After passing through the catalyst, the exhaust gases travel through the base of the furnace to be sampled by the quick inlet capillary (QIC), with the remainder sent to the vent line. A scroll pump draws the gas through the QIC to the mass spectrometer, with the line heated to a maximum of 200 ˚C. It is also possible to implement a bypass configuration, in which the flow avoids the sample to allow for purging or blank testing. By turning the three way switch the gas flow takes an alternative route avoiding the quartz capillary containing the catalyst and proceeds via either the QIC or a second vent line.

2.6.2 Mass spectrometry

2.6.2.1 Theory

Mass spectrometry is an analytical technique used to obtain mass spectral data for the molecular and structural identification of compounds. It works by bombarding the sample with high energy electrons to produce molecular and fragmentated ions. These ions are then separated by either electric or magnetic fields according to Newton's second law (Equation 2.6.1) and Lorentz force law (Equation 2.6.2):

$$F = ma$$

Equation 2.6.1: *Where F is the force applied, m is the mass and a is the acceleration of the ion*.

$$F = e(E + vB)$$

Equation 2.6.2: *Where e is the ionic charge, E the electric field, v is the velocity and B the magnetic field experienced by the ion.*

A mass spectrum therefore consists of molecular and fragmentated ions, separated based on their mass-to-charge ratio (*m/z*). This technique benefits from being sensitive towards analyte concentrations as low as 10^{-9} g, along with being able to perform continuously for the collection of time-resolved data. Within this work it has been used for the identification of post catalytic reaction mixtures.

2.6.2.2 Hiden Analytical QGA mass spectrometer

A mass spectrometer (MS) comprises of three parts: (1) an ion source, (2) a mass analyser and (3) a detector and the relevant set-up for the Hiden Analytical QGA mass spectrometer will now be discussed. Firstly, a vaporised sample enters the ionisation chamber, where it is bombarded with high energy electrons, generated by a tungsten filament. This induces the ejection of electrons from the sample to result in molecular and fragmentation ions, $[M^{+\cdot}]$, with predominantly single charged ions produced (Equation 2.6.3).

$M + e^- \rightarrow M^{+\cdot} + 2e^-$

Equation 2.6.3: *Fragmentation*

These ions then travel to the mass analyser, which are traditionally a high-powered magnet. These magnet selectors diffract the positively charged ions based on their *m/z*. However, in this work a quadrupole MS is used within the Hiden equipment (Figure 2.6.2). Here, an electric current separates the ions due to the different *m/z* values causing differing motions through the analyser. A quadrupole mass analyser consists of four symmetrical rods, positioned parallel to the direction of flow of the ions (Figure 2.6.2). The quadrupole is then supplied with both a radio frequency (RF) and a direct current (DC). The RF:DC ratio and the *m/z* value of the ions entering the quadrupole field define the oscillations and path of the molecular or fragmentated ions. Only resonant ions will produce stable oscillations and travel to the detector. Unstable oscillations result in non-resonant ions colliding with the rods and thus becoming undetected. As the voltage gradually changes, keeping the RF:DC current the same, it allows for the scanning of the mass spectrum. As the DC and RF voltage can be easily and rapidly changed, whilst maintaining stable conditions it is extremely suitable to be integrated in the CATLAB set-up for continuous scanning during catalytic reactions. This mass analyser set-up, however, suffers from only selected or known masses being analysed, rather than scanning over the *m/z* range as a magnetic selector does.[15]

After separation the molecular and fragmented ions are then electronically detected. Within this work there were two possible MS detectors; either a Faraday or a continuous scanning electron multiplier (SEM). In the case of the Faraday detector, the incident ion beam simply hits the dynode surface of the Faraday cup to give up their electrical charge, neutralising the ions. This is then converted into a voltage by the dynode emitting electrons to induce a current, which is directly proportional to the ion current. However, for low ion currents and better time resolved measurements SEM detectors are commonly used. In a continuous SEM on entering the incident ion beam collides with a dynode causing a secondary emission of electrons. These electrons then travel down the SEM by repeatedly colliding with the next a dynode, to result a cascade of electrons (Figure 2.6.3). The higher

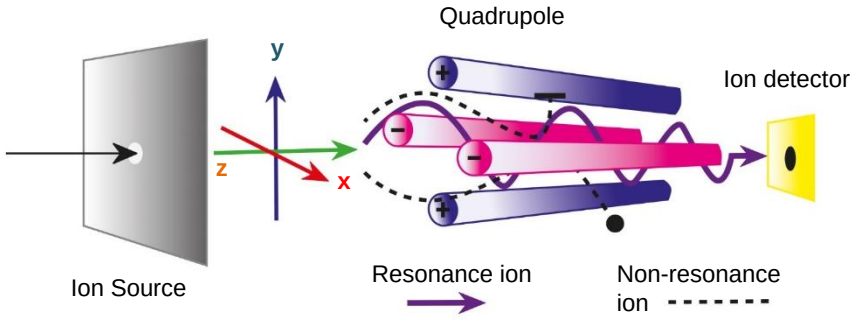

Figure 2.6.2: *A quadrupole MS schematic showing the path of resonance and non-resonance ions through the quadrupole field*

the initial electron velocity, the larger the number of secondary electrons. The Faraday detector benefits from longevity and to stability at high temperatures making it extremely robust, however, is less sensitive, whereas, the SEM is best suited for low concentration samples, yet does suffer from a slower response time due to the secondary emission process.[16]

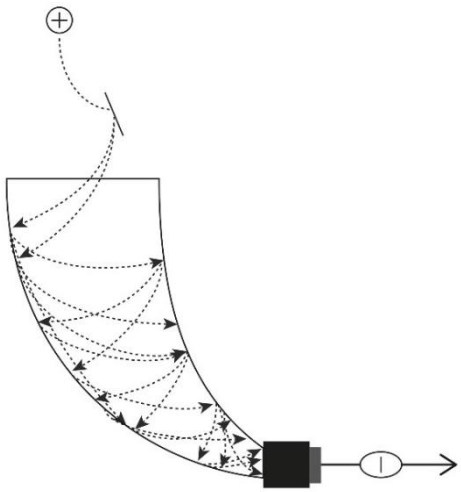

Figure 2.6.3: *Continuous secondary electron multiplier schematic of the cascade of electrons travelling to the dipole*

2.7 Infrared spectroscopy

Infrared (IR) spectroscopy is used to detect the molecular vibrations observed within the infrared region of the electromagnetic spectrum (400 – 4000 cm^{-1}). These molecular vibrations have characteristic frequencies that allow of the identification of specific functional groups. Within heterogenous catalysis IR spectroscopy is used to monitor the interaction between absorbed species and the catalyst.[17] IR spectrometers benefit from their rapid acquisition times, ease of use and affordability.

For IR absorption bands to be detected, the vibrational movements must result an electric dipole moment change. Molecules can vibrate in a variety of different modes such as stretching, bending, wiggling and rocking.[18] Therefore, how a molecule interacts with a surface, such as a catalyst, can affect its vibrational movement, providing vital surface information. For example, CO chemisorption is often used to understand the activity of supported nanoparticle catalysts. Assigning the CO absorption bands, found in the region 1800 – 2000 cm^{-1} can identify how CO has bound to the surface, at either linear or bridged sites.[19] Any changes in band intestines and wavelengths can provide information on the morphology and nature of the active binding sites.

The IR data collected in this project was performed by a transmission IR spectrometer. By preparing the sample into a pressed pellet with minimal quantities, it is

carefully loaded into a sealed reaction chamber and exposed to specific gaseous environment. IR radiation is then transmitted through the sample to produce a spectrum that is representative of the whole sample. Assuming a known quantity of the sample has been used it can allow for quantitative assessment of the surface coverage.

2.8 Mechanochemical set-up

To perform mechanochemical synthesis within this work, a planetary ball mill was used with ZrO_2 milling vessels and Yttria-stabilised zirconia (YTZ®) media. Figure 2.8.1A depicts a schematic cross-section of a milling jar with media. The milling media were first placed into the ZrO_2 grinding jars, with a weight ratio of media to the total precursor powder at 10:1. The prepared jars were weighted and balanced before securing in the planetary ball mill. Pre-mixed powders were placed on top of the milling media, with the jar sealed and secured inside the mill (Figure 2.8.1B). Once the lid was locked shut, 5 min of milling was performed to check jars were firmly secured. The mill operated at room temperature with 10 min intervals taken every 30 min to ensure the mill did not overheat. The jar rotated in the opposite direction to that of the axis of the mill to result in a centrifugal force, causing the milling media to travel though chamber of the jar (see section 1.4.3) and collide with the opposite wall. Once milling was completed, the milling jar was removed with heat proof gloves and opened within a fume cupboard. A sieve (~ 800 µm sieve fraction) was used to separate the milling media and loose powder. A spatula was used to remove the material that had become compressed against the wall of the jar.

In order to prevent contamination from the milling jars and media between experiments, rigorous cleaning was performed. This can be performed two ways: (1) soaking overnight in concentrated HCl acid or when particularly dirty (2) quartz sand with a small amount of water can be effective in wearing down a small layer from the grinding jar surface. Before starting each experiment, the equipment must be dry.

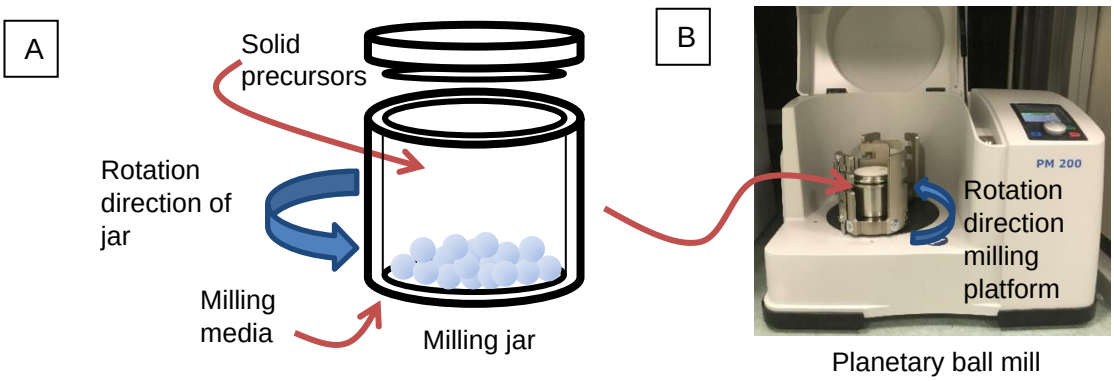

Figure 2.8.1: (A) *Schematic drawing of a milling jar with grinding media and* ***(B)*** *image of the Retsch 2–station Planetary Ball Mill, PM200 with their opposing rotational axis*

2.9 Synchrotron Radiation

A synchrotron is a particle accelerator that is a source of intense X-ray radiation.[7] Since the development of the first synchrotron in 1946, their continual development has often come in parallel with the advancement of scientific research within fields from archaeology to health and medicine. Synchrotron radiation benefits over lab-based X-ray sources due to its tunability to specific energies along with high flux and brilliance.[20] The high photon flux results in an increased number of photons s^{-1} unit $bandwidth^{-1}$ combined with the high brilliance that concentrates the direction and wavelength of the photons, to result in highly resolved data.

To produce synchrotron radiation, electrons are first emitted by an electron gun and accelerated in a linear accelerator (LINAC) (Figure 2.9.1). The electrons are then transferred to a booster ring where they are further accelerated to a higher energy. These high energy electrons are then injected, in a parallel orbit to the existing electrons, into a large storage ring where they are circulated by a series of magnets separated by straight sections. This storage ring is 'topped-up' frequently by small injections from the booster ring to maintain the current. Electrons are maintained on a circular closed path by the use of bending magnets. At each bending magnet the electrons are deflected by the magnetic field to give off electromagnetic radiation known as synchrotron light (Figure 2.9.2A). The beam is then captured and focussed by mirrors and crystal optics in order to optimise the wavelength for desired techniques at specific beamlines. A sample is then exposed to the synchrotron radiation at a beamline where detectors are used to record the X-rays that pass through or are emitted from the sample.[20]

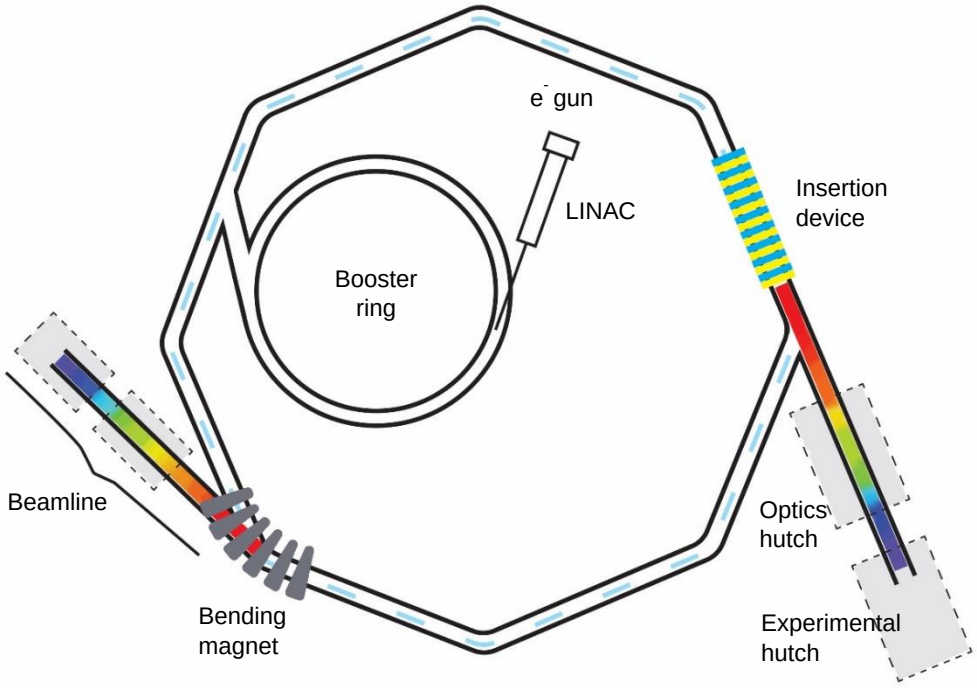

Figure 2.9.1: *Simplified schematic of a synchrotron layout in order to produce X-ray radiation*

Initially bending magnets were the only way to achieve synchrotron radiation, however, since the development of third generation synchrotrons, insertion devices are also commonly used. These are fitted at the straight sections within the storage ring and result in a vastly higher flux and brilliance output, compared to bending magnet radiation. Insertion devices comprise of an arrangement of magnetics, which can be further classified into either wigglers or undulators (Figure 2.9.2B). Both wiggler and undulator devices have similar magnet configurations with alternating polarity, causing the electrons to oscillate, producing synchrotron radiation at each turn.[21] These insertion devices differ by the resultant energy range of radiation, defined by the size of the deflected angle. Wigglers (Figure 2.9.2Bi), like bending magnets, produce a fan of radiation, with their output energy controlled by increasing the number of magnets. Increasing the number of poles, *N*, produces an increase in emitted photons by a factor of *N.* In comparison, undulators (Figure 2.9.2Bii) have a much smaller angular defection and produce collimated radiation at specific energy ranges. Controlling the separation gap between the alternating magnetic poles results in different energy ranges, e.g. the smaller the gap, the higher the magnetic field, resulting in a higher energy of the undulator peak.[7,22]

Each beamline on a synchrotron has a unique set-up in order to control and attenuate the radiation, dependent on the technique and information desired. The following sections will cover how synchrotron radiation can be used for advanced material characterisation of bulk structures (i.e. XAS) and near surface sensitive techniques (i.e. XPS) relevant to this work.

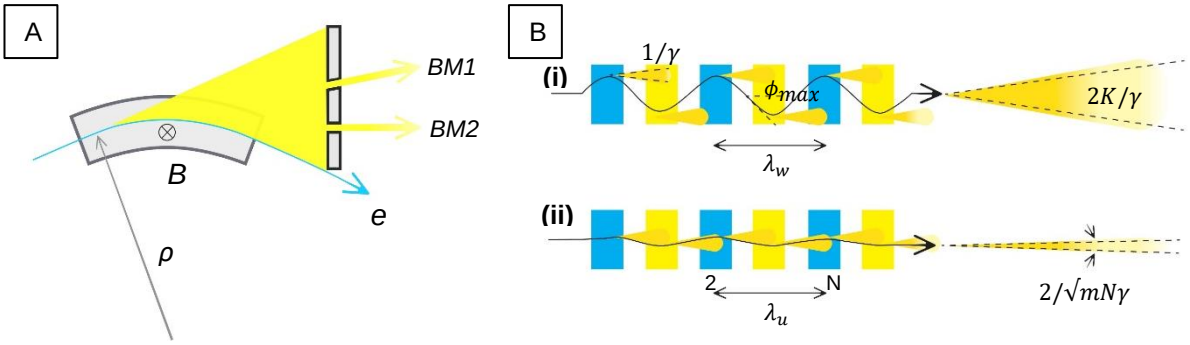

Figure 2.9.2: *Schematics of producing synchrotron radiation by either* ***(A)*** *bending magnet; where the arc of the electron radius, ρ, determines the energy output, or* ***(B)*** *insertion devices* ***(i)*** *a wiggler; produces broad range of radiation and* ***(ii)*** *an undulator; where energy range is controlled by changing the distance between the opposing magnetic poles*

2.9.1 X-ray absorption spectroscopy

2.9.1.1 Background

X-ray absorption spectroscopy (XAS) is powerful characterisation technique which determines the geometric and electronic configuration of materials. It analyses how X-rays are absorbed by a specific atom, at energies near and above its core-level electron binding energy.[23] XAS is element specific and can therefore provide valuable information of the

local environment surrounding the central absorbing ion. As it does not rely on periodic ordering it can be applied to materials with little or no long-range order, ideally suited to those prepared by ball milling, to give a per atom average structure. Furthermore, measurements are often simple, versatile, allow for trace elements to be detected and have the ability to run fast *in situ* experiments to produce high resolution data.[23]

Traditionally XAS required the use of tuneable synchrotron radiation, and the development of this technique has often run in parallel with the development of synchrotron facilities. The first X-ray absorption spectrum was observed over a hundred years ago, in 1913, by de Brogile.[24] However, it wasn't until the ground breaking work of Sayer, Stern and Lytle in 1971, who applied Fourier analysis to experimental data, which led to the exponential growth within this technique. This resulted in the ability to quantitatively determine structural parameters such as bond distance, coordination number along with thermal and disorder parameters.[24]

2.9.1.2 Theory

As X-ray radiation is transmitted through a sample, absorption events attenuate the beam according to Beer-Lamberts Law (Equation 2.9.1). Absorption characteristics of specific materials can then be calculated by applying the mass absorption coefficient (Equation 2.9.2). Here, each element absorption coefficient within the material is combined to give a mass-weighted summation (Equation 2.9.3).

$$\frac{I_t}{I_0} = e^{-\mu t}$$

Equation 2.9.1: *Where I_0 is the incident and I_t the transmitted X-ray intensities, μ is the mass absorption coefficient and t is the sample thickness.*

$$\mu_m = \frac{\mu}{\rho}$$

Equation 2.9.2: *Where μ_m is the mass absorption coefficient and ρ is the material density*

$$log\left(\frac{I_t}{I_0}\right) = \sum_i w_i t_i \left(\frac{\mu_m}{\rho}\right) i$$

Equation 2.9.3: *Mass weighted summation*

X-ray absorption is therefore dependent on the atomic number, as varying *Z* character can interact differently with the incoming photon energy. As the number of electrons increases, for higher *Z* elements, increasing amounts of the incident beam is absorbed by the atom. Also, as the energy of the X-ray beam increases, the transmission through the sample increases. However, when the incident energy is equal to that of the

core orbital binding energy a sharp rise in absorption occurs, known as the absorption edge. During a XAS measurement X-rays scan across energies close to that of the absorption edge of the element of interest. The sample then absorbs photons of sufficient energy in order to excite an electron from the core to an empty state or to the continuum.[25] Depending on which shell is being assessed, it corresponds to a different absorption edge, labelled using the principle quantum numbers.

However, further classification is required when describing the electron transition from the orbital. For an electron excited from the first shell there is only the 1*s* orbital, thus it is always the K-edge. However, at the second and third shells (L and M) edges there are multiple absorption edges. For example, at the L- edge it is possible to assess either the L_1, L_2 or L_3-edge. Here the L_1 corresponds to an excitation from the 2s and is the highest energy of the L-edges. However, after the promotion of an electron from the 2*p* orbital two absorption edges are observed, occurring due to the spin-orbital coupling after the creation of an electron hole. Using Hund's rule (Equation 2.9.4) two *j* states are calculated to be $2p_{3/2}$ and $2p_{1/2}$, corresponding to L_3 and L_2-edges, respectively. The L_2 is of a higher energy due to a more stable ion configuration.

$$j = l + s$$

Equation 2.9.4: *Where l is the orbital angular momentum, s the electron spin (±½)*

When an inner shell electron, most commonly the core shell, of the absorbing atom is excited by an incident beam of radiation it can transition to either unoccupied valence orbitals or be promoted as a wave from the absorbing atom into the continuum (Figure 2.9.3A). This, therefore, results in X-ray absorption spectra being compiled of two regimes

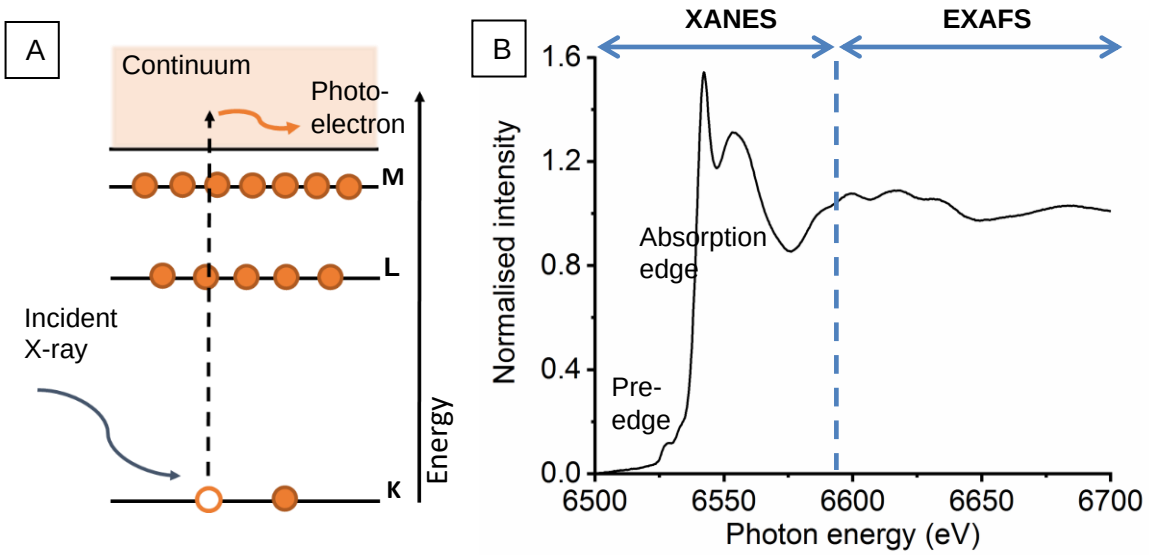

Figure 2.9.3: (A) *Schematic of incoming X-ray exciting an electron from the inner shell with sufficient energy to be promoted into the continuum and* ***(B)*** *an example of a XAS spectrum at the Mn K-edge consisting both XANES and EXAFS regimes for* $LaMnO_3$

(Figure 2.9.3B): X-ray absorption near edge structure (XANES) and extended X-ray absorption fine structure (EXAFS).

2.9.1.3 XANES

The XANES region contributes to roughly the first ~50 eV of a XAS spectrum and occurs due to the core level electron promotion to unoccupied states. For a transition to be allowed it must follow the selection rule $\Delta\ell = \pm 1$. For example, when an electron is excited from the 1*s* orbital (*l* = 0) it is promoted to the next available *p* orbital state and is so called a dipole allowed transition. This results in a sharp, prominent rise in the absorption spectrum, the edge. The more 'probable' the transition then the greater the intensity and sharpness of this feature. The position of this edge is equivalent to the binding energy of the photo-excited electron, dependent on the Z (atomic number). Furthermore, by changing the oxidation state it alters the energy of core orbitals, shifting the edge position.

However, transitions can be observed to unoccupied states that are normally forbidden by the dipole section rules due to the hybridisation effect. For example, *p*-*d* orbitals with the correct symmetry and geometry can overlap. At the Mn K-edge this results in a seemingly 1*s* → 3*d* transition, with the electron promoted to the *p*-character of the hybridised orbital. For 1st row transition metals these local or non-local excitations are commonly observed before the edge, E_0, within the pre-edge region. However, we must also consider quadrapole interactions, which do not follow the dipole selection rules and allow for 1*s* → 3*d* transitions. Their probability is less likely than that of an allowed dipole transition and therefore are often much lower in intensity.[26] The size and shape of the pre-edge features is highly influenced by the symmetry and geometry surrounding the central absorbing atom.

Analysis of XANES spectrum is challenging due to the region being dominated by multiple-scattering events, where the long mean free path of the photoelectron results in scattering from many atoms. Advanced theoretical calculations can be applied to model XANES by molecular orbital (DFT) and multi scattering theories (FEFF program), however, interpretation by comparisons to appropriate reference materials is widely accepted. Overall XANES can provide information on the geometric structure, the type of atomic neighbours and the oxidation state all surrounding the absorbing atom.[27]

2.9.1.4 EXAFS

The EXAFS regime occurs when an electron has been given enough energy to be released into the continuum. Here, the electron is thought of as a spherical wave, interacting with the electron density of neighbouring atoms to produce a backscattering interference pattern (Figure 2.9.4). EXAFS therefore provides information on bond distances, coordination number and the neighbours around the absorbing atom, independent of chemical bonding.[23]

Important approximations and limits can be applied to the EXAFS regime which allow for quantitative interpretation, not currently possible for XANES spectra.[23]

Once the photoelectron has been promoted into the continuum it behaves as a wave and the de Broglie equation can be applied using its wavelength, λ (Equation 2.9.5). This can then be related to the photoelectron wave vector, k, along with its kinetic energy, E, and momentum, p, whilst considering the mass of an electron, m_e, to form Equation 2.9.6.

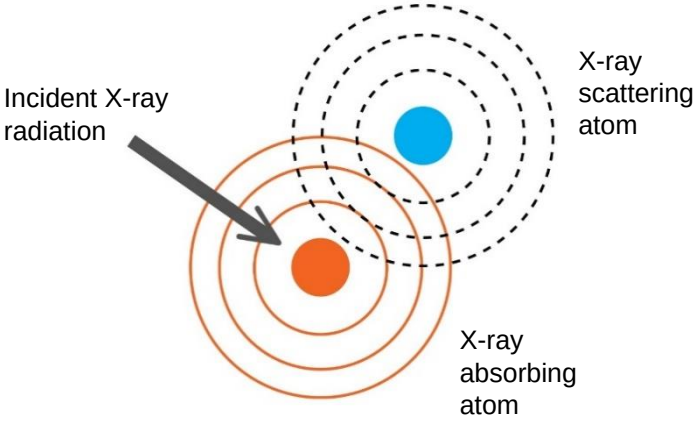

Figure 2.9.4: *Diagram representing incoming X-ray to a specific absorbing atom and how a neighbouring atom can scatter the excited electron*

$$\lambda = h/p$$

Equation 2.9.5: *Where h is Plank's constant and p is related to the electron's momentum.*

$$\hbar k = \sqrt{(2Em_e)}$$

Equation 2.9.6: *Where* $\hbar = h/2\pi$*, E is the kinetic energy and* m_e *is the mass of an electron,* $2Em_e = p^2$

Therefore, by understanding EXAFS in terms of wave behaviour of the promoted photoelectron, the X-ray energy can be converted to *k*, the wavenumber of the photoelectron, when the photon energy is above absorption edge, E_0 (Equation 2.9.7.) The relationship between *k* and the wavelength (Equation 2.9.8) results in the backscattering signal being a sine wave.

$$k = \sqrt{\frac{2m_e(E-E_0)}{\hbar^2}}$$

Equation 2.9.7: *Where* E_0 *is the absorption edge*

$$\lambda = \frac{2\pi}{k}$$

Equation 2.9.8

For EXAFS we are interested in oscillations above the edge and, therefore, any changes in the absorption as a function of *k* is then defined the EXAFS fine-structure function, *χ(E)* (Equation 2.9.9). As the value of *k* increases the oscillations in the EXAFS spectrum decay rapidly, with it possible to change the weighting in the order of 1 – 3 for *k*.

$$\chi(k) = \frac{\mu(k) - \mu_0(k)}{\Delta\mu_0(k)}$$

Equation 2.9.9: *Where μ(k) is the absorption coefficient, $\mu_0(k)$ is the background smoothing function of the absorption of an isolated atom and $\Delta\mu_0$ is the measured change in absorption μ(k) at the energy E_0*

As previously mentioned in section 2.9.1, the model proposed by Sayer, Stern and Lytle was crucial to quantify the backscattering oscillations, *k,* as pseudo radial distributions. The model is based on single scattering events, where the photoelectron scatters from one neighbour before returning back to the absorbing atom, having an interatomic distance of $2R_j$. The oscillations within the EXAFS region, > 50 eV, can then be stated as a function of photoelectron wavenumber, χ(k), to give the EXAFS equation (Equation 2.9.10). Therefore, information such as scattering distances, R_j, and number of nearest neighbours, N_j, from the central absorbing atom can now be achieved.

$$\chi(\mathrm{k}) = \sum_{\mathrm{j}} \frac{\mathrm{N_j f_j(k)} e^{-2\mathrm{k}^2\sigma_{\mathrm{j}}^2}}{\mathrm{kR_j^2}} \sin\left[2\mathrm{kR_j} + \delta_{\mathrm{j}}(\mathrm{k})\right]$$

Equation 2.9.10: *Where f(k) and δ(k) are scattering properties of nearest neighbours, N is the number of neighbouring atoms, R_j is the distance to neighbouring atoms and σ^2 is disorder in neighbour distance*

Using Equation 2.9.10, a relationship between each of these parameters helps explain the resulting backscattering spectrum. The coordination number (CN) of neighbouring atoms are linearly proportional to the amplitude in their EXAFS feature. However, this amplitude is further affected by two factors; S_0^2 which allows scattering events to not all be a single electron process and the mean squared disorder, σ^2. The σ^2 factor is a measure of the variation in the distribution of neighbours in a shell around the central absorbing atom. This can either refer to static or dynamic disorder, such as disorder within the structure or due to bonds experiencing thermal vibrations, respectively. Heavier elements, with high *Z*, and longer bonds vibrate less and would expect to have lower σ^2, and vice versa. Care must be taken when understanding the effect of σ^2, due to its exponential dependence on *k*, where high *k* values can cause the EXAFS oscillations to dampen out. This can make it hard to deduce CNs and result in inaccurate scattering

distances calculated. Furthermore, as the wavenumber increases past the edge for materials with high structural disorder and low *Z* character neighbours' the oscillations will also tend to be dampened. Finally, *f(k)* and *δ(k)* parameters allow for identification of their nearest neighbours. *f(k)* is a measure of the backscattering amplitude as a function of *k*, with *δ(k)* the phase shift experienced when the photoelectron leaves and returns back to the central absorbing atom.

2.9.2 XAS Data Acquisition

Acquisition of XAS data is performed on specifically designed beamlines, depending on the desired information, e.g. if the aim is to achieve high spectral resolution, time or spatially resolved data. In general, however, for a beamline to produce well resolved and good quality data a number of factors must be considered when configuring the optics. These include reducing the synchrotron radiation beam intensity to a bandwidth of ~1 eV, accommodating for any fluctuations in the incident X-ray beam, and focusing the beam for small sample sizes.

The majority of XAS data in this work was collected in transmission mode at the B18 beamline, Diamond Light Source, Didcot, UK. This beamline utilises synchrotron radiation at a bending magnet and its specifically optimised configuration allows efficient and reliable performance without compromising the X-ray flux (Figure 2.9.5).[28,29] Before radiation reaches the monochromator, the light first passes through slits and is reflected by a flat, cylindrically bent mirror to collimate the incoming beam. At the monochromator, the X-ray is tuned to scan over a wavelength range, resulting in a XAS spectrum. The B18 monochromator comprises of two crystals, either Si(111) or Si(311) selected for 2-20 keV or 4-35 keV energy ranges, respectively, resulting from different crystal *d*-spacing. To achieve the desired photon energies, *λ*, the incident beam is set at specific angle, *θ*, to the crystal monochromator which satisfies Bragg's Law (Equation 2.1.1). Once a data point has been measured the monochromator moves repeatedly step by step to scan through the full spectrum.

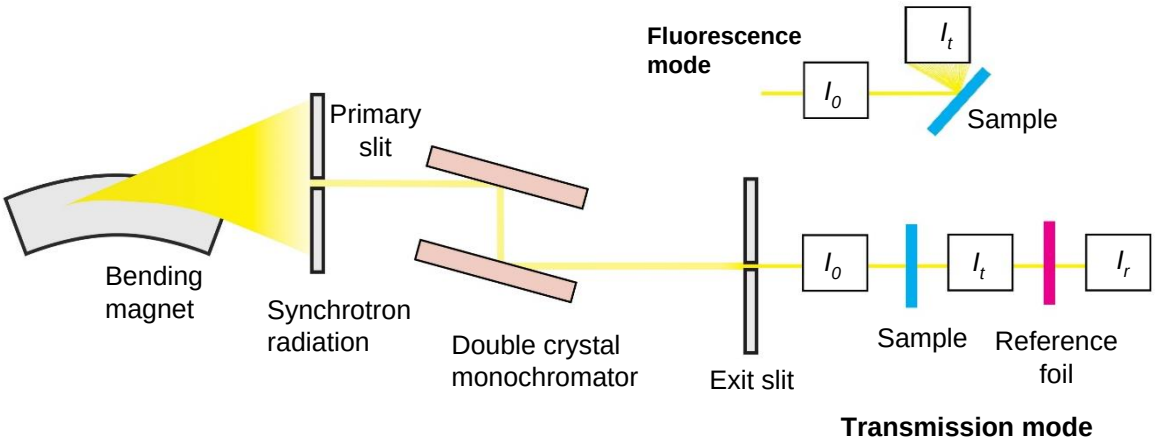

Figure 2.9.5: *Schematic of a typical XAS beamline for both fluorescence and transmission modes*

After the monochromator, mirrors allow for focusing of the beam and slits help control the beam size and shape. When in transmission mode the sample is placed between two ion chambers before, (I_0), and after (I) the sample, which measures the change in X-ray flux. These ion chambers are filled with inert gases, which on exposure to X-ray radiation ionise. The ionised gas molecules then generate a current by travelling towards an electrode, which detects the relative change absorbance as a result of the radiation passing through the sample.[22] Applying the Beer-Lambert law ($I = I_0 e^{-\mu t}$) to the measured photon intensity, a change in the absorption coefficient is observed within the XAS spectrum. These ion chambers must be perfectly inline to cancel out any beam fluctuations on data analysis. The beam also passes through a reference foil after transmission through the sample, with a known edge energy, of the element being measured. This allows for calibration of the sample to the reference energy.

Whilst transmission mode is often used, low dilution samples that result in a small absorption require the use of a fluorescence mode. Here the incident energy (I_0) and fluorescence X-rays (I_f) following a secondary emission. The sample is at a 45˚ angle and detector at 90˚ both to the incident beam (Figure 2.9.5).

This set-up described allows for a maximum scan time of 15 min, however, for well time-resolved data, such as *in situ* catalytic processes, time scales of less than 1 min need to be achievable. This is a limitation of the scanning method for monochromators, with moving times hard to reduces below this time. In order to achieve quick and reliable data collection at B18 in this work, a Quick EXAFS (QEXAFS) set-up was used. Here, instead of scanning each data point step-by-step, the monochromator is mounted on a goniometer, where it moves at a constant velocity through the required angles for the desired X-ray absorption spectrum.[30]

2.9.3 Data analysis

The transmission XAS data collected throughout this work was processed using the Demeter IFEFFIT software with Horae package (Athena and Artemis), based on the

IFEFFIT programming interface by Newville.[31] Athena allows for background subtraction, normalisation, energy calibration, data series alignment, deglitching and merging of data. Whilst Artemis is able to produce structure models, consisting of multiple scattering paths, of the EXAFS Fourier transform data.

The raw data is first imported into Athena, where it is converted into readable formats, such as *μ(E)* or a Fourier transform. The E_0 is set as either half the edge jump or the maximum of the initial first derivative inflection. This edge energy is then calibrated to the known energy from literature of the reference foil. For multiple spectra the data is then aligned, by the same energy shift, to the reference channel of the calibrated spectrum. To improve data quality and reliability multiple acquisitions of the same sample spot are merged together to produce an average spectrum. Pre-edge and post-edge processing functions allow for the background subtraction from the instrument and isolated atom absorption. This data processing prepares the XAS data for Artemis software.

Artemis analyses of EXAFS Fourier transform data by FEFF calculations to chosen theoretical reference materials. After importing the processed data from Athena, crystallographic data, in a. cif format. is converted into a FEFF, suitable for Artemis. Appropriate scattering paths are then used in the fitting window to produce a structure model of the sample. Parameters used within the EXAFS Equation 2.9.10, E_0, S_0^2 or amplitude, CN, ΔR and σ^2 are applied and refined to model the data. For highly ordered, crystalline samples of known structures fixed parameters can be used for CN to help minimise the unknowns. However, care must be taken to achieve an appropriate fitting model, to calculate suitable numbers. Artemis is primarily suitable for low scattering shells and small data sets as limitations do exist. For example, fits require an initial structure idea and it is arbitrary and time consuming to model large data sets.[27]

2.9.4 Secondary emission

X-ray fluorescence techniques, such as X-ray emission spectroscopy (XES) and high energy resolution fluorescence detection (HERFD), can provide complementary information to transmission XAS. Secondary emission occurs after the promotion of a core-level electron, creating an excited state with a core hole. Relaxation results in the core hole being filled by a higher energy electron from dipole allowed orbitals (Figure 2.9.6). During this de-excitation either an electron or a fluorescence photon is measured. Depending on which orbital the electron decays from, it can result in specific emission lines that are highly characteristic of a specific element.[32]

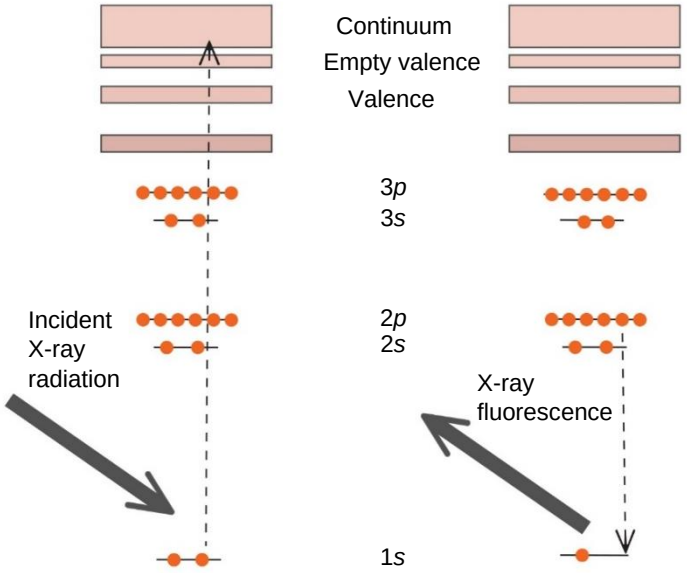

Figure 2.9.6: *The creation of a core hole and the de-excitation of allowed higher energy electrons to give off X-ray fluorescence*

By performing XES and HERFD additional information may be attained about the local charge density and electron configuration not always possible by traditional XAS. Further information on these techniques has been assessed in greater detail in the following sections.

2.9.5 Non-resonant X-ray emission spectroscopy

XES provides information on the electronic structure and charge density, as well as distinguishing the ligand environment of 3*d* transition metals.[33] In XAS, as previously discussed, the absorption of an incident X-ray beam results in a core-shell electron being excited into dipole allowed unoccupied density states or further into the continuum. With non-resonant XES the incident X-ray beam is tuned well above the absorption edge, so the core-electron is promoted into continuum. This creates an excited state, with a core hole, for the absorbing atom which has a lifetime of $\tau = 10^{-15}$ s before it is filled by an electron from a higher dipole allowed orbital. This de-excitation event releases a fluorescence photon, and depending on the specific transition, different emission lines can be detected, to give rise to element specific characteristic spectra. For example, at the K-edge the core hole formed in the 1*s* orbital can be filled by an electron transition from 2*p* or 3*p* orbitals. The K fluorescence emission line nomenclature follows: Kα from a 2*p* → 1*s* transition, Kβ main lines for a 3*p* → 1*s* transition and for Kβ satellites a valence-to-core (VTC) transition occurs (Figure 2.9.7A). These different emission lines have varying intensities in the order of Kα > Kβ main lines > Kβ VTC (Figure 2.9.7B).

The spectral shape of Kα or Kβ emission lines is highly dependent on the nature of the core-hole and its final state configurations. These core-to-core transitions are dominated

by two major effects; (1) spin-orbital interactions, where the electron spin interacts with its own orbital momentum and (2) electron-electron interactions between the hole and the valence electrons. At the Kα emission line the excited state $1s^1\ 2p^5 3d^{n+1}$ is dominated by the 2*p* spin-orbital splitting, which is ten times greater for a 2*p* hole final state in comparison to the 3*p* hole final state. The Kα emission line, therefore, produces the highest intensity spectra. The Kβ region detects two lower intensity features; $K\beta_{1,3}$ main peak and a shoulder, Kβ'. The Kβ main line is instead dominated by electron-electron interactions between the 3*p* – 3*d* orbitals. Due to the exchange interaction between the electron spin of the 3*p* shell to the valence orbitals the Kβ main lines have good ligand chemical sensitivity. Furthermore, a shift in the $K\beta_{1,3}$ peak position is less dependent on geometric structure surrounding the central absorbing atom and thus can be linearly correlated to the oxidation state, previously an issue within XANES.

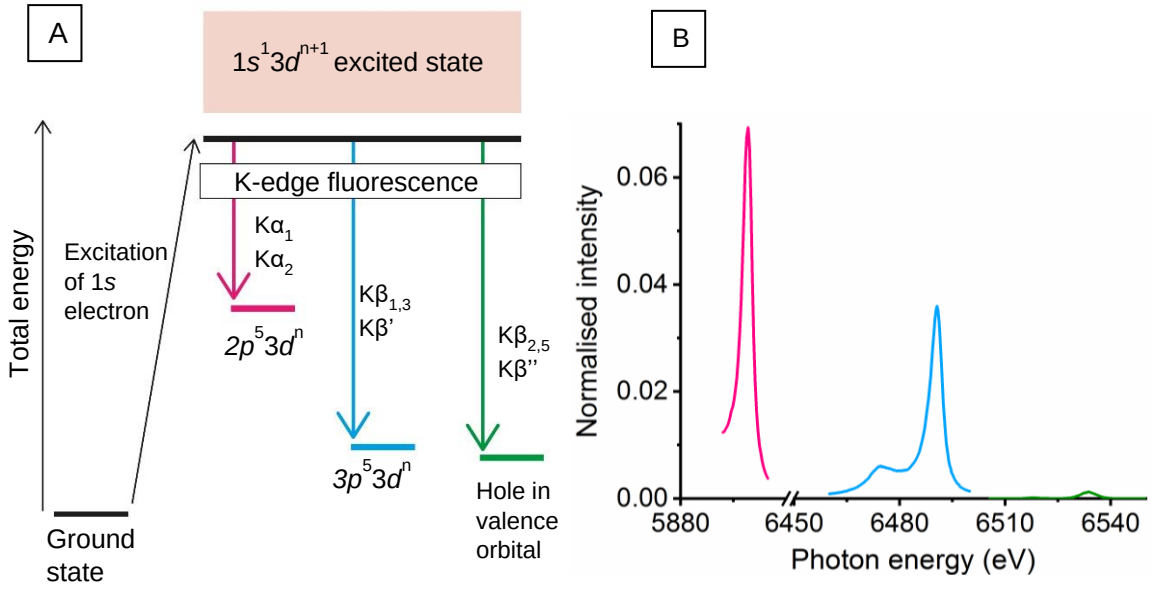

Figure 2.9.7: (A) *K-edge XES emission lines and* ***(B)*** *corresponding spectra showing the comparison of energy range and intensity at the Mn K-edge Kα, Kβ main lines and Kβ VTC emission lines of crystalline* $LaMnO_3$

At higher energies, even lower intensity Kβ VTC emission lines are detected. These directly reflect the electronic configuration of orbitals participating within the chemical bond. The VTC transitions are much more sensitive to local changes and provide valuable information on the local geometry and electronic structure. Two peaks are observed within this region, denoted as $K\beta_{2.5}$ and Kβ'', with the latter peak position particularly sensitive to the ligand species and its bond length.

2.9.6 High energy resolution fluorescence detection

High energy resolution fluorescence detection (HERFD) is a technique that produces high resolution XANES through X-ray fluorescence detected XAS. Traditional XAS spectra, commonly of 3*d* transition metals, often contain broad, unresolved features within the XANES region (Figure 2.9.8A). By performing HERFD the sharpening of spectra features,

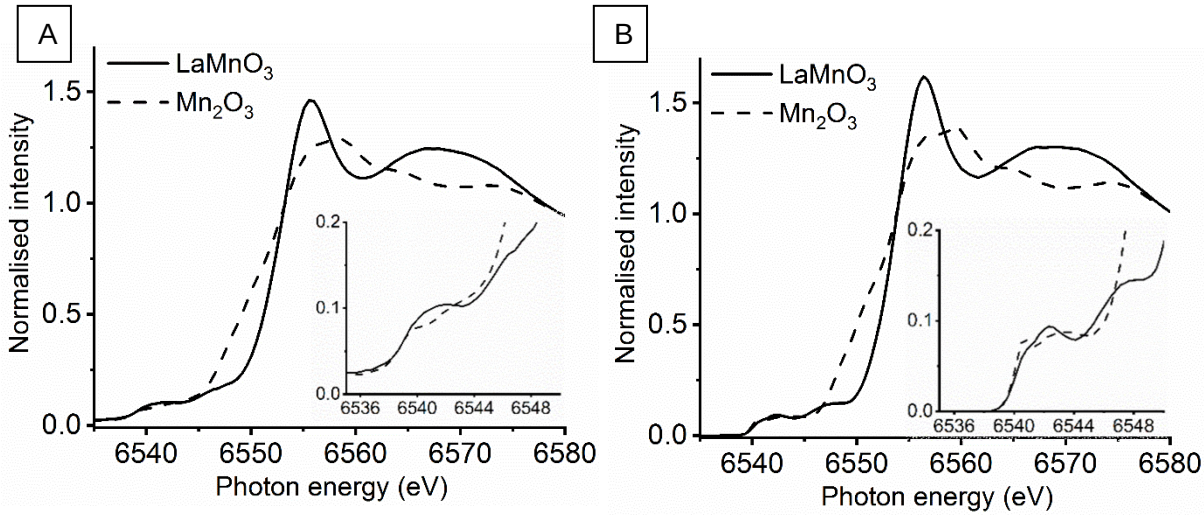

Figure 2.9.8: *Comparison of* ***(A)*** *traditional XANES spectra and* ***(B)*** *HERFD spectra for crystalline $LaMnO_3$ and Mn_2O_3 with highlighted pre-edge regions*

especially better separation within the pre-edge and absorption edge, provides information on electronic configuration and geometric structure (figure 2.10.2.1B). Because of this, HERFD can be extremely beneficial when trying to understand the electronic and geometric properties of catalysts with a transition metal active site.

HERFD can be understood with the same principles as resonant inelastic X-ray scattering (RIXS). Eisenberger *et al*. in 1976 that measured the intensity of a specific emission line across the absorption edge to form the technique known HERFD.[34] As previously discussed, after the excitation of a core 1*s* electron an excited state is created where an electron from a higher energy orbital then relaxes to fill this core hole. However, after de-excitation the system does not always return to its initial ground state, giving rise to an excited final state (Figure 2.9.9). This excitation can be a consequence of local or non-local excitations, whereby an electron is promoted to unoccupied hybridised orbitals within the absorbing atom or as a charge transfer to a bound neighbouring atom. The overlap of these multiple transitions broaden the lifetime of the core hole, smearing spectral features

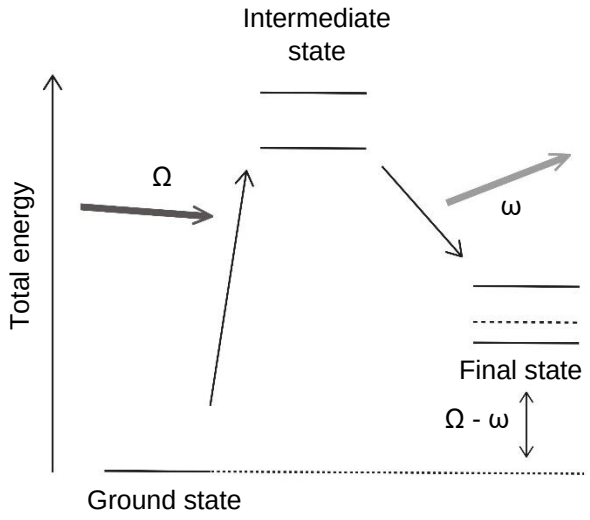

Figure 2.9.9: *Energy level diagram showing the energy of the incident X-ray, Ω, and X-ray fluorescence, ω, with the final excited state defined by the energy transfer Ω – ω.*

within XANES. HERFD seeks to overcome this by measuring XAS below the core lifetime hole. During a HERFD measurement the detector is set to specific emission line with a resolution higher than its natural width to allow only photons of interest to reach the detector. This lowers the signal-to-noise ratio, vastly improving the intrinsic spectral resolution. By performing these measurements electronic structure and configuration can now be resolved, which were not previously possible by traditional XAS, i.e. of polycrystalline or highly dilute materials.[35]

2.9.7 XES and HERFD Set-up

Both XES and HERFD at the Mn K-edge were performed at the scanning branch of the I20-beamline, Diamond Light Source, UK. This beamline utilises synchrotron radiation produced by a wiggler insertion device, where the configuration is specifically optimised for measurements of low concentration elements and/or complex, disordered materials (Figure 2.9.10).[36]

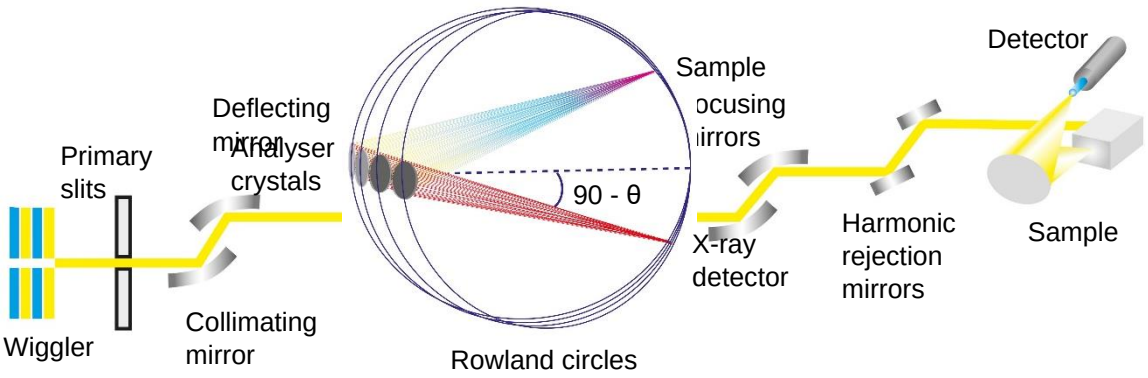

Figure 2.9.11: *Visualisation of the detection for emitted X-ray radiation being focused by crystal analysers in a Johann configuration based on a 1 m Rowland circle*

After the X-ray radiation exits the wiggler, it first passes through primary slits and to defecting mirrors to prepare the beam for the correct conditions for the monochromator. Here, a four-bounce monochromator is used, which can rotate around two primary axes to produce a fixed exist of the monochromatic beam whilst not being affected from variations in the angular position of the source radiation.[37] Depending on the energy requirement of the experiment, Si(111) or Si(311) crystals are used for 4 – 19 keV or 7 – 34 keV, respectively. After the monochromator vertical defecting mirrors allow for the beam to be focused at the sample position. For the experiments performed in this project, the X-ray emission module was selected as the end station. Here, the X-ray emission spectrometer is based on a Rowland circle with a 1 m diameter, operating in a Johann configuration in the vertical plane (Figure 2.9.11). On I20-scanning this spectrometer is capable of detecting an energy range of 4 – 20 keV, along with the use of a large set of varying cuts of crystals to cover Kα and Kβ emission lines.

2.9.8 Energy dispersive EXAFS

To obtain rapid acquisition of EXAFS in a single shot, energy dispersive EXAFS (EDE) technique can be applied. This is a vastly different approach to the XAS previously described, which scan step-by-step through the incident energies. Instead EDE exposes the entire XAS spectrum directly to the sample. This can result in a single energy point taking less than 1 ms, making it ideal for the *in situ* study of dynamic systems to help understand the fundamental steps in material synthesis and catalyst performance.[30]

EDE is achieved by generating and focusing a polychromatic X-ray radiation beam using a crystal with a curved elliptical shape, known as a polychromator. The X-ray beam is continuously diffracted from one side of the crystal to the other, thus producing a correlation between the X-ray propagation direction and its energy (Figure 2.9.12). This stationary optic configuration allows for the energy to be intrinsically stable at the focal point during acquisition.[22] A position-sensitive detector then collects the signal after transmission through the sample, detecting the X-ray intensity of each wavelength. This technique is highly suited to using synchrotron radiation, with its large horizontal divergence allowing for a large energy bandwidth to be produced to cover the full EXAFS spectrum. It can even allow for the simultaneous measurement of two absorption edges, however is limited to performing measurements in transmission mode.

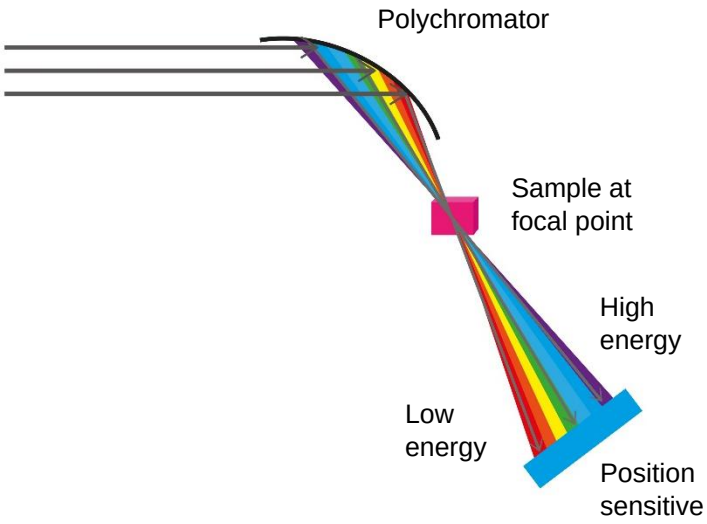

Figure 2.9.12: *Schematic showing the path of an X-ray from dispersion at the polychromator, through the sample to detector*

Though this approach to measuring EXAFS possesses unique possibilities not previously possible by tradition XAS there are many challenges to performing successful EDE experiments. The background ion chamber, I_0, cannot be recorded simultaneously with the transmission through the sample and must be measured at a different time point. This can cause difficulties in data processing for in-line normalisation of data sets. By performing two I_0 measurements, before and after transmission, it can start to overcome the variation in beam instability of I_0. The X-ray radiation source is required to be extremely stable as the polychromatic beam is focussed onto the sample. The high photon flux at this focal position can often induce beam damage to the sample. Furthermore, to achieve data into the EXAFS region by this dispersive method samples are required to be homogenous, otherwise parasitic scattering can occur.[38]

2.9.9 EDE beamline Set-up

The energy dispersive experiments were performed at I20-EDE beamline, Diamond Light Source, UK. This beamline works simultaneously alongside the scanning branch by collecting X-ray radiation from different wiggler insertion devices. The optical configuration is specifically designed to produce a broad energy band pass and high photon flux (Figure 2.9.13).[36] After the X-ray radiation exits the wiggler, it first passes through primary slits and to a defecting mirror to focus the beam in the vertical direction of the sample. This mirror is coated with Rh and Pt stripes to produce an operating energy range of 6 – 26 keV. Next the beam is polychromatised by a single bounce curved crystal, the polychromator, in the horizontal plane. At the end station a position sensitive detector is used.

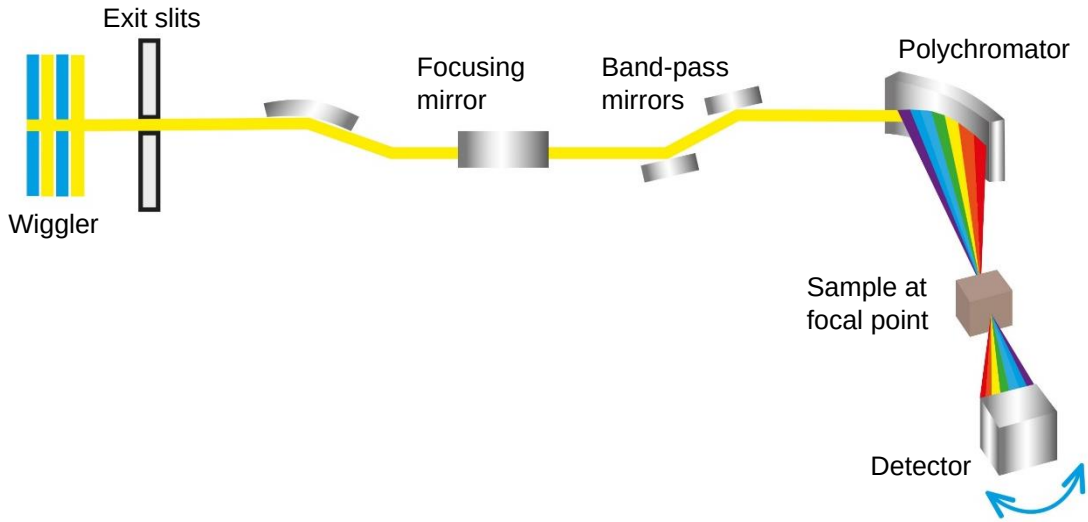

Figure 2.9.13: *Schematic diagram of the dispersive branch of the I20 beamline*

2.10 References

1 R. Guinebretiere, *X-ray diffraction by polycrystalline materials*, ISTE Ltd, 2007.

2 R. E. Dinnebier, A. Leineweber and J. S. O. Evans, in *Rietveld Refinement: Practical Powder Diffraction Pattern Analysis using TOPAS*, 2019, p. 16.

3 J. Sharma and B. C. Beard, *Chem. Phys. Energ. Mater.*, 1990, 569–585.

4 J. Jiang and A. Kucernak, *Electrochim. Acta*, 2002, **47**, 2381–2386.

5 J. F. Watts and J. Wolstenholme, in *An Introduction to Surface Analysis by XPS and AES*, 2005, pp. 1–15.

6 J. F. Watts and J. Wolstenholme, in *An Introduction to Surface Analysis by XPS and AES*, 2019, pp. 19–67.

7 C. Fan and Z. Zhao, Eds., *Synchrotron Radiation in Materials Science*, Wiley-VCH, 2018.

8 L. Zhong, D. Chen and S. Zafeiratos, *Catal. Sci. Technol.*, 2019, **9**, 3851–3867.

9 Z. Luo, *A practical guide to transmission electron microscopy: fundamentals*, Momentum Press, 2016.

10 M. De Graef, in *Introduction to Conventional Transmission Electron Microscopy*, ed. C. U. Press, 2003, pp. 136–234.

11 Z. Luo, *A practical guide to Transmission Electron Microscopy, Volume II*, Momentum Press, 2016.

12 F. Hofer, F. P. Schmidt, W. Grogger and G. Kothleitner, *IOP Conf. Ser. Mater. Sci. Eng.*, 2016, **109**, 0–9.

13 R. Brydson, *Aberration-Corrected Analytical Transmission Electron Microscopy*, 2011.

14 W. G. McMillan and E. Teller, *J. Phys. Chem.*, 1951, **55**, 17–20.

15 J. M. Thompson, *Mass Spectrometry*, Pan Standford Publishing, 2018.

16 P. L. Urban, Y. Chen and Y. Wang, *Time-Resolved Mass Spectrometry*, Wiley, 2016.

17 J. Ryczkowski, *Catal. Today*, 2001, **68**, 263–381.

18 B. Stuart, *Introduction* in *Infrared spectroscopy*, 2005, p. 1.

19 S. M. Rogers, C. R. A. Catlow, C. E. Chan-Thaw, D. Gianolio, E. K. Gibson, A. L. Gould, N. Jian, A. J. Logsdail, R. E. Palmer, L. Prati, N. Dimitratos, A. Villa and P. P. Wells, *ACS Catal.*, 2015, **5**, 4377–4384.

20 P. Willmott, *An Introduction to Synchrotron Radiation*, Wiley, 2nd edn., 2019.

21 G. Bunker, in *Introduction to XAFS*, Cambridge University Press, 2010, pp. 36–105.

22 J. Evans, *X-Ray Absorption Spectroscopy for the Chemical and Materials Sciences*, John Wiley & Sons Ltd., 2017.

23 M. Newville, *J. Synchrotron Radiat.*, 2001, **8**, 322–324

24 J. A. van Bokhoven and C. Lamberti, Eds., *X-ray Absorption and X-ray Emission Spectroscopy: Theory and Applications*, Wiley-VCH, 1st edn., 2016.

25 G. Hutchings, M. Davidson, R. Catlow, C. Hardacre, N. Turner and P. Collier, Eds., *Modern Developments in Catalysis*, World Scientific, 2016.

26 T. Yamamoto, *X-Ray Spectrom.*, 2008, **37**, 572–584.

27 G. Bunker, in *Introduction to XAFS*, Cambridge University Press, 2010, pp. 134–188.

28 A. J. Dent, G. Cibin, S. Ramos, A. D. Smith, S. M. Scott, L. Varandas, M. R. Pearson, N. A. Krumpa, C. P. Jones and P. E. Robbins, *J. Phys. Conf. Ser.*, 2009, **190**, 0–4.

29 A. J. Dent, G. Cibin, S. Ramos, S. A. Parry, D. Gianolio, A. D. Smith, S. M. Scott, L. Varandas, S. Patel, M. R. Pearson, L. Hudson, N. A. Krumpa, A. S. Marsch and P. E. Robbins, *J. Phys. Conf. Ser.*, 2013, **430**, 0–7.

30 A. J. Dent, *Top. Catal.*, 2002, **18**, 27–35.

31 B. Ravel and M. Newville, *J. Synchrotron Radiat.*, 2005, **12**, 537–541.

32 G. Bunker, in *Introduction to XAFS*, Cambridge University Press, 2010, pp. 189–192.

33 U. Bergmann and P. Glatzel, *Photosynth. Res.*, 2009, **102**, 255–266.

34 P. Eisenberger, P. M. Platzman and H. Winick, *Phys. Rev. Lett.*, 1976, **36**, 623–626.

35 K. Hamalainen, D. P. Siddons, J. B. Hastings and L. E. Berman, *Phys. Rev. Lett.*, 1991, **67**, 2850–2853.

36 S. Diaz-Moreno, S. Hayama, M. Amboage, A. Freeman, J. Sutter and G. Duller, *J. Phys. Conf. Ser.*, 2009, **190**, 0–4.

37 S. Hayama, G. Duller, J. P. Sutter, M. Amboage, R. Boada, A. Freeman, L. Keenan, B. Nutter, L. Cahill, P. Leicester, B. Kemp, N. Rubies and S. Diaz-Moreno, *J. Synchrotron Radiat.*, 2018, **25**, 1556–1564.

38 M. A. Newton and A. J. Dent, in *In-situ Characterization of Heterogeneous Catalysts*, 2013, pp. 75–119.

Chapter 3

Understanding the mechanochemical synthesis of $LaMnO_3$ and its catalytic behaviour

This chapter presents work investigating how planetary ball milling induces a chemical reaction on solid precursors to result in a new phase. A combination of both lab-based and synchrotron techniques has been explored to provide new insights into the mechanochemical synthesis of $LaMnO_3$ and its catalytic behaviour, with a manuscript published in "*Dalton Transactions*"[1] R. H. Blackmore, M. E. Rivas, T. E. Erden, T. D. Tran, H. R. Marchbank, D. Ozkaya, M. Briceno de Gutierrez, A. Wagland, P. Collier and P. P. Wells. Understanding the Mechanochemical Synthesis of $LaMnO_3$ and its Catalytic Behaviour. *Dalt. Trans.*, 2020, **49**, 232–240.

Authors T. Eralp Erden and T. D. Tran have been listed on this paper due to their running analysis of XPS and STEM-EELS data, respectively. D.Ozkaya and M. Briceno de Gutierrez provided further guidance towards TEM analysis. H. R. Marchbank helped with initial XRD Rietveld refinement. A. Wagland and P. Collier were included due to their industrial involvement with Johnson Matthey. M. E. Rivas and P.P. Wells were industrial and academic supervisors of this project.

Further topics regarding the mechanochemical synthesis of $LaMnO_3$ under an argon environment were published in "*Physical Chemistry Chemical Physics - PCCP*"[2] R. H. Blackmore, M. E. Rivas, G. F. Tierney, K. M. H. Mohammed, D. Decarolis, S. Hayama, F. Venturini, G. Held, R. Arrigo, M. Amboage, P. Hellier, E. Lynch, M. Amri, M. Casavola, T. Eralp Erden, P. Collier and P. P. Wells. The electronic structure, surface properties, and *in situ* N_2O decomposition of mechanochemically synthesised $LaMnO_3$. *Phys. Chem. Chem. Phys.*, 2020, **22**, 18774–18787

Authors G. F. Tierney, D. Decarolis, S. Hayama, F. Venturini, G. Held, R. Arrigo, M. Amboage, P. Hellier, E. Lynch, M. Amri, M. Casavola listed on this paper were included due to their support as either beamline staff or as help to complete beamtime experiments over numerous 24 h days. K. M. H. Mohammed analysed Mn Kβ XES data, M. Amri the *in situ* ball milling XRD data and T. Eralp Erden provided guidance towards NAP-XPS analysis.

3.1 Introduction

Perovskite structures, ABO_3, have long been recognised for their catalytic capabilities, with the potential to become suitable substitutes for noble metals in electrocatalysis and automotive exhaust applications.[3,4] Current commercially available catalysts commonly consist of expensive and rare platinum group metals (PGM), such as Pt, Rh and/or Pd. Their synthetic routes frequently comprise of multiple process steps, large solvent volumes and require treatment of waste materials, all at a large energy cost. It is this that drives the need to develop new 'cleaner' and sustainable synthetic routes of 'earth-abundant' catalytically active materials.

With the properties of catalysts highly dependent on the method of preparation, a change in the synthetic route results in differences of phase composition, surface area and particle size, all of which affects crystallinity, texture and morphology.[5] Synthetic routes traditionally used for the synthesis of perovskite materials, such as co-precipitation and sol-gel, require a final high temperature annealing step to achieve the final crystalline perovskite phase. These elevated temperatures cause sintering of the particles to produce materials with low surface areas and thus reduced catalyst activity.[6,7] Mixed metal oxides with perovskite structures are known to readily form via mechanochemical grinding from single metal oxide precursors.[7–9] This presents a clear opportunity to progress the mechanochemical synthesis of perovskites and to optimise the performance in sustainable energy technologies and emission control strategies.[10]

The mechanochemical synthesis of $LaMnO_3$ from single La and Mn oxide precursors has been well reported throughout literature, however, there is limited information on the intermediate steps during milling.[8,11,12] Work completed by *Bolarin et. al.* showed that an orthorhombic crystalline perovskite phase was produced after 4.5 h of milling without the need of a high temperature calcination step in a SPEX 8000 D mixer mill, with the particle size decreasing exponentially with milling time.[11] *Escobedo et. al.* also performed milling experiments in a SPEX 8000 D mixer mill, however, aimed to further understand how different Mn oxide precursors (MnO_2, Mn_2O_3 and Mn_3O_4) along with different milling jars and media material altered the final material composition of crystalline perovskite phases.[12] They were able to deduce that an initial mixture of Mn_2O_3 with La_2O_3 required the lowest milling time for $LaMnO_3$ formation. Experiments performed by *Zhang et. al.* in a planetary ball mill showed that a crystalline $LaMnO_3$ phase was formed after 3 h with a final surface area of 10 $m^2\ g^{-1}$. Their experimental conditions of 700 rpm and 15 mm ZrO_2 milling media were able to produce similar perovskite structures with different A-sites (Pr, Nd and Sm).[8] Though the mechanochemical synthesis of $LaMnO_3$ has clearly been documented already within literature, these studies only assess the crystalline content as a function of milling time by iterative lab-based techniques, such as XRD or TEM with selected area electron diffraction (SAED). With amorphous material known to commonly be produced by

mechanochemistry, and signs of this observed from broadening of the diffraction peaks in their XRD, it suggests more comprehensive analysis is required. Furthermore, these studies do not perform testing of the mechanochemical synthesised $LaMnO_3$. Systematic studies of other perovskite systems, such as $LaCoO_3$ and $LaCo_{(1-x)}Fe_xO_3$, still only perform XRD analysis with respect to the milling synthesis but provide a greater understanding of testing and suitability of these milled materials to specific applications.[7,13–15]

The ever-increasing need for environmental protection and tightening emission control regulations has led to the continual research towards the decomposition of the environmental pollutant N_2O (deN_2O). N_2O emissions result in the depletion of the stratospheric ozone layer, whilst contributing to the greenhouse effect; having a global warming potential (GWP) ~310 times that of CO_2 and an atmospheric half-life of <115 years.[10,16,17] Though Rh on a zirconia-alumina support is reported to be among the most effective catalysts for deN_2O, its low thermal stability and high precious metal cost prevents its widespread industrial application.[18] This can also be reflected within zeolite systems, which are predominately only active for low reaction temperatures.[19] Mixed metal oxide systems have shown potential as deN_2O catalysts at high reaction temperatures.[20] $LaMnO_3$, and related perovskite structures, have been reported within literature to show a strong correlation between their preparation method, with resulting structure, and catalytic activity.[21] The most efficient catalysts are thought to have an increased ratio of Mn(III)/Mn(IV), with good redox recyclability, along with high oxygen mobility and improved oxygen desorption. Work by *Ivanov et al.* were able to highlight the importance oxygen surface exchange properties and bulk oxygen mobility for $La_{1-x}Sr_xMnO_3$.[22] These studies synthesise perovskites via the Pechini (sol-gel) method, inducing structural distortion and/or defects though (partial) substitution of either the A or B sites. However, synthesising $LaMnO_3$ by mechanochemistry can also produce materials with high levels of distortion, along with defects to produce improved catalytically active materials with high oxygen mobility, at a lower energy cost.[23]

Difficulties arise when analysing the mechanochemical synthesis, where the continuous movement of the planetary ball mill and milling media does not allow for *in situ* monitoring. Furthermore, the production of highly disordered materials cannot be assessed by lab-based techniques alone. The approach in this work has, therefore, been to use advanced characterisation techniques, such as X-ray absorption spectroscopy (XAS), alongside XRD, and TEM, on ***ex situ*** 'time-slices' to understand the chemical transformations occurring within ball milling. XAS does not rely on periodic ordering and is highly sensitive to the local structural changes within the materials. It produces an overall per atom average of the bulk material and is ideally suited to studying ball milled samples to provide information on both amorphous and crystalline phases.[24]

To provide a more in-depth insight into the evolution of perovskite formation and the effect of milling atmosphere, the mechanochemical synthesis of $LaMnO_3$, from La_2O_3 and Mn_2O_3, has been investigated by XAS, which has not been previously been reported. By performing deN_2O on the final milled materials it demonstrated how the mechanochemical routes introduce active sites, via oxygen vacancies, for improved catalytic performance.

3.2 Material and methods

3.2.1 $LaMnO_3$ Sample Preparation

Mechanochemical synthesis. The mechanochemical synthesis of mixed metal oxides was investigated using lanthanum (III) oxide (Alfa Aesar, 99.9 %) and manganese (III) oxide (Alfa Aesar, 98.0 %) precursors for the preparation of perovskite $LaMnO_3$. The samples were prepared using a 4–station Fritsch Pulverisette 5 Planetary Ball Mill with 250 mL ZrO_2 grinding jars, at Johnson Matthey, Sonning Common, UK. Measurements of Mn_2O_3 (3.33 g) and La_2O_3 (6.74 g) starting materials were used in order to synthesise stoichiometric $LaMnO_3$ (10 g). Care was taken to ensure the La precursor used was either fresh or had been calcined overnight (>12 h) at 500 ˚C to guarantee a La_2O_3 phase. 50 g of Yttria-stabilised zirconia (YTZ®) 5 mm milling media was used. The mill operated at room temperature at 400 rpm for 4 hours. Note, that a separate jar was milled for each 'time-slice' and a jar containing sand (10 g) and water to balance the mill.

To investigate the effect of milling atmosphere the mechanochemical synthesise of $LaMnO_3$ was performed under an inert gaseous (argon) environment. Care was taken to keep every parameter the same as the previous experiment, except for the change in milling atmosphere. Both Mn_2O_3 and La_2O_3 were separately degassed with the grinding jars and YTZ 5mm milling media placed in an oven overnight to remove any air or surface moisture before transferring into the glove box. Here, the ZrO_2 grinding jars were prepared in an argon glove box, sealed and then transferred out of the glove box to the planetary ball mill at Johnson Matthey. After milling was completed the jars were then moved back into the glove box for the powder to be removed. These materials were stored in the glove box, sampling when required for analysis. A proportion of the material was also exposure to air and analysed.

Sol-gel synthesis. $LaMnO_3$ was also prepared by the sol-gel Pechini method.[25] First, equivalent molar ratios of ethylene glycol (2.56 g) and citric acid (8.68 g) were separately dissolved in 15 mL of water. Once combined, six drops of concentrated nitric acid were added at 60 ^oC, continuously stirring until a gel formed. Stoichiometric ratios of manganese (II) nitrate tetrahydrate (Alfa Aesar, 98 %) and lanthanum (III) nitrate hexahydrate (Sigma-Aldrich, 99.99 %) were separately dissolved in water (15 mL) and added at the same time to the gel, whist stirring. Once the gel had reformed, the resulting material was transferred to a calcination boat with high walls to allow for volume expansion. The gel was dried at 200 ^oC for 1 hour and further calcined at 700 ^oC for 4 hours with a ramp of 0.5 $^oC\ min^{-1}$.

3.2.2 *Ex situ* Characterisation

X-ray diffraction (XRD) patterns were collected on a Bruker AXS D8 diffractometer, Johnson Matthey, Sonning Common, UK. This diffractometer used a Cu *Kα* radiation

source, which is scanned over a range of $10 < 2\theta < 130°$. Phase identification of the data was conducted using Bruker DIFFRA.EVA V4.2 in order to assign the phases to the correct powder diffraction file (PDF). The structure files (.str) or crystallographic information files (.cif) were downloaded from Johnson Matthey's structural database. Peak fitting and refinement of the .cifs to the experimental data was performed using the Reitveld method on Bruker DIFFRA.TOPAS V4.2. Crystallite sizes were calculated using the volume weighted column height LVol-IB method.

Inductively coupled plasma – optical emission spectroscopy (ICP-OES) measurements were performed by the analytical department at Johnson Matthey, Sonning Common, UK. First, 100 mg of sample was dissolved in concentrated HCl and then ramped to 240 °C and held for 40 min. The resulting solution was then used for ICP-OES analysis using a Perkin Elmer Optical Emission Spectrometer Optima 3300 RL. A plasma powder of 1300 watts and pump speed of 1.5 mL min^{-1}. Flows for argon plasma were set to 15 L min^{-1} and then 1.5 L min^{-1} and 0.8 L min^{-1} for the auxiliary and nebuliser argon flow, respectively.

X-ray Absorption Spectroscopy (XAS) measurements were collected in transmission mode at both the Mn K-edge (6539 eV) and La L_3-edge (5483 eV) on the B18 beamline at the Diamond Light Source, UK. A QEXAFS set up with a Si(111) double crystal monochromator was used. Mn K-edge XAS spectra and La L_3-edge XAS were acquired with a time resolution of 20 min per spectrum (k_{max} = 14) and 5 min per spectrum (k_{max} = 10), respectively and averaged over 3 scans. A low k range could only be achieved at the La L_3-edge due its close proximity to the La L_2-edge (5890 eV). The XAS spectra were acquired concurrently with the appropriate foil placed between I_t and I_{ref}.

The *ex situ* samples were prepared as 13 mm pressed pellets on homogeneous mixing with cellulose, which allowed for an appropriate concentration. For the argon milled samples were characterised under an inert sample environment. The pellets were prepared in an argon glove box and transferred to a sealed cell with Kapton windows for XAS measurements to be performed.

The XAS data was processed using the Demeter IFEFFIT software with Horae package (Athena and Artemis), using IFEFFIT programming.[26] Athena allowed for background subtraction, normalisation, energy calibration, data series alignment, deglitching and merging of data. Whilst Artemis was used to produce structure models of the EXAFS Fourier transform data. The amplitude reduction factor, S_0^2, was derived using EXAFS analysis of appropriate reference spectra foil of known coordination numbers.

X-ray Photoelectron Spectroscopy (XPS) experiments were carried out on a Thermo Escalab 250, using monochromatised Al Kα radiation with a 650 μm spot size. Charge compensation was provided by the in-lens electron flood gun at a 2 eV setting and the "401" unit for "zero energy" argon ions. Sensitivity factors after Scofield were used in

quantification, which was measured and analysed performed by Johnson Matthey, Sonning Common, UK.

The **specific surface area analysis** was performed by the Brunauer-Emmett-Teller (BET) method on all ball milled perovskites was therefore determined by krypton adsorption, using a Quantachrome Autosorb iQ "E" at Johnson Matthey, Sonning, UK. Samples were initially heated to 368 K under vacuum for 12 h to remove any absorbed species on the surface before gas adsorption/desorption experiments began. The krypton adsorption/ desorption measurements were then performed at 77 K, achieved using liquid N_2, with relative pressure of P/P_0 = 0.175.

Transmission electron microscopy (TEM) samples were prepared by grinding a small quantity between two glass slides and then dusted onto a holey carbon coated Cu TEM grid. TEM analysis was completed by the Johnson Matthey analytical department. The samples were examined in the JEM 2800 (Scanning) Transmission Electron Microscope using the following instrumental conditions: Voltage (kV) 200; C2 aperture (um) 70 and 40. Dark-field (Z-contrast) imaging in scanning mode using an off-axis annular detector. The SE signal was acquired simultaneously with the other STEM images providing topological information of the sample. Compositional analysis by X-ray emission was detected in scanning mode.

Electron energy loss spectroscopy (EELS) was performed by the Johnson Matthey analytical department, at I14 ePSIC, Diamond Light Source, UK. Measurements were acquired using GIF Quantum 965ER spectrometer equipped on the probe-corrected JEOL ARM200CF Transmission Electron Microscope. EELS elemental mapping was completed in Scanning TEM (STEM) mode to achieve atomic resolution with a HAADF detector used for imaging. To access the oxidation states, Mn $L_{3,2}$-edges were acquired at high energy-resolution using 0.025 eV energy dispersion. To avoid beam damage which can induce a change in oxidation state spectrum images were acquired with average beam doses less than 25 × 106 e^- nm^2.

3.2.3 Catalytic activity testing

The decomposition of N_2O was carried out in a Hiden fixed-bed quartz CATLAB reactor with A temperature range of 100–800 ˚C, with a ramp rate of 10 ˚C min^{-1} was used. The reaction was performed at 30 mL min^{-1} flow of 0.5% N_2O/He over 400 mg of catalyst with sieve fraction 125–250 μm to result in a GHSV = 18 000 h^{-1}. The exhaust gas composition analysed using a Hiden QGA mass spectrometer for He (m/z = 4), N_2 (m/z = 28), O_2 (m/z = 32), N_2O(m/z = 46).

3.3 Results and discussion

3.3.1 The mechanochemical synthesis of $LaMnO_3$ in atmospheric conditions

To assess the long range structural changes as a function of milling time, XRD studies have been performed on 'time-slices' throughout the mechanochemical synthesis (Figure 3.3.1). The first clear insight is the nature of the La precursor, where at time 0 h the Bragg peaks correspond to $La(OH)_3$ as opposed to La_2O_3; this is attributed to the well-established moisture/atmospheric sensitivity of La.[8,27] Elemental analysis by ICP-OES of the milled materials confirmed the time 0 h starting material to have correct molar quantities of La (0.393 mol) and Mn (0.397 mol) for stoichiometric $LaMnO_3$. This indicates that during or after milling the La hydroxide phase is formed on extended exposure to moisture in the air. ICP-OES analysis was also able to confirm low Zr contamination from the milling jars and media (Table 3.3.1.1).

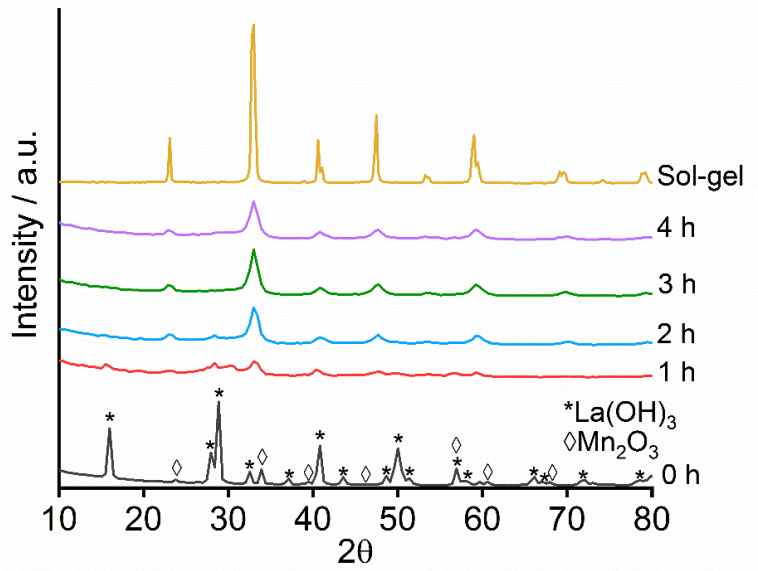

Figure 3.3.1: *X-ray diffraction patterns to show the formation of crystalline $LaMnO_3$ during milling under atmospheric conditions*

Table 3.3.1.1: *Percentage composition of La, Mn and Zr (from milling media/jar) during the mechanochemical synthesis of $LaMnO_3$*

Sample	% La	% Mn	% Zr
1 h	53.5	23.2	< 0.01
2 h	54.4	22.2	0.11
3 h	55.1	22.1	0.12
4 h	54.6	21.9	0.30

Rietveld refinement was performed on the XRD data to extract the crystalline composition weight percentage (wt %) at each time interval to follow the evolution of $LaMnO_3$ (Figure 3.3.2). As the milling time increased the presence of $La(OH)_3$ and Mn_2O_3 precursors decreased, both being completely absent after 3 h milling. The presence of La_2O_3 is detected between 0.5 – 1 h of milling, forming possible Mn_2O_3 interactions, indicating stabilisation by milling.[27] Peaks corresponding to $LaMnO_3$ begin to appear at 1 h and their intensity increases with milling time. At time 3 h 100% of the crystalline content is now $LaMnO_3$; the mechanochemical action of ball-milling has achieved the transformation of single oxide precursors to an ordered perovskite phase without the need of high temperature thermal annealing step.

There are clear indications in the XRD data that these milled samples are more complex than a 100% crystalline perovskite phase. The final material (*i.e.* 4 h milling time) has low intensity diffraction peaks and broad features in the base line, suggesting smaller crystallite size and / or low crystallinity.[7] Calculating the crystallite size of $LaMnO_3$ by the LVol-IB method confirmed a small size of 6.2 nm after 4 h of milling. The broad features apparent in the baseline are often attributed to amorphous content, which is largely undetectable by XRD. It is, therefore, important to understand more about this amorphous material as its production is a known a common consequence of ball milling and can often influence a material's catalytic properties.[28]

Using XAS, *ex situ* measurements at the Mn K-edge and La L_3-edge were performed on the milling 'time-slices' to analyse the local environment surrounding the absorbing atom. The reaction series has been compared to precursors Mn_2O_3 and $La(OH)_3$ and sol-gel synthesised $LaMnO_3$.

XANES. By comparing XANES at the pre-edge and edge regions of the XAS spectra it can probe changes to the local geometry and electronic configuration surrounding the central absorbing atom. The normalised XANES spectra collected at the Mn K-edge (Figure

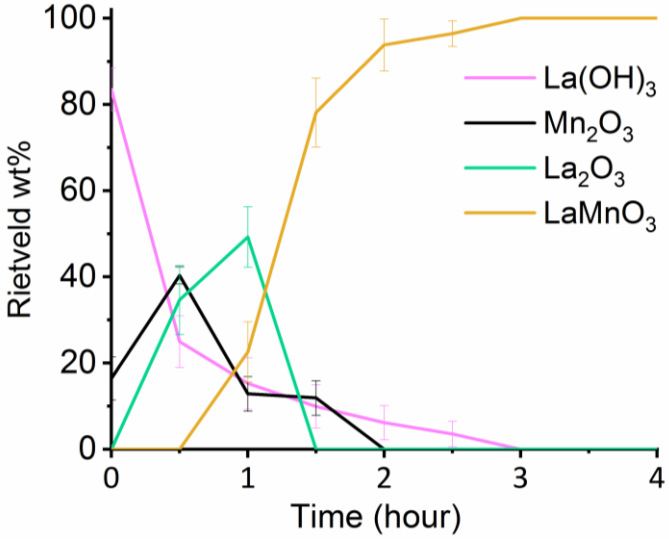

Figure 3.3.2: *XRD crystalline composition weight percentage analysis during the mechanochemical synthesis of $LaMnO_3$*

3.3.3) shows prominent changes at 1 h of milling, with no alterations observed from 2 – 4 h. At the Mn K-edge the spectra the main absorption edge corresponds to a 1*s* → 4*p* transition. The pre-edge features observed here can originate from either: (a) local or non-local hybridisation of Mn 3*d* – 4*p* orbitals to result in an dipole allowed transition from the core 1*s* orbital to the *p*-character of the unoccupied hybridised orbital, or (b) a low intensity quadrupole transition, which does not follow dipole selection rules, 1*s* → 3*d*.[29] Within the pre-edge region of Mn_2O_3 feature **(1)** is observed at 6540 eV, with an additional feature **(2)** observed at 6542 eV after 1 h of milling (Figure 3.3.3B). Increasing milling time has little effect on the position of pre-edge features, with both 1 h and 4 h milled spectra following the same line profile. Clear spectral differences are observed between the final 4 h milled perovskite and the sol-gel synthesised analogous, specifically the absence of the higher energy transition **(3)** at 6546 eV.

As milling time increases from 1 h to 4 h (Figure 3.3.3A) a change can be observed spectra at the main edge **(a)** and at **(b)** 6570 eV, indicating a transition from precursor Mn_2O_3 to $LaMnO_3$. Care must be taken when using the position of the edge energy as a measure of oxidation state. Recent work has shown the dependence of this energy is not only on Z_{eff} but effected by the type and geometry of the surrounding ligands. Therefore, no reliable conclusion on oxidation state during milling can be formed (see Chapter 4 for Mn Kβ-emission XES).[30]

The sol-gel synthesised $LaMnO_3$ shows a sharper rise in the main absorption peak, with less pre-edge and main edge features compared to the 4 h ball milled sample. The Mn K-edge corresponds to a dipole transition of a 1*s* core electron to any *p*-like unoccupied states.[31] As the 4*p* states of Mn here hybridises with O 2*p*-orbitals and 3*d*-orbitals of neighbouring Mn atoms, the local *p*-density of states is, therefore, sensitive to the charge distribution and local distortions of Mn-O bonds, as well as to any variations in the 3*d* – O 2*p* hybridisation that is believed to affect the electronic states near the Fermi level.[32]

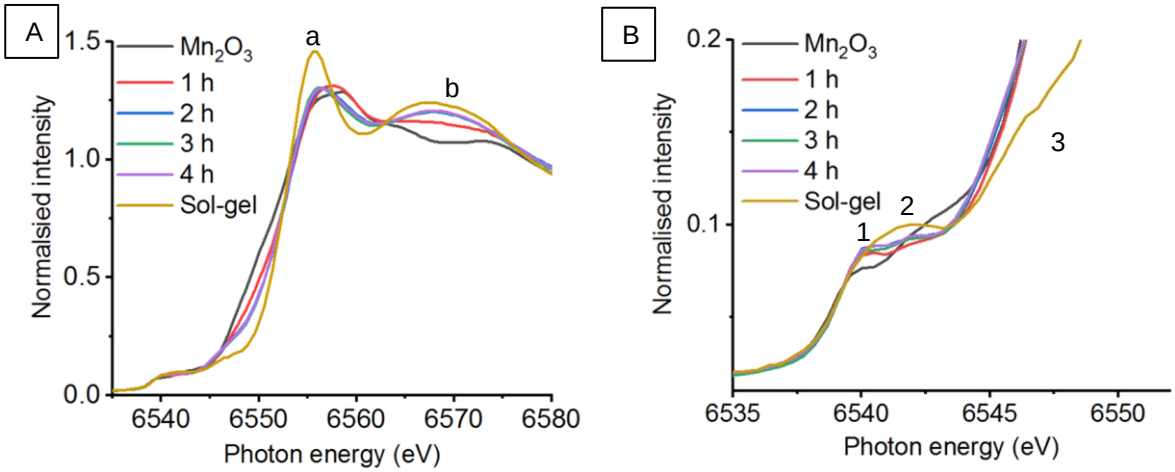

Figure 3.3.3: ***(A)*** *XANES spectra at the Mn K-edge of 'time-slices' throughout the mechanochemical synthesis of $LaMnO_3$ compared to the Mn_2O_3 precursor and a sol-gel synthesised $LaMnO_3$ with* ***(B)*** *highlighted pre-edge region*

Furthermore, the number of *s* – *p* transitions is reflected in the amount of different coordination environments; *i.e.* an increase in the number of *s* – *p* transitions is indicative of reduced symmetry. Therefore, this indicates that the sol-gel sample has a higher symmetry surrounding the central Mn absorbing atom, with more equivalent *p*-orbitals compared to ball milled samples. These differences within the electronic properties of the milled materials can suggest a reduction in particle size, changes in geometry and / or the formation of a disordered amorphous phase.

A linear combination fit (LCF) of the Mn K-edge XANES region, $-20 < E_0$ eV < 50, was performed in Athena (Figure 3.3.4). Using the precursor Mn_2O_3 and sol-gel $LaMnO_3$ as reference materials their fraction component (0 – 1) was calculated to indicate the progress through the mechanochemical synthesis. The LCF shows an overall trend of the precursor Mn_2O_3 steadily decreasing with a corresponding increase in $LaMnO_3$ species from 0 – 2.5 h of milling (Figure 3.3.4). After 2.5 – 4 h of milling the fraction contribution of the reference materials fluctuate around 50/50. This analysis approach is limited due to the high proportion of unknown intermediates in the milled materials and therefore lack of appropriate reference materials. The LCF method here is forced to produce an output combination of only Mn_2O_3 and $LaMnO_3$ to equal 1. This produces results that show how the sol-gel synthesised $LaMnO_3$ differs from the mechanochemically synthesised $LaMnO_3$, rather than the progress through the synthesis.

XANES spectra collected at the La L_3-edge consists predominantly of an intense allowed $2p \rightarrow 5d$ electron transition (Figure 3.3.5). The edge position remains at a consistent energy for all the milling 'time-slices'. However, after mixing of the La precursor with Mn_2O_3 at time 0 h in a pestle and mortar a significant reduction in the main absorption peak **(A)** is observed. This is also reflected in the 1 - 4 h milled samples, suggesting a more disordered environment, with a lower symmetry surrounding the central La absorbing atom

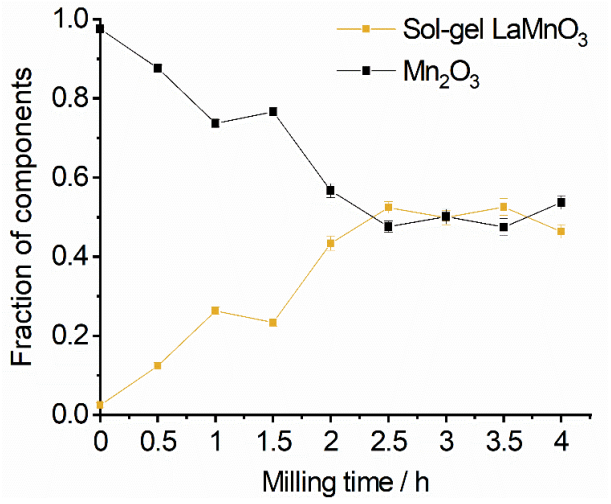

Figure 3.3.4: *Linear combination analysis at the Mn K-edge of XANES spectra during 'time-slices' through the mechanochemical synthesis of $LaMnO_3$ using Mn_2O_3 and sol-gel synthesised $LaMnO_3$ as reference materials*

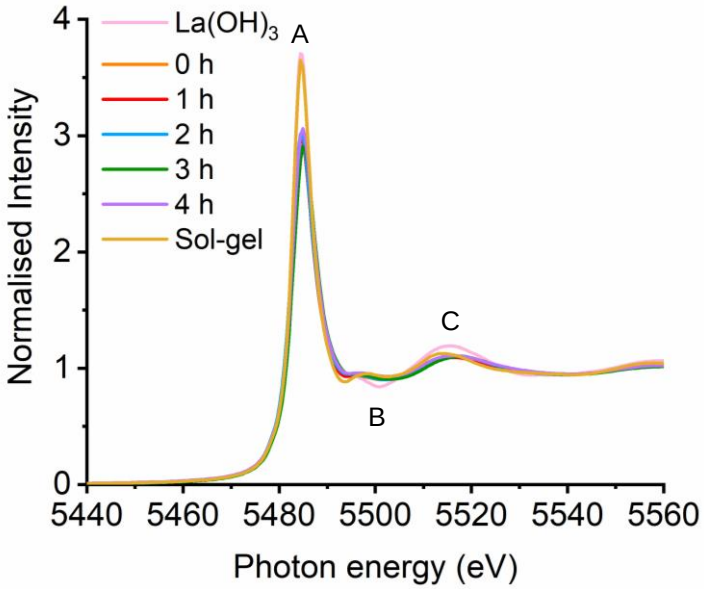

Figure 3.3.5: *XANES spectra at the La L_3-edge for $LaMnO_3$ prepared by sol-gel synthesis and hourly 'time-slices' during ball milling, compared to $La(OH)_3$ precursor*

compared to the reference materials; sol-gel synthesised $LaMnO_3$ and $La(OH)_3$. A decrease in the amplitude of this peak can also be attributed to a reduction in particle size, a common consequence of ball milling, as seen in the XRD.[33] Further structural changes are observed in the XANES, with the absence of feature **(B)** at 5500 eV and a reduction in **(C)** at 5515 eV compared to the $La(OH)_3$ spectrum; indicating a transformation towards the sol-gel perovskite structure in the absence of milling. Clear spectral variations are, however, still observed after 4 h of milling compared to the sol-gel synthesised $LaMnO_3$.

EXAFS Analysis. Following the changes observed in the XANES region, the EXAFS part of the X-ray absorption spectrum has now been assessed to understand the changes to the local coordination environment of both Mn and La (Figure 3.3.6 and Figure 3.3.7). To understand the structure of the milled materials, it was important to first analyse the start and desired end point of the synthesis, *i.e.* Mn_2O_3 and sol-gel $LaMnO_3$.

The Mn_2O_3 spectrum was fitted to 4 single scattering paths; two Mn–O and two Mn–Mn (Figure 3.3.8). Here, the number of Mn–O scattering paths have been simplified from three to two, in order to minimise fitting parameters due to their close proximity in length. The CN of the scattering paths were adjusted accordingly, reflecting Jahn Teller distortion of the d^4 Mn^{3+} ion in Mn_2O_3. This, however, does in turn increase the static disorder within the system, which is reflected in the σ^2 values for the Mn-O scattering paths (Table 3.3.1.2). For Mn-Mn scattering, only the two nearest single-scattering paths were needed to provide a good model of the data.

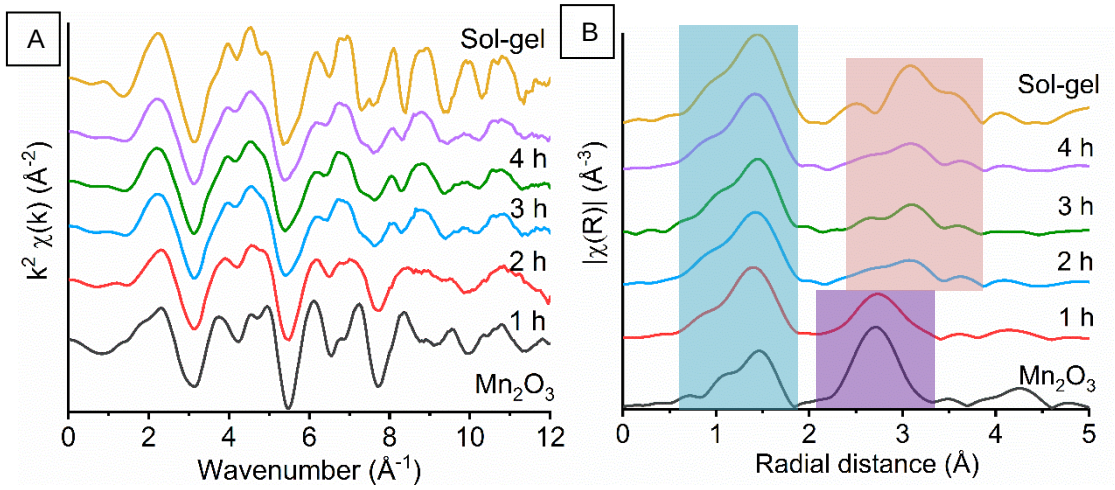

Figure 3.3.7: *k^2 weighted EXAFS oscillations at the Mn K-edge* ***(A)*** *and its respective nonphase-corrected Fourier transform* ***(B)*** *for $LaMnO_3$ synthesised by sol-gel and by ball milling from 1 h - 4 h compared to precursor Mn_2O_3 (Mn-O, Mn-Mn and Mn-La scattering paths are highlighted blue, purple and orange box, respectively)*

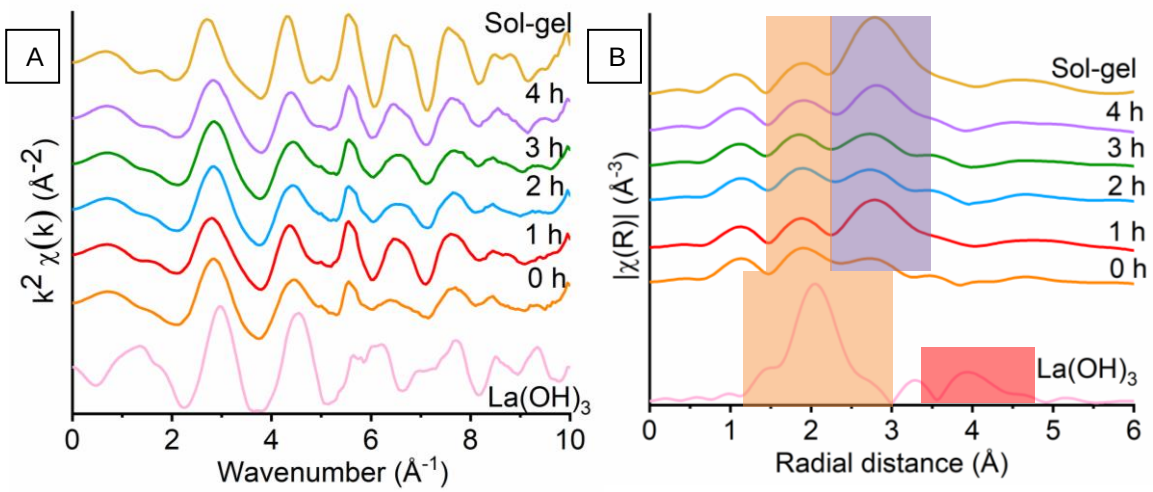

Figure 3.3.7: *k^2 weighted EXAFS oscillations at the La L_3-edge* ***(A)*** *with nonphase-corrected Fourier transform (**B**) for $LaMnO_3$ synthesised by sol-gel and by ball milling compared to the precursor $La(OH)_3$ (La-O, La-La and La-Mn scattering paths are highlighted green, yellow and red box, respectively)*

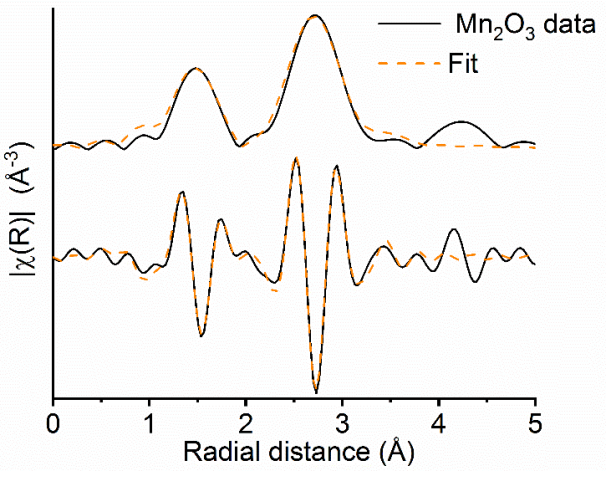

Figure 3.3.8: *Mn K-edge EXAFS data of Mn_2O_3 showing the magnitude and imaginary components of the k^2-weighted FT data and fits*

Table 3.3.1.2: *EXAFS fitting parameters for the Mn K-edge for spectra collected at 'time-slices' throughout the mechanochemical synthesis of $LaMnO_3$ compared to Mn_2O_3 and sol-gel synthesised $LaMnO_3$ Fitting parameters: $S_0^2 = 0.7$ as determined by the use of a Mn foil standard; Fit range $3 < k > 12$, $1.2 < R > 3.85$. [a]CN fixed to known structures and the number of scattering paths reduced in order to minimise fitting parameters [b]All refined CN are within 10% error margin*

Sample	Bond (Abs-Sc)	CN	E_0 (eV)	σ^2 / Å^2	R / Å	R_{factor}
[a]Mn_2O_3	Mn-O1	4.0	-6(2)	0.007(1)	1.92(2)	0.02
	Mn-O2	2.0		0.011(6)	2.27(3)	
	Mn-Mn1	6.0		0.0070(8)	3.10(2)	
	Mn-Mn2	6.0		0.012(3)	3.57(3)	
[a]Time 0	Mn-O1	4.0	-6(2)	0.005(1)	1.92(1)	0.03
	Mn-O2	2.0		0.009(6)	2.27(3)	
	Mn-Mn1	6.0		0.0070(5)	3.09(4)	
	Mn-Mn2	6.0		0.012(2)	3.57(1)	
[b]Time 1 h	Mn-O1	3.9(3)	-8(7)	0.0038(9)	1.90(1)	0.03
	Mn-Mn1	4.1(5)		0.010(1)	3.07(1)	
	Mn-Mn2	6.3(6)		0.015(2)	3.58(2)	
[b]Time 2 h	Mn-O	5.0(2)	-7(2)	0.0065(4)	1.91(3)	0.04
	Mn-La1	5.9(5)		0.013(1)	3.24(4)	
	Mn-La2	2.0(2)		0.0039(1)	3.38(1)	
[b]Time 3 h	Mn-O	4.9(2)	-6(1)	0.0070(4)	1.92(3)	0.01
	Mn-La1	5.9(4)		0.012(2)	3.27(1)	
	Mn-La2	1.9(1)		0.003(1)	3.40(1)	
[b]Time 4 h	Mn-O	5.0(1)	-7(1)	0.0054(3)	1.90(2)	0.01
	Mn-La1	5.9(5)		0.014(1)	3.24(1)	
	Mn-La2	2.0(1)		0.0043(3)	3.37(1)	
[a]Sol-gel	Mn-O	6.0	-5(2)	0.0058(5)	1.93(4)	0.02
	Mn-La1	6.0		0.0071(6)	3.34(6)	
	Mn-La2	2.0		0.0020(9)	3.70(9)	

The sol-gel $LaMnO_3$ EXAFS data (Figure 3.3.9) was modelled with three single scattering paths; one Mn–O and two Mn–La. The crystal structure of $LaMnO_3$ identifies three unique Mn-O distances, however, to reduce the number of parameters in the EXAFS model, a sole Mn-O scattering path was used with a CN of 6 (Table 3.3.1.2). The crystal structure of $LaMnO_3$ also identifies 4 single scattering Mn-La distances between 3.24 Å and 3.65 Å; again to reduce the number of parameters in the EXAFS fitting model, a good correlation between the experimental data and simulated fit was achieved by incorporating two Mn-La scattering paths at 3.24 Å and 3.65 Å (Figure 3.3.9).

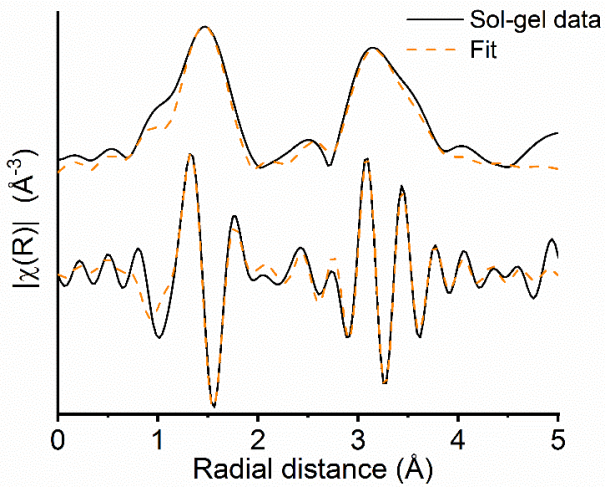

Figure 3.3.9: *Mn K-edge EXAFS data of $LaMnO_3$ showing the magnitude and imaginary components of the k^2-weighted Fourier transform data and simulated fits*

Preparing the simplified models of both the precursor and expected final material by reducing the number of parameters allows for an easier to fit and comparison to the resulting mixture of materials from milling. The time 0 h sample, consisting of Mn_2O_3 and $La(OH)_3$ before milling, produced a good model when the data was fitted to the same scattering paths as Mn_2O_3, as no reaction is expected to occur between the precursors before milling (Figure 3.3.10).

Visual comparison of the Mn K-edge data of the milled materials, Mn_2O_3 and sol-gel $LaMnO_3$ show that there are observable differences from as early as 1 h of milling (Figure 3.3.11). Inspecting the Fourier transform EXAFS data for the 1 h milled sample there are features at the same distances as observed from Mn_2O_3, indicating similar scattering paths when modelling the EXAFS data (Table 3.3.1.2). However, only one Mn-O scattering path was included in the fitting model, with a corresponding CN of 4; it is still expected that 6 oxygen atoms surrounding the central Mn atom. The higher σ^2 value reported for the Mn-O2 scattering path, 0.007 $Å^2$, compared to Mn-O1, 0.011 $Å^2$ in Mn_2O_3 fitting parameters

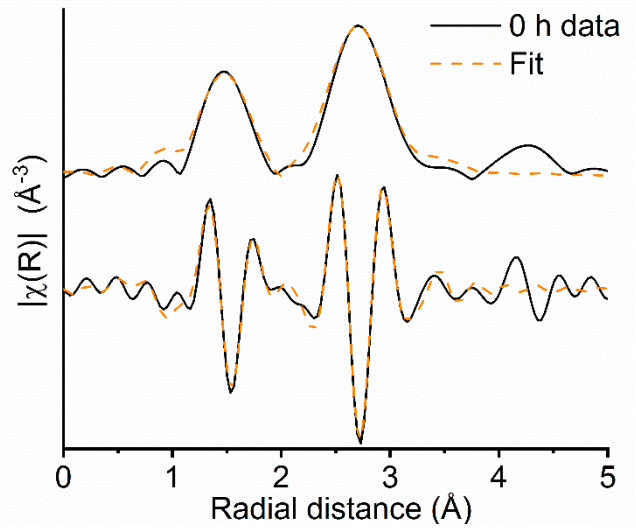

Figure 3.3.10: *Mn K-edge EXAFS data after time 0 h of milling showing the magnitude and imaginary components of the k^2-weighted Fourier transform data and simulated fits*

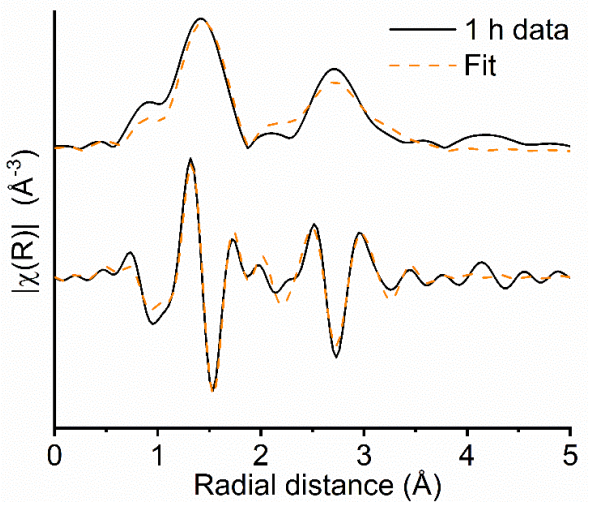

Figure 3.3.11: *Mn K-edge EXAFS data after time 1 h of milling showing the magnitude and imaginary components of the k^2-weighted Fourier transform data and simulated fits*

results from an elongated long bond length of 2.27 Å causing a higher thermal disorder. However, after ball milling for 1 h static disorder is introduced into the sample, as well as the thermal disorder already present, thus increasing σ^2. This large σ^2 dampens the EXAFS signal for the Mn-O2 scattering path and it is therefore hard to detect the oxygen atoms located at large distances from the Mn absorbing atom. Furthermore, due to oxygen having a limited back-scattering amplitude at these longer distances it makes any inclusion on the Mn-O2 path unreliable. This path is therefore absent in the fitting model, however, it does not exclude the existence of the longer Mn–O bond distances but implies a significant degree of structural disorder. Due to the σ^2 of Mn-O1 decreasing from Mn_2O_3 to time 1 h, at 0.007 $Å^2$ to 0.0038 $Å^2$, respectively, it suggests a more ordered Mn-O1 environment. This is further reflected in the EXAFS Fourier transform within the first coordination shell when an increase in peak intensity is observed. Two Mn-Mn scattering paths were then incorporated within the fitting model with reduced CN. However, small discrepancies are observed between the simulated fit and experimental data within the second coordination shell. Difficulties arose when fitting EXAFS data of mixtures due to unknown intermediates or highly disordered amorphous material as they contain scattering paths vastly different to the expected crystalline structures.

Previously, within both the XANES and EXAFS Fourier transform, changes are observed at 2 h of milling indicating a shift towards a perovskite structure. Furthermore, the XANES and EXAFS show no change from 2 - 4 h of milling and therefore similar fitting models are expected for all 3 milled samples. The 2 - 4 h ball milled EXAFS data were well-modelled to the three single scattering paths; one Mn-O and two Mn-La, with values consistent within the errors of sol-gel $LaMnO_3$ fit (Figure 3.3.12).

Observations within the XANES region suggests clear electronic and geometric differences within the first coordination sphere surrounding the central Mn atom between ball milled and sol-gel samples, but it is unclear what causes these changes due the broad,

unresolved features. Parameters calculated by the simulated fits for 2 – 4 h of milled material suggest a degree of oxygen deficiency with a calculated CN of 5, compared to the expected octahedral configuration CN of 6 for the sol-gel synthesised $LaMnO_3$. Commonly, large errors are reported within CN calculated by EXAFS analysis, however, the parameters calculated here for the Mn-O coordination show a trend towards the expected value. Also a decrease in the EXAFS k^2-oscillation amplitude is correlated to either a decrease in CN or σ^2. With both the 4 h milled and sol-gel $LaMnO_3$ exhibiting similar σ^2 values, at 0.0054 and 0.0058 $Å^2$ respectively, it suggests there is a proportion of oxygen deficiency present within 4 h milled material. A further two Mn-La scattering paths were used within the fitting model for the 4 h milled material at 3.24 Å and 3.37 Å, and for the crystalline sol-gel $LaMnO_3$ sample at 3.34 Å and 3.70 Å. The Mn-La scattering paths for the 4 h milled sample suggest that there are two Mn La species; one crystalline $LaMnO_3$ corresponding to the 3.37 Å scattering path and an amorphous species at a much shorter scattering path of 3.24 Å than an expected crystalline distance. This shorter scattering path has a corresponding high σ^2 of 0.014 $Å^2$ in agreement that a highly disordered species is produced via mechanochemical grinding, as well as a proportion of expected crystalline material. Though this shorter scattering path shows similarities with the Mn-Mn scattering length calculated in Mn_2O_3, Mn-La and Mn-Mn have very different back scattering amplitudes and it was therefore possible to distinguish between when performing EXAFS modelling. Comparisons at the k^2 EXAFS oscillations suggests that 2 - 4 h milled materials were more representative of $LaMnO_3$, rather than Mn_2O_3.

EXAFS modelling at the La L_3-edge was proven complicated due to the low *k* range resulting from the following L_2-edge and because of the sensitive nature of La forming different phases on exposure to air. However, using observations at both the Mn K-edge and La L_3-edge EXAFS Fourier transform data, reaction insights into the mechanochemical synthesis of $LaMnO_3$ can be proposed (Figure 3.3.13). At the La L_3-edge XAS data shows significant structural alterations as early as 0 h of milling, indicating La-Mn scattering is already present. No further changes were observed from 1 to 4 h (Figure 3.3.7). However, at the Mn K-edge Mn-Mn scattering is still detected after 1 h of milling, which suggests that the Mn environment is predominantly still in its Mn_2O_3 bulk form with the La species dispersed over its surface (Figure 3.3.6). As milling time increases, it allows for both precursors to undergo mechanical activation. After 2 h of milling at the Mn K-edge a shift is observed within the second coordination shell corresponding to a Mn-La scattering path, indicative of $LaMnO_3$ formation.

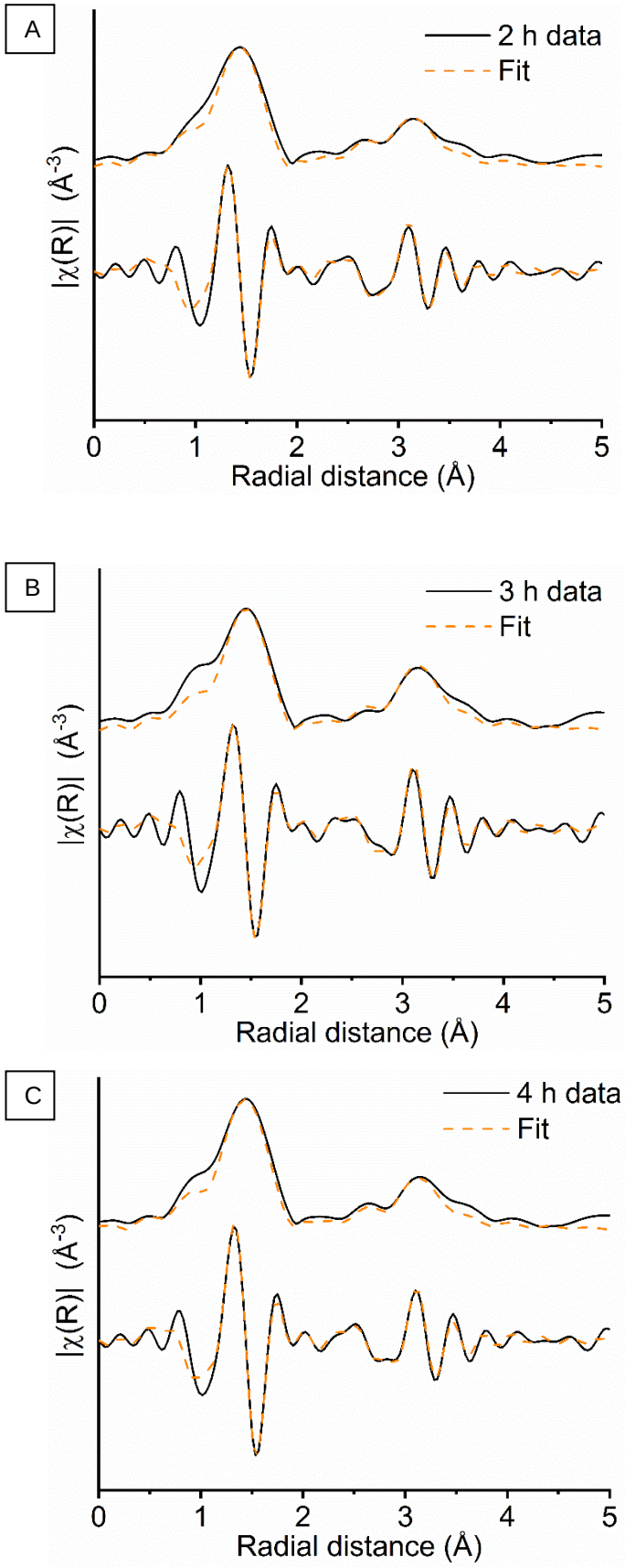

Figure 3.3.12: *Mn K-edge EXAFS data after* ***(A)*** *2 h,* ***(B)*** *3 h and* ***(C)*** *4 h of milling showing the magnitude and imaginary components of the k^2-weighted Fourier transform data and simulated fits*

The XAS observations further highlight differences in the information obtained from XRD studies. It shows the importance of advanced characterisation in understanding the amorphous content and how it effects the evolution of the perovskite $LaMnO_3$ by mechanochemical synthesis. Even after 3 and 4 h milling, where 100 % crystalline $LaMnO_3$ is observed via XRD, clear differences are observed in the diffraction and XAS data compared to the sol-gel synthesised sample. By performing advanced characterisation, it has resulted in the understanding of complex and disordered materials to provide further insights into the mechanochemical synthesis of $LaMnO_3$, not previously reported.

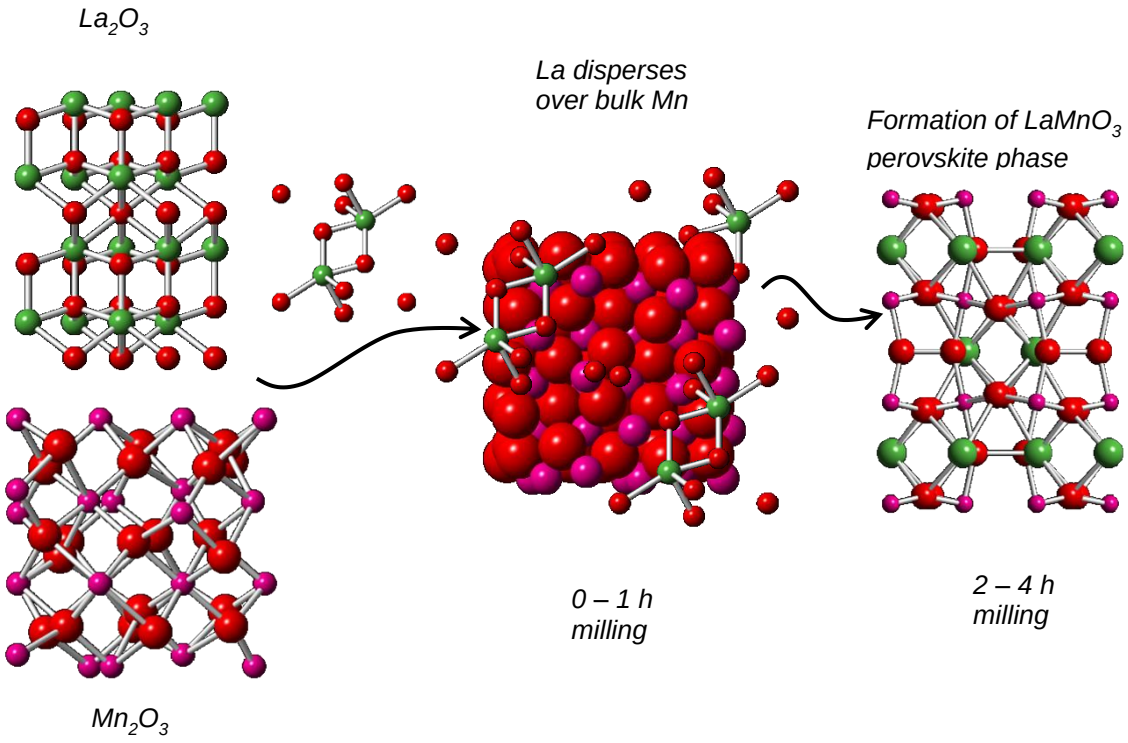

Figure 3.3.13: *Schematic of insights into the mechanochemical synthesis of $LaMnO_3$ resulting from XAS measurements at both the Mn K-edge and La L_3-edge*

3.3.2 The mechanochemical synthesis of $LaMnO_3$ in an inert (argon) atmosphere

Assessing the composition of 'time-slices' during the mechanochemical synthesis of $LaMnO_3$ under atmospheric conditions, it was observed that the La oxide precursor was significantly hygroscopic and readily formed a hydroxide, $La(OH)_3$.[27] Elemental analysis detected the correct stoichiometry for the precursor to be La_2O_3, indicating the hydroxide phase formed during or after milling on prolonged exposure to air. As a consequence of the La sensitivity, care was taken to use either fresh or baked La precursor to ensure an initial La_2O_3 phase. When performing milling experiments with $La(OH)_3$ and Mn_2O_3 at the correct stoichiometry, the final perovskite phase was extremely unstable, decomposing towards the initial metal oxides on prolonged exposure to the air. To understand the importance of the La_2O_3 phase and how its moisture sensitivity effects perovskite formation, the same milling procedure was conducted under an argon milling atmosphere. Samples have been analysed under both an argon environment and on subsequent exposed to air.

XRD. When acquiring the XRD under an argon environment the sample holder produced a 'hump' within the diffraction pattern at ~20 2θ (Figure 3.3.14A, B). Crystalline La_2O_3 and Mn_2O_3 phases were confirmed prior to milling (Figure 3.3.14A). After only 1 h of milling a dramatic decrease in Bragg peak intensities is observed, along with broadening in the peak baseline; indicating a high proportion of amorphous and disordered material. Rietveld analysis detected no crystalline Mn_2O_3 at 1 – 4 h of milling, whereas La_2O_3 wt% steadily decreased with milling time (Figure 3.3.15A). After 1 h of milling 67% of the crystalline content was ascribed to $LaMnO_3$, with 96 wt% achieved after 4 h. However, it would be prudent to consider the vast quantity of amorphous material and the implications of the inert sample holder making the refinement of these materials challenging.

On exposure of these 'time-slices' to air, the XRD shows sharper and higher intensity Bragg peaks (Figure 3.3.14C) indicating the formation of a more ordered long-range structure. Most significantly, the diffraction peaks corresponding to crystalline $La(OH)_3$ are now detected. The lower wt% of $LaMnO_3$ calculated on exposure to air for the argon milled samples is expected to be attributed to the increased proportion of crystalline precursors, rather than decomposition of the perovskite phase. Furthermore, Rietveld refinement calculated 4 h was not sufficient to reach 100% of the crystalline content to be $LaMnO_3$, unlike its air milled analogue (Figure 3.3.1). This indicates the importance of atmospheric conditions, such as oxygen or moisture, on the formation of a crystalline perovskite phase and that an increase in milling time is required for the formation of $LaMnO_3$ from La_2O_3 instead of $La(OH)_3$.

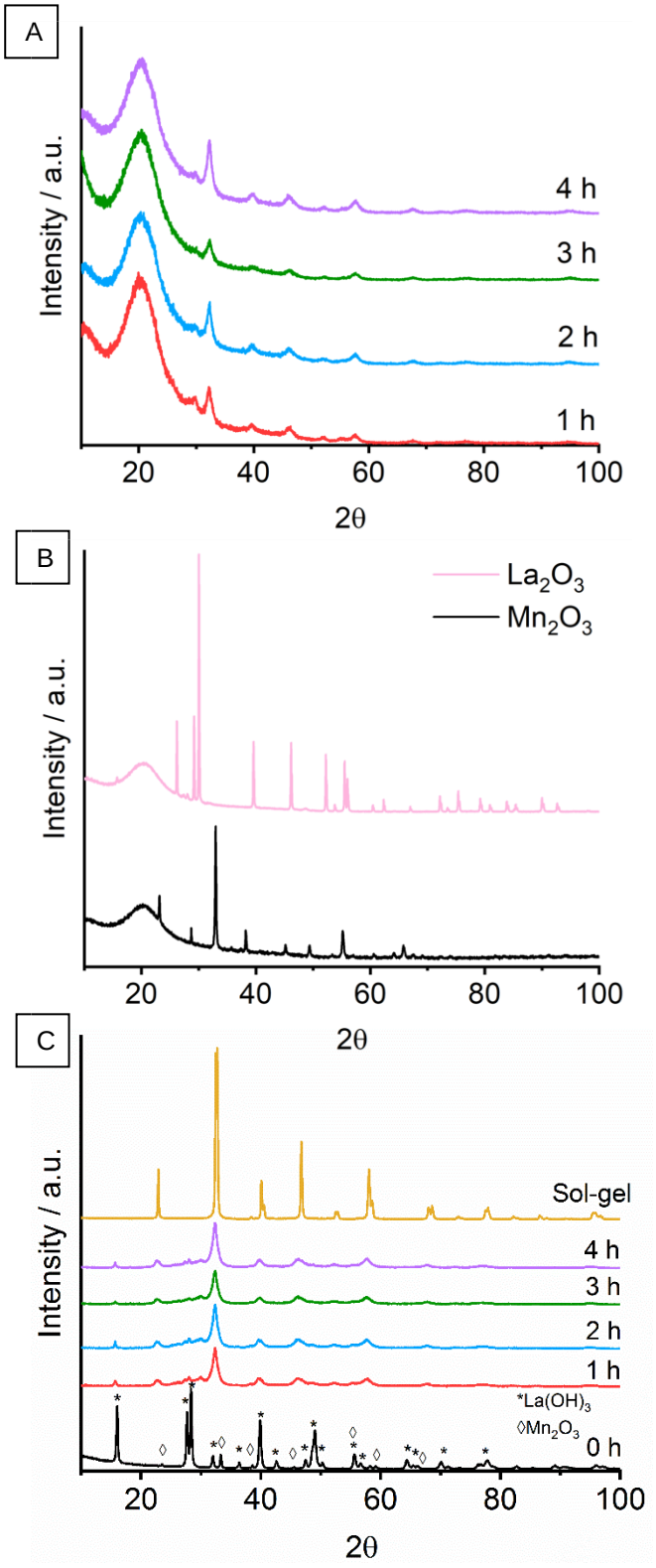

***Figure 3.3.14**: XRD performed under inert (argon) atmosphere of **(A)** precursors La_2O_3 and Mn_2O_3, **(B)** 'time-slices' to show the crystalline formation of $LaMnO_3$ by mechanochemistry (the XRD sample holder results in 'hump' at ~20 2θ) and **(C)** following subsequent exposure to air, compared to sol-gel synthesised $LaMnO_3$*

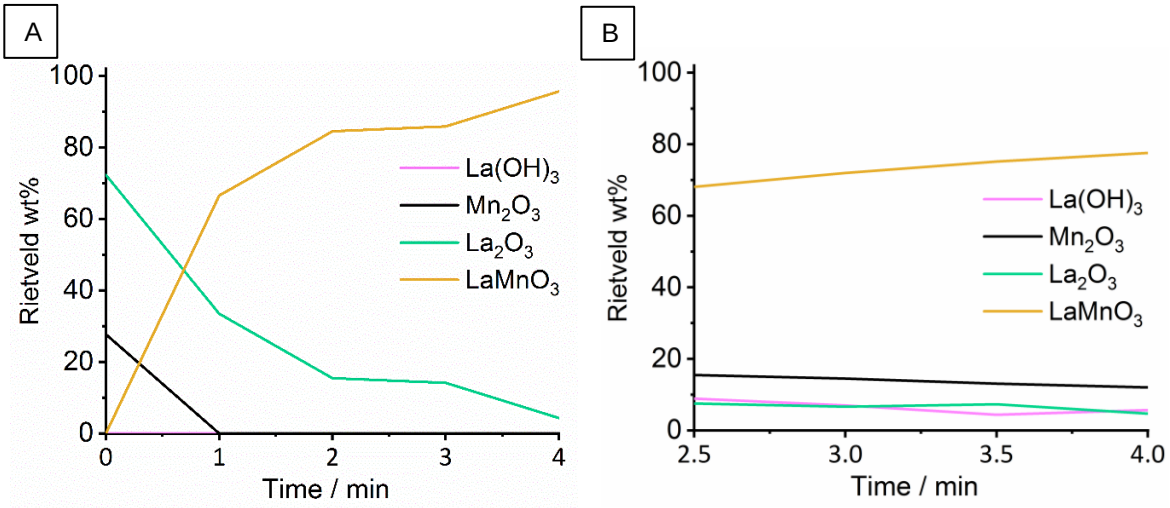

Figure 3.3.15: *XRD crystalline composition weight percentage analysis during the mechanochemical synthesis of $LaMnO_3$ under an* ***(A)*** *inert and* ***(B)*** *atmospheric sample environment*

XANES. The normalised XANES spectra were collected at the Mn K-edge in both inert and atmospheric sample environments (see experimental section 3.2.2) on *ex situ* 'time-slices' during milling to investigate the formation of $LaMnO_3$ with respect to time (Figure 3.3.16). First assessing the XANES measurements performed under an inert environment, the spectra shows the evolution of the feature at 6570 eV after just 1 h. Previously, this was linked to perovskite formation, where in the XANES spectrum of crystalline reference $LaMnO_3$ assigned to this transition the MnO_6 octahedron surrounded by 8 La ions.[34] This can therefore indicate the amorphous content, implied in the XRD patterns, possess an overall perovskite-like arrangement. However, observations within the pre-edge region can suggest both perovskite and Mn_2O_3 geometries remain due to transitions at **(1)** and **(2)**, respectively.[35,36] No significant spectral changes are observed on increasing the milling time to 3 h. Issues occurred with the data quality of samples measured under an inert atmosphere, resulting from the challenging environment used to prepare *ex situ* pellets, where it was not possible to guarantee a fully homogenous pellet.

On subsequent exposure of these inert milled samples to air, small variations within the Mn K-edge XANES spectra (Figure 3.3.16C, D) can be observed. Whilst the pre-edge follows comparable spectral features to when under an argon atmosphere, the sharper absorption peak and increased amplitude of the feature at 6570 eV indicates a slightly more ordered, regular ligand environment. Although, it is interesting to note that a large increase in crystalline peaks is detected within the diffraction patterns for the argon exposed 'time-series' (Figure 3.3.14), only subtle changes are visible within the XANES. This, once again, indicates the bulk material, including the amorphous content, has an average structure similar to the crystalline phase.

Also, on exposure to air changes within the spectra can be now observed up to 2 h of milling, corresponding to the previous XANES 'time-series' for the air milled $LaMnO_3$ (Figure 3.3.3). There are no significant changes detected on increasing the milling time to 4 h. This

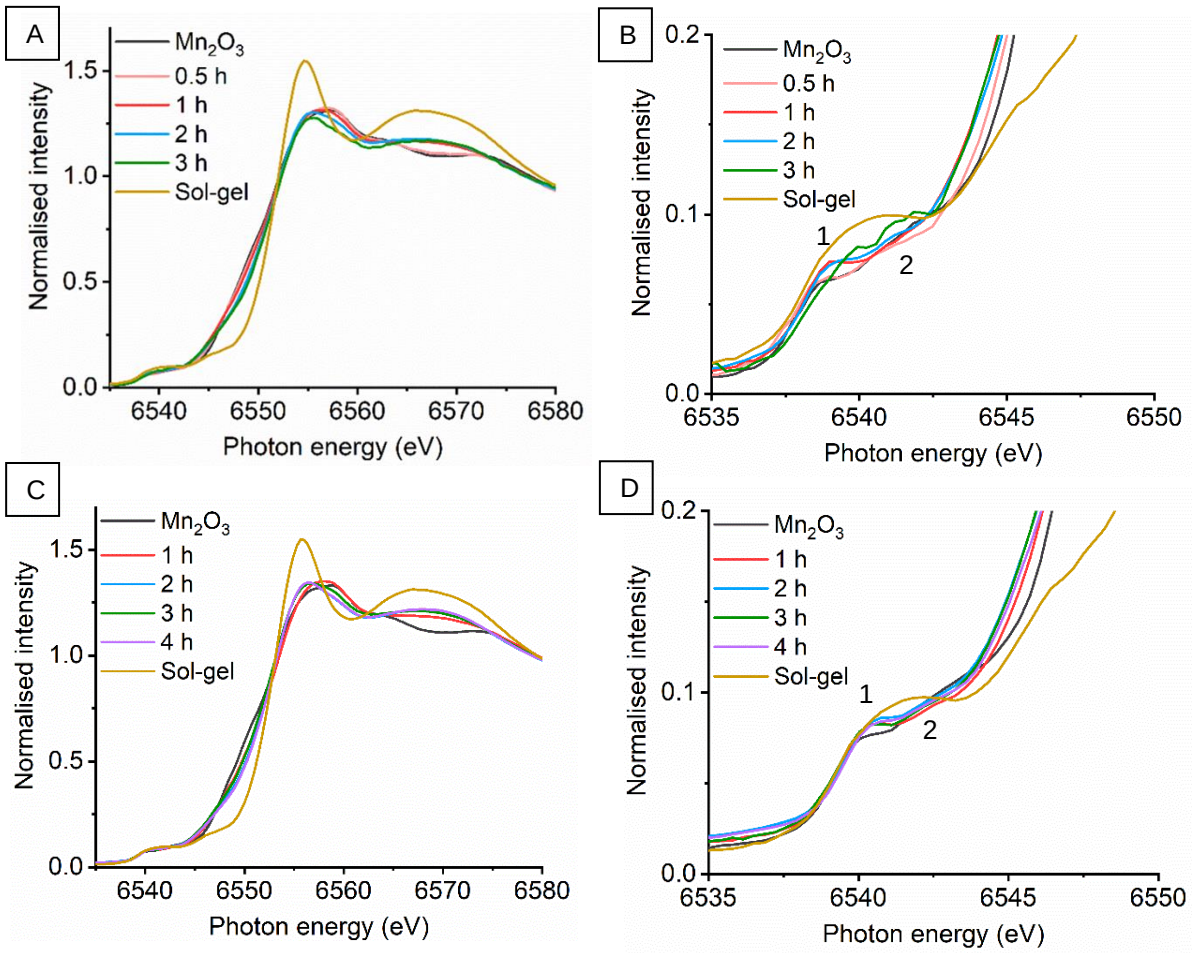

***Figure 3.3.16**: Mn K-edge **(A)** XANES and **(B)** pre-edge showing the formation of $LaMnO_3$ by mechanochemistry characterised under an inert sample environment and on subsequent exposure to air, **(C)** and **(D)**, respectively*

highlights the importance of the initial stages of milling for perovskite formation, independent of milling atmosphere.

A linear combination fit (LCF) of the Mn K-edge XANES region was performed for the exposed argon milled 'time-slices' (Figure 3.3.17) equivalent to the previous LCF study (section 3.3.1).The LCF analysis shows the change in phase distribution is comparable to

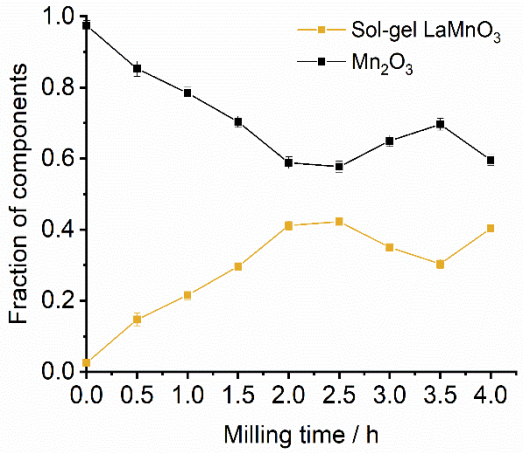

***Figure 3.3.17:** Linear combination analysis at the Mn K-edge of XANES spectra during 'time-slices' for the exposed argon milled $LaMnO_3$*

the air milled reaction pathway. However, a lower proportion of $LaMnO_3$ is indicated after 4 h of milling in argon, in agreement with XRD studies (Figure 3.3.14).

XANES spectra collected at the La L_3-edge (Figure 3.3.18) for the exposed argon milled samples show small alterations after just mixing La_2O_3 with Mn_2O_3 in a pestle and mortar, *i.e.* time 0 h. Though not as prominent as the changes observed previously for air milled time 0 h, there is a small decrease in the absorption peak amplitude (0 h spectral line behind sol-gel $LaMnO_3$). More significant changes are detected after 1 h of milling, where the lower absorption peak height corresponds to a reduction in particle size.[33] Even after 4 h of milling, spectral variations are still detected compared to the sol-gel synthesised $LaMnO_3$, indicating a disordered structure for the argon milled samples.

EXAFS. The EXAFS region has now been investigated for the argon milled 'time-slices' under an inert environment and on subsequent exposure to air (Figure 3.3.19). Initially focusing on the EXAFS Fourier transform data, whilst under an inert sample environment, similarities can be observed to the air milled 'time-series' (Figure 3.3.6). The initial alterations within the second coordination shell indicate a breakdown of the extended Mn_2O_3 structure after 1 h. After 2 h of milling a shift in the second coordination shell to a higher scattering distance can be detected, previously ascribed to Mn-La scattering. However, visual comparisons of the EXAFS k^2-oscillations for the 1 – 3 h argon milled samples measured under an inert atmosphere were challenging due to the prominent glitches present at ~8.5 $Å^{-1}$. It was therefore not possible to deduce unique scattering paths.

Exposure of these argon milled samples to air produced comparable EXAFS data to the inert characterised data set. Moreover, the improvement of data quality within the k^2 EXAFS oscillations allowed for suitable fitting models to be produced on these milling 'time-slices'.

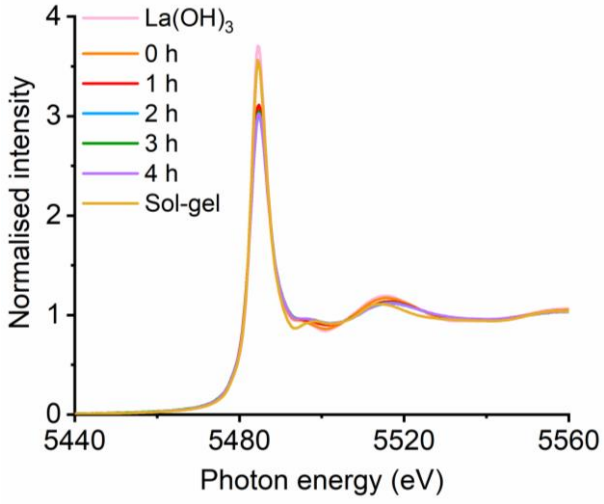

Figure 3.3.18: *XANES spectra at the La L_3-edge for $LaMnO_3$ prepared by sol-gel synthesis and 'time-slices' for exposed argon milled $LaMnO_3$*

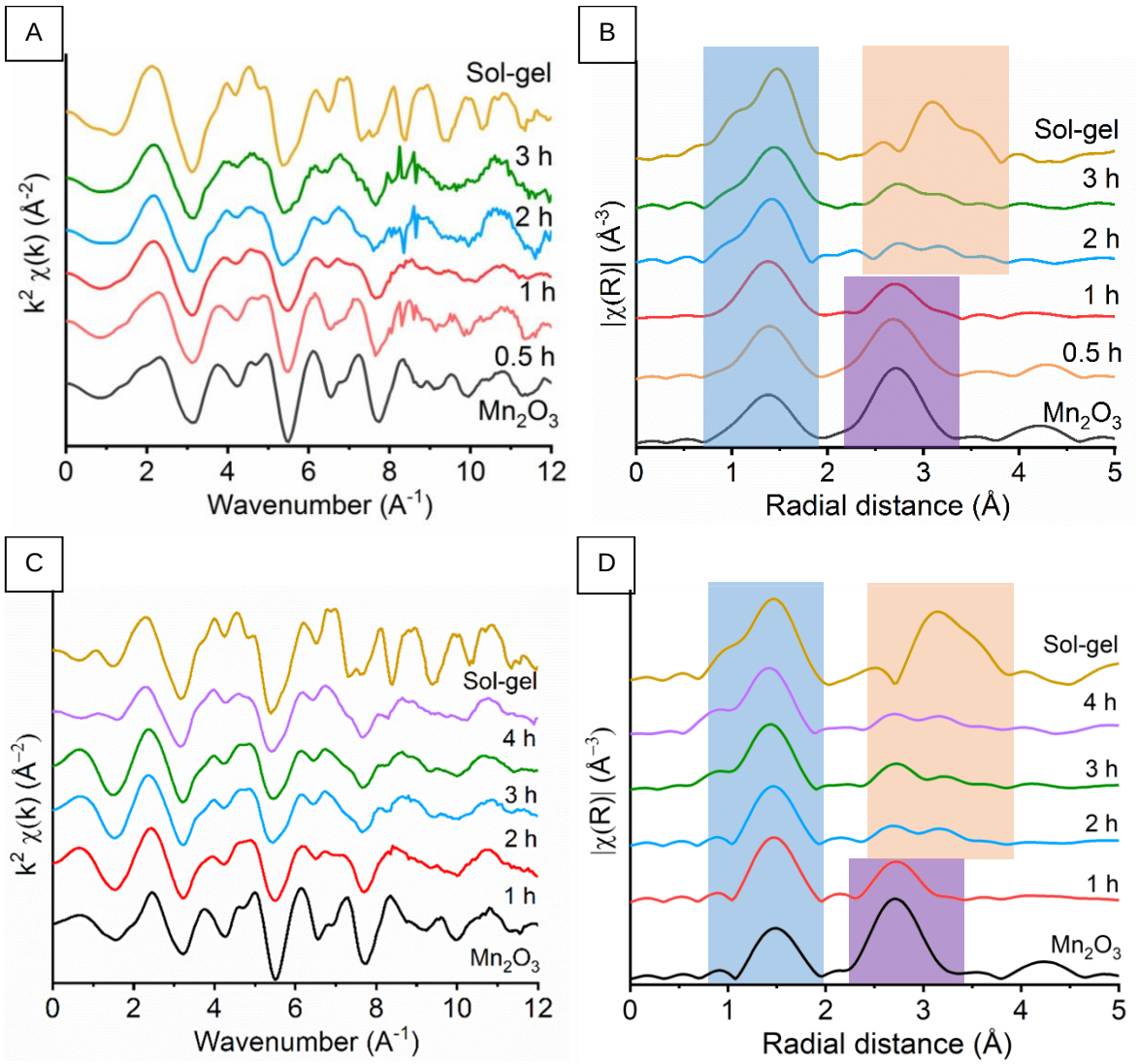

Figure 3.3.19: *Argon milled* ***(A)*** *k^2 weighted EXAFS oscillations at the Mn K-edge and* ***(B)*** *its respective nonphase-corrected Fourier transform 'time-slices' and respective exposure to air* ***(C)***, ***(D)*** *for the synthesis of $LaMnO_3$ compared to sol-gel $LaMnO_3$ and precursor Mn_2O_3 (Mn-O, Mn-Mn and Mn-La scattering paths are highlighted blue, purple and orange box, respectively)*

Table 3.3.2.1: *EXAFS fitting parameters for the Mn K-edge for spectra collected at 'time-slices' during the mechanochemical synthesis of $LaMnO_3$ under an inert environment after exposure to air, compared to precursor Mn_2O_3 and sol-gel synthesised $LaMnO_3$. Fitting parameters: $S_0^2 = 0.7$ as determined by the use of a Mn foil standard; Fit range $3 < k > 14$, $1.2 < R > 4.0$. [a]CN fixed to known structures and the number of scattering paths reduced in order to minimise fitting parameters [b]All refined CN are within 10% error margin*

Sample	Bond (Abs-Sc)	CN[b]	E_0 (eV)	σ^2	R / Å	R_{factor}
[a]Time 0 h (Mn_2O_3)	Mn-O1	4.0	-3(2)	0.006(1)	1.94(1)	0.03
	Mn-O2	2.0		0.006(4)	2.27(3)	
	Mn-Mn1	6.0		0.007(1)	3.11(1)	
	Mn-Mn2	6.0		0.014(3)	3.61(3)	
[b]Time 1 h	Mn-O1	3.5(4)	-3(2)	0.003(2)	1.91(1)	0.05
	Mn-O2	2.4(8)		0.016(2)	2.27(5)	
	Mn-Mn1	3.2(5)		0.007(1)	3.12(1)	
[b]Time 2 h	Mn-O1	3.8(6)	-3(1)	0.005(1)	1.91(1)	0.02
	Mn-O2	1.8(6)		0.015(9)	2.27(6)	
	Mn-Mn1	1.3(4)		0.006(5)	3.11(3)	
	Mn-La1	4.4(7)		0.013(4)	3.35(1)	
[b]Time 3 h	Mn-O1	4.1(2)	-7(5)	0.0049(3)	1.90(1)	0.02
	Mn-La1	6.3(4)		0.011(1)	3.31(1)	
	Mn-La2	1.9(1)		0.049(1)	3.13(1)	
[b]Time 4 h	Mn-O	4.9(1)	-9(2)	0.0062(1)	1.90(1)	0.03
	Mn-La1	6.0(1)		0.010(1)	3.30(1)	
	Mn-La2	2.0(1)		0.0050(1)	3.13(2)	
[a]Sol-gel	Mn-O	6.0	-3(4)	0.0058(5)	1.93(4)	0.02
	Mn-La1	6.0		0.0071(6)	3.34(6)	
	Mn-La2	2.0		0.0020(9)	3.70(9)	

The simulated fitting model calculated for the 1 h 'time-slice' indicates the sample is still predominantly Mn_2O_3 in character, whilst possessing a reduced Mn-Mn scattering CN of 3.2 (Table 3.3.2.1) (Figure 3.3.20A).

On increasing the milling time to 2 h the EXAFS data was well-modelled to 4 single scattering paths; two Mn-O, one Mn-La (Figure 3.3.20B). Scattering paths corresponding to both Mn_2O_3 and $LaMnO_3$ have been included to effectively model the second coordination sphere, indicating a mixed composition. With Mn-Mn scattering still detected at 2 h of milling, it implies a slower rate of perovskite formation compared to the atmospheric milled conditions.

The 3 and 4 h argon milled samples show consistent k^2 EXAFS oscillations to the sol-gel $LaMnO_3$ (Figure 3.3.20C, D). Within the first coordination shell for the 3 h exposed argon sample, a Mn-O CN of 4 was calculated (Table 3.3.2.1). However, a CN of 6 is still predicted, comparable to the 1 h air milled fitting model in section 3.3.1 (Table 3.3.1.2). On increasing in milling time to 4 h, the Mn-O CN of 4.9 indicates the structure is more consistent with the expected perovskite structure, whilst still possessing a degree of oxygen deficiency. The two Mn-La scattering paths simulated at 3.13 Å and 3.30 Å suggest there

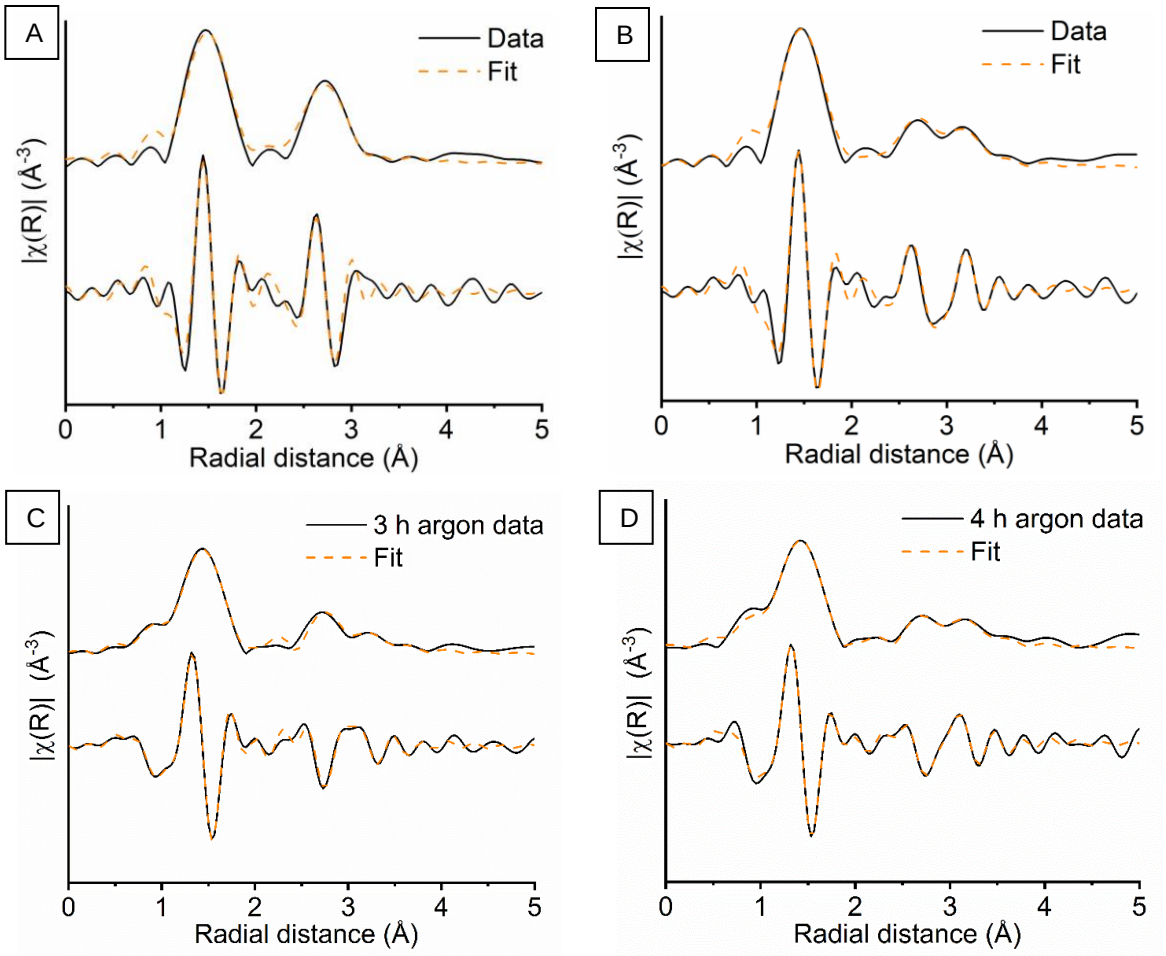

Figure 3.3.20: *Mn K-edge EXAFS data during milling under argon for* ***(A)*** *1 h* ***(B)*** *2 h* ***(C)*** *3 h and* ***(D)*** *4 h and subsequent exposure to air for the synthesis of* $LaMnO_3$*, showing the magnitude and imaginary components of the* k^2*-weighted Fourier transform data and simulated fits*

are two Mn La species; one crystalline $LaMnO_3$ and one amorphous species, comparable to the final air milled material.

With EXAFS analysis not suitable at the La L_3-edge, visual comparisons in the EXAFS Fourier transform (Figure 3.3.21) have been combined with Mn K-edge data (Figure 3.3.19) to understand how $LaMnO_3$ evolves during ball milling in an inert atmosphere. As with the proposed air milled reaction scheme (Figure 3.3.13), the XAS once again suggests La disperses over bulk Mn in the initial stages of milling. However, from the EXAFS perspective a longer milling time of 3 h is required to reach a perovskite-like phase for the argon milled samples, compared to 2 h for atmospheric milling conditions.

By understanding how both air and argon milling atmospheres effect perovskite formation it can begin to form an in-depth knowledge of how chemical transformations occur depending on the milling parameters. When milling under atmospheric conditions a reaction time of 2 h indicated the formation of an overall bulk perovskite phase. However, in the absence of air the $LaMnO_3$ phase proved difficult to form, with characterisation indicating highly disordered structures formed. By just exposing these argon milled 'time-slices' to air it was possible for greater long-range crystallite phases to form. Traditionally high temperatures are required for crystallisation to take place, suggesting that the amorphous metastate formed under inert milling possess a higher free energy than the final crystalline phases on exposure to air. Milling for 4 h under argon was not sufficient to form 100% crystalline $LaMnO_3$. This strongly suggests the importance of an air milling atmosphere to aid the evolution of the perovskite phase; whether it is incorporation of oxygen species into the lattice or La moisture sensitivity that contributes.

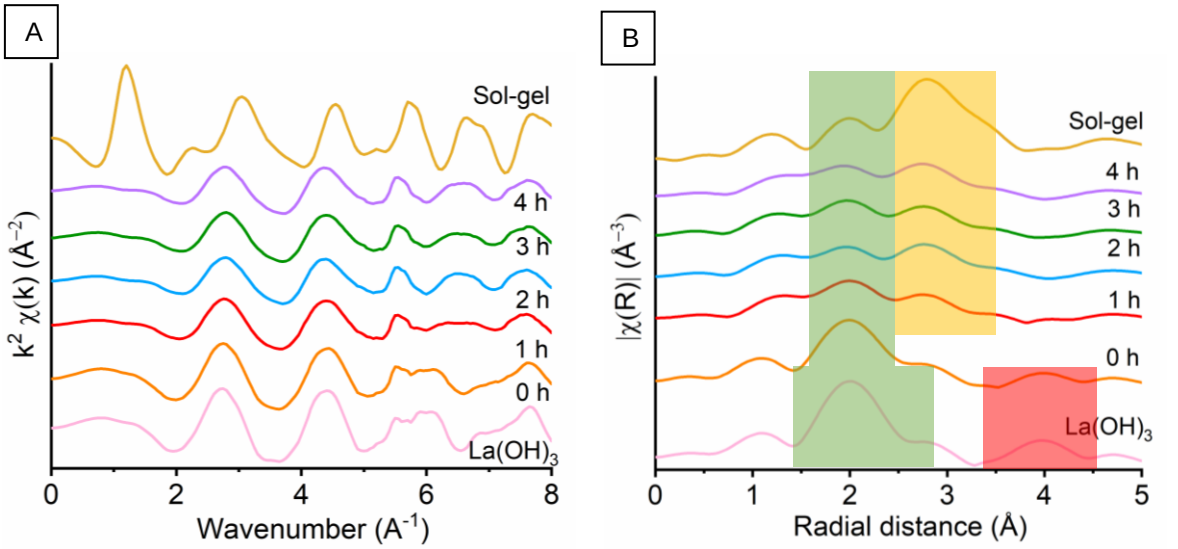

Figure 3.3.21: (A) *k^2 weighted EXAFS oscillations at the La L_3-edge with* ***(B)*** *nonphase-corrected Fourier transform at 'time-slices' during the mechanochemical synthesise of $LaMnO_3$, compared to a sol-gel $LaMnO_3$ perovskite and $La(OH)_3$ (La-O, La-La and La-Mn scattering paths are highlighted green, yellow and red box, respectively)*

3.3.3 Understanding catalytic properties of mechanochemical synthesised materials

To understand the properties of the final milled materials for catalytic applications, both 3 and 4 h of the air milled and exposed argon milled materials have been further characterised by XPS, TEM and STEM-EELS following comparisons by the XAS and XRD. The 3 and 4 h 'time-slices' have been selected due to their highest proportion of the perovskite phase.

To further investigate the variations in surface composition and identify possible active sites for catalysis, XPS measurements have been performed to understand O, Mn and La surface environments. The atomic percentage ratios (at. %) of La, Mn and O species at the surface for the air and argon milled, and sol-gel synthesised $LaMnO_3$, have been compared to the expected stoichiometric perovskite ratios (Table 3.3.3.1). The atomic percentage ratios show the argon milled samples to have the highest proportion of La to Mn on its surface. The XRD for the 3 and 4 h argon milled samples detected 71 and 77 wt% of the crystalline content as $LaMnO_3$, respectively. Whereas 100% was calculated for both the air milled catalysts. With the argon milled samples having a slower rate of perovskite formation, a higher La content on the surface is consistent with the previous in-sights into the mechanochemical synthesis. Here, the La is said to disperse over bulk Mn at the earlier stages of milling (section 3.3.1). Elsewhere, it is found that all samples have a sub-stoichiometric oxygen content at the surface. For both the argon milled catalysts the decrease in the Mn:O ratio could be a reflection of the increased La proportion.

Figure 3.3.22 shows the oxygen 1*s* XPS signals at the surface for air and argon ball milled and sol-gel synthesised $LaMnO_3$. The argon milled samples follow a vastly different spectral profile compared to that of both the air milled and sol-gel synthesised $LaMnO_3$. After deconvolution of the O 1*s* region by curve fitting, three spectral features are recognised at 529.3 eV - 529.6 eV, 531.1 eV - 531.7 eV and 533.4-534.0 eV. Here, the lowest binding energy region at 529.3 eV - 529.6 eV is assigned to lattice-type oxygens in the perovskite (O_2^{2-}), with the region between 531.1 eV - 531.7 eV corresponding to adsorbed species,

Table 3.3.3.1*: Surface At% ratio of both 3 and 4 h air and inert milled $LaMnO_3$ compared to sol-gel synthesised sample*

	Air milled		**Argon milled**			
	3 h	**4 h**	**3 h**	**4 h**	**Sol-gel**	**Expected**
Mn : La	1 : 1.1	1 : 1.2	1 : 1.7	1 : 1.7	1 : 1	1 : 1
La : O	1 : 0.2	1 : 0.2	1 : 0.2	1 : 0.2	1 : 0.2	1 : 0.33
Mn : O	1 : 0.2	1 : 0.2	1 : 0.1	1 : 0.1	1 : 0.2	1 : 0.33

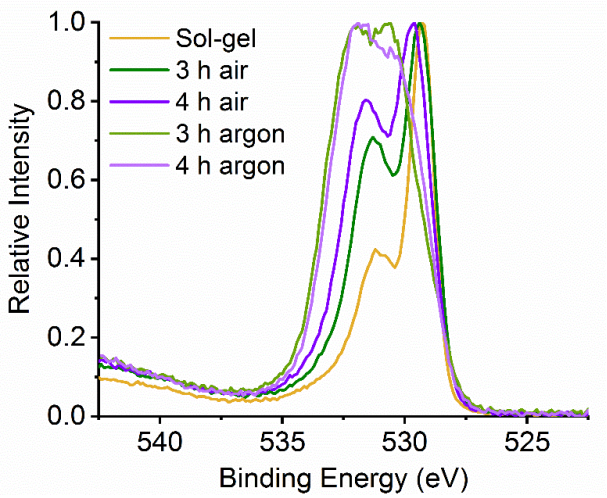

Figure 3.3.22: *XPS spectra in the O 1s region of 3, 4 h ball milled samples in both atmospheric and inert (argon) milling environments compared to sol-gel synthesised*

such as O^{2-}, O^{-} or OH^{-}.[37–39] The final peak at ~533.5 eV is then assigned to adventitious carbon, with analogous C-O peaks also being detected in the C 1*s* XPS region at 286.2 eV and 288.6 eV.[37–39]

It is commonly assumed that the active oxygen species adsorbed on the surface of perovskites, observed here within the 531.1 eV - 531.7 eV region, compensate for lattice oxygen vacancies.[39] Therefore, by comparing the proportion of adsorbed oxygen to lattice oxygen it can give an indication of the changes occurring at the adsorption centres, with respect to the synthetic route.[40–42] However, the specific surface areas of all the samples must first be comparable. The ball milled and sol-gel $LaMnO_3$ surface areas were assessed by BET theory, reporting values within range of one another; at ~4-6 $m^2\ g^{-1}$ for the ball milled samples and ~8 $m^2\ g^{-1}$ for the sol-gel $LaMnO_3$. Evaluating the absorption centres as a ratio of lattice oxygen to absorbed oxygen can now be assessed independent of surface area. After the removal of the adventitious carbon peak, both argon milled samples have a much greater intensity for the 531.1 eV - 531.7 eV binding peak, indicating more adsorbed species on the surface compared to the other $LaMnO_3$ samples. Both the air milled and sol-gel $LaMnO_3$ follow a similar peak profile over the O 1*s* region. After curve fitting, the relative intensity of the 531.1 eV - 531.7 eV feature associated decreases in the order 3 and 4 h argon milled > 3 h air milled > 4 h air milled and sol-gel synthesised $LaMnO_3$. This raises an interesting point, as the sol-gel prepared sample possessed the highest surface area compared to the ball milled samples. Therefore, at the surface of these differently synthesised perovskites profound changes must occur to the surface chemistry, providing modifications to the active centres for adsorption. Previously, it has been concluded by others that the perturbation of the surface, through oxygen vacancies, are a significant cause to increasing the number of adsorbed oxygen species.[40–42]

The La 3*d* XPS region (830 – 860 eV) has now been assessed for the $LaMnO_3$ catalysts (Figure 3.3.23). A typical double doublet splitting is observed, with the lower

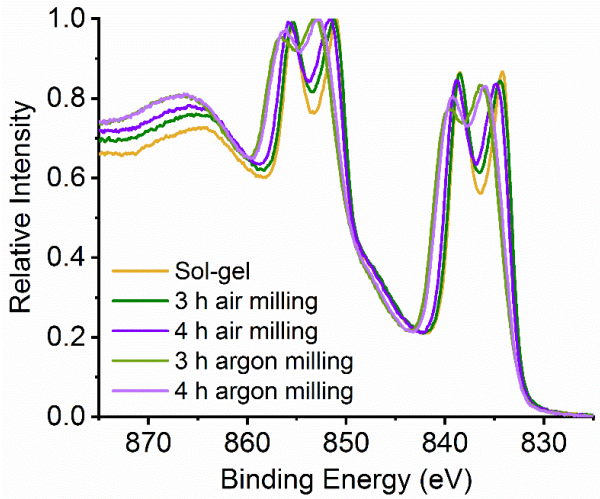

Figure 3.3.23: *XPS spectra in the La 3d region of 3, 4 h ball milled samples in both atmospheric and inert (argon) milling environments compared to sol-gel synthesised $LaMnO_3$*

energy doublet, 830 – 845 eV being assigned to La $3d_{5/2}$, and the higher energy feature, 850 – 860 eV assigned to La $3d_{3/2}$.[43] By assessing the peak splitting of the La $3d_{5/2}$ doublet it can be used to understand the nature of the La species.[44] For all samples the La $3d_{5/2}$ peak splitting values are indicative of La(III) species. However, once again the argon milled samples follow a different spectral profile to that of the other $LaMnO_3$ samples. The argon milled La $3d_{5/2}$ peak splitting of 3.7 eV is assigned to $La(OH)_3$ species at the surface of the perovskite. Alternatively, the La $3d_{5/2}$ peak splitting of 4.6 eV for the air milled and sol-gel prepared materials is indicative of La_2O_3 species. This is consistent with the higher percentage of adsorbed oxygen species within the O 1*s* region for the argon milled samples. Furthermore, in agreement with $La(OH)_3$ diffraction peaks detected in the XRD for exposed 3 and 4 h argon milled $LaMnO_3$ (Figure 3.3.14).

Two peaks are observed within the spectra recorded at the Mn 3*s* XPS region, ~83 and ~88 eV, for the differently synthesised $LaMnO_3$ samples (Figure 3.3.24). The splitting of the Mn 3*s* peak arises due to the final state effect of parallel and anti-parallel coupling between the spins of the remaining 3*s* electron and the 3*d* electrons.[45] Therefore, at a higher oxidation state, *i.e.* lower number of *d* electrons, the separation between these two peaks will decrease, allowing for Mn oxidation state assessment.[46] In Figure 3.3.24 all the samples follow the same Mn 3*s* spectral profile, with a peak splitting value of ~4.9 eV. This peak splitting indicates the presence of mixed Mn(IV)/Mn(III) valency at the surface, with literature reporting a peak splitting of 5.4 eV and 4.4 eV for Mn_2O_3 and MnO_2, repectively.[47,48] This suggests significant structural variance at the surface in both the ball milled and sol-gel $LaMnO_3$, compared to the bulk structure observed by XAS. It is these mixed valences present in Mn based perovskites that are responsible for its redox capabilities and therefore catalytic activity. [49]

The XPS analysis of the O 1*s*, La 3*d* and Mn 3*s* regions signifies the importance of surface sensitive techniques, as well as bulk structure analysis in order to understand how

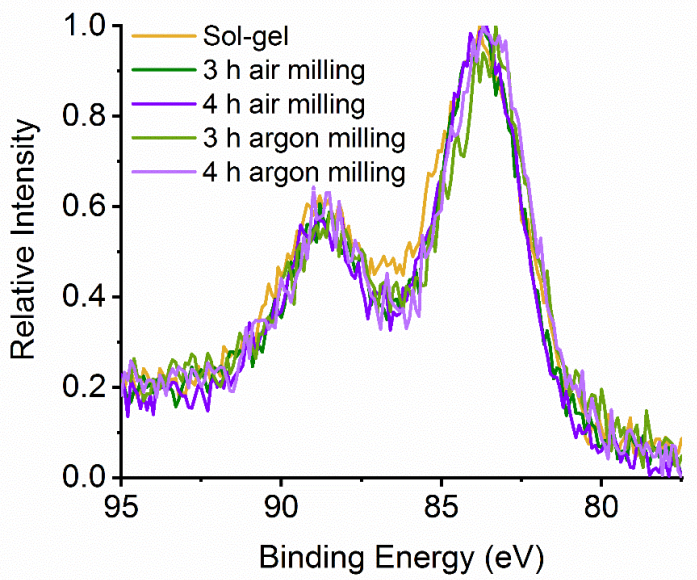

Figure 3.3.24: *XPS spectra in the Mn 3s region of 3, 4 h ball milled samples in both atmospheric and inert (argon) milling environments compared to sol-gel synthesised $LaMnO_3$*

different synthetic routes effect the structural and catalytic properties of these $LaMnO_3$ materials.

To understand the changes in morphology between the ball milled and sol-gel synthesised $LaMnO_3$, a scanning electron (SE) signal was acquired by a transmission electron microscopy (TEM) imaging to provide topological information. Figure 3.3.25 shows the 3 and 4 h air and exposed argon milled samples to have predominately similar agglomerated morphology on the same size scale. The sol-gel synthesised $LaMnO_3$, however, has a much larger size scale with a 'honey-comb' cage-like structure observed, stereotypical to a Pechini sol-gel synthesis.[25]

Bright field (BF) imaging was then performed on a TEM to achieve high magnification lattice resolution images (Figure 3.3.26). For the 3 h air milled sample small crystalline particles are visible, with 4 h of milling having a similar microstructure. This is further reflected within the argon milled samples, with phase boundaries observed for the 4 h argon milled material, suggesting a mixed composition. Difficulties arose in distinguishing between the particles for size distribution analysis due to agglomeration and the high proportion of overlapping crystallites. An amorphous phase is suggested to surround the exterior of the agglomerated particles, in agreement with broadening of the XRD base line for the milled samples. The sol-gel prepared $LaMnO_3$ presents vastly larger particle sizes at > 20 nm, contained within a highly uniform structure.

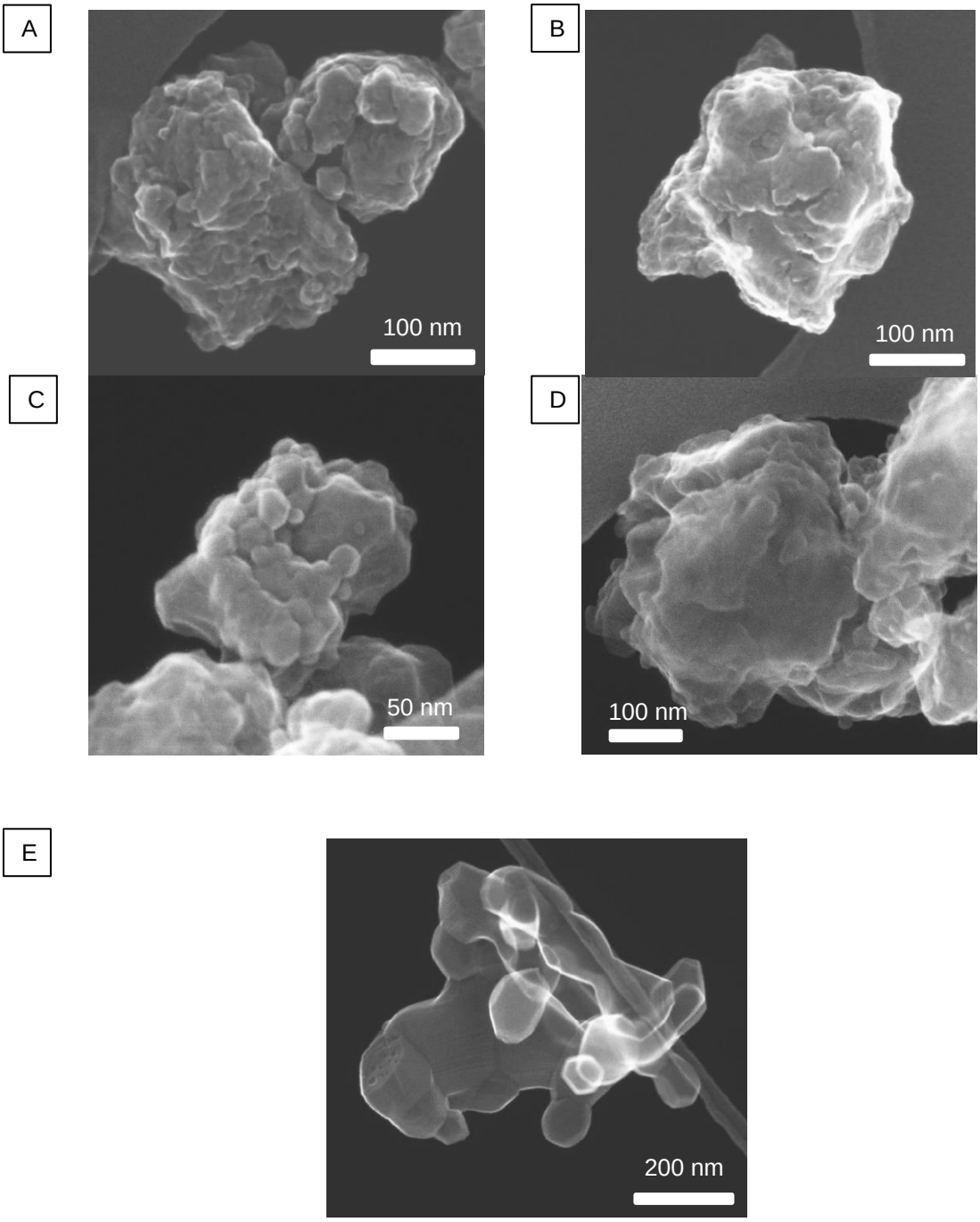

Figure 3.3.25: *SE images showing the morphological changes between* ***(A)*** *3 h* ***(B)*** *4 h ball milled in air,* ***(C)*** *3 h* ***(D)*** *4 h ball milled in argon and* ***(E)*** *sol-gel synthesized* $LaMnO_3$

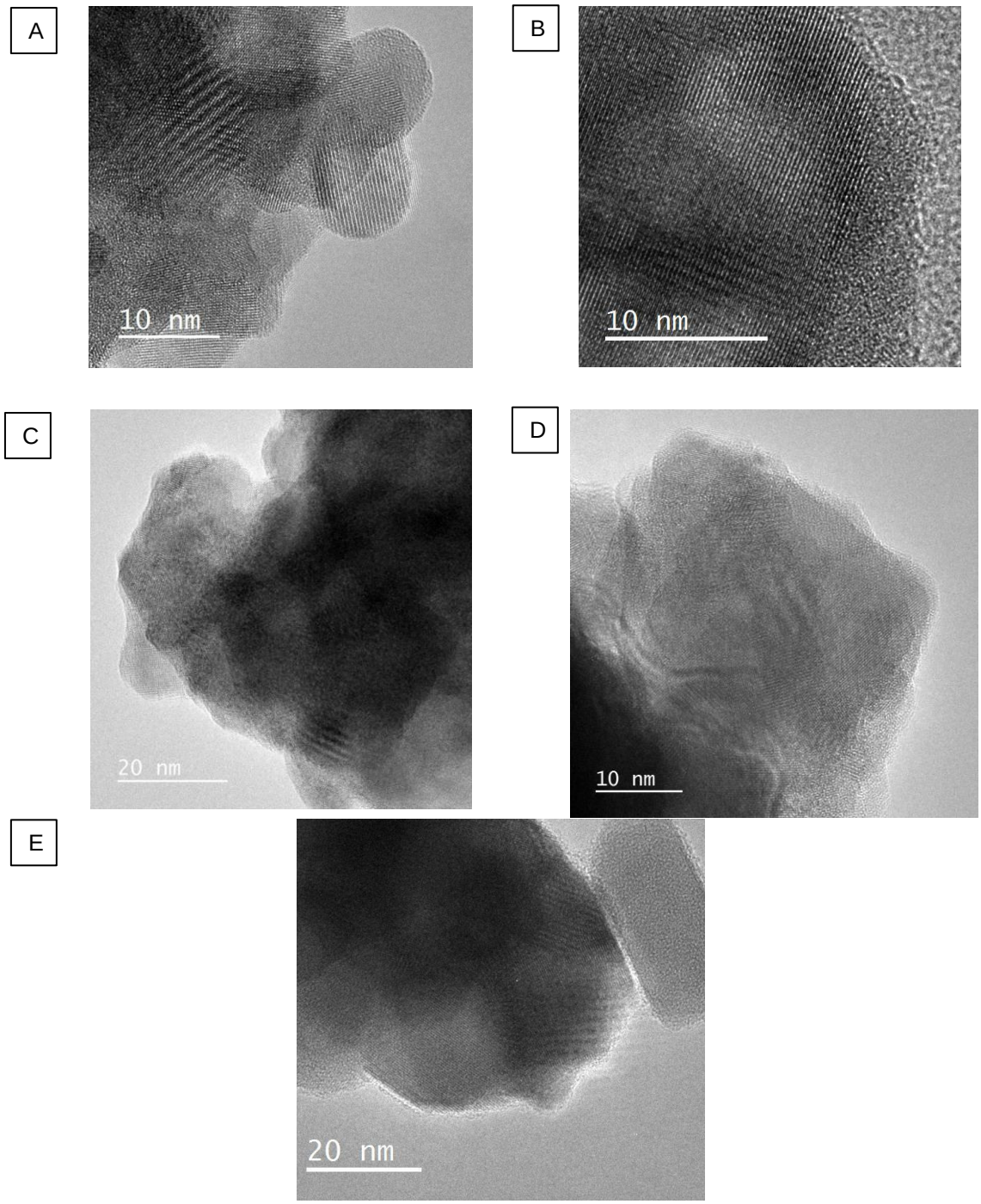

Figure 3.3.26: *BF-TEM images at magnified lattice resolution for* ***(A)*** *3 h* ***(B)*** *4 h ball milled in air,* ***(C)*** *3 h* ***(D)*** *4 h ball milled in argon and* ***(E)*** *sol-gel synthesised* $LaMnO_3$

Performing compositional analysis by X-ray emission detection in scanning mode on a TEM, elemental mapping images were produced for each La, Mn and O (Figure 3.3.27) of air milled, argon milled and sol-gel synthesised $LaMnO_3$. All materials show a homogenous composition of La, Mn and O. However, this analysis has been measured on a micro-size scale and therefore can be challenging to detect smaller discrepancies. It is also important to note that this is only one sample area and not fully representative of the overall bulk composition.

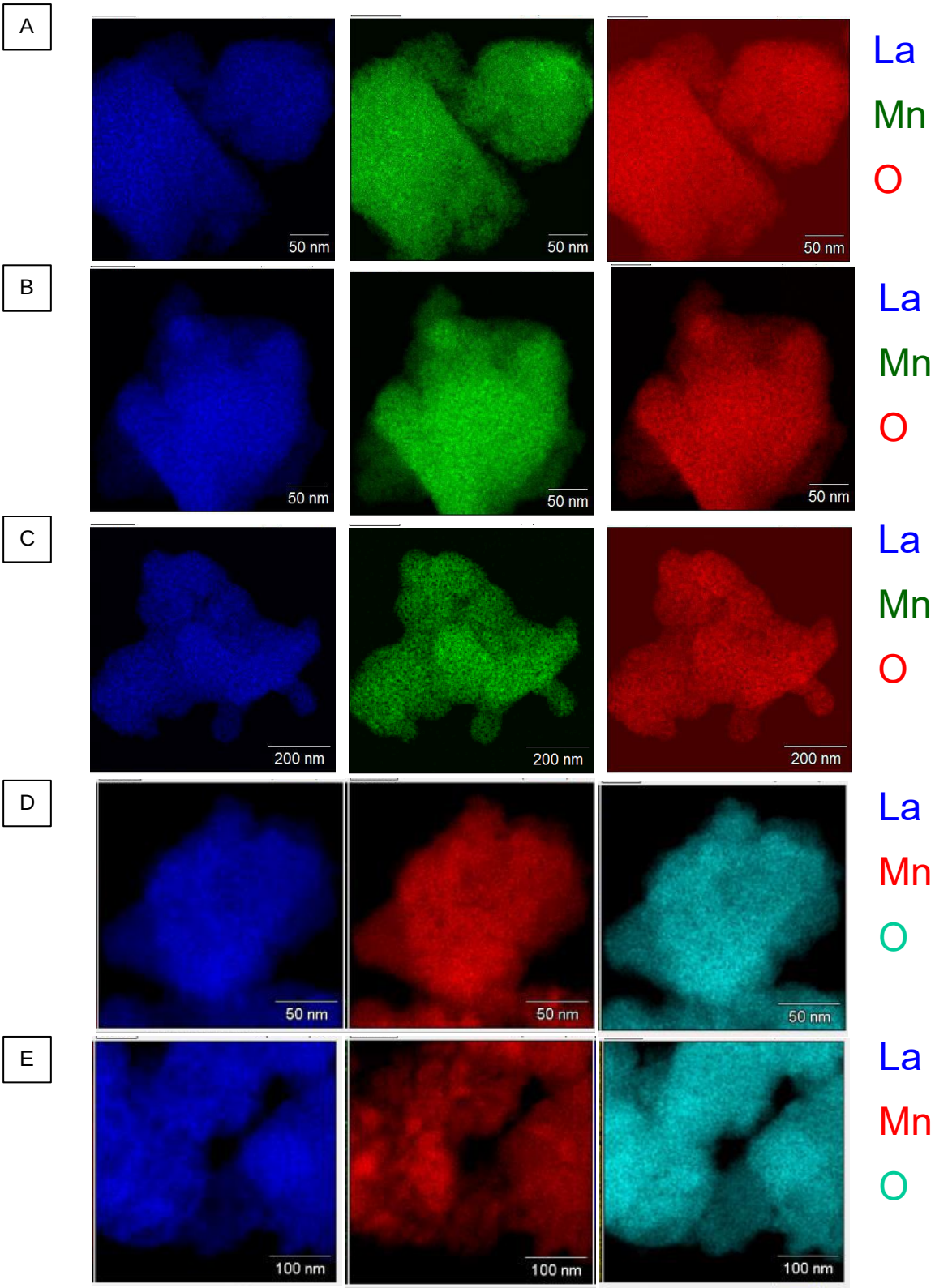

Figure 3.3.27: *Composition analysis by EDX in scanning mode for La, Mn and O for* ***(A)*** *3 h* ***(B)*** *4 h ball milled in air,* ***(C)*** *3 h* ***(D)*** *4h in argon and* ***(E)*** *sol-gel synthesised* $LaMnO_3$

To achieve high resolution TEM to further investigate the spatial composition within the $LaMnO_3$ samples, scanning transmission electron microscopy and elemental energy loss spectroscopy (STEM-EELS) has been performed, alongside with elemental mapping with atomic resolution by Johnson Matthey at I14, Diamond Light Source. Figure 3.3.28 shows the atomic percent maps containing La (blue), Mn (green), O (red), with the corresponding HAADF-STEM and atomic percentage composition line profiles for the sol-gel, 3 and 4 h milled perovskites. Due to the limited allocation of time for these experiments performed at I14, Diamond Light Source, it was not possible to complete experiments on the argon milled $LaMnO_3$ samples.

First assessing the line profile of the sol-gel synthesised $LaMnO_3$ (Figure 3.3.28A), it confirms that the interior of the particle, at a depth of 1.2 nm, is consistent with the stoichiometric perovskite composition, *i.e.* La (20 at. %), Mn (20 at. %) and O (60 at. %). As the line profile approaches the edge of the particle, towards a depth of ~0.8 nm, a Mn-

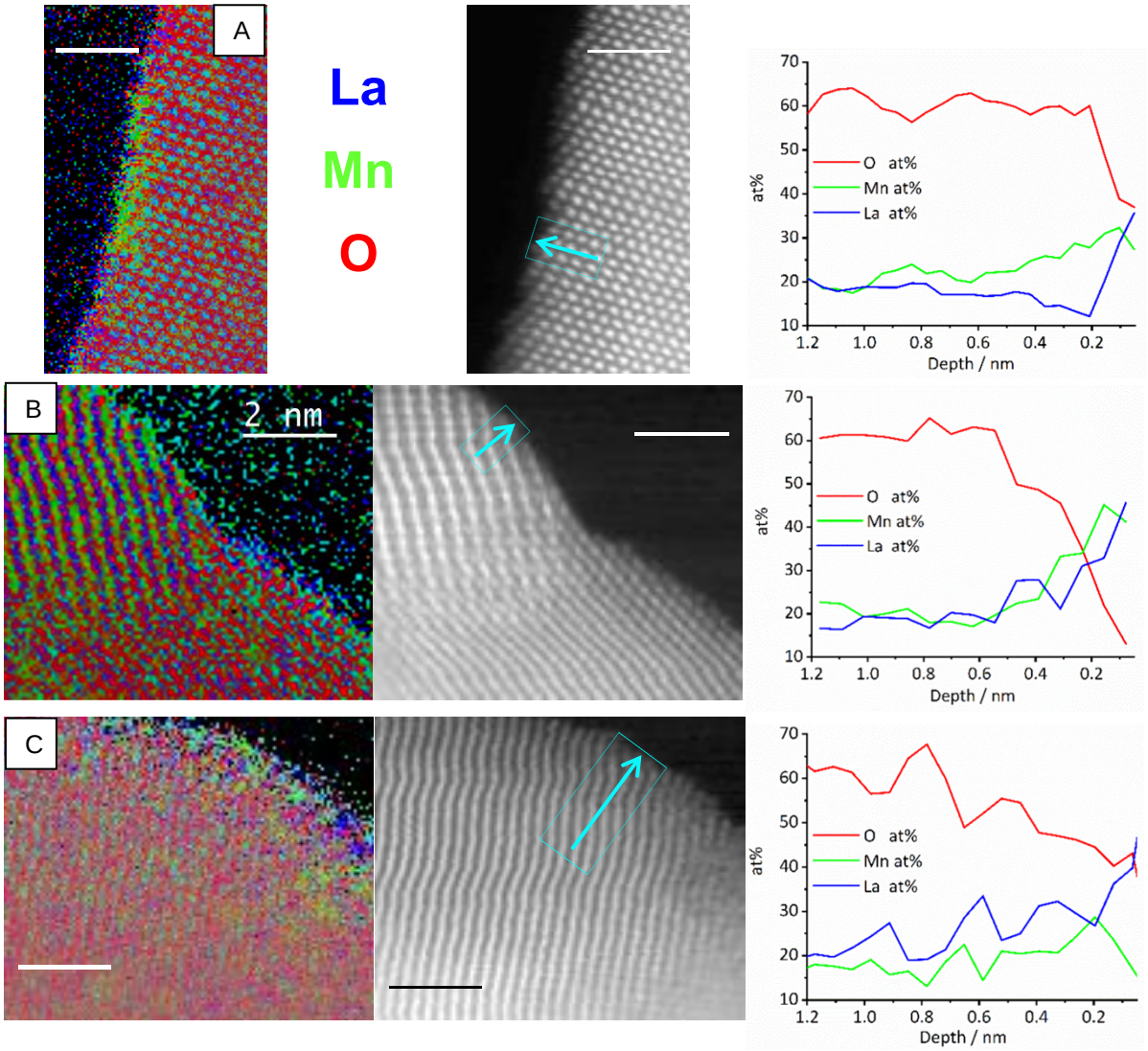

***Figure 3.3.28**: STEM-EELS atomic percentage elemental mapping (left column), HAADF-STEM images with integrated profiling lines (central column) and line profiling along the arrow, for the atomic percentage of La (blue), Mn (green) and O (red) for **(A)** sol-gel synthesised, **(B)** 3 h milled and **(C)** 4 h milled $LaMnO_3$*

enriched area (~28 at. %) is detected, with a corresponding decrease in La content (~12 at. %). Here, STEM-EELS imaging has confirmed a level of structural heterogeneity, with the enriched Mn areas not present across the entirety of the catalyst sub-surface. This heterogeneity makes any assignment of the origin of the Mn(IV) content, detected at the surface through XPS analysis of the Mn 3*s* region, difficult to ascribe. Further increasing the line profile towards the surface, an oxygen deficiency can be observed within the last few atomic layers of ~2 Å.

The STEM-EELS performed on air milled samples (Figure 3.3.28B, C) both show a degree of oxygen deficiency as the line profile tends to the surface. The nature of this oxygen deficiency extends slightly deeper into the sample (~5 Å) compared to the sol-gel perovskite. This deficiency is even more pronounced for the 3 h milled sample (Figure 3.3.28B compared to the 4 h milled (Figure 3.3.28C). The La and Mn concentration within the air milled samples tend to have a consistent fluctuation (20 ± 3 at. %) within the crystal bulk and both increase at the same rate as they enter the O vacancy layer. However, at the surface of the 4 h air milled sample La dominates the content at the end of the line profile, suggesting the presence of La residue coupled with a reduction in Mn species at the surface of the perovskite crystal. These different phases detected by STEM-EELS of all samples suggest a significant structural variance at the surface that could result in a Mn(IV)/Mn(III), stated by the Mn 3*s* XPS region.

It is important to note that the STEM-EELS data here needs to be taken in the context of the sample population presented. The observation of Mn surface at.% is consistent throughout the samples presented, which is a reassuring sign of reliability for these values. By combining these all these advanced characterisation techniques, EXAFS, XPS and STEM-EELS, it will allow for the comprehensive understanding and assessment of catalytic activity, along with what beneficial properties result from the mechanochemical synthesis for $LaMnO_3$.

3.3.4 Decomposition of N_2O over differently synthesised $LaMnO_3$ catalysts

The decomposition of N_2O (deN_2O) was performed over the differently synthesised $LaMnO_3$ catalysts, with the light-off temperature curves detailing the percentage conversion of deN_2O to N_2 shown in Figure 3.3.29. The 4 h air milled and sol-gel synthesised $LaMnO_3$ show similar activity, which begins at ~350 ^oC with 100% conversion achieved by 550 ^oC. However, the 3 h air milled and both argon milled catalysts show an early on-set conversion of N_2 at lower temperatures. The 3 h air milled sample shows activity starting just above 300 ^oC, with the argon milled $LaMnO_3$, having an even lower starting activity temperature below 300 ^oC. The 3 h air milled catalyst achieves 100% decomposition at the same temperature to the 4 h air milled sample, 550 ^oC, opposed to a higher 100 % conversion temperature of 600 ^oC for the argon milled materials.

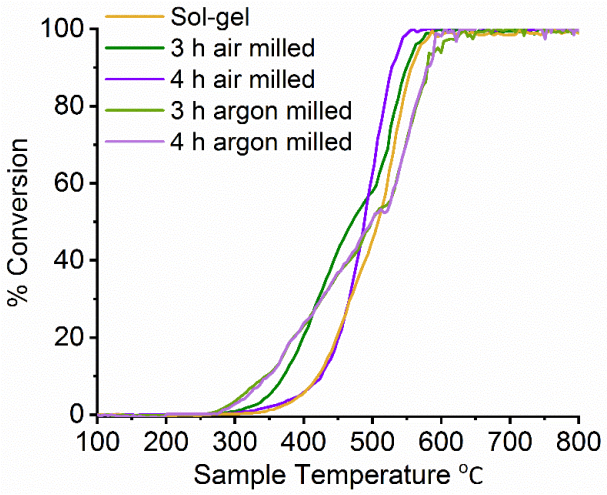

Figure 3.3.29: *The percentage conversation of N_2O decomposition to N_2 over air and argon ball milled and sol-gel synthesised $LaMnO_3$ light-off curve*

Catalytic activity is often strongly correlated to the surface area and morphology of the acting catalyst. Assessing the surface areas by BET theory calculated values of ~ 4 – 6 m^2g^{-1} for ball milled samples, compared to 8 m^2g^{-1} for sol-gel synthesised $LaMnO_3$. Images acquired by TEM showed all the ball milled samples have predominately similar agglomerated morphology on the same size scale (Figure 3.3.25). The sol-gel synthesised $LaMnO_3$, however, is on a much larger size scale whilst possessing a cage-like structure. This suggests both the surface area and morphology do not have a contributing effect to the catalytic activity.

To understand the improved activity, the nature of the active site, ascribed to Mn in $LaMnO_3$, must be considered. During the deN_2O a Mn(III) site is expected to partially oxidise to Mn(IV) to provide reaction oxygen. This reduced Mn can then re-oxidise by gas phase oxygen or from mobile oxygen from sub-lattice layer of the perovskite.[49] The ease at which the Mn can fluctuate between two oxidation states relates to oxygen mobility of the sample. XPS analysis of the Mn 3*s* region for all samples show the same Mn(IV)/Mn(III) mixed valency. This demonstrates that the activity can be linked to oxygen vacancies, as within the O 1*s* region, both 3 h air milled and argon milled catalysts presented a high proportion of vacant oxygen sites. Here, the extra oxygen vacancies can provide additional active sites for deN_2O. Furthermore, with oxygen desorption reported as the rate determining step during deN_2O, the reaction can be an indication of the effectiveness of Mn redox ability.[50] It suggests at lower temperatures the 3 h air and argon milled catalysts indicate increased oxygen mobility.[51] With the sol-gel synthesised $LaMnO_3$ having the highest surface area with a honeycomb structure compared to the agglomerated ball milled materials it indicates that the catalytic activity is not solely dependent on surface area. It further emphasises the importance of structural properties such as vacancies, defects, distortion and amorphous content for the ball milled catalysts.

Within the XPS analysis of the argon milled catalysts, a higher proportion of La was detected at the surface, yet these samples have the lowest on-set temperature of N_2O conversion. This raises an interesting point as Mn is said to be the active site, combined with the La electronic configuration not possessing redox capabilities, being stable within a 3+ oxidation state.[52] However, a decrease in the multiplet splitting of the XPS La 3*d* region for the argon milled catalysts corresponds to a higher percentage of adsorbed oxygen species in the O 1*s* region. Further work is required to understand importance of the role of La and O during deN_2O and how the other XPS regions are affected (continued in Chapter 4).

Two distinct regions within the light-off curve are observed for all ball milled $LaMnO_3$ during deN_2O. As the temperature increases above 500 ^oC a feature in the light-off curve suggests a phase transformation is occurring, and thus altering the catalytic activity. Elevated temperatures would be expected to cause a calcination-like process of the ball milled perovskites. XRD performed on samples post deN_2O confirms a higher level of crystallinity for the $LaMnO_3$ phase, *i.e.* increased peak intensity and reduced line broadening (Figure 3.3.30).

XAFS performed at both the Mn K-edge and La L_3-edge (Figure 3.3.31) for the $LaMnO_3$ catalysts post deN_2O all show comparable structures. Within the XANES all samples follow similar spectral profiles, with the sol-gel synthesised species only having a higher intensity in the La L_3-edge XANES. Further similarities can be observed in the EXAFS oscillations and corresponding Fourier transform. Appropriate models of the EXAFS Fourier transform data for the post deN_2O $LaMnO_3$ catalysts were produced using three scattering paths; one Mn-O and two Mn-La (Figure 3.3.32). Within the first coordination shell the calculated Mn-O CN is remains consistent with the previous EXAFS models for the fresh $LaMnO_3$ catalysts. However, with the exception of the 4 h air milled perovskite, which has a reduced Mn-O CN to 4.3. This reduced Mn-O CN of the 4 h air milled sample could indicate

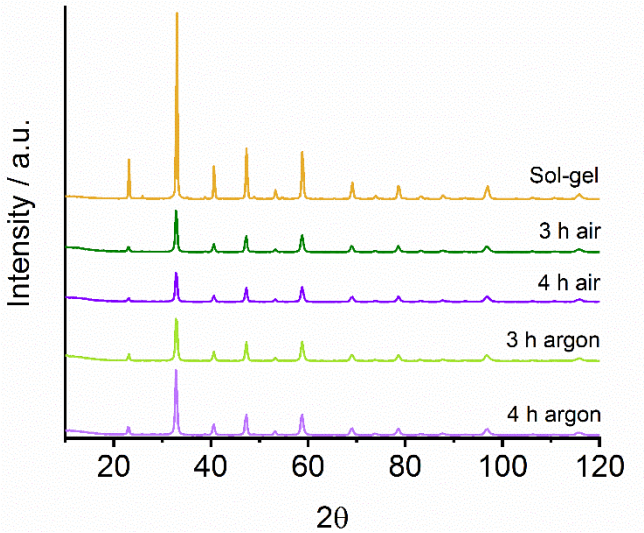

Figure 3.3.30: *XRD patterns of differently synthesised $LaMnO_3$ catalysts post deN_2O*

that oxygen from the perovskite lattice is used during deN_2O, however, with no observable shift in Mn K-edge XANES edge compared to the other catalysts suggests further investigation is required.[22,53,54]

Both the Mn-La scattering paths are now all comparable to the crystalline lengths at ~3.32 Å and ~3.70 Å (Table 3.3.4.1); corresponding to the XRD, which indicated an increase in the perovskite crystalline phase for the ball milled materials after deN_2O. As a consequence of the phase transformation at the end of the catalytic reaction the light-off profiles are not reversible. However, these materials show sufficient scope to be effective at lower temperatures where the observed phase transformation has not yet occurred.

Reproducible catalytic runs were performed on a different batch of each of the differently synthesised $LaMnO_3$ catalysts (Figure 3.3.33). The majority of samples follow a similar percentage conversation light-off curve compared to the previous deN_2O performance (Figure 3.3.29). However, the 3 h air milled catalyst shows much higher activity between 350 – 550 ^oC and the 4 h air milled catalyst only reached 100 % conversion at 600 ^oC, 50 ^oC more than in previous testing. The light-off curves, however, still follow comparable similar trends as discuss for Figure 3.3.33), whilst also emphasising the inconstancies of reproducibly in the mechanochemical synthesis.

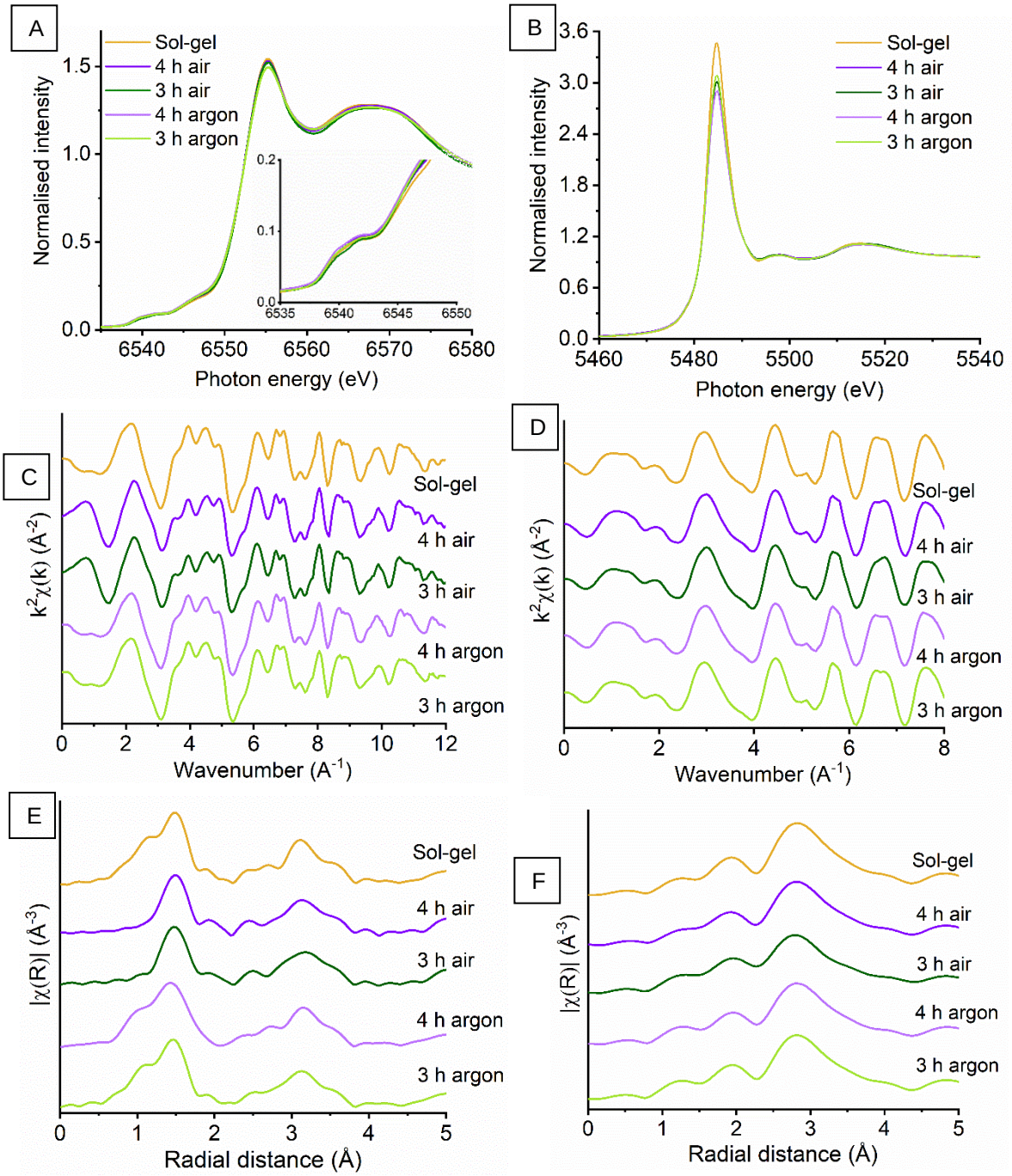

Figure 3.3.31: *Post catalytic characterisation of the ball milled and sol-gel synthesised $LaMnO_3$; XANES at the **(A)** Mn K-edge and **(B)** La L_3-edge, k^2 weighted EXAFS oscillations at the **(C)** Mn K-edge and **(D)** La L_3-edge with corresponding Fourier transform spectra **(E)** and **(F)**, respectively*

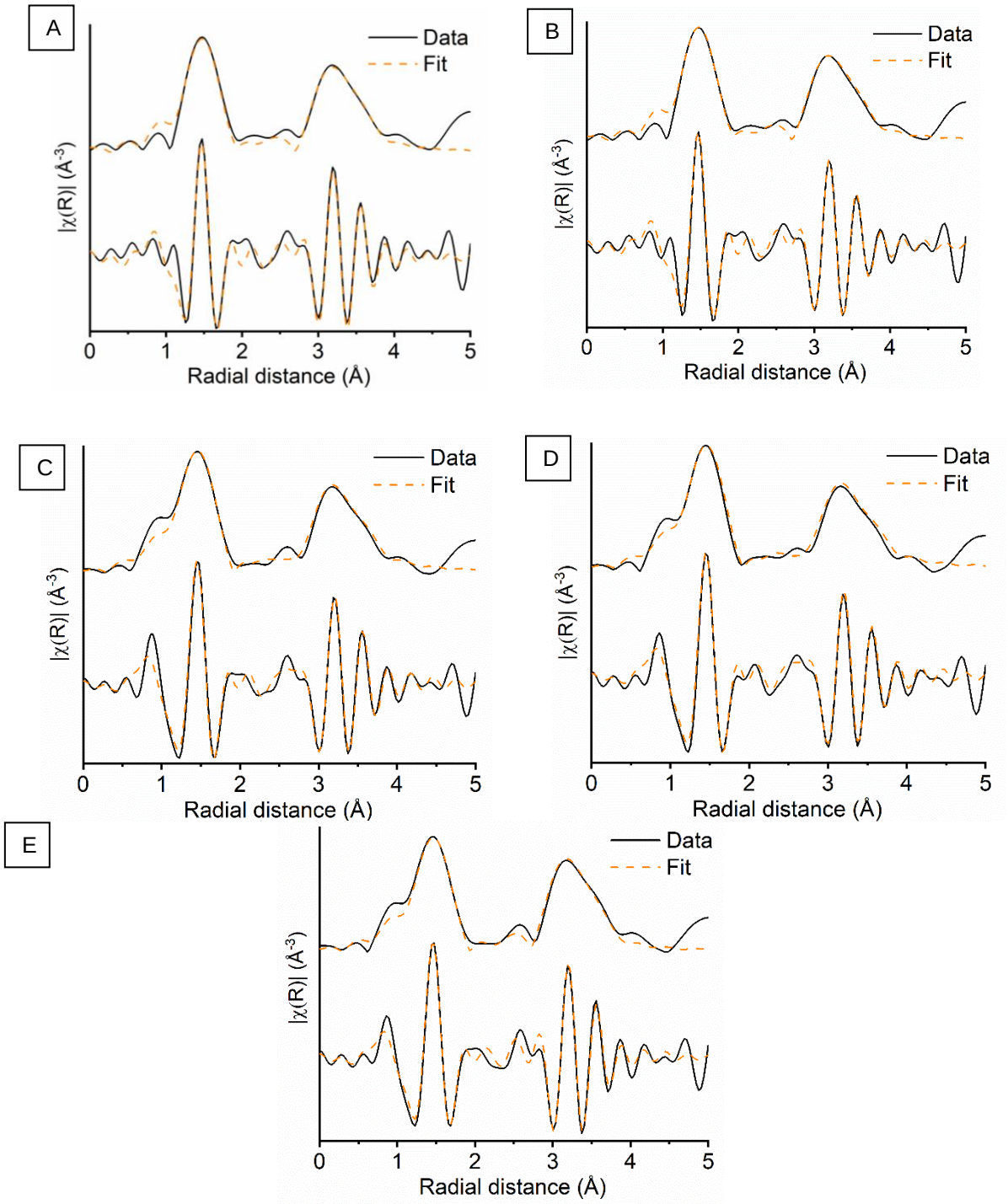

Figure 3.3.32: *Mn K-edge EXAFS fits after deN_2O over* ***(A)*** *3 h air milled* ***(B)*** *4 h air milled* ***(C)*** *3 h argon milled* ***(D)*** *4 h argon milled and* ***(E)*** *sol-gel $LaMnO_3$*

Table 3.3.4.1: *EXAFS fitting parameters for the Mn K-edge for spectra collected after deN_2O for differently synthesised $LaMnO_3$ catalysts. Fitting parameters:* $S_0^2 = 0.7$ *as determined by the use of a Mn foil standard; Fit range* $3 < k > 14,\ 1.2 < R > 4.0$. [a]*CN fixed to known structures and the number of scattering paths reduced in order to minimise fitting parameters* [b]*All refined CN are within 10% error margin*

	Sample	Bond (Abs-Sc)	CN	E_0 (eV)	σ^2	R / Å	R_{factor}
Argon milled	**Time 3 h**	Mn-O1	4.2(5)	-6(2)	0.004(1)	1.94(1)	0.02
		Mn-La1	6.0(7)		0.010(2)	3.32(3)	
		Mn-La2	2.0(3)		0.003(1)	3.72(2)	
	Time 4 h	Mn-O	5.3(6)	-6(2)	0.006(1)	1.93(1)	0.02
		Mn-La1	6.0(7)		0.010(4)	3.32(1)	
		Mn-La2	2.0(1)		0.003(1)	3.72(1)	
Air milled	**Time 3 h**	Mn-O	4.3(4)	-6(2)	0.004(1)	1.94(1)	0.03
		Mn-La1	6.0(7)		0.010(2)	3.30(3)	
		Mn-La2	2.0(3)		0.003(1)	3.70(2)	
	Time 4 h	Mn-O	4.3(4)	-5(1)	0.004(1)	1.94(1)	0.04
		Mn-La1	5.9(8)		0.009(1)	3.32(1)	
		Mn-La2	2.0(4)		0.003(1)	3.71(2)	
	Sol-gel	Mn-O	5.9(5)	-6(2)	0.007(1)	1.94(1)	0.03
		Mn-La1	5.8(8)		0.008(1)	3.33(2)	
		Mn-La2	2.1(4)		0.003(1)	3.73(2)	

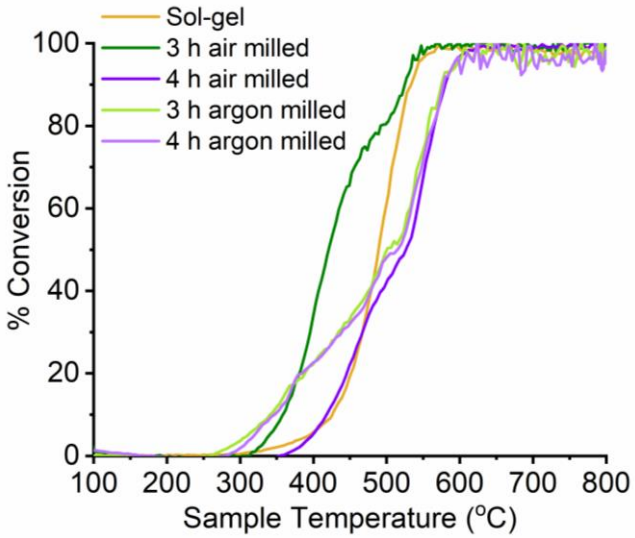

Figure 3.3.33: *Repeat N_2O decomposition to show the reproducibility of $LaMnO_3$ catalysts*

3.4 Conclusions

$LaMnO_3$ has been successful synthesised via mechanical grinding from La_2O_3 and Mn_2O_3 in the absence of high temperature thermal annealing. This work, therefore, presents new insights into how the mechanical action of ball milling is successful in achieving the chemical transformation from single metal oxide precursors to a perovskite phase, in the absence of solvent.

Whilst performing milling under ambient conditions XRD reported 100% of the crystalline content to be $LaMnO_3$ after 3 h of milling, however, observations within the Fourier transform EXAFS deducted that perovskite-like structures were formed after 2 h. This can be attributed to a proportion of amorphous material, commonly known to produce via milling. Whilst milling under an argon atmosphere XRD indicated that it was more challenging for the crystalline perovskite phase to form; though 96% $LaMnO_3$ was recorded at 4 h of milling under an inert atmosphere, it is evident there was a large proportion of amorphous content. Only on the exposure of these samples to air did the XRD 'time-slices' show an increase in long-range structure, yet, amorphous materials were still suggested to remain.

XAS measurements at both the Mn K-edge and La L_3-edge allowed for the analysis of both Mn and La local environments. These combined results suggest that even without high energy milling under atmospheric conditions the La species disperses over the Mn_2O_3 bulk. As milling time increases both precursors undergo mechanical activation to result in the formation of perovskite-like structures after 2 h. For the argon milled samples, La dispersion was observed in the early stages of milling, however, 3 h of milling was required to produce a perovskite-like EXAFS fitting model. This indicates that air plays an important role in the formation of the perovskite phase, whether it is oxygen incorporation into the lattice or the moisture sensitivity of the La precursor.

DeN_2O performed on all ball milled and sol-gel synthesised $LaMnO_3$ samples showed the 3 h air milled and both exposed argon milled catalysts to have a much earlier on set conversion to N_2O. With TEM and EXAFS modelling on all ball milled samples showing similar morphology and bulk structures, it indicates the importance of surface sensitive techniques for understanding deN_2O. XPS of the O 1*s* region detected that both argon milled catalysts possessed a much higher proportion of oxygen vacancies, through an increase in surface adsorbed oxygen species. After curve fitting the 3 h air milled catalyst also showed a greater ratio of surface:lattice oxygen, compared to that of the 4 h air milled and sol-gel perovskites. STEM-EELS further reflected this behaviour in the 3 h air milled sample, along with indicating significant structural variation at the surface for all $LaMnO_3$ materials. With reduced surface areas and agglomerated morphologies for all ball milled samples it suggests that the oxygen vacancies on the surface play a dominant role in the deN_2O. However, the use of elevated temperatures during the catalytic reaction resulted in

significant structural alterations on the ball milled catalysts. Whilst it is no longer possible to reproduce this activity on consecutive deN_2O experiments, the catalysts show exciting scope at lower temperatures, prior to the phase transformation.

3.5 References

1 R. H. Blackmore, M. E. Rivas, T. E. Erden, T. D. Tran, H. R. Marchbank, D. Ozkaya, M. Briceno de Gutierrez, A. Wagland, P. Collier and P. P. Wells , *Dalt. Trans.*, 2020, **49**, 232–240.

2 R. H. Blackmore, M. E. Rivas, G. F. Tierney, K. M. H. Mohammed, D. Decarolis, S. Hayama, F. Venturini, G. Held, R. Arrigo, M. Amboage, P. Hellier, E. Lynch, M. Amri, M. Casavola, T. Eralp Erden, P. Collier and P. P. Wells, *Phys. Chem. Chem. Phys.*, 2020, **22**, 18774–18787.

3 W. F. Libby, *Science*, 1971, **171**, 499–500.

4 R. Voorhoeve, D. Johnson, J. Remeika and P. Gallagher, *Science.*, 1977, **195**, 827–833.

5 S. Keav, S. Matam, D. Ferri and A. Weidenkaff, *Catalysts*, 2014, **4**, 226–255.

6 P. Baláž, M. Achimovičová and M. Baláž, *Chem. Soc. Rev.*, 2013, **42**, 7571–7637.

7 S. Kaliaguine, A. Van Neste, V. Szabo, J. E. Gallot, M. Bassir and R. Muzychuk, *Appl. Catal. A Gen.*, 2001, **209**, 345–358.

8 Q. Zhang and F. Saito, *J. Alloys Compd.*, 2000, **297**, 99–103.

9 B. D. Stojanovic, *J. Mater. Process. Technol.*, 2003, **143**–**144**, 78–81.

10 M. Konsolakis, *ACS Catal.*, 2015, **5**, 6397–6421.

11 A. M. Bolarín, F. Sánchez, A. Ponce and E. E. Martínez, *Mater. Sci. Eng. A*, 2007, **454**–**455**, 69–74.

12 C. A. C. Escobedo, F. S. De Jesús, A. M. Bolarín Miró and J. Muñoz-Saldaña, *Phys. Status Solidi Curr. Top. Solid State Phys.*, 2007, **4**, 4054–4063.

13 V. Szabo, M. Bassir, A. Van Neste and S. Kaliaguine, *Appl. Catal. B Environ.*, 2002, **37**, 175–180.

14 V. Szabo, M. Bassir, A. Van Neste and S. Kaliaguine, *Appl. Catal. B Environ.*, 2003, **43**, 81–92.

15 V. Szabo, M. Bassir, J. E. Gallot, A. Van Neste and S. Kaliaguine, *Appl. Catal. B Environ.*, 2003, **42**, 265–277.

16 T. Yamashita and A. Vannice, *J. Catal.*, 1996, **161**, 254–262.

17 S. Kumar, Y. Teraoka, A. G. Joshi, S. Rayalu and N. Labhsetwar, *J. Mol. Catal. A Chem.*, 2011, **348**, 42–54.

18 G. Centi, S. Perathoner and Z. S. Rak, *Appl. Catal. B Environ.*, 2003, **41**, 143–155.

19 Y. Li and J. N. Armor, *Appl. Catal. B Environ.*, 1993, **1**, 21–29.

20 S. Alini, F. Basile, S. Blasioli, C. Rinaldi and A. Vaccari, *Appl. Catal. B Environ.*, 2007, **70**, 323–329.

21 N. Richards, J. H. Carter, L. A. Parker, S. Pattisson, D. G. Hewes, D. J. Morgan, T. E. Davies, N. F. Dummer, S. Golunski and G. J. Hutchings, *ACS Catal.*, 2020, **10**, 5430–5442.

22 D. V. Ivanov, E. M. Sadovskaya, L. G. Pinaeva and L. A. Isupova, *J. Catal.*, 2009, **267**, 5–13.

23 P. Granger, V. I. Parvulescu, S. Kaliaguine and W. Prellier, in *Perovskites and Related Mixed Oxides Concepts and Applications*, eds. P. Granger, V. Parvulescu,

S. Kaliaguine and W. Prellier, Wiley-VCH, 2015, pp. 3–23.

24 F. Ali, A. V. Chadwick and M. E. Smith, *J. Mater. Chem.*, 1997, **7**, 285–291.

25 L. A. Isupova, G. M. Alikina, S. V. Tsybulya, A. N. Salanov, N. N. Boldyreva, E. S. Rusina, I. A. Ovsyannikova, V. A. Rogov, R. V. Bunina and V. A. Sadykov, *Catal. Today*, 2002, **75**, 305–315.

26 B. Ravel and M. Newville, *J. Synchrotron Radiat.*, 2005, **12**, 537–541.

27 Y. Zhao, *Materials (Basel).*, 2012, **5**, 1413–1438.

28 S. L. James, C. J. Adams, C. Bolm, D. Braga, P. Collier, T. Friščić, F. Grepioni, K. D. M. Harris, G. Hyett, W. Jones, A. Krebs, J. Mack, L. Maini, a G. Orpen, I. P. Parkin, W. C. Shearouse, J. W. Steed and D. C. Waddell, *Chem. Soc. Rev.*, 2012, **41**, 413–47.

29 T. Yamamoto, *X-Ray Spectrom.*, 2008, **37**, 572–584.

30 M. Tromp, J. Moulin, G. Reid and J. Evans, in *AIP Conference Proceedings*, 2007, **882,** 699–701.

31 D. Rybicki, M. Sikora, J. Przewoznik, C. Kapusta and J. F. Mitchell, *Phys. Rev. B*, 2018, **97**, 1–8.

32 M. Sikora, C. Kapusta, K. Knížek, Z. Jirák, C. Autret, M. Borowiec, C. J. Oates, V. Procházka, D. Rybicki and D. Zajac, *Phys. Rev. B - Condens. Matter Mater. Phys.*, 2006, **73**, 1–5.

33 H. Aritani, H. Yamada, T. Yamamoto, T. Tanaka and S. Imamura, *J. Synchrotron Radiat.*, 2001, **8**, 593–595.

34 A. Y. Ignatov, N. Ali and S. Khalid, *Phys. Rev. B - Condens. Matter Mater. Phys.*, 2001, **64**, 1–16.

35 F. Farges, *Phys. Rev. B - Condens. Matter Mater. Phys.*, 2005, **71**, 1–14.

36 V. Cuartero, S. Lafuerza, M. Rovezzi, J. García, J. Blasco, G. Subías and E. Jiménez, *Phys. Rev. B*, 2016, **94**, 1–10.

37 K. Jirátová, J. Mikulová, J. Klempa, T. Grygar, Z. Bastl and F. Kovanda, *Appl. Catal. A Gen.*, 2009, **361**, 106–116.

38 V. P. Santos, M. F. R. Pereira, J. J. M. Órfão and J. L. Figueiredo, *Appl. Catal. B Environ.*, 2010, **99**, 353–363.

39 A. Machocki, T. Ioannides, B. Stasinska, W. Gac, G. Avgouropoulos, D. Delimaris, W. Grzegorczyk and S. Pasieczna, *J. Catal.*, 2004, **227**, 282–296.

40 S. K. Gupta, M. Sahu, P. S. Ghosh, D. Tyagi, M. K. Saxena and R. M. Kadam, *Dalt. Trans.*, 2015, **44**, 18957–18969.

41 Y. Yang, S. Zhang, S. Wang, K. Zhang, H. Wang, J. Huang, S. Deng, B. Wang, Y. Wang and G. Yu, *Environ. Sci. Technol.*, 2015, **49**, 4473–4480.

42 J. Zhu, H. Li, L. Zhong, P. Xiao, X. Xu, X. Yang, Z. Zhao and J. Li, *ACS Catal.*, 2014, **4**, 2917–2940.

43 R. Dudric, A. Vladescu, V. Rednic, M. Neumann, I. G. Deac and R. Tetean, *J. Mol. Struct.*, 2014, **1073**, 66–77.

44 T. S. Kharlamova, A. S. Matveev, A. V. Ishchenko, A. N. Salanov, S. V. Koshcheev, A. I. Boronin and V. A. Sadykov, *Kinet. Catal.*, 2014, **55**, 361–371.

45 D. J. Lam, B. W. Veal and D. E. Ellis, *Phys. Rev. B*, 1980, **22**, 5730–5739.

46 V. R. Galakhov, M. Demeter, S. Bartkowski, M. Neumann, N. A. Ovechkina, E. Z. Kurmaev, N. I. Lobachevskaya, Y. M. Mukovskii, J. Mitchell and D. L. Ederer, *Phys. Rev. B*, 2002, **65**, 1–4.

47 M. A. Stranick, *Surf. Sci. Spectra*, 1999, **6**, 31–38.

48 M. A. Stranick, *Surf. Sci. Spectra*, 1999, **6**, 39–46.

49 J. Chen, M. Shen, X. Wang, G. Qi, J. Wang and W. Li, *Appl. Catal. B Environ.*, 2013, **134**–**135**, 251–257.

50 C. S. Swamy and J. Christopher, *Catal. Rev.*, 1992, **34**, 409–425.

51 N. Gunasekaran, S. Rajadurai and J. J. Carberry, *Catal. Letters*, 1995, **35**, 373–382.

52 H. Najjar and H. Batis, *Catal. Rev.*, 2016, **58**, 371–438.

53 S. Royer, D. Duprez and S. Kaliaguine, *Catal. Today*, 2006, **112**, 99–102.

54 R. J. H. Voorhoeve, J. P. Remeika and L. E. Trimble, *Ann. N.Y. Acad. Sci.*, 1976, **2**, 272.

Chapter 4

The electronic structure, surface properties, and *in situ* N_2O decomposition of mechanochemically synthesised $LaMnO_3$

This chapter presents work further investigating how milling induces a chemical reaction using advanced synchrotron characterisation techniques. A combination of both *ex situ* and *in situ* measurements have been explored to provide in-depth information on the oxidation state and electronic configuration of mechanochemically synthesised $LaMnO_3$, alongside its behaviour towards the decomposition of N_2O. The manuscript has been published in "Physical Chemistry Chemical Physics - PCCP"[1] R. H. Blackmore, M. E. Rivas, G. F. Tierney, K. M. H. Mohammed, D. Decarolis, S. Hayama, F. Venturini, G. Held, R. Arrigo, M. Amboage, P. Hellier, E. Lynch, M. Amri, M. Casavola, T. Eralp Erden, P. Collier and P. P. Wells. The electronic structure, surface properties, and *in situ* N_2O decomposition of mechanochemically synthesised $LaMnO_3$. *Phys. Chem. Chem. Phys.*, 2020, **22**, 18774–18787

Authors G. F. Tierney, D. Decarolis, S. Hayama, F. Venturini, G. Held, R. Arrigo, M. Amboage, P. Hellier, E. Lynch, M. Amri, M. Casavola listed on this paper were included due to their support as either beamline staff or as help to complete beamtime experiments over numerous 24 h days. K. M. H. Mohammed analysed Mn Kβ XES data, M. Amri the *in situ* ball milling XRD data and T. Eralp Erden provided guidance towards NAP-XPS analysis. P. Collier was included due to their industrial involvement with Johnson Matthey. M. E. Rivas and P. P. Wells were industrial and academic supervisors of this project.

4.1 Introduction

Developing synthetic routes and catalytic processes that are both economically viable and sustainable represents a significant challenge for chemists today. To meet this ambition, the development of new technologies can no longer rely on iterative trial and error approaches and must instead be design-led using sophisticated characterisation methods.[2]

Synchrotron techniques, such as X-ray absorption spectroscopy (XAS), have multiple benefits, which aid the in-depth understanding of chemically important yet complex systems.[3–5]

Chapter 3 reported the advantages of *ex situ* XAS for studying the preparation of mixed metal oxides prepared through mechanochemistry; this solvent-free synthesis route produces less waste than traditional methods and prepares materials with enhanced catalytic properties.[6] As a significant amount of amorphous material was produced through stages of milling, traditional characterisation methods, such as X-ray diffraction (XRD), were unsuitable. Using XAS, that provides structural insights on all length scales, allowed for further information about the principal chemical steps within the milling process. Furthermore, these studies also increased the understanding of how these materials promote the catalytic decomposition of the environmental pollutant N_2O (deN_2O).

However, even after performing conventional XAS at the Mn K-edge information such as the local charge density and electronic configuration still eluded us. Traditional XANES suffers from the broadening of the lifetime, caused by the overlapping of multiple transitions, which smears spectral features found within the XANES (section 2.9.6). This is further complicated by the complex nature of these disordered milled materials. Furthermore, analysis of the XANES region, unlike EXAFS, can require the use of complex DFT calculations which is not always readily available to general beamline users. Improving the resolution can thus allow a comparative approach to reported species within the literature. This work discusses the use of further advanced characterisation techniques, such as high energy resolution fluorescence detection (HERFD) to improve XANES spectral resolution,[7,8] and X-ray emission spectroscopy (XES) to attain information on electronic structure and oxidation state.[9,10]

Chapter 3 focused solely on the use of *ex situ* characterisation for both understanding of the mechanochemical synthesis and catalytic performance of $LaMnO_3$. By monitoring reactions *in situ* it provides vital information on how catalytic materials react under working conditions.[11] In doing so it can provide new insights into the structure-activity relationship for catalysts, often different to the material properties characterised *ex situ*; this approach allows for the detection of intermediate states which often only exist at short timescales mid-reaction. *In situ* experiments are limited, however, by their need for rapid acquisition times, often only accessible with synchrotron radiation.[11] Furthermore, they require suitable cell designs that not only mimic real-life conditions but meet the beamlines specifications.[12]

Whilst the use of X-ray absorption and photoelectron spectroscopy with synchrotron radiation to acquire real-time data is becoming well established within catalysis, only recently have developments towards *in situ* analysis of mechanochemical reactions been performed.[13,14] Following this preparation route real-time is extremely challenging as

commercial equipment does not allow for direct reaction monitoring. However, work by Friščić *et. al.* successfully analysed the evolution of a MOF by synchrotron XRD, using a modified PMMA milling jar.[15–17]

By combining local structural and electronic techniques, along with surface sensitive characterisation, it can be a powerful tool for understanding how structural properties affect catalysis. In turn this knowledge can lead to the development of new technology opportunities. Herein, we report an in-depth analysis during the mechanochemically synthesised $LaMnO_3$ by XES and HERFD, not previously reported. Furthermore, we can now link these structural properties of the final material to the enhancement of catalytic activity for the *in situ* deN_2O combined with near ambient pressures X-ray photoelectron spectroscopy (NAP-XPS).

4.2 Materials and methods

4.2.1 $LaMnO_3$ sample preparation

See experimental section 3.2.1, Chapter 3.

4.2.2 Understanding mechanochemical synthesis

X-ray Absorption Spectroscopy (XAS) at the Mn K-edge, see Chapter 3 (section 3.2.2).

XES/HERFD-XANES measurements were performed on the scanning branch of the I20 beamline at the Diamond Light Source, Didcot, UK. Measurements were taken using a Si(111) four-bounce monochromator using a high-resolution X-ray emission spectrometer.[18] The spectrometer was equipped with either three Ge (440) or three Ge(333) crystal analysers to allow for Kβ or Kα spectra, respectively, to be measured.[18] One spectrum with a time resolution of 8 min was used for both $K\beta_{1,3}$ or $K\alpha_1$. Valence-to-core (VTC) measurements at the $K\beta_{2,5}$ emission line were also performed using three Ge(333) crystal analysers at 25 min spectrum^{-1} with a total of four spectra collected per sample.

Mn $K\beta_{1,3}$ XES spectra were fitted using three Voigt functions which represent the $K\beta_{1,3}$, $K\beta_x$ and Kβ' peaks.[19] Prior to the fitting, spectra were normalized, and linear background was subtracted. During the fitting, peak splitting was kept constant at theoretical values[20]; (i) splitting between $K\beta_{1,3}$ and Kβ' peaks ≈ 14 – 16 eV and (ii) $K\beta_x$ was lower than main, $K\beta_{1,3}$, peak by ~3 eV. Same fitting procedures were applied on spectra taken for Mn standard materials for comparison purposes.

HERFD were measured by scanning the incident energy and detecting the fluorescence intensity at the maximum of the Mn $K\beta_{1,3}$ or $K\alpha_1$ emission line with time resolution of ~ 20 min spectrum^{-1}, with 3 spectra collected. Data processing, background submission and normalisation was performed using Athena package.

***In situ* XRD ball milling** was performed at the ID15A beamline at the European Synchrotron Radiation Facility (ESRF) using the a modified MM200 Retsch mill reported by Halasz *et. al*.[16,17] The set-up comprised of a PMMA milling jar containing one 5 mm WC milling media with Mn_2O_3 and La_2O_3 precursor powders (Figure 4.2.1). The mill operating at 30 Hz for ~19 h. The *in situ* XRD was collected at 69 KeV, λ = 0.17971 Å with a beam size of 300 × 300 μm^2. A Dectris Pilatus X area detector was used with an exposure of 5 s and a readout time of 120 s. The incident wavelength and detector distance (430 mm) were calibrated using a NIST CeO_2. The Raw data frames were integrated using the internal ESRF Matlab.Eva 5.0.0.22/PDF -4+ 2020 software package was used for phase identification and data plotting.

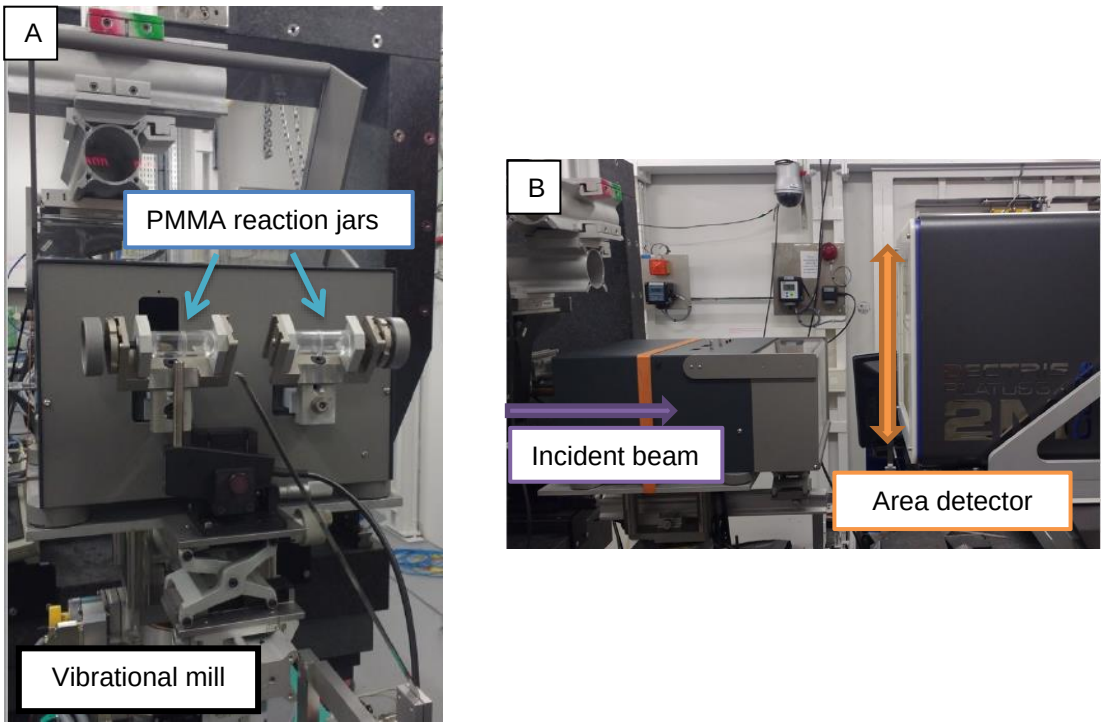

Figure 4.2.1: *Images supplied by the ID15a beamline, ESRF of* ***(A)*** *the vibrational mill and* ***(B)*** *set-up used for the monitoring of in situ milling by XRD*

In situ **high pressure EDE-XAFS** were performed at I20-EDE, the energy dispersive beamline at the Diamond Light Source, Didcot, UK. Energy-dispersive EXAFS was collected at the Mn K-edge (6539 eV) in transmission mode using a Si(111) polychromator. A diamond anvil cell (DAC) was specifically fitted with 0.5 mm thick diamond windows to reduce the diamonds absorption and enable XAS measurements at the low energy Mn K-edge (Figure 4.2.2). Four samples were measured: **(1)** the reference Mn_2O_3 starting material, **(2)** a homogeneous mixture, achieved by low energy milling, of La_2O_3 and Mn_2O_3, **(3)** La_2O_3 and Mn_2O_3 after 30 min of high energy planetary ball milling and **(4)** subsequently 1 h of milling. The powders were loaded into a mini-anvil cell. The single-crystal diamond mini-anvils were then mounted on fully perforated diamonds.

Figure 4.2.2 shows the DAC on the I20-EDE beamline, aligned for pressure measurements. The pressure was quantified using the ruby fluorescence method.[21] The dispersive X-ray beam was then focussed on the sample in the DAC with a spot size of 0.05 mm diameter. Spectra were recorded every 2 GPa of pressure. Attempts to minimise the diamond single crystal reflections were achieved by performing multiple scans at different yaw and top angles. The remaining diamond single crystal reflections were deglitched following a similar procedure to Hong *et al.*[22]

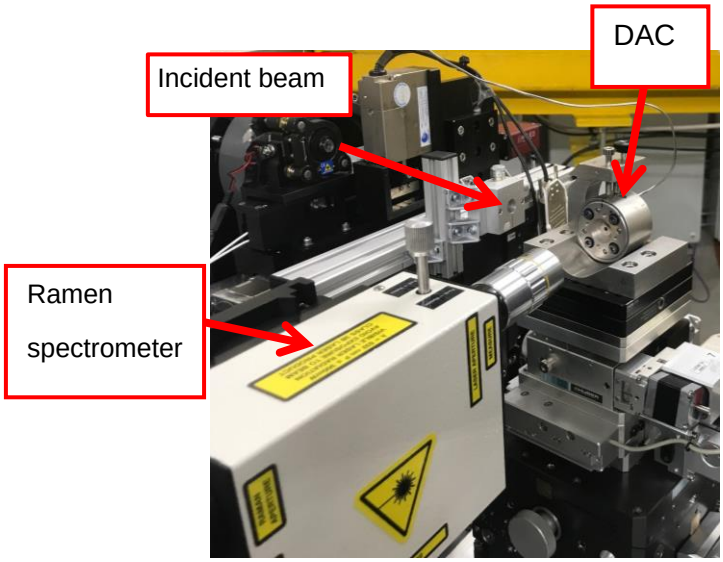

Figure 4.2.2: *DAC set-up with Raman spectrometer on the I20-EDE beamline, DLS*

4.2.3 Understanding catalytic activity

For the initial deN_2O performance runs see Chapter 3 section 3.2.3.

XES/HERFD-XANES see section 4.2.2 for measurement information. Due to the low signal and high absorbance of the reaction capillary HERFD-XANES measurements were performed using the peak maxima of the more intense Mn Kα_1 emission line. The differently synthesised $LaMnO_3$ catalysts (sol-gel prepared, 4 h air milled and 4 h argon milled) were prepared for *in situ* HERFD-XANES by mixing the corrected concentration for appropriate absorbance at the Mn K-edge with boron-nitrate. These were then subsequently pressed and sieved to a 125 – 250 μm faction, to ensure an even flow through the catalyst bed. An average of three spectra were collected at temperature points 250, 300, 350 and 375˚C in a Kapton capillary under a flow of 0.5% N_2O/He. A quartz capillary was too absorbing to produce suitable spectra (Figure 4.3.18) and therefore Kapton capillary was used, which only allowed for a maximum temperature of 375 ˚C. Figure 4.2.3 shows the set-up on the I20-scanning beamline at DLS with a quartz capillary and heating coils located above and below the sample; the thermocouple was placed in the middle of the catalyst bed. This plug flow reactor was then placed at 45˚ to the incident beam and to the detector.

After performing deN_2O, the different $LaMnO_3$ catalysts were then re-pressed into 13 mm pellets to performed XES and HERFD-XANES measurements at the Mn K$\beta_{1,3}$ emission line (see section 4.2.2).

NAP-XPS was performed at the beamline B07-C (VerSoX) at the Diamond Light Source. Spectra were recorded at the La 3*d*, Mn 2*p*, O 1*s*, C 1*s* and Mn 3*s* levels at 834.5 – 855 eV, 641 – 655 eV, 529 – 532 eV, 284 - 289 eV and 82 – 89 eV binding energies,

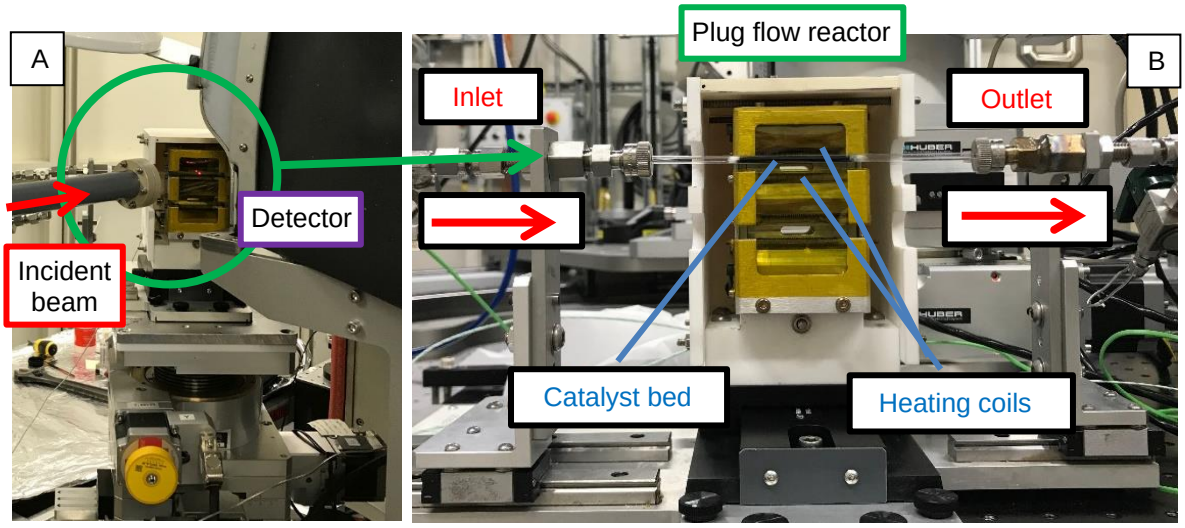

Figure 4.2.3: *DeN_2O in situ set-up on the I20-scanning beamline, DLS showing* ***(A)*** *the plug flow reactor positioned on the beamline at a 45 ˚C angle to the beam and detector with* ***(B)*** *a close view of the plug flow reactor and catalyst bed in a quartz capillary*

respectively, during the deN_2O. Samples were pressed into an 8 mm pellets containing 50 mg of $LaMnO_3$ (Figure 4.2.4).The reaction was performed under 0.5% N_2O in He, with scans performed at room temperature (RT) in vacuum, RT with 10 mbar of N_2O and then subsequently at 400˚C and 600˚C (still under 10 mbar of N_2O). The measurements were performed at specific incident energies for each XPS region to ensure the same kinetic energy / depth of the emitted electron (~350 eV). To achieve a variable depth profile the Mn 3*s* region was recorded with an incident energy of 1200 eV. Each XPS region was aligned to a reference C 1*s* peak at 284.8 eV[23] to compensate for charging effects. Peak positions and FWHM determined after using Shirley background subtraction on CasaXPS, with all residual standard deviations of the curve fitting reported to be under 1.

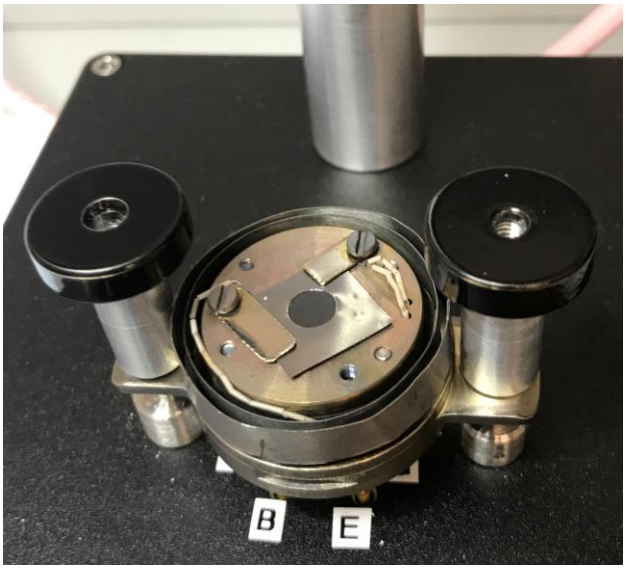

Figure 4.2.4: *NAP-XPS sample holder on the B07 beamline, DLS, with a 8 mm pressed pellet of 50 mg $LaMnO_3$*

4.3 Results and discussion

4.3.1 Understanding the mechanochemical synthesis of $LaMnO_3$

4.3.1.1 Milling under atmospheric conditions

HERFD-XANES. Figure 4.3.1 shows the XANES and HERFD-XANES spectra, with expanded pre-edge regions for the Mn oxide reference compounds (Mn_2O_3, Mn_3O_4, MnO_2 and $LaMnO_3$). By assessing the HERFD-XANES spectra of the reference Mn oxides it will then allow for the interpretation of the ball milled intermediates and final material. After performing HERFD-XANES at the Mn K-edge (Figure 4.3.1) the level of spectral resolution has now vastly improved compared to that of the conventional XANES data (Figure 4.3.1C). This increased resolution is more clearly pronounced in the pre-edge region, which shows more defined, higher intensity transitions, well separated away from the main edge.

At the Mn $K\beta_{1,3}$ HERFD-XANES the main edge corresponds to an allowed 1*s* → 4*p* transition. The position of this main edge transition is therefore dependent on the oxidation state of the system, with an increase in formal charge on the Mn resulting in the transition shifting to higher energy. The features observed within the pre-edge region, however, can result from multiple transitions. Here, the pre-edge features are assigned to 1*s* → 3*d* transitions that are either quadrupolar or dipolar, with the latter normally forbidden by dipole selection rules. An allowed 1*s* → 3*d* dipole transition can occur through local mixing of the 3*d*/4*p* wavefunctions and by the presence of non-local excitations. These non-local excitations result between the 3*d* and 4*p* states of neighbouring metal sites, with an oxygen-mediated intersite hybridisation, e.g. Mn(4*p*)-O(2*p*)-Mn'(3*d*).[24] The size and shape of the pre-edge features is therefore highly dependent on the geometry of central absorbing atom, which now will be assessed for the Mn oxide reference compounds.[8]

Assessing the pre-edge region for Mn_2O_3 two clear peaks can be observed at 6540.8 eV and 6543.0 eV (Figure 4.3.1D), which arise due to the Mn_2O_3 structure containing two different Mn(III) coordination sites. Both Mn sites have 6-fold coordination towards oxygen, with one site adopting a more regular centrosymmetric O_h geometry, whereas the other displays a large degree of Jahn-Teller distortion. The work by Farges showed that the lower energy peak at 6540.8 eV is assigned to the centrosymmetric Mn site and the higher energy peak at 6543.0 eV to the Jahn-Teller distorted Mn site.[25]

With Mn_3O_4 containing both Mn(II) and Mn(III), the understanding gained from the Mn_2O_3 assessment can now be applied to the mixed valent pre-edge features. The intense peak at 6540.5 eV for Mn_3O_4 corresponds to the tetrahedrally coordinated Mn(II) site. This tetrahedral geometry allows for 3*d*-4*p* local hybridisation, resulting in an intense dipole transition. A low intensity peak is then observed at a higher energy of 6542.6 eV, originating

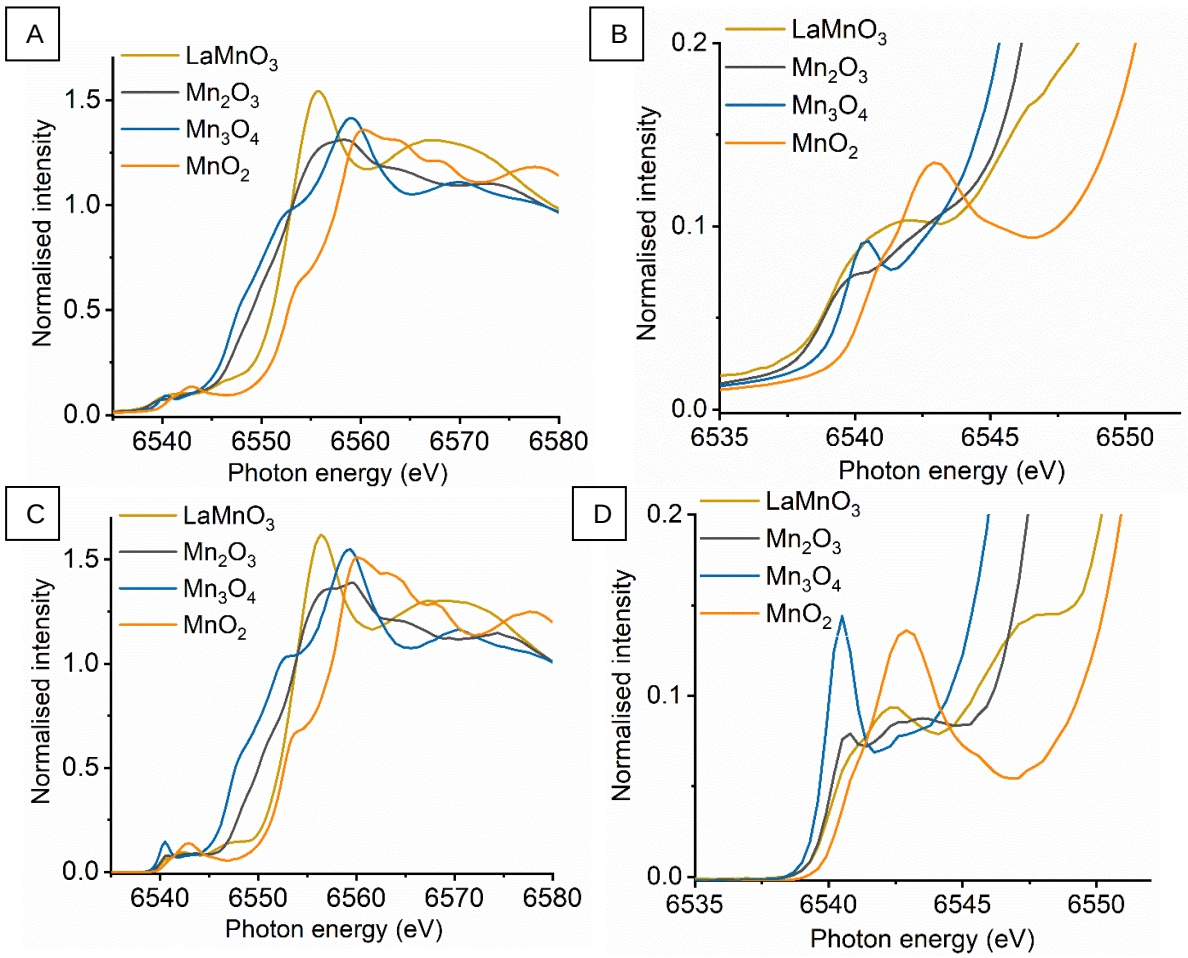

Figure 4.3.1: *Reference Mn (II), (III), (IV) oxides and sol-gel synthesised $LaMnO_3$ at the Mn K-edge by* ***(A)*** *conventional XANES with* ***(B)*** *highlighted pre-edge compared to* ***(C)*** *HERFD-XANES with* ***(D)*** *highlighted pre-edge compared*

from the Mn(III) site. It should be noted that the intensity of these two peaks, at 6540.5 eV and 6542.6 eV, does not relate to the proportion of Mn(II) and Mn(III) present within the sample. Work by Radu *et al.* observed the Mn(II) peak to be a single feature, with the Mn(III) feature extending below the Mn(II) peak due to the multiplet effect of the final state ($1s^1 3d^5$).[26]

Pre-edge features for MnO_2 presents a vastly different spectral shape compared to the other Mn oxide reference materials. Here, the Mn(IV) cation in MnO_2 is positioned in an octahedral site with tetra valency. The pre-edge region for Mn(IV) is extremely complex and even HERFD-XANES struggles to resolve the features.[25] Again, work by Farges shows that the broad feature observed at 6542.9 eV is a combination of 1*s*→3*d* quadrupole transitions and non-local excitations.[25]

$LaMnO_3$, synthesised here by the Pechini method[27], shows two features in the pre-edge region observed at 6542.3 eV and a shoulder at, 6547.7 eV. The lower energy peak at 6542.3 eV has been further suggested to be a combination of two overlapping peaks arising from both a 1*s*→ 3*d* quadrupole transition and a 1s→3*d*4*p* non-local transition. The non-local transition occurs from hybridisation between the 3*d* – 4*p* states of neighbouring metal

sites through an oxygen-mediated intersite, Mn(4*p*)-O(2*p*)-Mn'(3*d*).[28] The shoulder observed at 6547.8 eV is often overlooked when assessing the Mn K-edge XANES of $LaMnO_3$. However, work by Ignatov *et al*. showed they could not effectively model this shoulder within $LaMnO_3$ XANES without considering the contribution of *d* and *f* orbitals, suggesting this shoulder arises due to Mn 4*p* and La 5*d* hybridisation.[29]

Using this analysis of reference Mn oxides, it can now be used to effectively assess the changes during the evolution of $LaMnO_3$ by mechanochemical synthesis under atmospheric conditions (Figure 4.3.2). Once again on measuring HERFD-XANES at the Mn K-edge (Figure 4.3.2C) there is a much greater level of spectral resolution compared to the previous XANES data (Figure 4.3.2A). By assigning the changing features within the pre-edge region of Mn it can provide important information about the chemical steps occurring during the milling process for the formation of the perovskite phase. After just 1 h of milling there are already clear differences in the HERFD-XANES spectrum compared to the Mn_2O_3 starting material. Within the pre-edge region there is a decrease in intensity of the transitions at **(1)** 6540.8 eV and **(2)** 6543.0 eV. With the feature at **(1)** assigned to 1*s*→ 3*d* quadrupole transition a decrease in this transition indicates that there have been alterations to the local geometry of Mn sites. The decrease in the intensity of the transition at **(2)**, which

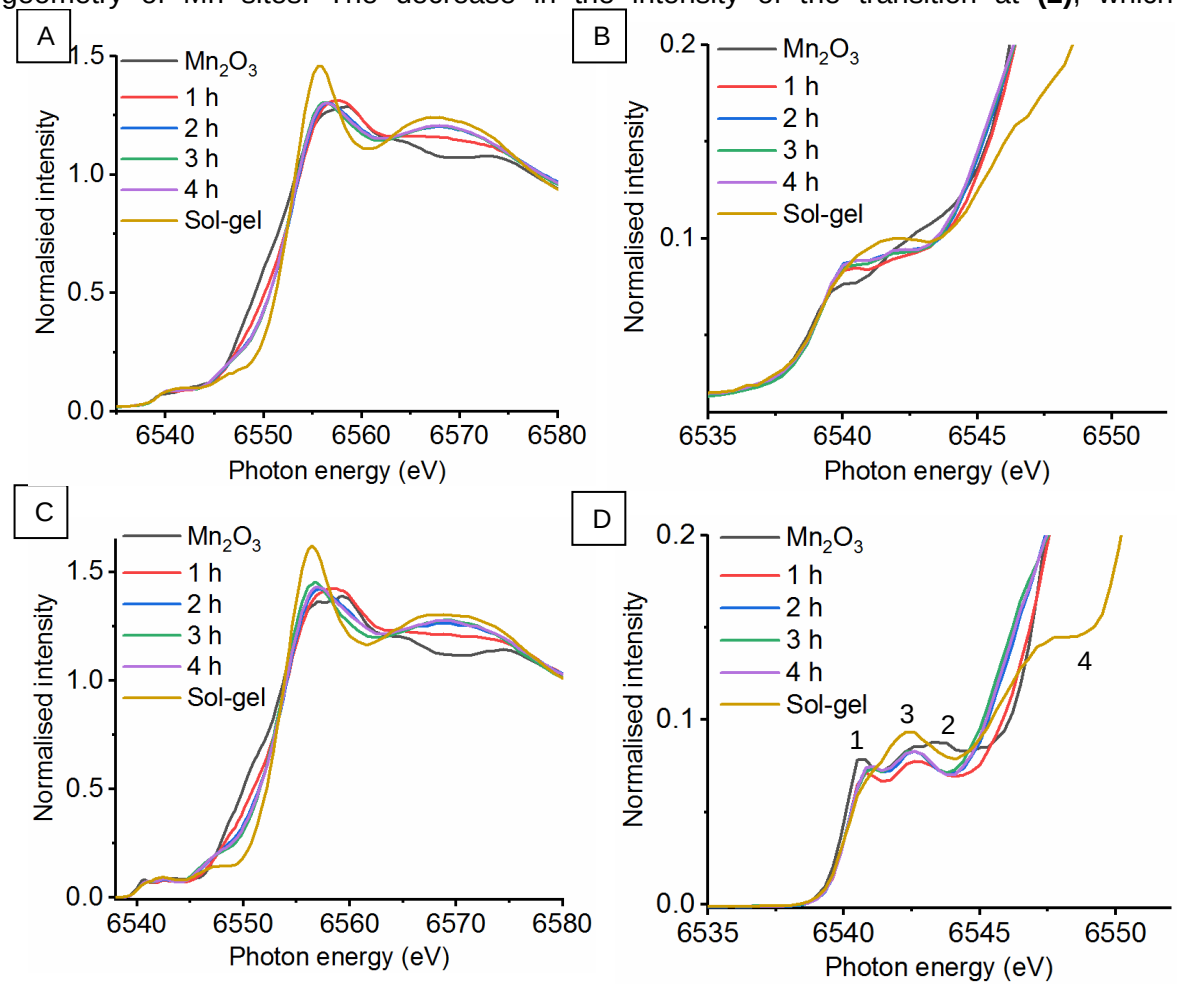

Figure 4.3.2: *'Time-slices' during the mechanochemical synthesis if $LaMnO_3$ at the Mn K-edge measured by* ***(A)*** *conventional XANES with* ***(B)*** *highlighted pre-edge compared to* ***(C)*** *HERFD-XANES with* ***(D)*** *highlighted pre-edge compared*

corresponds to a non-local excitation to a neighbouring Mn site, indicates that the extended Mn_2O_3 structure has been significantly disrupted. This reduction suggests less hybridisation between the non-local 3*d* – 4*p* states and, therefore, a reduced optimal Mn-O-Mn arrangement. As the milling time increases from 1 to 2 h, there is then an increase in intensity of the transitions associated with $LaMnO_3$ at **(3)** 6542.3 eV and a shift to a higher energy position of **(1)**, indicating that there are changes to the local structure indicative of the formation of a perovskite unit. There are no further apparent changes in the spectra from 2-4 h of milling.

Comparing the final ball milled $LaMnO_3$ material to the sol-gel reference, clear differences are observed, most noticeably the lower intensity transitions at **(3)** 6542.3 eV and **(4)** at 6547.7 eV. With the peak at **(3)** assigned to a 1*s* → 3*d*4*p* non-local hybridised transition between neighbouring Mn sites, the strength of this transition is dictated by the metal-oxygen bond length and the metal-oxygen-metal bond angle.[30] The strongest transition, and optimum hybridisation, is achieved by a short bond length and a linear bond angle.[28] In the Chapter 3, the Mn-O bond lengths calculated by EXAFS for both the sol-gel and mechanochemically prepared $LaMnO_3$ to have comparable distances, within the error range of the technique (Table 3.3.1.2). This suggests that the changes to the metal-oxygen-metal bond angle are strongly reflected in the intensity of the feature seen at **(3)** for these materials. The final ball milled $LaMnO_3$ is a complex mixture of both amorphous and crystalline content, suggesting multiple metal-oxygen-metal bond angles.[6] With the crystalline $LaMnO_3$ having a higher intensity peak for the transition at **(3)** it confirms the presence of a more linear metal-oxygen-metal bond angle. Furthermore, the absence of the shoulder at **(4)** for the ball milled materials suggests the lack of Mn4*p* La5*d* hybridisation.[29] In Chapter 3 the EXAFS fitting model for the ball milled materials required two Mn-La scattering paths at 3.24(1) Å and 3.37(1) Å , which is significantly different to that observed for the crystalline sol-gel sample (Table 3.3.1.2). These changes in Mn-La coordination disrupt the Mn4*p* La5*d* hybridisation and affect the transition at **(4)**.

By assessing the pre-edge region of the HERFD-XANES spectra it has provided a greater detailed understanding of changes to the local geometry during the mechanochemical synthesis of $LaMnO_3$ and the differences compared to the sol-gel synthesised perovskite.

Mn Kβ emission. When comparing the XANES of the different Mn oxide reference materials (Figure 4.3.3), it shows the XANES is strongly influenced by the local geometry around the absorbing atom and therefore cannot always provide an accurate oxidation state assessment. Therefore, Mn $K\beta_{1,3}$ emission spectroscopy has been performed in order obtain more reliable information on the Mn charge during the mechanochemical synthesis of $LaMnO_3$.

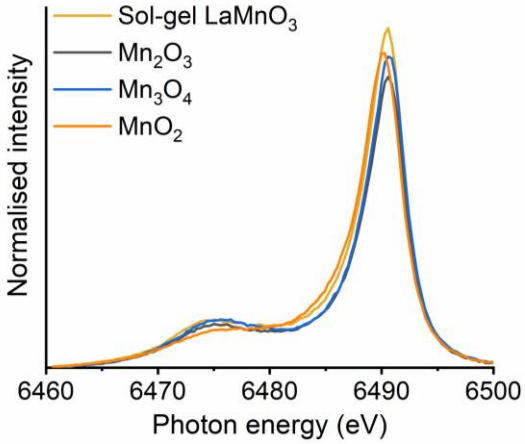

Figure 4.3.3: *Mn Kβ XES mainlines for Mn reference oxides and sol-gel synthesised $LaMnO_3$*

Figure 4.3.3 shows the Mn Kβ mainlines, which consists of a strong Mn $K\beta_{1,3}$ peak, at a higher energy and a Mn Kβ' satellite at a lower energy, for the 3*p*→1*s* emission of reference Mn oxides and a sol-gel synthesised $LaMnO_3$. The splitting of these peaks originates from the strong coupling interaction between the 3*p* hole and the total spin of the 3*d* electrons.[31,32] Any shift in the energy of the Mn $K\beta_{1,3}$ peak position results from a combination of effective nuclear charge (Z_{eff}) and spin state. Work by Beckwith *et al.* showed that for Mn complexes the Z_{eff} and 3*d* spin effects oppose one another.[33] Therefore, any increase in oxidation state will correspond to a decrease in total spin, shifting the Mn $K\beta_{1,3}$ peak to a lower energy.[24]

In assessing the Mn reference materials, it will once again improve the understanding of oxidation state changes through milling of $LaMnO_3$. To extract the accurate peak positions, the Mn Kβ XES spectra were fitted with three Voigt functions, which represent the $K\beta_{1,3}$, $K\beta_x$ and Kβ' peaks (Figure 4.3.4).[19,20] These features within the Mn Kβ XES can be explained through the 3*p*3*d* exchange interaction model.[19,34] On the creation of a 1*s* core hole, coupling to the $3d^4$ electrons, gives rise to two intermediate states; ^4D and ^6D. Therefore, following dipole selection rules, relaxation of this 1*s* core hole occurs from the 3*p* state, leaving one unpaired electron. This unpaired 3*p* electron can now form two possible orientations, relative to the spin of the 3*d* electrons. This gives rise to two final states, ^4F and ^6F corresponding to Kβ' and $K\beta_{1,3}$, respectively. Furthermore, when a 3*d* electron switches orientation in the ^5P final state a shoulder occurs on the lower energy side of the $K\beta_{1,3}$ line, ascribed as the $K\beta_x$.

First fitting the Mn oxide reference materials, the Mn $K\beta_{1,3}$ peak positions for MnO_2, Mn_2O_3 and M_3O_4 species at 6490.26, 6490.66 and 6490.73 eV, respectively (Table 4.3.1.1). This is in strong agreement with the work by Beckwith *et al.*, as with increasing oxidation state the $K\beta_{1,3}$ peak position shifts towards a lower energy. However, when considering the reference sol-gel synthesised $LaMnO_3$ sample, an energy of 6490.55 eV is recorded. With

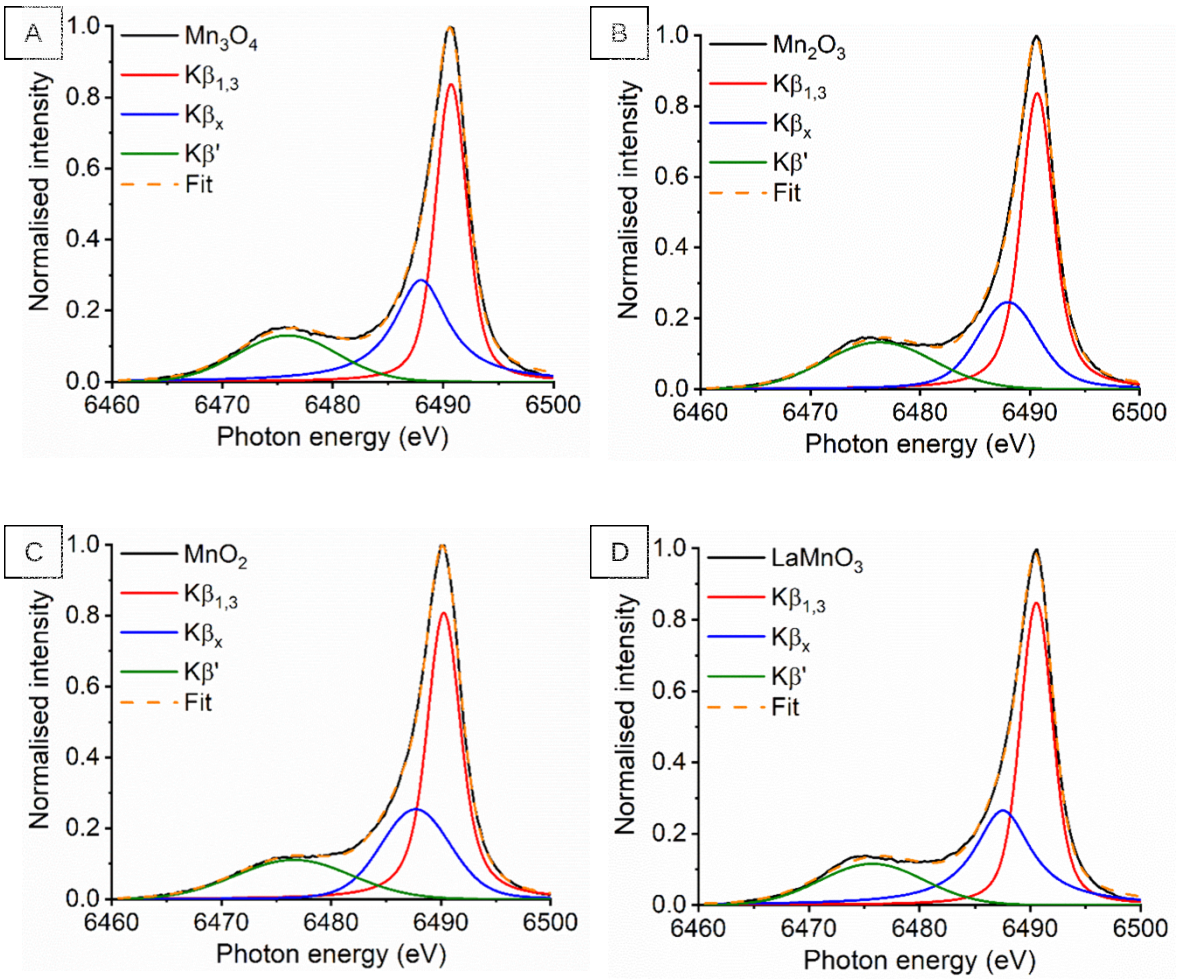

Figure 4.3.4: *Mn Kβ mainlines fitted using 3 symmetric Voigt curves (Kβ$_{1,3}$, Kβ' and Kβ$_x$) for Mn reference materials* ***(A)*** *Mn_3O_4* ***(B)*** *Mn_2O_3* ***(C)*** *MnO_2 compared to* ***(D)*** *sol-gel synthesised $LaMnO_3$*

both Mn_2O_3 and $LaMnO_3$ possessing a Mn(III) oxidation state it is not expected that there is a difference of ± 0.11 eV. This could indicate that the $LaMnO_3$ sample is partially oxidised, however, a previous Mn K-edge EXAFS fit to the sol-gel $LaMnO_3$ is well modelled with a 6-fold coordination to oxygen (section 3.3.1). With the variation in the in the Mn Kβ$_{1,3}$ peak position for the Mn(III) oxidation state it raises an interesting point. It is a commonly accepted practice for researchers to determine the oxidation state of materials via the fingerprint method, *i.e.* compare the sample in question to a variety of appropriate references materials which possess different oxidation states. However, it is clear this is not the case here for the manganite materials, and other factors such as electronic structure, geometry and ligand type must also be considered, even when measuring the Mn Kβ$_{1,3}$ XES.

Table 4.3.1.1: *Mn $K\beta_{1,3}$ peak positions for reference Mn oxides and sol-gel synthesised $LaMnO_3$ compared to 'time-slices' throughout the mechanochemical synthesis of $LaMnO_3$*

Compound	$K\beta_{1,3}$ max (eV)	Oxidation state
MnO_2	6490.26	4
Mn_2O_3	6490.66	3
Mn_3O_4	6490.73	2/3
Sol-gel $LaMnO_3$	6490.55	3
1 h of milling	6490.57	3.0-3.3
2 h of milling	6490.53	
3 h of milling	6490.54	
4 h of milling	6490.56	

Subtle changes can be observed within the Mn Kβ mainlines during the mechanochemical synthesis of $LaMnO_3$ (Figure 4.3.5). To extract the information within the XES spectra the same fitting procedures were applied to hourly 'time-slices' throughout milling, as for the Mn reference materials (Figure 4.3.6). By assessing the position of the fitted Mn $K\beta_{1,3}$ peak for the reference Mn oxide materials as a function of oxidation state it can now allow us to extract oxidation state information. With both the precursor, Mn_2O_3, and final material, $LaMnO_3$, possessing a Mn(III) oxidation state it would be expected that as milling time increases the Mn $K\beta_{1,3}$ peak position decreases from 6490.66 – 6490.55 eV. The Mn $K\beta_{1,3}$ peak positions for 1, 2, 3 and 4 h of milling were recorded at 6490.57, 6490.53, 6490.54 and 6490.56 eV, respectively (Table 4.3.1.1). These positions of the Mn $K\beta_{1,3}$ emission lines suggests that the milled materials have an average oxidation state higher than the Mn(III) oxidation state expected. However, there is an associated error in determining the positions of deconvoluted peaks. When this is taking into consideration, alongside the variance Mn(III) reference materials (Mn_2O_3 and sol-gel $LaMnO_3$), all that can be reliably confirmed is that the net oxidation state for all milled samples is very similar to that of the sol-gel prepared $LaMnO_3$.

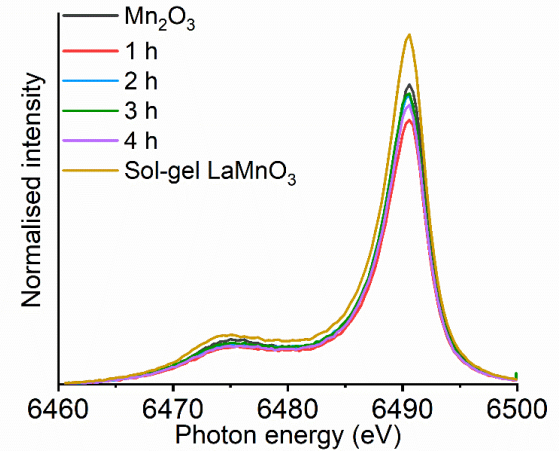

Figure 4.3.5*: Mn Kβ XES mainlines for 'time-slices' during the mechanochemical synthesis of $LaMnO_3$ compared to precursor, Mn_2O_3 and sol-gel synthesised $LaMnO_3$*

It is also diligent to consider that the sol-gel $LaMnO_3$ may not be a pure Mn(III) oxidation state. Whilst the overall bulk analysis of the sol-gel perovskite within Chapter 3 suggested Mn(III) state from EXAFS modelling, the surface analysis by both XPS and STEM-EELS indicated the sample to have a mixed valency of Mn(IV)/Mn(III). However, with the low surface area to volume ratio detected for all $LaMnO_3$ samples, ~4.2 – 7.8 m^2 g^{-1}, it would be considered unlikely to be reflected in the bulk oxidation state.

The ambiguity that remains surrounding the oxidation state of materials during the mechanochemical synthesis of $LaMnO_3$ after performing Mn Kβ XES shows limitations within this technique. Without prior knowledge of the intermediates produced during milling it is difficult to selected appropriate reference materials. Therefore, analysis of Mn Kβ XES can require the use of complex density function theory (DFT) calculations, not commonly readily available.[35–37]

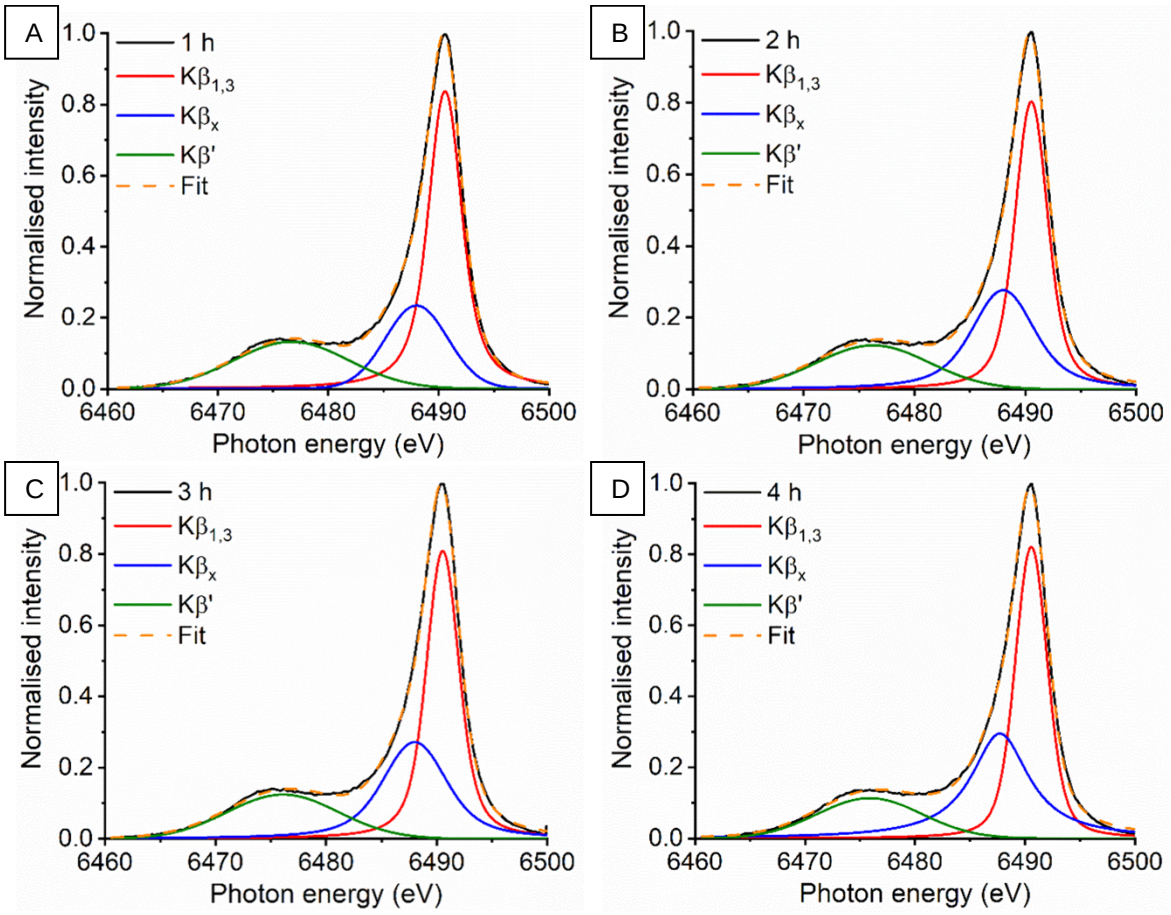

***Figure 4.3.6**: Mn Kβ mainline fitted using three symmetric Voigt curves ($Kβ_{1,3}$, Kβ' and $Kβ_x$) during the mechanochemical synthesis of $LaMnO_3$ after **(A)** 1 h **(B)** 2h **(C)** 3 h and **(D)** 4 h*

4.3.1.2 Milling under inert (argon) conditions

HERFD-XANES. The previous HERFD-XANES analysis of the reference Mn oxides, has now been used to assess the changes during the evolution of $LaMnO_3$ by mechanochemical synthesis under an argon atmosphere (Figure 4.3.7), further expanding on findings in section 3.3.2. The vastly improved spectral resolution that comes on performing HERFD-XANES at the Mn K-edge compared to conventional XANES can be observed in Figure 4.3.7.

After just 1 h of milling there are already clear differences in the HERFD-XANES spectrum compared to the Mn_2O_3 starting material. Within the pre-edge region (Figure 4.3.7D) a decrease in the intensity of feature at **(2)** 6543.0 eV is observed. This indicates significant alterations to the extended Mn-O-Mn structure. However, it can be assumed there is no change to the local electronic structure of the Mn sites, with the feature at **(1)** 6540.8 eV remaining.

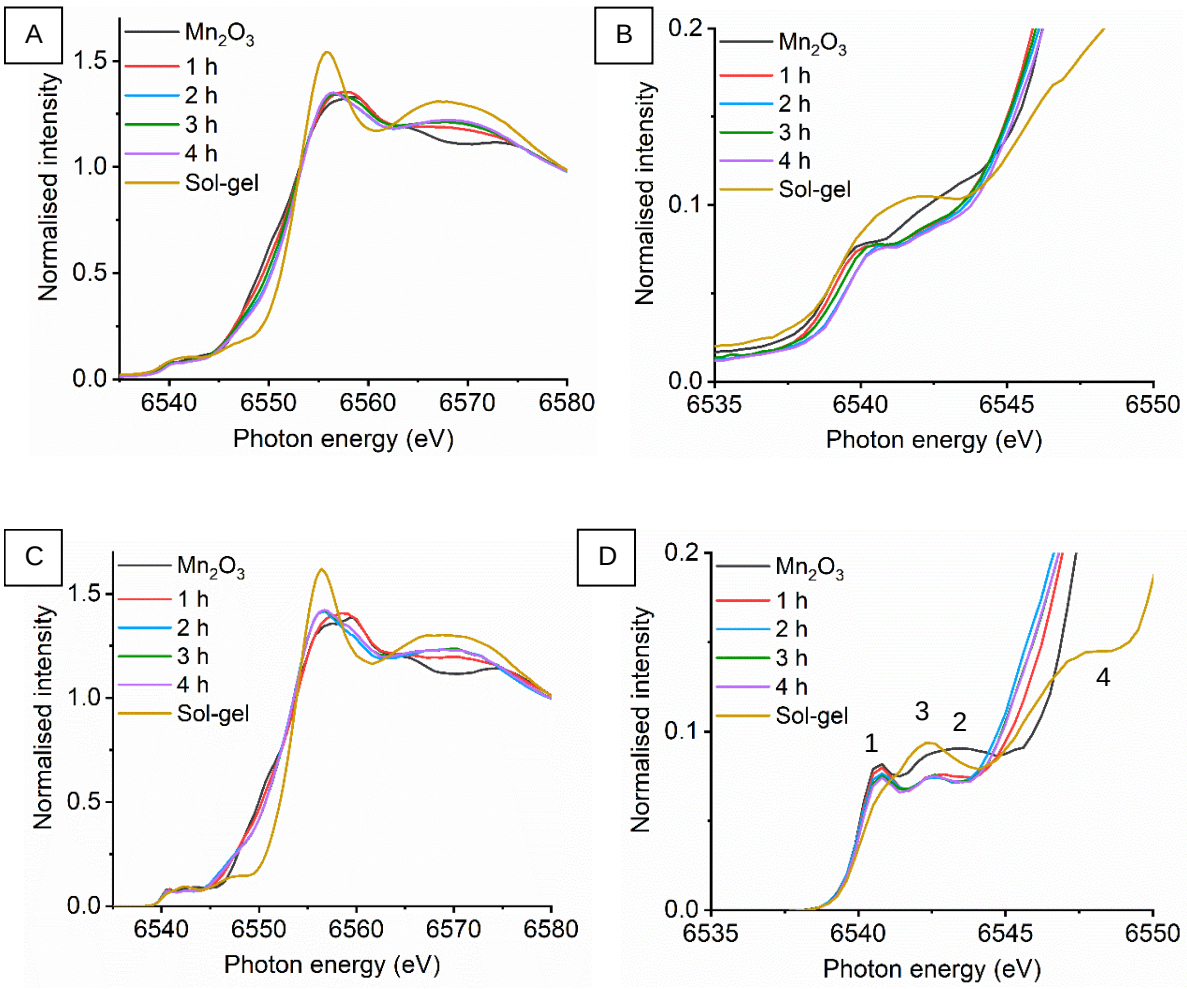

Figure 4.3.7: *'Time-slices' during the mechanochemical synthesis of $LaMnO_3$ under an inert (argon) environment at the Mn K-edge measured by* ***(A)*** *conventional XANES with* ***(B)*** *highlighted pre-edge compared to* ***(C)*** *HERFD-XANES with* ***(D)*** *highlighted pre-edge*

On increasing milling time from 1 - 2 h only a small reduction in intensity is observed in the transitions at **(1)** and **(2)**, with no further change observed from 2 to 4 h of milling. With the transition at **(1)** remaining after 4 h of milling it indicates that there are still similarities consistent with precursor Mn_2O_3 structure. This corresponds with the wt% calculated by Rietveld refinement of XRD data for the argon milled material, which still recorded crystalline Mn_2O_3 at 4 h of milling (Figure 3.3.14). However, the low intensity peak at **(3)** 6542.3 eV for the argon milled materials indicates comparisons to the extended Mn environment of the sol-gel synthesised $LaMnO_3$. With the EXAFS fit for the final argon milled material modelling a Mn-O distance comparable to that of the sol-gel perovskite, the difference in intensity of the transition at **(3)** indicates that the argon milled samples have highly disordered Mn-O-Mn bond angle; resulting from a reduction in 3*d*-4*p* non-local hybridisation.[28,30] With the final milled material having both the transition at **(1)** remaining but the evolution of the peak at **(3),** it suggests that an argon milling environment can be detrimental in producing a perovskite phase. Indicates that while milling under argon the extended Mn_2O_3 structure was able to break down but with no change was observed within the local structure surrounding the Mn sites.

As with the air milled $LaMnO_3$, the shoulder at **(4)** 6547.7 eV is absent for the argon milled 'time-slices', compared to the sol-gel perovskite. This lack of Mn4*p* La5*d* hybridisation can also be reflected in the EXAFS fitting model for the argon milled materials, which recorded two Mn-La scattering paths at 3.13(1) Å and 3.30(1) Å (Table 3.3.2.1).[29] This varies dramatically from the crystalline scattering paths for the sol-gel $LaMnO_3$, suggesting a disordered Mn-La extended structure.

Mn Kβ emission. Here the Mn Kβ mainlines show that after just 1 h of milling a reduction in the intensity of the Mn $K\beta_{1,3}$ peak is observed, with no further changes observed from 1 to 4 h of milling (Figure 4.3.8). Using the fitting analysis observed in Figure 4.3.6, the Mn Kβ mainlines have now been assessed for the final argon milled $LaMnO_3$ material (Figure 4.3.9). The Mn $K\beta_{1,3}$ peak position is recorded at 6490.60 eV, which is consistent of a Mn(III) oxidation state being between both Mn_2O_3, 6490.66 eV, and sol-gel $LaMnO_3$, 6490.55, values.

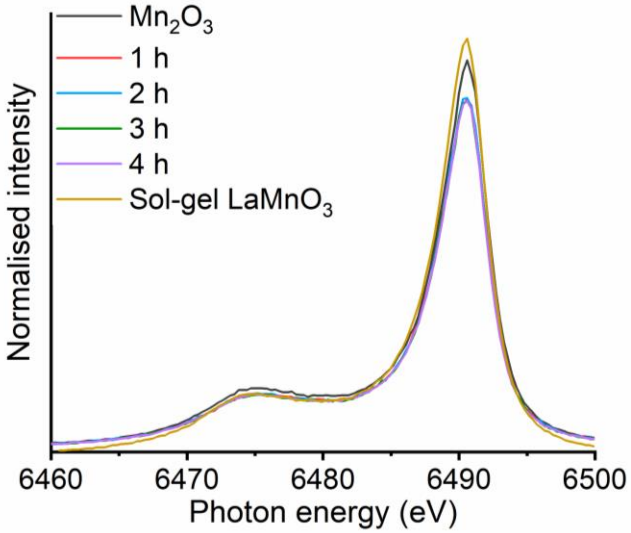

Figure 4.3.8: *Mn Kβ XES mainlines for hourly 'time-slices' during the mechanochemical synthesise of $LaMnO_3$*

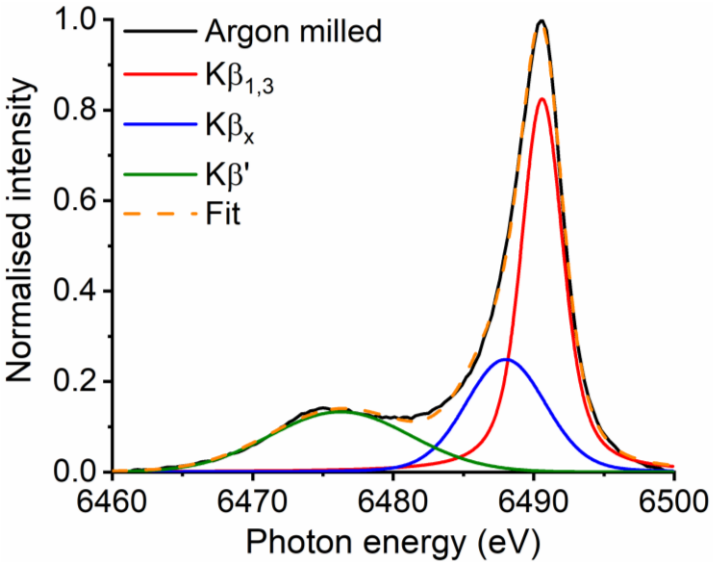

Figure 4.3.9: *Mn Kβ mainline fitted using three symmetric Voigt curves ($Kβ_{1,3}$, Kβ' and $Kβ_x$) for mechanochemically synthesised $LaMnO_3$ in an argon environment after 4 h of milling*

4.3.1.3 Monitoring *in situ* ball milling via XRD

Previously the approach of *ex situ* analysis by various characterisation techniques on 'time-slices' during mechanochemical synthesis of $LaMnO_3$ has provided further insights into the milling of mixed metal oxides. However, it is considered that for an ideal assessment of a reaction that *in situ* monitoring is required.[38] When stopping the mechanochemical synthesis for each separate 'time-slice' the reaction may not actually be quenched, and further exposure to external factors, such as air, can result in structural alternations. Analysing these 'time-slices' off-line can limit the information retrieved, as the materials are no longer under the operating conditions of the mill.[17]

Using the modified vibrational MM200 Retsch mill set-up on ID15A beamline (section 4.2.2), ESRF, France, reported by Halasz *et al.* at the Ruđer Bošković Institute, *in situ* XRD during milling of La_2O_3 and Mn_2O_3 was performed.[16] The use of this modified vibrational mill with a PMMA reaction jar has shown great success in monitoring mechanochemical synthesis of MOF materials.[15,17] However, while performing the milling experiment with one WC milling media on the single metal oxide precursors it was not possible to observe the evolution of the perovskite phase $LaMnO_3$, even after 19 h at a maximum frequency of 36 Hz. Figure 4.3.10 shows the comparison between initial and final XRD patterns, whereby phase ID reported only La_2O_3, $La(OH)_3$ and Mn_2O_3 diffraction peaks after 19 h of milling. The small proportion of broadening in the baseline of diffraction peaks indicates a small proportion of either disordered material or decrease in particle size, both a common consequence of milling. Attempts to assist the mechanochemical action between the two metal oxides by preheating the starting mixture, increasing the number of WC media and by ion and liquid assisted grinding (ILAG) with either H_2O or NH_4NO_3 were unsuccessful.

The use of a vibrational mill and soft PMMA milling jar (required in order to collect the XRD data) provided a much lower energy to that of the to the ZrO_2 grinding jars and planetary ball mill previously used, results in a reduced impact energy transferred to the powdered materials. This suggests that the collisions between the milling media and jar are extremely important for the precursor powders to mechanically activate and subsequently form the new perovskite phase. Therefore, though it was possible to measure milling *in situ* it was not suitable comparison to simulate the exact same conditions experience within a planetary ball mill for mixed metal oxide materials. With commercially available milling equipment not permitting the direct monitoring of reactions due to its dynamic set-up it can be extremely challenging to understand the chemical steps involved for a new phase to evolve. One possible solution can be to attempt mimicking some of the conditions the powdered materials experienced within the mill. Therefore, the work next details efforts towards simulating a proportion of impact force by performing systematic high pressure experiments.

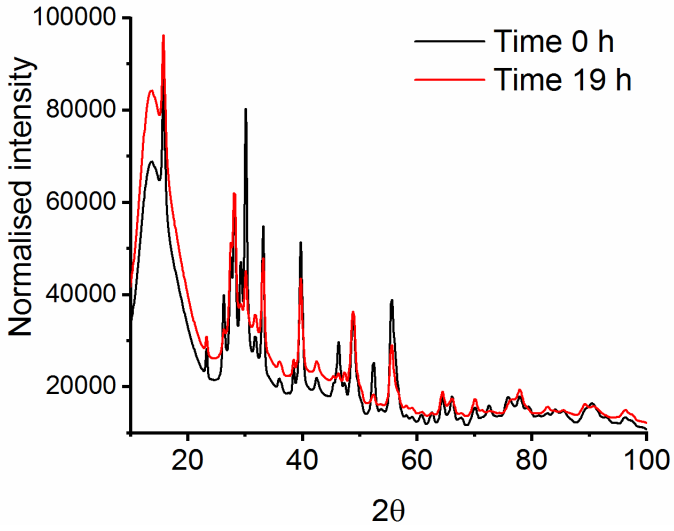

Figure 4.3.10: *XRD patterns at time 0 h and time 19 h after milling La_2O_3 and Mn_2O_3 using a PMMA vibrational mill*

4.3.1.4 *In situ* high pressure EDE experiments

Previous attempts to monitor milling *in situ* by XRD were unsuccessful in observing the perovskite phase due to implications of the modified set-up. Therefore, high pressure energy dispersive EXAFS (EDE) experiments have now been performed on four different precursor materials; (A) the reference Mn_2O_3 starting material, (B) a homogeneous mixture of La_2O_3 and Mn_2O_3, (C) La_2O_3 and Mn_2O_3 after 30 min of high energy planetary ball milling and (D) subsequently after 1 h of milling. Using a diamond anvil cell (DAC) experiments were performed to simulate the pressure forces experienced during planetary ball milling. Performing Mn K-edge EDE allowed for the investigation of extreme pressure effects and how the presence of La precursors has on the structural and electronic properties around the Mn local environment. Though high pressures have been applied to already synthesised mixed metal oxides, there is limited information on using pressure alone to synthesise the $LaMnO_3$ phase.[39,40]

Systematic studies were performed on Mn_2O_3 and three homogeneous mixtures of La_2O_3 and Mn_2O_3; 0, 0.5 and 1 h 'time-slices' after planetary ball milling (Figure 4.3.11). Due to the complex nature of the experimental set-up, perforated diamond windows were required to be fitted into the DAC to minimise diamonds absorbance whilst measuring at the Mn K-edge, ~6539 eV. Initial studies on Mn_2O_3 were able to reach a maximum pressure of 15 GPa, (with Raman spectroscopy measuring the fluorescence of a ruby contained within the gasket, alongside the powders) to prevent the initial breaking of the diamond windows at the early stages of the beamtime. With the latter samples a higher pressure of 30 GPa was reached. The diamond single crystal reflections visible in the spectra were minimised by scanning multiple measurements in different orientations and then deglitched following Hong *et al.* procedure.[22] However, a few glitches remained, limiting the data set size and overall quality.

Comparing the EDE spectra for the reference precursor material Mn_2O_3 from 0 – 15 GPa of pressure showed no significant changes (Figure 4.3.11A). This was also reflected in the spectra for the mixture of Mn_2O_3 and La_2O_3 (Figure 4.3.11B). Further attempts to induce structural changes by using pre-milled samples after 0.5 and 1 h in a planetary ball mill were also unsuccessful, even up to pressures of 30 GPa (Figure 4.3.11C,D).

This indicates that either higher pressures or a combination of pressure and temperature are required to mimic the conditions that drive mechanochemical transformations. It is also diligent to consider the type of pressure applied to the powdered materials in a planetary ball mill. The opposing circular motion of the central axil and rotating jars does not only result in compression, experienced in a DAC, but rather the transfer of mechanical action in the form of sheer and fiction to the materials.[41] Ultimately, this information combined with the results from the *in situ* vibrational mill, confirms that the mechanochemical synthesis of these metal oxide systems are extremely complicated to monitor *in situ*.

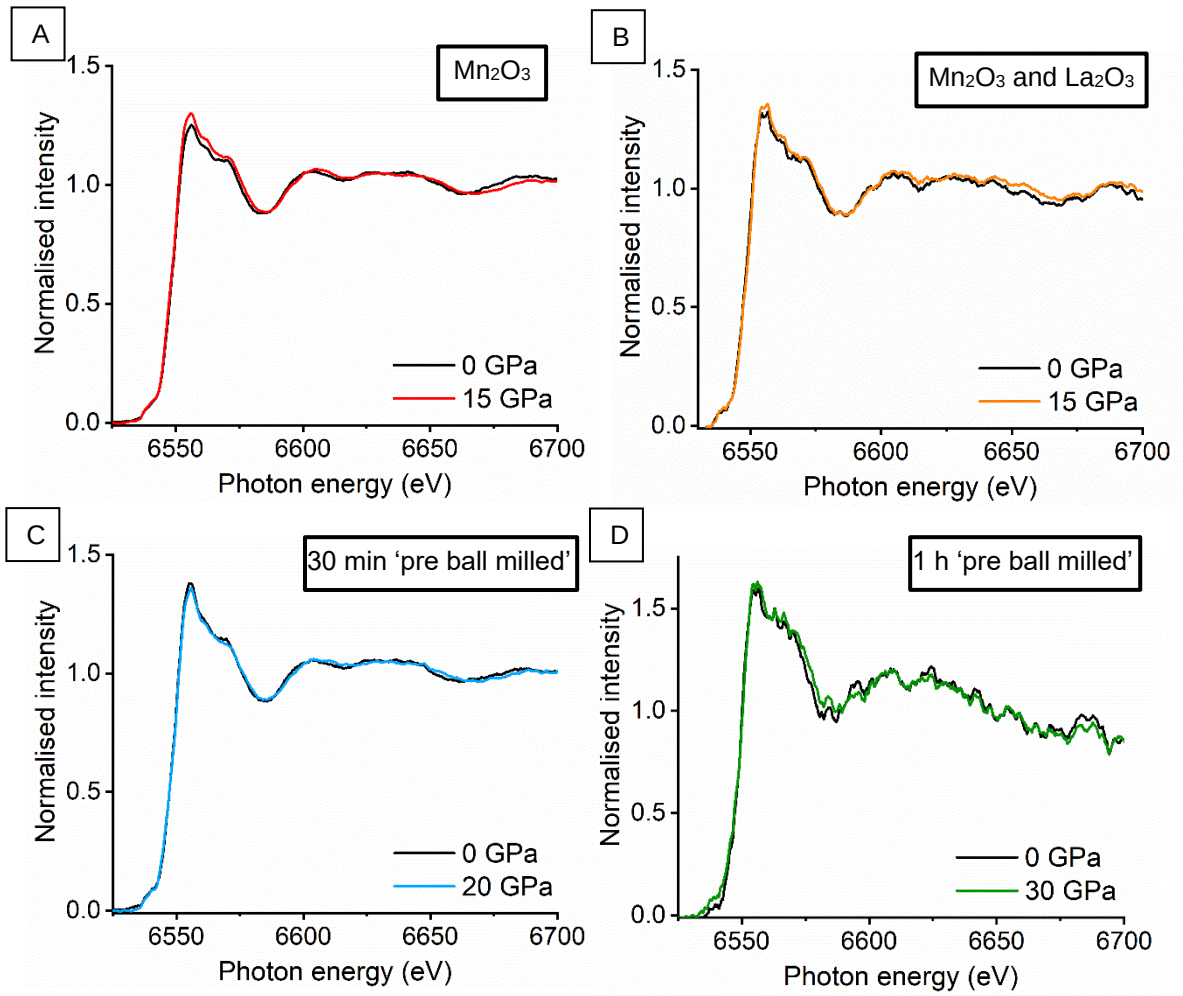

Figure 4.3.11: *In situ high pressure EDE spectra a comparing initial to final pressure for* ***(A)*** *Mn_2O_3,* ***(B)*** *La_2O_3 and Mn_2O_3* ***(C)*** *La_2O_3 and Mn_2O_3 mixture after high energy ball milling for 30 min and* ***(D)*** *La_2O_3 and Mn_2O_3 mixture after high energy ball milling for 1 h*

4.3.2 Understanding the catalytic activity of mechanochemically synthesised $LaMnO_3$ towards the decomposition of N_2O

In Chapter 3 (section 3.3.4) it was reported how the 4 h argon ball milled $LaMnO_3$ catalyst showed a greater activity towards N_2O decomposition at lower temperatures compared to the 4 h air milled, and sol-gel synthesised analogues (Figure 4.3.12). *Ex situ* characterisation on the fresh catalyst highlighted that, though the ball milled materials show similarities in their bulk structural properties, variations at the surface of $LaMnO_3$ correlated to the changes in catalytic activity. Within this section advanced characterisation techniques have now been applied in order to explore the effect of milling and milling environment on final the $LaMnO_3$ structure, alongside its catalytic properties and behaviour.

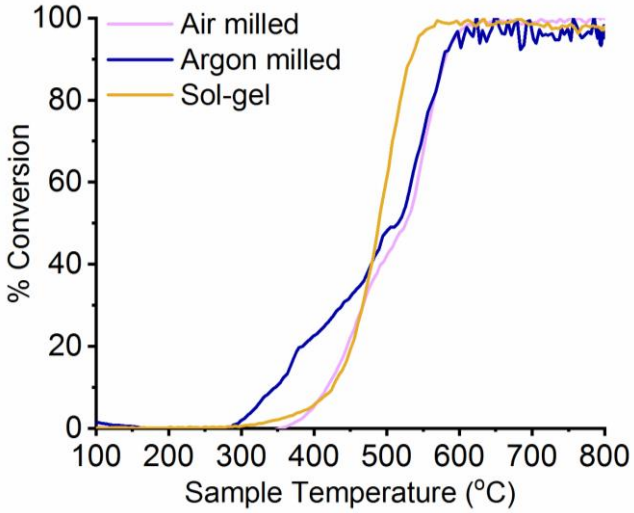

Figure 4.3.12: *The percentage conversion of $N_2O \rightarrow N_2$ over differently synthesised $LaMnO_3$ catalysts*

4.3.2.1 *Ex situ* analysis of ball milled $LaMnO_3$ catalysts for deN_2O

Valence-to-Core (VTC). The information attained from the Mn $K\beta_{1,3}$ emission line showed little to no changes between the different milling atmospheres, air and argon, for the mechanochemically synthesised catalysts. To probe any further structural differences between the $LaMnO_3$ materials Mn Kβ valence-to-core (VTC) spectroscopy has been performed.

These low intensity features, observed at energies well above the Kβ mainlines, measures the decay of an electron from an allowed valence orbital to fill the Mn 1*s* core hole. VTC spectra therefore directly reflects the orbitals participating in the chemical bond, producing information on the chemical environment of the surrounding oxygen ligands on the central Mn atom.[42] The Mn Kβ VTC spectra recorded here (Figure 4.3.13) consist of two characteristic peaks; ascribed as $K\beta_{2,5}$ for the high energy feature and Kβ'' for the lower energy satellite peak. Here, the $K\beta_{2,5}$ peak results from a transition to the Mn 1*s* from molecular orbitals (MO) with largely oxygen *p*-character, 2*p*, combined with some Mn *p*, 4*p* or 3*p*.[43] A consequence of a 3*d* → 1*s* quadrupole transition leads to complications when

quantifying the $K\beta_{2,5}$ peak intensity. However, the position of the $K\beta_{2,5}$ peak is reported in literature to shift 1 eV per oxidation state.[44] The lower energy satellite peak Kβ'' is then assigned to a transition from a MO with predominantly O 2*s* character, with some Mn *p*-contribution, to the Mn 1*s* core hole.[43] The intensity of this feature Kβ'' is linked to the mixing of Mn *p* character with O 2s orbitals; the more favourable the overlap the shorter Mn-O bond length.[45] Any changes to the energy position of the Kβ'' is sensitive towards ligand type, however, here the Kβ'' transition for all samples is recorded as expected for oxygen ligands.[43,44]

The VTC spectra of known Mn oxide reference compounds (MnO_2, Mn_2O_3 and Mn_3O_4) have first been assessed in order to interpret the ball milled and sol-gel prepared $LaMnO_3$ perovskite data (Figure 4.3.13A). Assessing the VTC spectrum for MnO_2, it presents both the highest energy for $K\beta_{2,5,}$ and Kβ'' peaks, at 6535.0 eV and 6519.0 eV, respectively, along with intensity compared to the other Mn oxide reference compounds (Table 4.3.2.1). MnO_2 has the highest oxidation state, at Mn(IV), increasing the the Z_{eff}. This stabilisation of the Mn 1*s* relative to its *p*-component, shifts the $K\beta_{2,5}$ transition 1.5 eV higher energy.[33,44] The Kβ'' peak has a greater intensity compared to the other Mn oxide references, even though there is minimal variation in Mn-O bond lengths. Pollock *et. al.* reported how the Kβ'' transition can also be dependent on bond angle for iron dimer species.[46] This indicates that MnO_2 has a different local geometry to the other Mn oxides, with its MO possessing a more favourable O 2*s* and Mn *p*-character mixing; in agreement with the pre-edge region in HERFD-XANES (Figure 4.3.1).

Both Mn_2O_3 and Mn_3O_4 compounds detect the same the $K\beta_{2,5}$ peak position, at 6533.5 eV, despite having oxidation states, Mn(III) and Mn(III)/Mn(II), respectively. This, once again, reflects the difficulties in extracting precise information about oxidation state for these materials, previously observed at the $K\beta_{1,3}$ emission line (Figure 4.3.4). The same

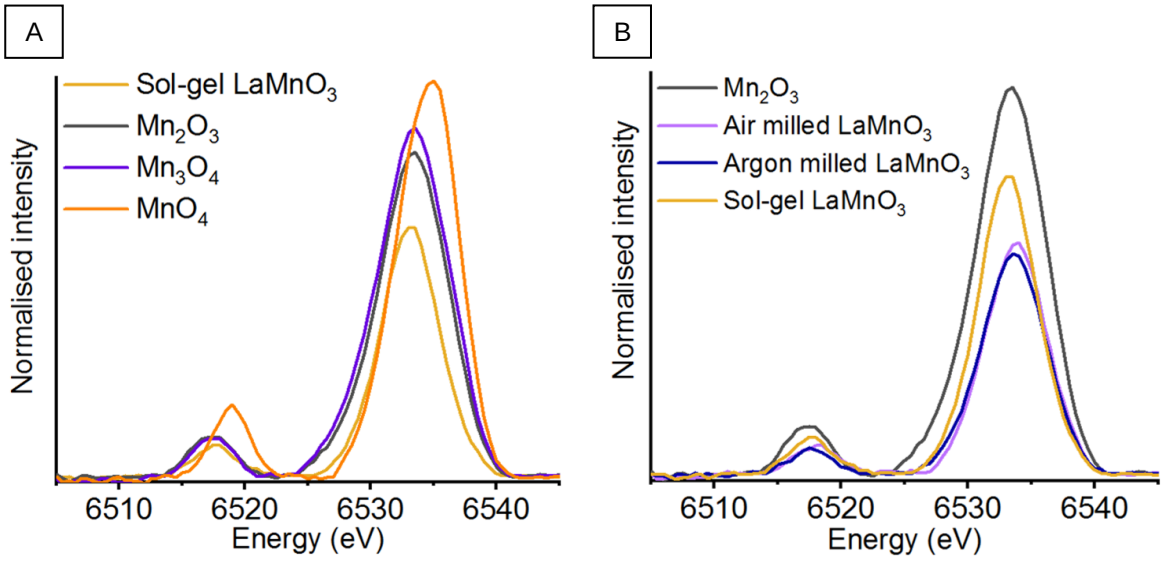

Figure 4.3.13: *Mn Kβ valance-to-core XES lines for* ***(A)*** *different reference Mn oxides and sol-gel prepared $LaMnO_3$ and* ***(B)*** *differently prepared $LaMnO_3$ catalysts*

Kβ'' position and intensity are also recorded, strongly indicating that both Mn oxides have similar oxygen ligand coordination environments. However, relative changes in the intensity of $K\beta_{2,5}$ can be an indication of the proportion of Mn *p* or O 2*p* character in the transition.[43] The higher intensity of $K\beta_{2,5}$ for Mn_3O_4 can reflect the tetrahedrally coordinated Mn(II) centre allowing for more *p*-contribution; also observed in the HERFD-XANES pre-edge region (Figure 4.3.1).

Table 4.3.2.1: *Mn Kβ VTC XES peak positions for reference Mn oxides and differently synthesised $LaMnO_3$*

Sample	**$K\beta_{2,5}$ (eV)**	**Kβ'' (eV)**
MnO_2	6535.0	6519.0
Mn_2O_3	6533.5	6517.3
Mn_3O_4	6533.5	6517.3
Sol-gel $LaMnO_3$	6533.2	6517.5
Air milled	6534.0	6518.3
Argon milled	6533.5	6517.5

Using this Mn Kβ VTC analysis of the reference Mn oxides assessment of the differently synthesised $LaMnO_3$, by sol-gel or mechanochemical synthesis, has been performed (Figure 4.3.13B). Here, the sol-gel $LaMnO_3$ presents the highest intensity peaks compared to both the ball milled catalysts. The increase in intensity for the $K\beta_{2,5}$ transition at 6533.2 eV for the sol-gel catalyst suggests increase Mn *p* / O 2*p* character. As all $LaMnO_3$ catalysts have comparable Mn-O bond lengths, previously calculated by EXAFS (Table 3.3.1.2 and Table 3.3.2.1), it can imply that the higher Kβ'' intensity at 6517.2 eV is linked to a more favourable bond angle. This corresponds to previous HERFD-XANES assessment, where the sol-gel catalysts showed a more linear Mn-O-Mn bond, due to a higher intensity feature in the pre-edge region.

For the ball milled materials the VTC spectra indicates similar oxygen ligand local geometry. Though a small increase in the position of both $K\beta_{2,5}$ and Kβ'' peaks is observed, the limitations within this technique, observed as well for $K\beta_{1,3}$ XES, makes it not possible to explicitly define the oxidation state. By performing Mn Kβ VTC it further highlights the difficulties in assessing these complex structures, even with the use of extremely sensitive advanced characterisation techniques.

4.3.2.2 *In situ* N_2O decomposition

To understand how the differently synthesised $LaMnO_3$ catalysts acts under operating conditions, *in situ* HERFD-XANES and NAP-XPS have been performed during deN_2O to assess both bulk and surface effects. Monitoring the active site under working conditions can provide insights into the catalytic process steps, such as reactant adsorption, reaction and desorption of products. In turn it will further understand the mechanism by which deN_2O occurs over the $LaMnO_3$ catalysts and why the 4 h argon milled has improved activity at lower temperatures 300 – 500 ˚C (Figure 4.3.12). Previous *ex situ* characterisation after deN_2O, by XRD and XAFS, also showed that the ball milled catalysts formed more regular, ordered perovskite structures, indicating a calcination process occurred (< 500 ˚C) alongside the catalytic reaction (Chapter 3, section 3.3.1).

HERFD-XANES and XES. *In situ* Mn $K\alpha_1$ XES and HERFD-XANES has been performed during deN_2O to assess any bulk structural changes to the Mn active site. Performing HERFD-XANES at the maximum of Mn $K\alpha_1$ emission line to improve the signal of the data due to difficulties incurring as a result of the quartz capillary thickness. The Kα for 3*d* transition metals is ~8x more intense than the $K\beta_{1,3}$ due to strong spin-orbital splitting of 2*p* levels (section 2.9.6).[47] A Kapton capillary was also used, up to a maximum temperature of 375 ˚C, and a with quartz capillary for the 600 ˚C measurement (see experimental section 4.3.2.2).

The 4 h air milled catalyst was first monitored at 250, 300, 350 and 375 ˚C under a constant flow of He, in the absence of the N_2O reactant, to investigate the effect of temperature on the ball milled structure, Within the HERFD-XANES (Figure 4.3.14A) the first clear observation is the shift of the raising edge ~1 eV to a lower energy with increasing temperature, indicative of a reduced Mn environment. This can be further reflected in the shift of the transition within the pre-edge region at **(1)** to 6540.8 eV (Figure 4.3.14B), which is assigned to the Mn(II) metal centre for Mn_3O_4 (Figure 4.3.1).[25,26] The use of elevated temperatures on a perovskite in an oxygen deficient environment could be expected to result in the reduction of the B-sites, as oxygen diffuses out of the lattice in an oxygen deficient environment.[48] Furthermore, the subtle changes observed within the pre-edge region with raising temperature suggest the ball milled perovskite is undergoing structural alterations.

Observations at the Mn $K\alpha_1$ XES (Figure 4.3.15A) show the position of the peak increases by 0.2 eV, further suggesting some reduced Mn nature on increasing temperature. However, it has been reported that the $K\alpha_1$ line is not a suitable measure for oxidation state assessment compared to the $K\beta_{1,3}$. This results from the Mn Kα 2p → 1s having lower chemical and valence electron configuration sensitivity to $K\beta_{1,3}$ as the 2*p* has less interaction with valence orbitals compared to 3*p*.[47]

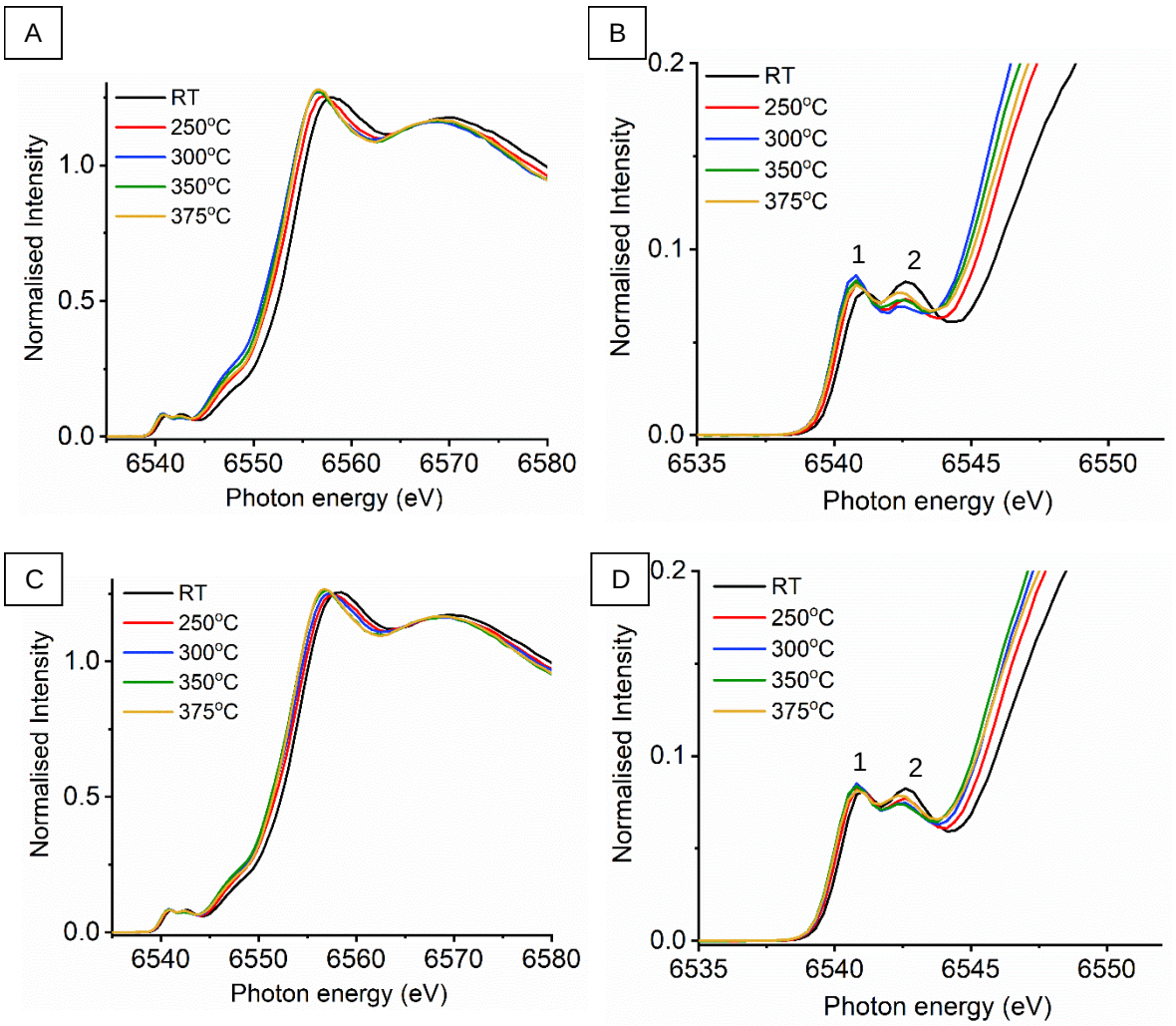

Figure 4.3.14: *Mn K-edge HERFD-XANES spectra for 4 h air milled $LaMnO_3$ during **(A)** heating under He gas with corresponding **(B)** highlighted pre-edge region compared to **(C)** deN_2O with **(D)** highlighted pre-edge region*

In situ deN_2O was then performed over the 4 h air milled catalyst, with measurements performed at the same temperature increments. Within the HERFD-XANES (Figure 4.3.14) a shift in the raising edge of ~1eV to a lower energy is observed with increasing the temperature to 375 ˚C. Once again, the pre-edge region records some Mn(II) character with a shift from 6541.1 eV to 6540.8 eV for the transition at **(1)**, at a lower intensity to the He environment. With comparable spectra observed under a purely He gas flow it can indicate changes in spectra observed under reaction conditions is solely a temperature effect. However, if the Mn site is being reduced under operating conditions, the diffusion of oxygen from the lattice to the surface can aid N_2O decomposition in a Mars-van Krevelen type mechanism.[49] The Mn $K\alpha_1$ XES (Figure 4.3.15B) shows an increase from 5899.0 to 5899.2 eV from 250 – 300 ˚C.

The sol-gel synthesised $LaMnO_3$ catalyst was next monitored by HERFD-XANES during deN_2O (Figure 4.3.16A, B). Though this sample presented more crystalline ordered perovskite structure compared to the 4 h air milled catalyst, they both followed similar catalytic activity for deN_2O (Figure 4.3.12). During the preparation of this sol-gel catalyst a final calcination temperature of 700 ˚C was used, and therefore the final material is expected

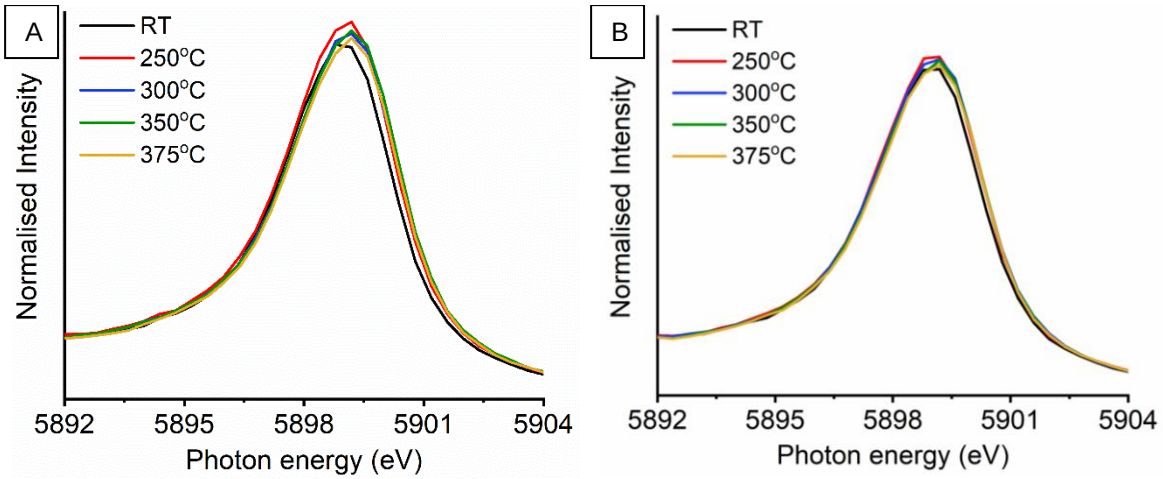

Figure 4.3.15: *Mn Kα₁ XES spectra for 4 h air milled $LaMnO_3$ during* ***(A)*** *heating under He gas compared to during* ***(B)*** *deN_2O*

to experience stability when exposed to the deN_2O reaction temperatures of up to 375 ˚C. However, clear alterations are observed within the HERFD-XANES spectra (Figure 4.3.16A, B), that therefore must be induced by the catalytic reaction.

With an increase in reaction temperature from 250 – 375 ˚C, the main edge is observed to shift to a lower energy, coupled with the peak at **(1)** 6540.8 eV now detected within the pre-edge region. The feature at **(1)** has previously not been observed for the RT sample. The most noticeable difference on increasing temperature is observed at the 6548 eV shoulder. This transition is assigned to hybridisation of Mn 4*p* and La 5*p* orbitals, which indicates structural alterations to the extended Mn/La structure whist under deN_2O operating conditions. Mn $K\alpha_1$ XES remains at a constant energy position, with an increase in intensity, at 5899.0 eV (Figure 4.3.17A).

Finally, on monitoring the HERFD-XANES spectra for the 4 h argon milled catalyst (Figure 4.3.16C, D) during *in situ* deN_2O the position of the main edge remains the least altered, compared to the previous two $LaMnO_3$ catalysts, on raising temperatures. However, it has previously been noted that the main edge of the argon milled catalyst at RT already began slightly to the left of the other $LaMnO_3$ materials (section 3.3.2). This is also reflected in the pre-edge region, where the feature at **(1)** was already at 6540.8 eV prior to the reaction, and therefore remains in the same position. However, with the raise in temperature an increase in the intensity of the transition at **(1)** 6540.8 eV is observed. Consistent Mn *Kα₁* spectra is measured throughout the experiment, with the maximum peak intensity remaining at 5899.0 eV (Figure 4.3.17B).

Figure 4.3.18 is an example of attempts to monitor deN_2O on the 4 h argon $LaMnO_3$ catalyst at higher temperature points, at 450˚C and 600˚C, with a quartz capillary. Even after using prolonged acquisition times, at 25 min spectrum^{-1}, and collecting a total of four scans, the averaged spectra produced a high signal-to-noise ratio making it challenging to assess any significant outcomes (section 4.3.2.2).

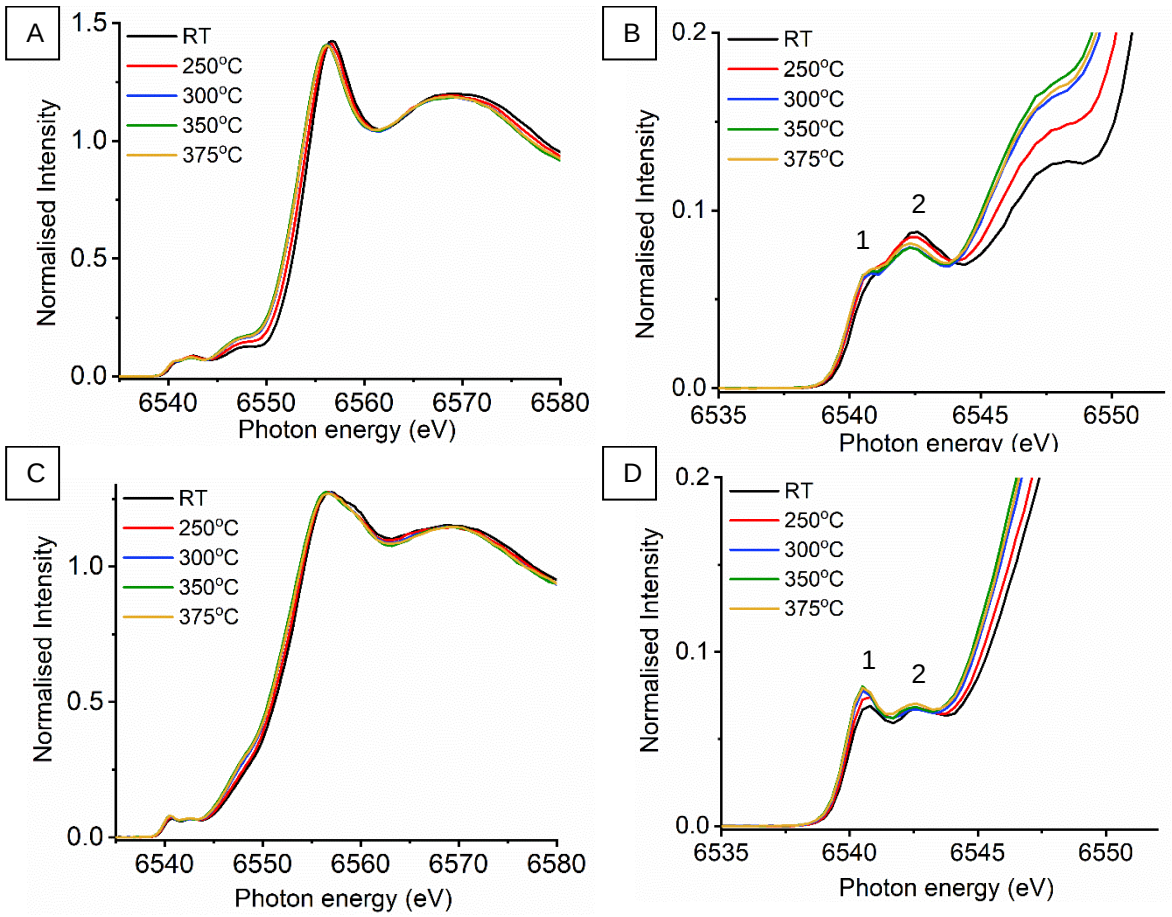

Figure 4.3.16: *Mn K-edge HERFD-XANES spectra during deN_2O for* ***(A)*** *sol-gel synthesised $LaMnO_3$ with* ***(B)*** *highlighted pre-edge region and* ***(C)*** *4 h argon milled $LaMnO_3$ with corresponding* ***(D)*** *highlighted pre-edge region compared*

Assessing the performance of the differently synthesised $LaMnO_3$ catalysts during deN_2O by *in situ* HERFD-XANES showed similarities in the shift of the main edge position along with transition **(1)** within the pre-edge region. This could be an indication of the importance of some Mn(II) character as an intermediate species during deN_2O. To assess whether these differences observed in the HERFD-XANES spectra are only induced under operating conditions *ex situ* HERFD-XANES has been performed on catalysts post deN_2O.

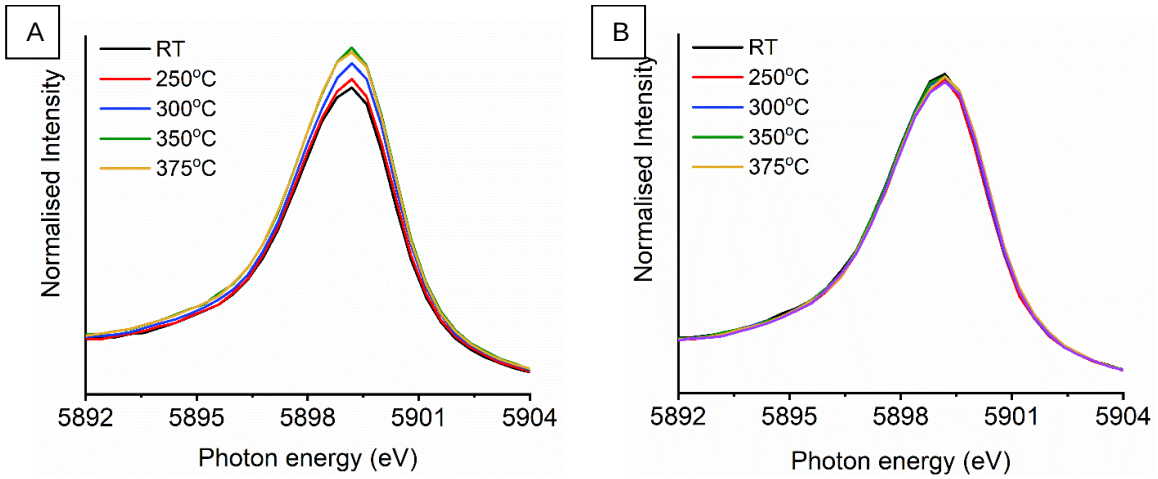

Figure 4.3.17: *Mn $K\alpha_1$ XES spectra during the deN_2O for* ***(A)*** *sol-gel synthesised $LaMnO_3$ and* ***(B)*** *4 h argon milled $LaMnO_3$*

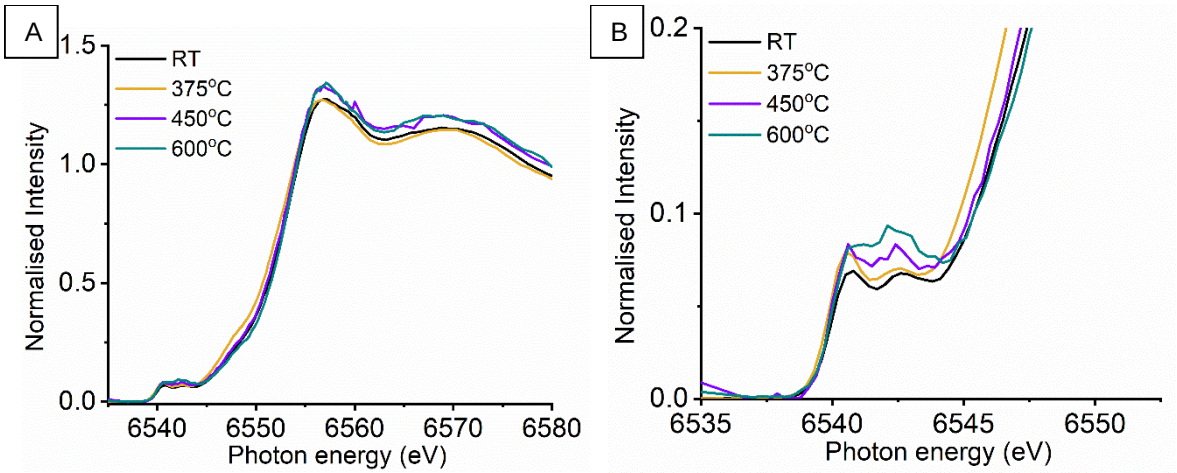

Figure 4.3.18: *Mn K-edge HERFD-XANES spectra during deN₂O for* ***(A)*** *4 h argon milled LaMnO₃* ***(B)*** *highlighted pre-edge region for spectra recorded with a quartz capillary at 450˚C and 600˚C, compared to RT and 375˚C spectra*

Post deN$_2$O *ex situ* HERFD and XES. Performing off-line *ex situ* HERFD-XANES will allow to determine whether (1) the spectra observed in Figure 4.3.14 and Figure 4.3.16 is only visible under reaction conditions or (2) if deN$_2$O at elevated temperatures results in non-reversible structural alterations on the LaMnO$_3$ catalysts. The HERFD-XANES measurements where performed using the energy position of the Mn K$\beta_{1,3}$ maxima for the LaMnO$_3$ catalysts after deN$_2$O temperature points at 375 ˚C and 600 ˚C and compared to a fresh catalyst and an analogous calcined catalyst in air at 600 ˚C.

Previous XRD studies (Figure 3.3.31) detected a higher level of crystallinity for the ball milled materials formed after deN$_2$O catalytic testing at 800 ˚C. Here the HERFD-XANES spectra (Figure 4.3.19) after performing deN$_2$O at 375 ˚C for all catalysts follow similar spectral profile to their analogous fresh sample. This corresponds to the deN$_2$O light-off curve (Figure 4.3.12) where the change in activity is not observed until after 500˚C for the ball milled samples. The spectra recorded at 600˚C are therefore comparable to the crystalline sol-gel sample. However, compared to the calcined in air, *i.e*. no deN$_2$O performed, the used catalysts show a decrease in the intensity at **(2)** indicating a less linear Mn-O-Mn geometric coordination.

Comparisons between the *in situ* and *ex situ* 375˚C spectra for all LaMnO$_3$ catalysts show increase in the transition at **(1)** exists only during deN$_2$O and therefore can be a direct result of an intermediate species formed under working conditions. This indicates that the overall bulk LaMnO$_3$ structure incurs a geometric arrangement, with some character similar to that of Mn(II) species. This could further imply a reduced Mn environment, however, due to the complex nature of determining oxidation states already assessed is it extremely challenging to deduce this. It is important to understand only a small proportion of deN$_2$O is occurring at 375˚C, with more catalytic testing at evaluated temperatures required to cohesive insights into the reaction mechanism for deN$_2$O over these LaMnO$_3$ catalysts.

Ex situ Mn $K\beta_{1,3}$ spectra (Figure 4.3.20) show decreased in intensity but no change in the position of Mn $K\beta_{1,3}$ for all the samples after heating in air and under a N_2O environment. This suggests no clear oxidation state changes have incurred on deN_2O and by calcining the samples in air.

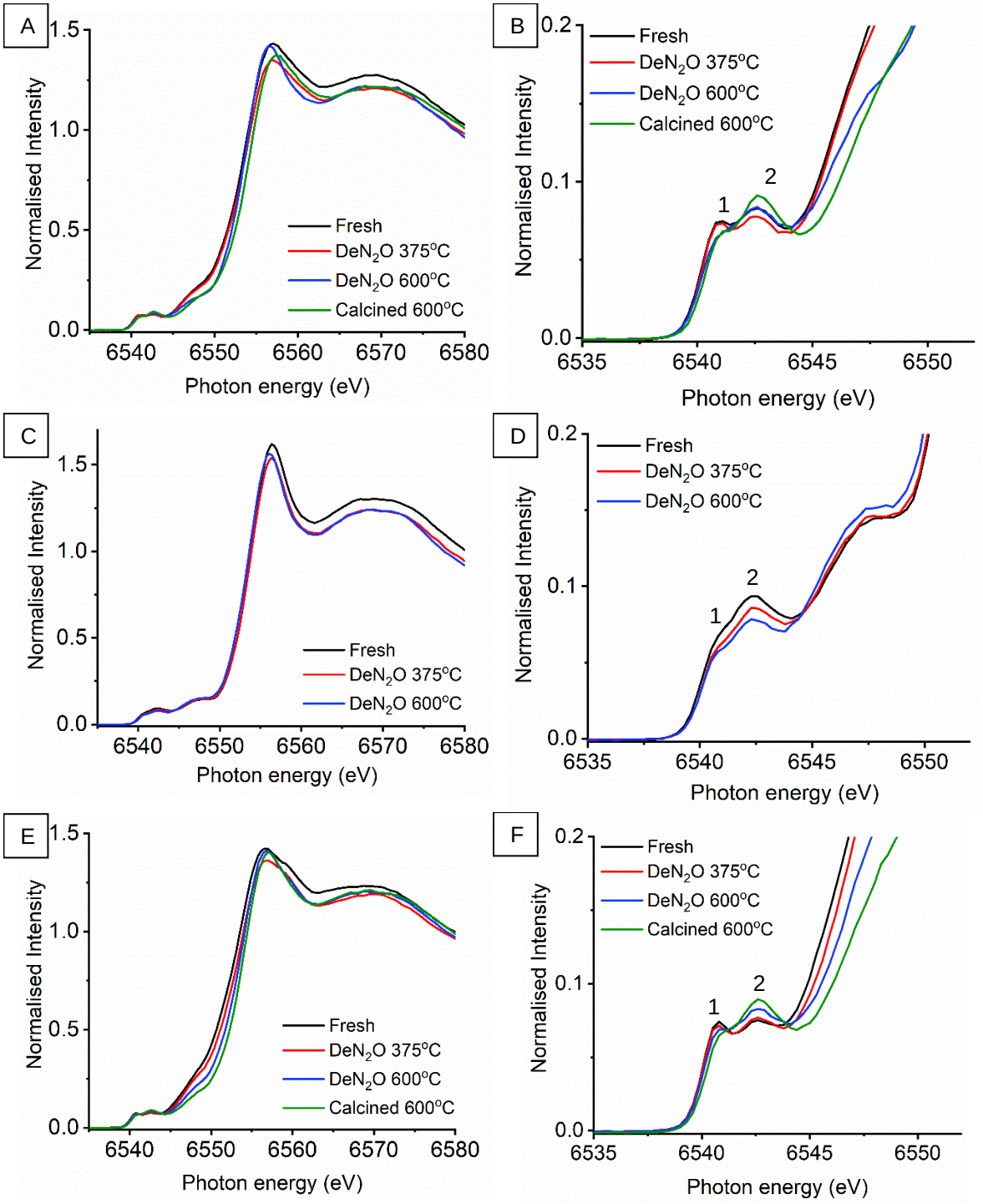

Figure 4.3.19: *Ex situ Mn K-edge HERFD-XANES spectra for* ***(A)*** *4 h air milled $LaMnO_3$ with* ***(B)*** *highlighted pre-edge region,* ***(C)*** *sol-gel synthesised $LaMnO_3$ with* ***(D)*** *highlighted pre-edge region compared to* ***(E)*** *argon milled $LaMnO_3$ with* ***(F)*** *highlighted pre-edge region after temperature points 375˚C and 600˚C, compared to the fresh catalyst and to the analogous calcined sample*

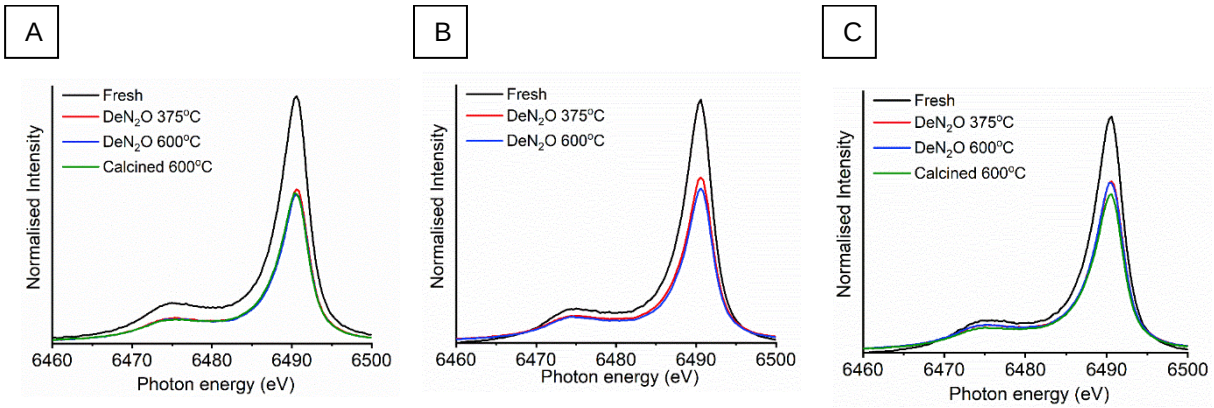

Figure 4.3.20: *Ex situ Mn Kβ$_{1,3}$ XES spectra for* ***(A)*** *4 h air milled LaMnO$_3$* ***(B)*** *sol-gel synthesised LaMnO$_3$ compared to* ***(C)*** *argon milled LaMnO$_3$ after temperature points 375˚C and 600˚C, compared to the fresh catalyst and to the analogous calcined sample*

NAP-XPS. With both HERFD-XANES and XES showing similarities during deN$_2$O for all LaMnO$_3$, it indicates that the improved activity of the argon milled LaMnO$_3$ cannot be explained by analysis of the bulk structures alone. In Chapter 3 it was possible to link improved catalytic activity towards deN$_2$O to the surface properties of the LaMnO$_3$ catalysts. Previous lab based XPS (section 3.3.3) was performed under vacuum with a fixed incident beam. This *ex situ* analysis of the surface of the catalysts often presents vastly different properties compared to that under reaction conditions.[50] However, by performing *in situ* deN$_2$O to assess the surface properties and stability of the LaMnO$_3$ catalysts it can provide new insights into N$_2$O adsorption, dissociation and desorption of O$_2$. Furthermore, controlling the incident energy allows for the same specific penetration depth of the surface for each XPS region.[51] In this section, NAP-XPS has been performed under working conditions during deN$_2$O with spectra recorded at the La3*d*, Mn2*p*, and O1*s* regions at 834.5 – 855 eV, 641 – 655 eV and 529 – 532 eV binding energies, respectively, for the differently synthesised perovskite catalysts. To achieve a comparison depth profile the Mn 3*s* region was performed with a greater incident energy. With the argon milled LaMnO$_3$ catalyst showing promising activity at lower temperatures (Figure 4.3.12) the surface properties during *in situ* deN$_2$O have been detailed and compared to the other LaMnO$_3$ catalysts.

Initially, the Mn XPS regions (Mn 2*p* and Mn 3*s*) have been assessed for the argon milled LaMnO$_3$ with scans performed at RT under a N$_2$O atmosphere and after heating at 400˚C and 600˚C (Figure 4.3.21). Within the Mn 2*p* region two main peaks are observed at ~641.5 eV and ~653 eV, originating from spin-orbit coupling, assigned as Mn2$p_{3/2}$ and Mn2$p_{1/2}$ respectively.[52] These peak positions provide an indication of the Mn oxidation state at the perovskite surface. Due to the broad and asymmetric nature of the peaks, deconvolution of both Mn2$p_{3/2}$ and Mn2$p_{1/2}$ peaks by curve fitting resulted in a total of four peaks for the region, suggesting a mixed valency.[52] The deconvoluted peak positions at RT in N$_2$O for Mn2$p_{3/2}$ were recorded at 641.5 eV and 643.2 eV and for Mn2$p_{1/2}$ at 653.3 eV and 655.6 eV represent Mn(III) and Mn(IV), respectively (Table 4.3.2.2).[53–55] On subsequent

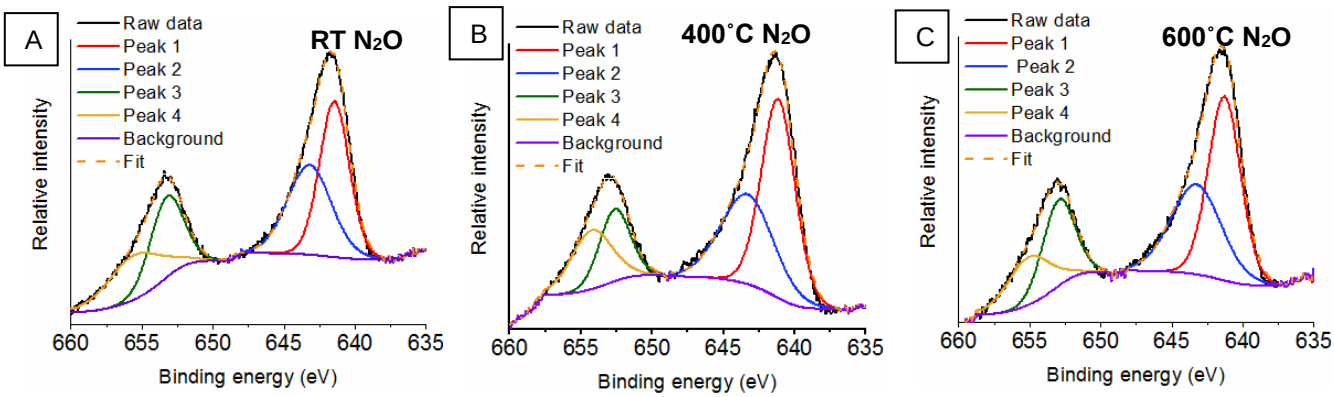

Figure 4.3.21: *NAP-XPS performed on the argon milled catalyst at the Mn2p region at* ***(A)*** *RT under a N_2O atmosphere and then heated to* ***(B)*** *400˚C and* ***(C)*** *600˚C*

heating to 400˚C and 600˚C the peak positions are observed to remain ±0.2 eV within each other. Assessment of the deconvoluted peaks areas for the Mn2$p_{3/2}$ region can give an indication of the relative abundance of Mn(III) and Mn(IV) contributions (Table 4.3.2.2).[56] Calculating a ratio of the areas for each measurement results in consistent 1: 1.3 ±0.1 ratio of Mn(IV):Mn(III) during *in situ* deN_2O for the argon milled catalyst.

Comparison of the argon milled catalyst to the air milled and sol-gel prepared $LaMnO_3$ show that there are distinct variations of the initial Mn(IV)/Mn(III) peak positions and area contributions (Figure 4.3.22 and Figure 4.3.23) (Table 4.3.2.3 and Table 4.3.2.4). However, on heating to 400˚C and 600˚C during deN_2O the Mn(IV)/Mn(III) ratios for all catalysts remain within ±0.2 of one another, with similar deconvoluted peak positions recorded. This is indicative of surface reactions occurring during catalysis that change the net oxidation state.

Table 4.3.2.2: *NAP-XPS deconvoluted peak positions and areas during in situ deN_2O of the argon milled catalyst at Mn 2p, Mn 3s, La 3d and O 1s regions*

Argon milled $LaMnO_3$		**RT vacuum**	**RT in N_2O**	**400˚C in N_2O**	**600˚C in N_2O**
Mn 2*p*	Peak 1	-	641.5, 46205	641.3, 52777	641.1, 63001
	Peak 2	-	643.2, 39338	643.3, 40166	643.3, 44761
	Peak 3	-	653.3, 26307	653.0, 24094	652.6, 20800
	Peak 4	-	655.6, 23371	655.1, 18093	654.3, 22707
	Spin coupling	-	11.8	11.7	11.5
	Ratio Mn(IV):Mn(III)	-	1.1	1.3	1.4
Mn 3*s*	Peak 1	83.12	83.18	83.55	83.36
	Peak 2	88.18	88.26	88.83	88.72
	Satellite	-	-	93.38	92.01
	Splitting	5.1	5.1	5.3	5.4
La 3*d*	Peak 1	834.19	834.52	833.9	834.0
	Peak 2	838.13	838.32	838.2	838.5
	Peak 3	836.46	836.79	836.0	836.2
	Peak 4	850.95	851.29	850.8	850.9
	Peak 5	854.91	855.26	855.1	855.3
	Peak 6	853.09	853.68	852.9	853.1
	La $3d_{5/2}$ splitting	3.9	3.8	4.3	4.4
	Spin coupling	16.8	16.8	16.9	16.8
O 1*s*	Peak 1	529.3, 4867	529.3, 26741	529.3, 46686	529.7, 37254
	Peak 2	531.3, 6909	531.1, 51708	531.5, 44746	530.9, 28693
	Peak 3	533.4, 1940	533.0, 16494	534.0, 1472	532.2, 6739
	Peak 4	-	534.6, 6911	-	-

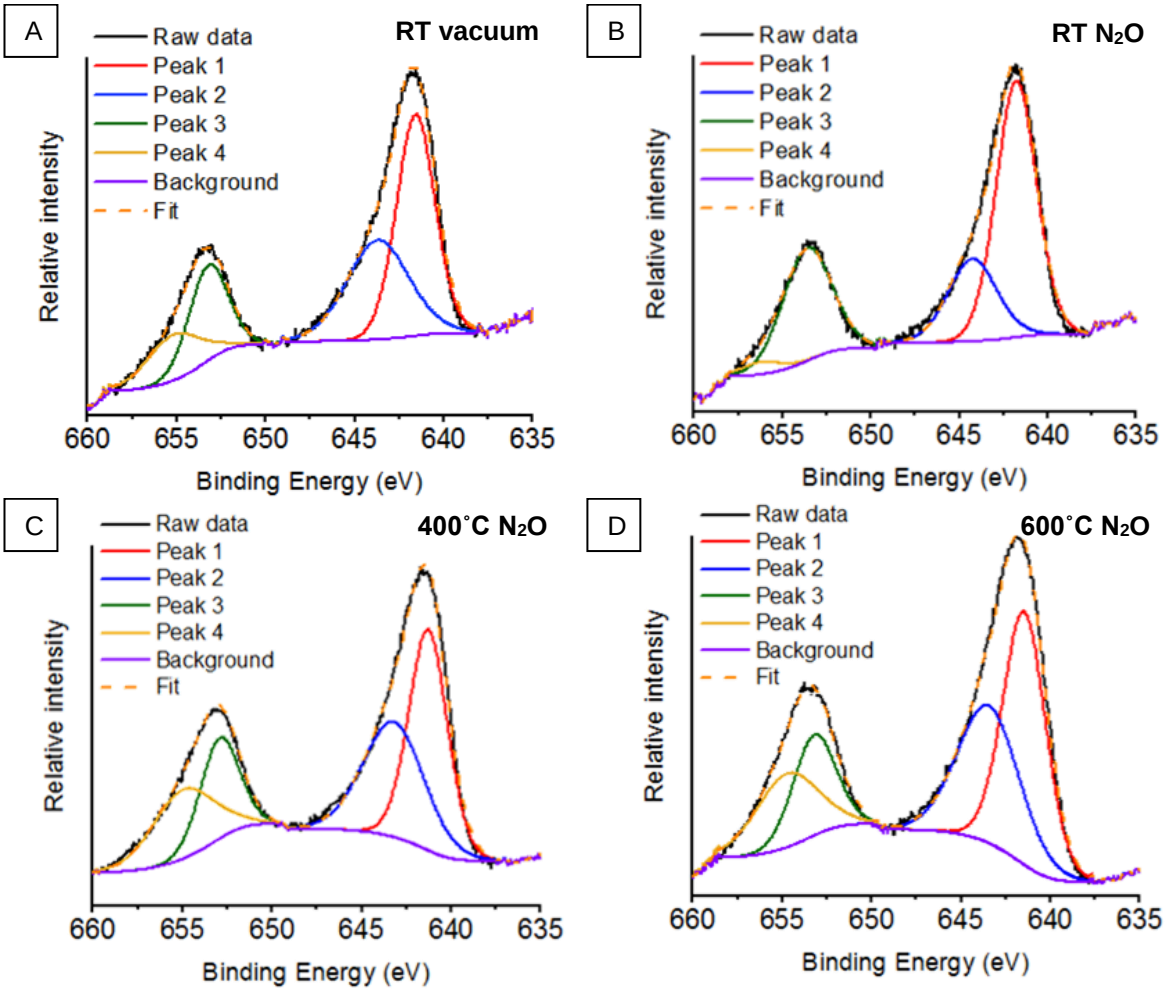

Figure 4.3.22: *NAP-XPS performed on the air milled catalyst at the Mn 2p region at* ***(A)*** *RT in vacuum,* ***(B)*** *at RT under a N_2O atmosphere and then heated to* ***(C)*** *400˚C and* ***(D)*** *600˚C*

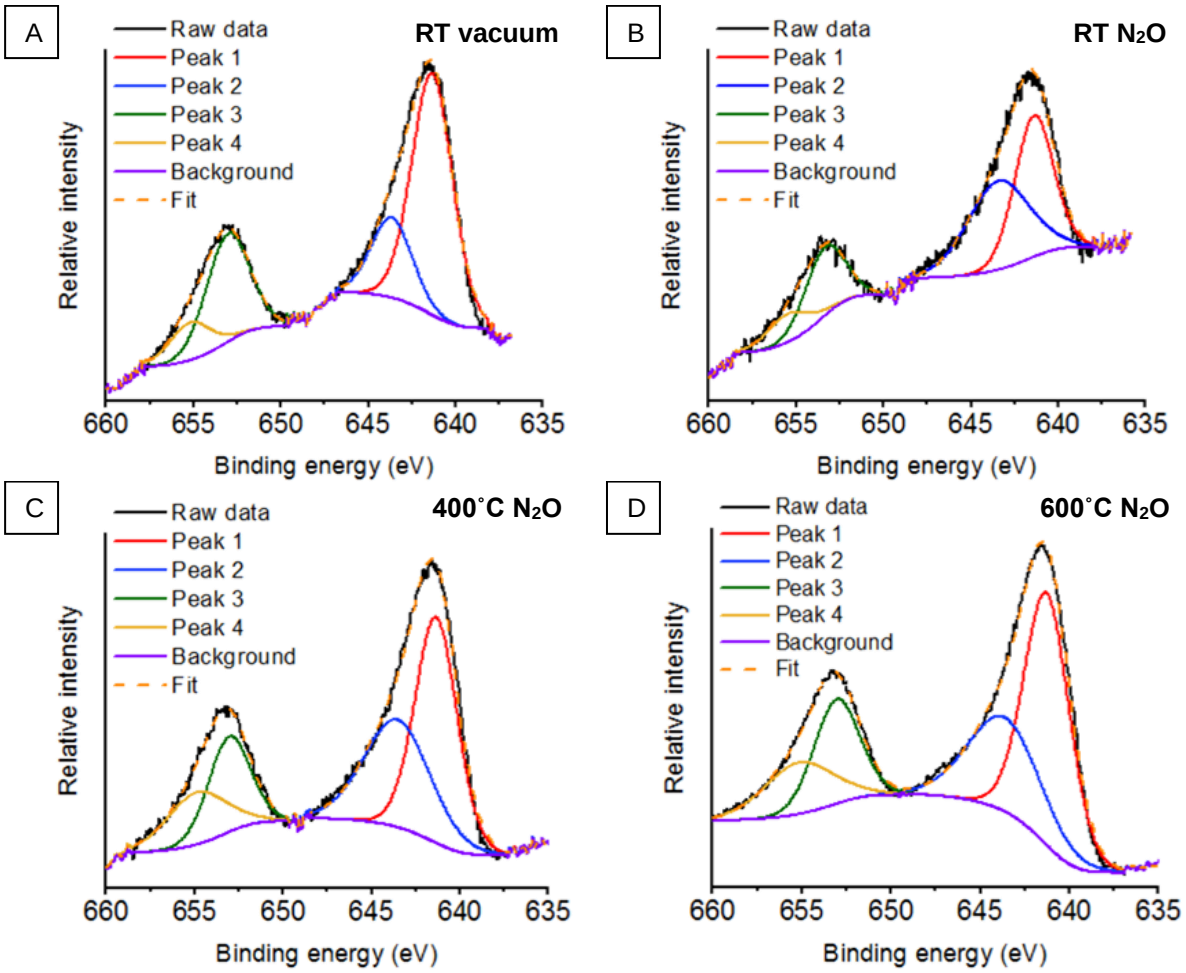

Figure 4.3.23: *NAP-XPS performed on the sol-gel synthesised catalyst at the Mn 2p region at* ***(A)*** *RT in vacuum,* ***(B)*** *at RT under a N_2O atmosphere and then heated to* ***(C)*** *400˚C and* ***(D)*** *600˚C*

Table 4.3.2.3: *NAP-XPS deconvoluted peak positions and areas during in situ deN_2O of the air milled catalyst at Mn 2p, Mn 3s, La 3d and O 1s regions*

Air milled $LaMnO_3$		**RT vacuum**	**RT in N_2O**	**400˚C in N_2O**	**600˚C in N_2O**
Mn2*p*	Peak 1	641.6, 37671	641.8, 50225	641.3, 71126	641.5, 86067
	Peak 2	643.7, 27363	644.3, 19745	643.2, 58775	653.5, 67777
	Peak 3	653.2, 16135	653.6, 26975	652.9, 32281	653.2, 34134
	Peak 4	655.2, 10737	656.3, 2412	655.0, 35168	654.8, 36277
	Spin coupling	11.7	11.9	11.7	11.8
	Ratio Mn(III):Mn(IV)	1.4	2.5	1.2	1.3
Mn3*s*	Peak 1	83.6	83.7	83.3	83.0
	Peak 2	88.6	88.7	88.6	88.3
	Satellite	92.0	91.9	92.3	92.3
	Splitting	5.0	5.1	5.3	5.3
La3*d*	Peak 1	834.0	834.1	834.95	834.6
	Peak 2	838.2	838.1	839.44	839.22
	Peak 3	850.9	836.4	837.23	837.05
	Peak 4	855.0	851.0	851.8	851.5
	Peak 5	853.0	855.0	856.29	855.97
	Peak 6	836.2	853.4	854.21	853.91
	La $3d_{5/2}$ splitting	4.1	4.0	4.5	4.6
	Spin coupling	16.8	16.9	16.8	16.9
O1*s*	Peak 1	529.2, 15913	529.2, 22031	529.4, 46689	530.2, 34509
	Peak 2	531.1, 20980	531.0, 32303	531.4, 34064	531.3, 37535
	Peak 3	533.3, 1540	533.1, 4718	533.9, 1349	533.4, 1516
	Peak 4	-	-	-	-

Table 4.3.2.4: *NAP-XPS deconvoluted peak positions and areas during in situ deN_2O of the sol-gel synthesised catalyst at Mn 2p, Mn 3s, La 3d and O 1s regions*

Sol-gel synthesised $LaMnO_3$		**RT vacuum**	**RT in N_2O**	**400˚C in N_2O**	**600˚C in N_2O**
Mn2*p*	Peak 1	641.6, 42127	641.4, 15869	641.3, 54139	641.3, 113016
	Peak 2	643.7, 14016	643.5, 15941	643.5, 40711	643.6, 67138
	Peak 3	653.3, 19832	653.4, 7762	653.1, 22587	653.0, 46964
	Peak 4	655.2, 6549	655.5, 3353	654.9, 17644	655.2, 35191
	Spin coupling	11.7	12.0	11.7	11.8
	Ratio Mn(III):Mn(IV)	3.0	1.0	1.3	1.7
Mn3*s*	Peak 1	-	83.33	83.08	83.11
	Peak 2	-	88.47	88.42	88.57
	Satellite	-	-	-	-
	Splitting	-	5.1	5.3	5.5
La3*d*	Peak 1	833.94	833.89	833.87	834.1
	Peak 2	838.1	838.08	838.19	838.44
	Peak 3	836.14	836.05	835.68	835.94
	Peak 4	850.77	850.68	850.73	850.95
	Peak 5	854.96	854.8	855.06	855.27
	Peak 6	852.97	852.73	852.6	852.79
	La $3d_{5/2}$ splitting	4.2	4.2	4.3	4.3
	Spin coupling	16.8	16.8	16.9	16.9
O1*s*	Peak 1	529.2, 10246	529.2, 6013	529.4, 30261	529.7, 66906
	Peak 2	531.0, 12478	531.3, 7440	531.3, 23633	531.2, 52792
	Peak 3	533.9, 1454	533.1, 2975	533.6, 3188	533.7, 1942
	Peak 4	-	-	-	-

The Mn 3*s* region provides complementary information, recorded at an increased kinetic energy of ~770 eV, for enhanced depth profiling. The splitting of the Mn 3*s* peak (Figure 4.3.24) at ~83.5 and ~88.5 eV (Table 4.3.2.2) is a final state effect due to the parallel and anti-parallel coupling between the spins of the remaining 3*s* electron and the 3*d* electrons.[57] On increasing oxidation state, i.e. a decrease of *d* electrons, the separation between these two peaks is known to decrease.[58] For the argon milled catalyst a Mn 3*s* peak splitting value of 5.1 eV is observed at RT in vacuum. This suggests a mixed Mn(IV)/Mn(III) valency, with literature reporting a peak splitting of 5.4 eV for Mn_2O_3 and 4.4 eV for MnO_2.[54,55] No change is observed for the Mn 3*s* peak splitting on the exposure to N_2O gas. However, on increasing temperature, this splitting increases to 5.4 eV, which is indicative of the Mn(III) oxidation state.[55] This increased depth-profiling observes the diffusion of sub-surface oxygen towards the exterior of the particle, which is responsible for the observed change in oxidation state.[48,59] Once this oxygen is closer to the surface it can then participate and aid with deN_2O.[60,61] With the mixed Mn(III) and Mn(IV) valences still observed at 600˚C at a lower depth penetration in the Mn 2*p* region it suggests this is a highly surface sensitive reaction.

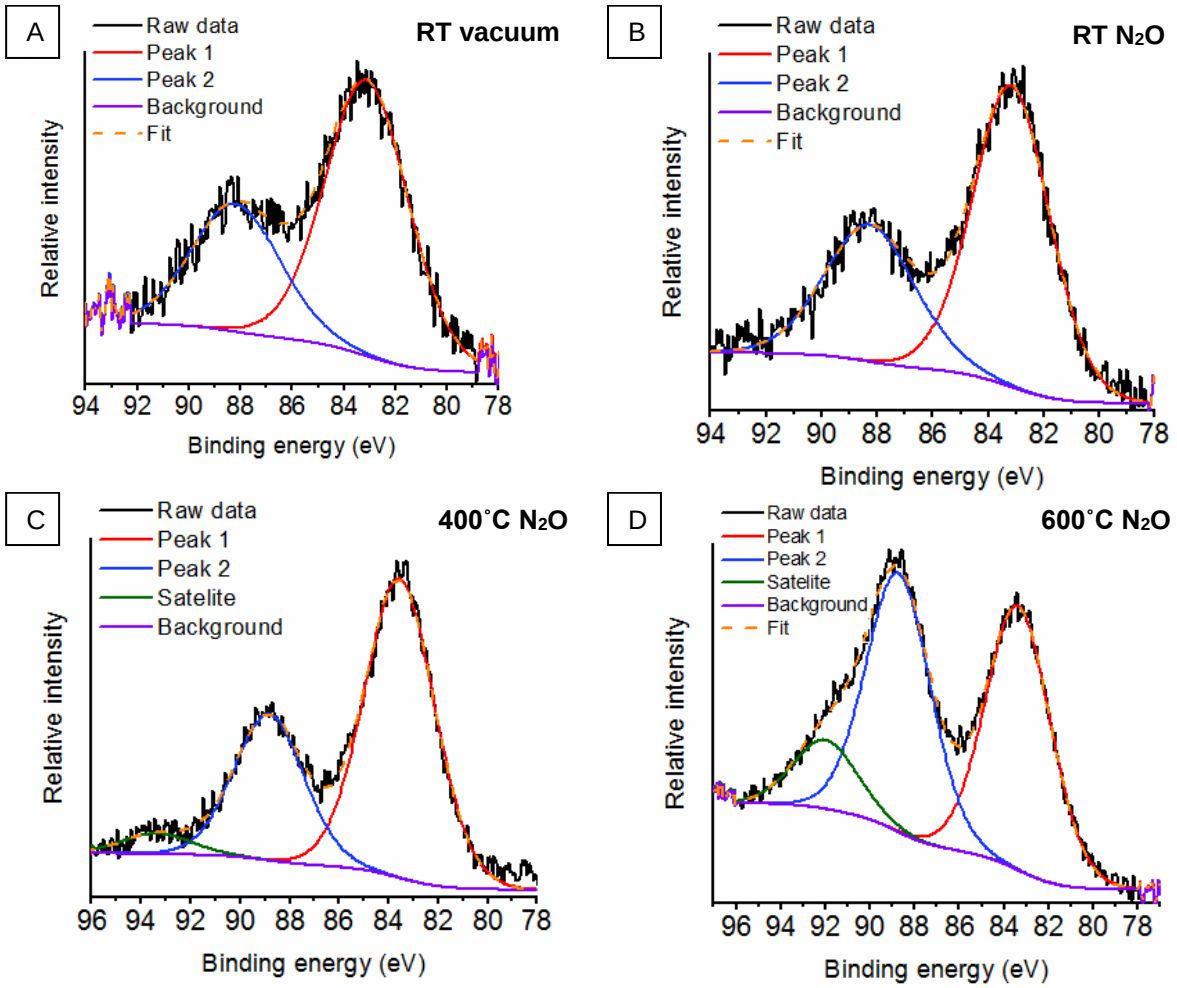

Figure 4.3.24: *NAP-XPS performed on the argon milled catalyst at the Mn 3s region at* ***(A)*** *RT in vacuum,* ***(B)*** *at RT under a N_2O atmosphere and then heated to* ***(C)*** *400˚C and* ***(D)*** *600˚C*

This surface sensitive approach has allowed for the detection of Mn(IV) species, previously not possible by bulk analysis of Mn K-edge HERFD-XANES. The presence of surface Mn(IV) is not expected the be reflected in the global average Mn oxidation state as a result of the low surface area, 4.2 – 7.8 m^2 g^{-1} of these perovskite catalysts.

This behaviour, of the Mn 3*s* splitting energy increasing as a result of elevated temperatures was also found for the other $LaMnO_3$ catalysts (Table 4.3.2.3 and Table 4.3.2.4) (Figure 4.3.25 and Figure 4.3.26). Understanding the Mn 2*p* and Mn 3*s* XPS regions highlights that, though the differently synthesised $LaMnO_3$ catalysts have varying surface properties, under working conditions there are similarities in how the Mn environment acts during deN_2O.

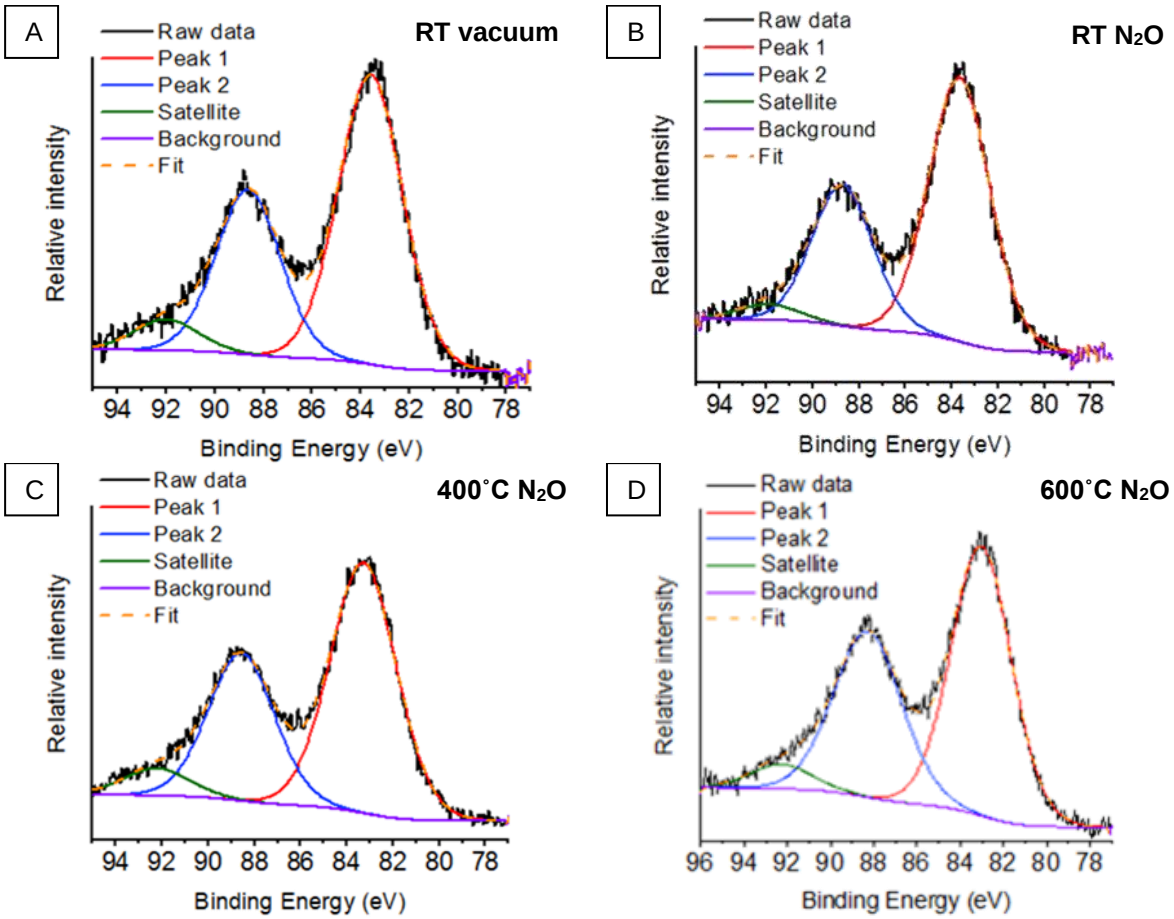

Figure 4.3.25: *NAP-XPS performed on the air milled catalyst at the Mn 3s region at* ***(A)*** *RT in vacuum, at* ***(B)*** *RT under a N_2O atmosphere and then heated to* ***(C)*** *400˚C and* ***(D)*** *600˚C*

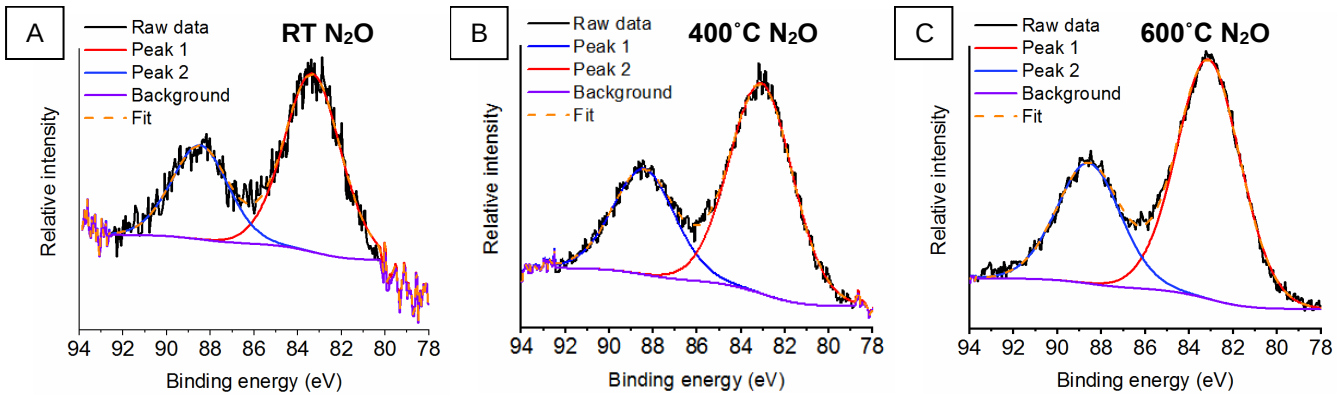

Figure 4.3.26: *NAP-XPS performed on the sol-gel $LaMnO_3$ catalyst at the Mn 3s region at* ***(A)*** *RT under a N_2O atmosphere and then heated to* ***(B)*** *400˚C and* ***(C)*** *600˚C*

The La 3*d* XPS region (Figure 4.3.27) shows the typical doublet splitting, with the lower energy doublet assigned to La $3d_{5/2}$ and the higher, La $3d_{3/2}$.[62] The peak splitting of the La $3d_{5/2}$ doublet has been used to understand the nature of the La species.[63] The asymmetric nature of the peaks within the La 3*d* region required three peaks to deconvolute each doublet.[64,65] For the argon milled catalyst, all the values of La $3d_{5/2}$ peak splitting during deN_2O are typical of La(III) compounds, which is further confirmed by the spin-orbit coupling values of 16.8 - 16.9 eV for all species (***Table 4.3.2.2***).[66] Initially, at RT under vacuum, the La$3d_{5/2}$ peak splitting of 3.9 eV is indicative of $La(OH)_3$ (Table 4.3.2.2). This is further confirmed by the presence of $La(OH)_3$ diffraction peaks in Figure 3.3.14. Increasing the

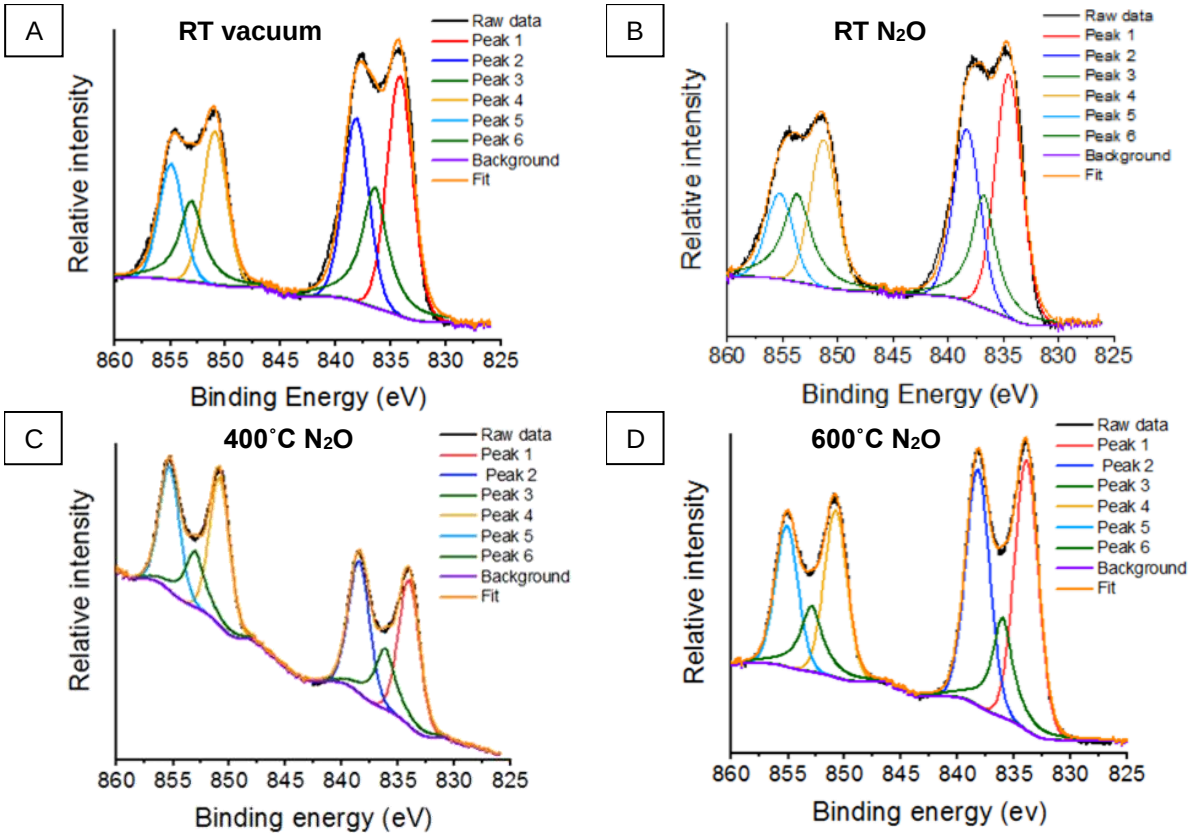

Figure 4.3.27: *La 3d region for the argon milled catalyst at* ***(A)*** *RT in vacuum,* ***(B)*** *RT under a N_2O atmosphere and then heated to* ***(C)*** *400˚C and* ***(D)*** *600˚C*

temperature during deN_2O results in an increase in the peak splitting value, indicative of the formation of an oxide species at the surface.[67]

Both the air milled and sol-gel $LaMnO_3$ start with a higher La 3$d_{5/2}$ splitting value of 4.1 eV and 4.2 eV respectively, compared to that of the argon milled catalyst; indicating a more oxide surface initially (Table 4.3.2.3 and Table 4.3.2.4) (Figure 4.3.28 and Figure 4.3.29).[68] The ball milled samples record a decrease in the La 3*d* splitting on exposure to N_2O (~ 0.1 eV). This could be indicative that the adsorbed N_2O is interacting with surface La species.

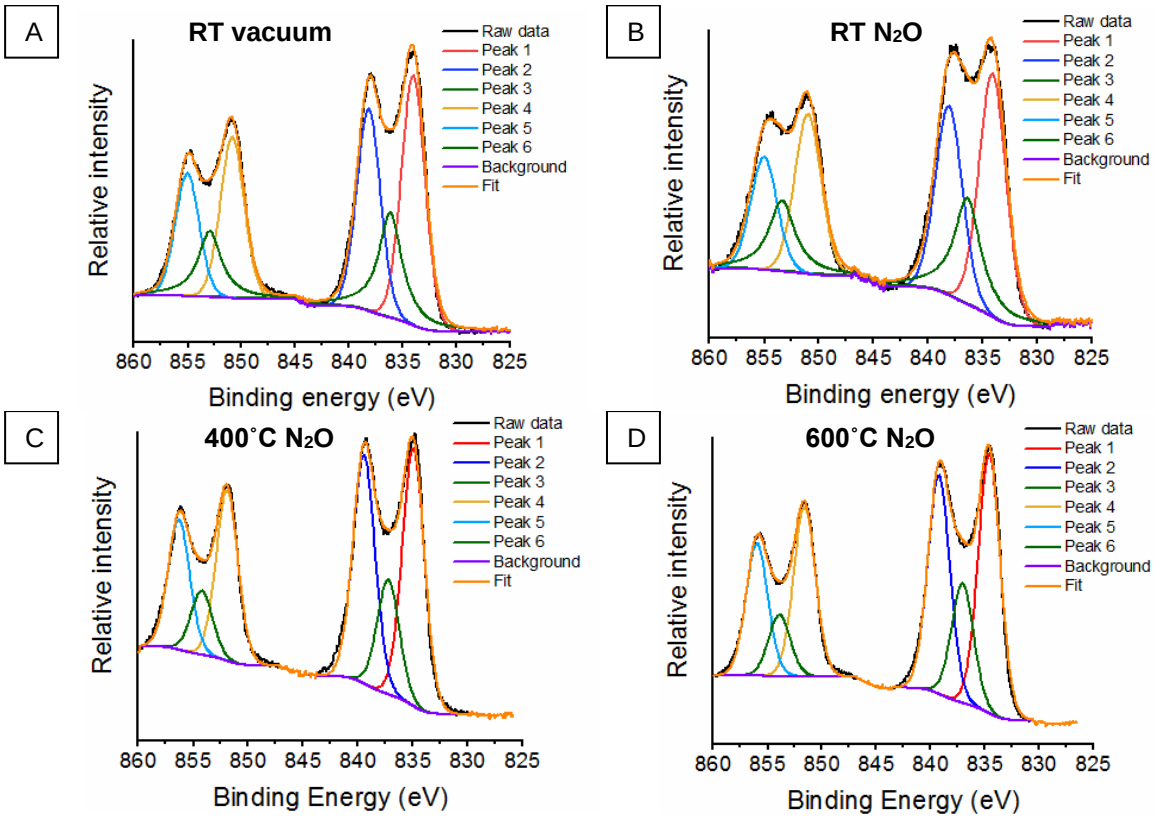

Figure 4.3.28: *La 3d region for the air milled catalyst at* ***(A)*** *RT in vacuum,* ***(B)*** *RT under a N_2O atmosphere and then heated to* ***(C)*** *400˚C and* ***(D)*** *600˚C*

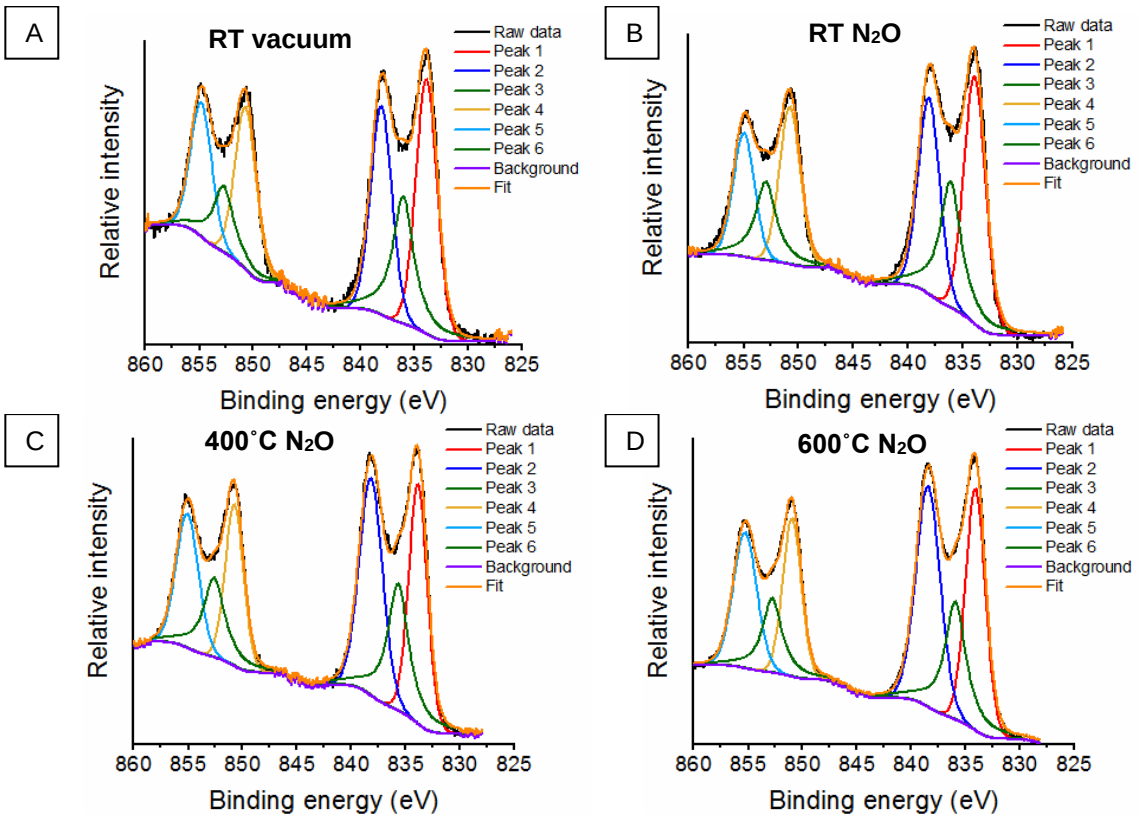

Figure 4.3.29: *La 3d region for the sol-gel synthesised catalyst at* ***(A)*** *RT in vacuum,* ***(B)*** *RT under a N_2O atmosphere and then heated to* ***(C)*** *400˚C and* ***(D)*** *600˚C*

Figure 4.3.30 shows the deconvoluted fitted peaks for the O 1*s* region in argon milled $LaMnO_3$ at RT under vacuum, on exposure to N_2O and then at subsequent heating to 400 ˚C and 600˚C. On deconvolution of the O 1*s* region three oxygen species can be identified (Table 4.3.2.2). In Table 4.3.2.2 and ***Figure 4.3.30***, peak 1 is assigned to lattice-type oxygens (O_2^{2-}), peak 2 to adsorbed species such as O_2^-, O^- or OH^- and peak 3 and 4 is associated with adsorbed adventitious carbon or molecular water.[56,66,69]

By monitoring *in situ* deN_2O by NAP-XPS clear changes can be observed within the O 1*s* region for the argon milled catalyst, which have not been previously reported. Whilst remaining at RT, on the introduction of N_2O an increase in the proportion of adsorbed species can be observed, along with the presence of a higher binding energy peak at 534.6 eV (***Figure 4.3.30***B). This indicative that N_2O has adsorbed on the surface at RT, in agreement with additional adsorbed species observed within the La 3*d* XPS data. A change in the area of peak 1, arising due to lattice-type oxygens, is observed on exposure to N_2O. This could indicate a possible rearrangement of the surface structure due to N_2O interaction. On increasing the temperature to 400 ˚C the surface adsorbed species decrease (Figure 4.3.30C). Further increase of the temperature to 600˚C (Figure 4.3.30D) shows a significant change in the peak shape, along with a 0.5 eV energy increase in the binding energy of peak 1. Here, the change in relative oxygen species abundance and peak positions could relate to either the hydrothermal removal of adsorbed oxygen species from the surface, as

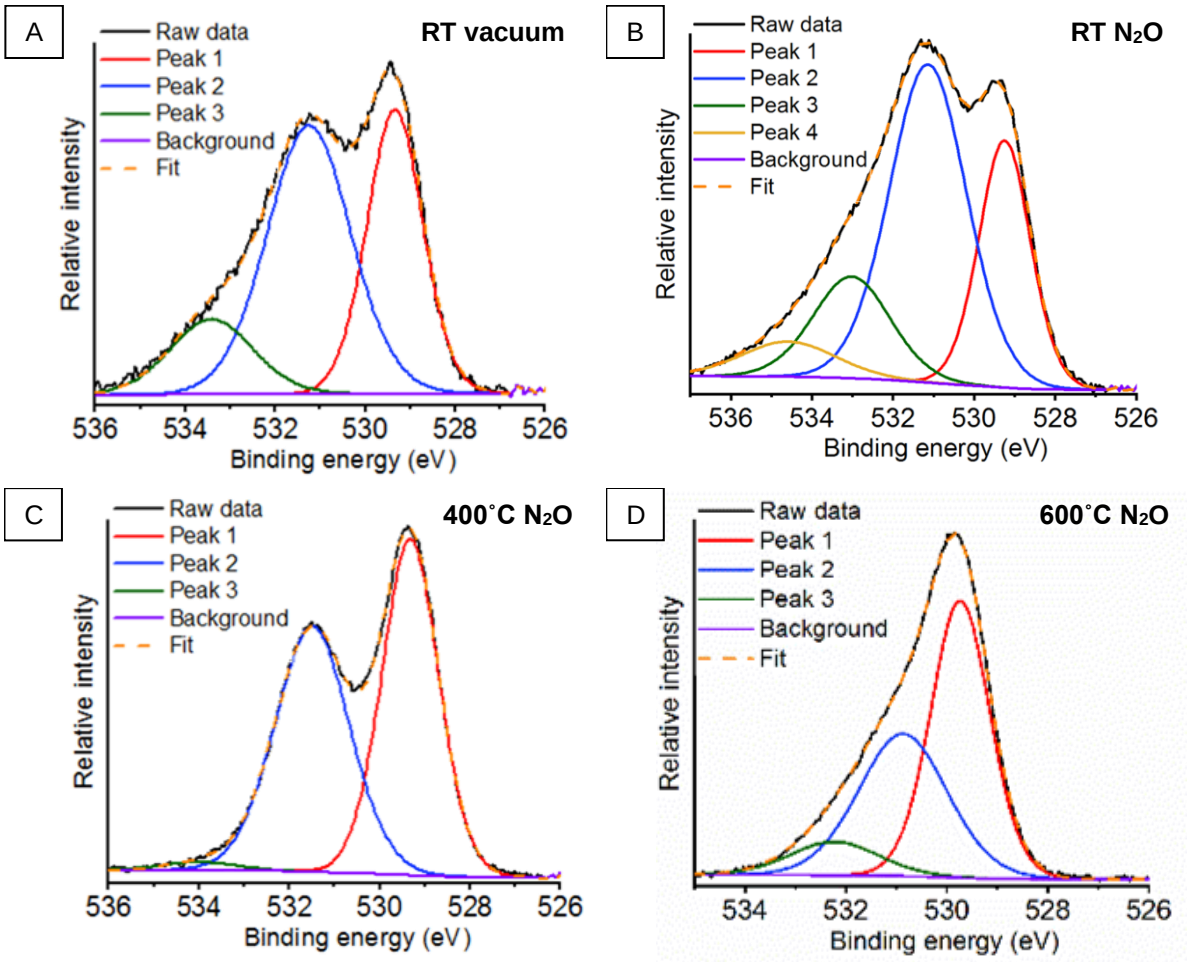

Figure 4.3.30: *O 1s region for the argon milled catalyst at* ***(A)*** *RT in vacuum,* ***(B)*** *RT under a N_2O atmosphere and then heated to* ***(C)*** *400˚C and* ***(D)*** *600˚C*

seen in the La 3*d* region (Table 4.3.2.2), or changes due to the Mn enivronment.[70,71] The Mn 2*p* and Mn 3*s* XPS data confirm that under these conditions the surface Mn species are relatively unchanged, whilst at greater depths oxygen is transferred towards the surface. Considering, that the O 1*s* data is acquired at the same depth penetration as the Mn 2*p*, it infers that the changes observed are correlated to changes in La speciation.

Both the air milled and sol-gel prepared $LaMnO_3$ also recorded a higher proportion of adsorbed species at the surface on exposure to N_2O (Table 4.3.2.3 and Table 4.3.2.4) (Figure 4.3.31 and Figure 4.3.32). Significantly, the air milled and sol-gel catalysts do not have peak 4, fitted at 534.6 eV for the argon milled $LaMnO_3$, present within the O 1*s* region. This suggests the increase in adsorbed N_2O species at the surface for the argon milled $LaMnO_3$ aids the deN_2O mechanism at lower temperatures, increasing the catalytic activity (Figure 4.3.12).[60,61] Furthermore, the air milled catalyst also suggests a rearrangement in surface structure due to exposure of N_2O, as a reduction in peak 1, corresponding to lattice-type oxygen, is observed.

The deN_2O catalytic testing observed an abrupt change to the light off profiles for the ball milled prepared samples that have been assigned to a phase transformation (Figure 4.3.12). This behaviour mirrors what is found in the O 1s XPS data; between 400˚C and 600˚C there are significant changes within the O 1s profile for the balled milled samples. Conversely, the sol-gel prepared $LaMnO_3$ shows a similar peak profile within the O 1s region at both 400˚C and 600˚C, suggesting a relatively stable oxygen environment.

Although the role of Mn towards the catalytic activity is clearly important, in this work the Mn 2*p* region shows minimal changes during deN_2O.[63] However, there are significant changes, within the La 3*d* and O 1*s* regions that have provided additional value in understanding the catalytic activity of these $LaMnO_3$ systems. Furthermore, variations within the *in situ* deN_2O NAP-XPS regions compared to the *ex situ* XPS reported in section 3.3.3 show the importance in tuning the incident beam in order to achieve equivalent data for each XPS region at the same penetration depth.

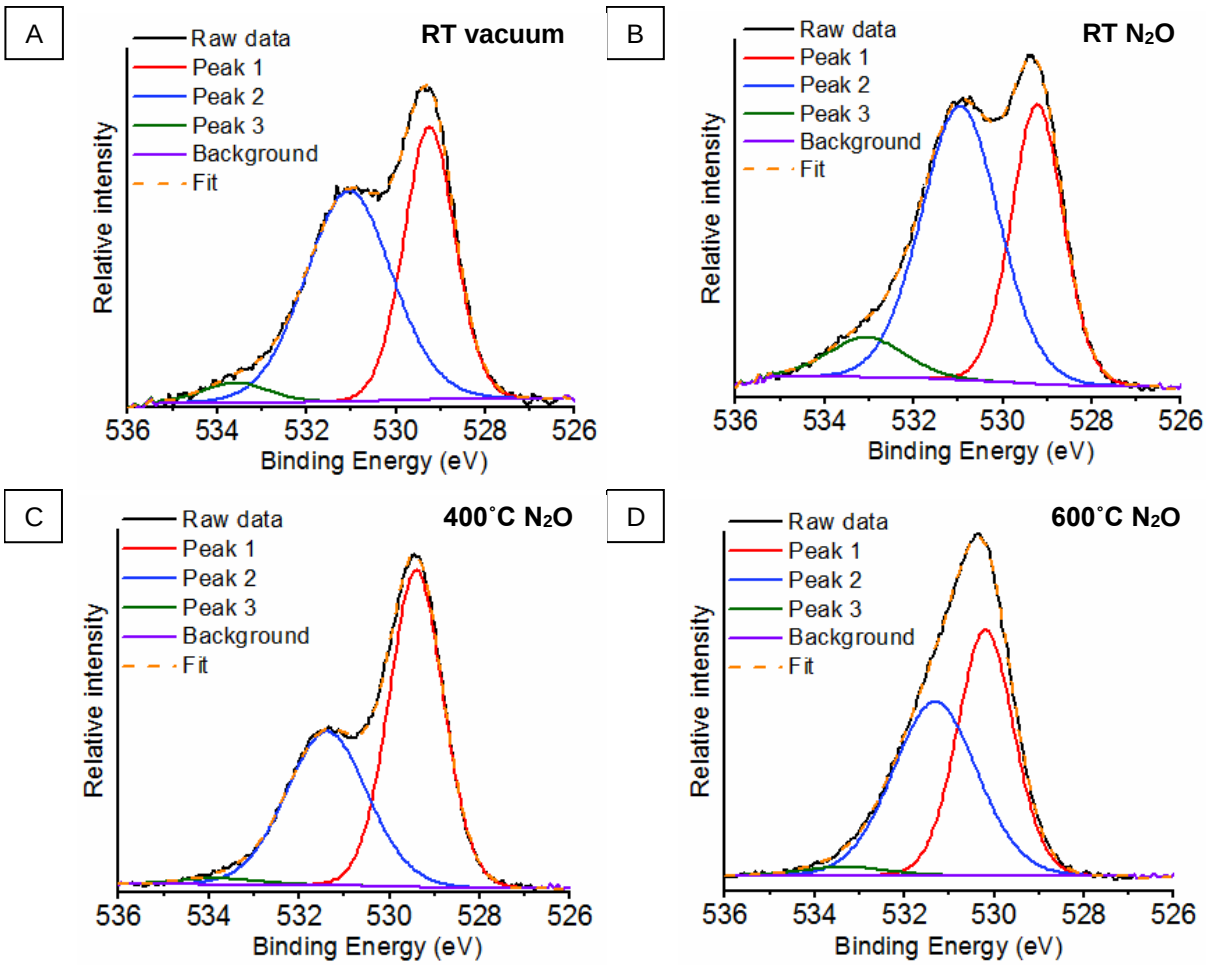

Figure 4.3.31: *O 1s region for the air milled catalyst at* ***(A)*** *RT in vacuum,* ***(B)*** *RT under a N_2O atmosphere and then heated to* ***(C)*** *400˚C and* ***(D)*** *600˚C*

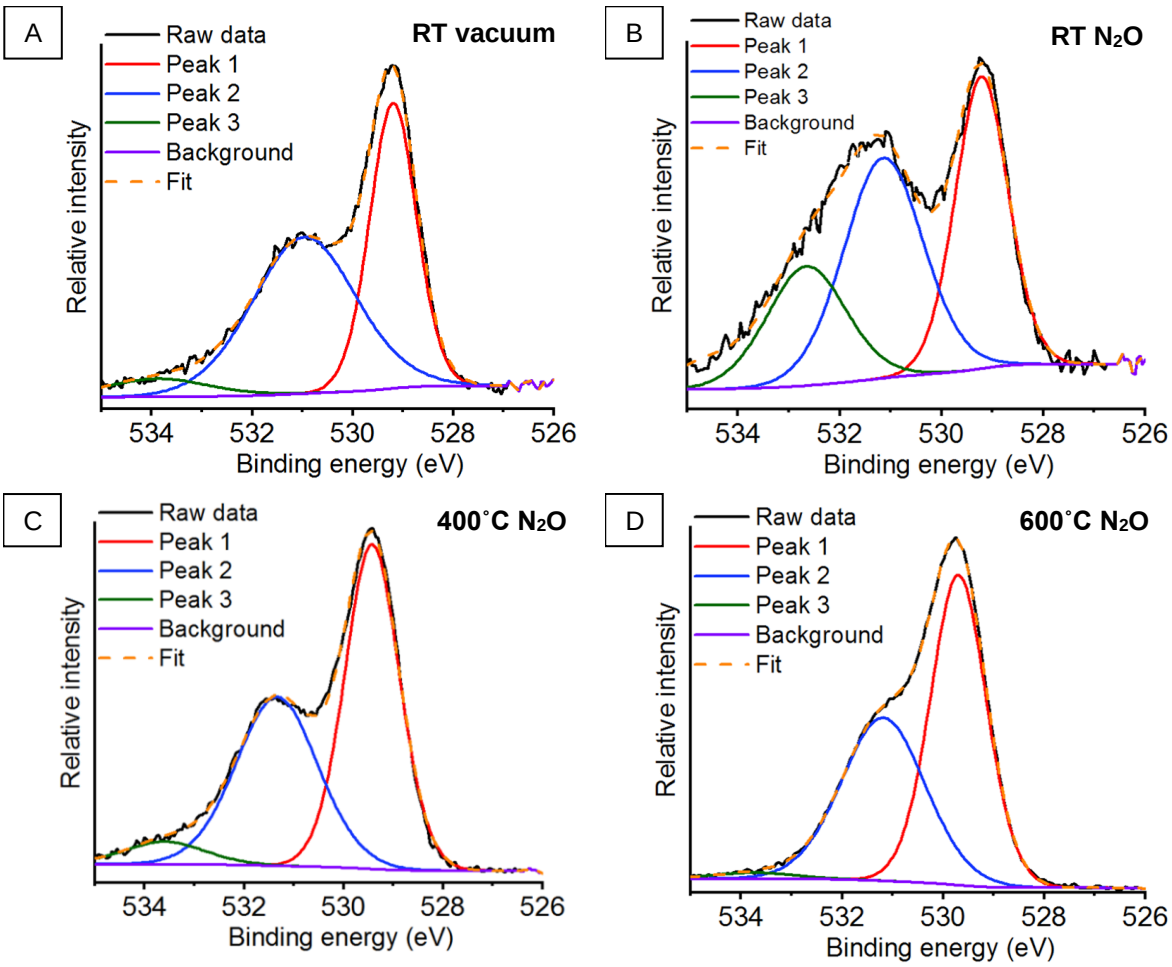

Figure 4.3.32: *O 1s region for the sol-gel synthesised catalyst at* ***(A)*** *RT in vacuum,* ***(B)*** *RT under a N_2O atmosphere and then heated to* ***(C)*** *400˚C and* ***(D)*** *600˚C*

4.4 Conclusions

This work successfully provided in-depth understanding into the electronic and geometric changes during the mechanochemical synthesis of $LaMnO_3$ under either air of argon milling atmospheres. By performing *ex situ* HERFD-XANES measurements on 'time-slices' during milling in air, Mn_2O_3 precursor features were successfully identified to decrease in the pre-edge region along with the evolution of peaks assigned to $LaMnO_3$. Similarities in the HERFD-XANES spectra were observed for the 'time-slices' under an argon environment, however, the final material still possessed some Mn_2O_3 character, in agreement with previous XRD studies. Significant alterations are observed within the ball milled perovskites which indicate disruption to the Mn-La coordination, specifically to the lack of Mn4*p* La5*d* hybridisation, in comparison to the sol-gel prepared $LaMnO_3$. XES performed at the Mn $K\beta_{1,3}$ emission line suggest a 'bulk' Mn(III) oxidation state throughout the mechanochemical synthesis for both milling atmospheres.

Efforts to perform *in situ* milling and to replicate the conditions experienced during milling by *in situ* high pressure experiments on La_2O_3 and Mn_2O_3 precursors were unable to induce any structural changes. This confirms that the mechanochemical synthesis of these metal oxide systems require high mechanical energies and is therefore extremely complicated to monitor *in situ*.

Though the argon milling environment decreased the proportion of crystalline $LaMnO_3$ after 4 h of milling it showed improved performance at lower temperatures compared to the air milled and sol-gel $LaMnO_3$. On monitoring *in situ* deN_2O by HERFD-XANES it was possible to deduce a specific catalytic intermediate which had similarities to the Mn(II) centre of Mn_3O_4. However, the bulk structural analysis of the all the $LaMnO_3$ catalysts reporting similar structures, indicating that the catalytic activity of deN_2O is strongly correlated to the proportion of oxygen vacancies recorded at the surface from *ex situ* XPS.

By performing *in situ* NAP-XPS deN_2O we were able to further this understanding of this improved catalytic activity whilst studying the different $LaMnO_3$ catalysts under working conditions. Within the O 1*s* region the argon milled catalyst showed a higher proportion of adsorbed species on exposure to N_2O at RT, indicating an increase interaction with this species. It also highlighted that all catalysts remained with a mixed Mn(III)/Mn(IV) valency, even at elevated temperatures of 600˚C whilst working under catalytic conditions.

This work, however, also demonstrates that even after the use of a large array of further advanced characterisation techniques (HERFD-XANES, XES and NAP-XPS) and modified equipment set-up (*in situ* milling and high pressure DAC) a proportion of ambiguity remains in understanding the structures of the ball milled material. Though these techniques have been successful within literature for more defined, crystalline materials, there is still a considerable amount of research required into understanding unknown complex and challenging structures, such as these produced by mechanochemistry.

4.5 References

1 R. H. Blackmore, M. E. Rivas, G. F. Tierney, K. M. H. Mohammed, D. Decarolis, S. Hayama, F. Venturini, G. Held, R. Arrigo, M. Amboage, P. Hellier, E. Lynch, M. Amri, M. Casavola, T. Eralp Erden, P. Collier and P. P. Wells, *Phys. Chem. Chem. Phys.*, 2020, **22**, 18774–18787.

2 J. F. Jenck, F. Agterberg and M. J. Droescher, *Green Chem.*, 2004, **6**, 544.

3 D. C. Koningsberger, B. L. Mojet, G. E. Van Dorssen and D. E. Ramaker, *Top. Catal.*, 2000, **10**, 143–155.

4 M. Newville, *J. Synchrotron Radiat.*, 2001, **8**, 322–324.

5 J. Evans, *X - Ray Absorption Spectroscopy for the Chemical and Materials Sciences*, John Wiley & Sons Ltd., 2017.

6 R. H. Blackmore, M. E. Rivas, T. E. Erden, T. D. Tran, H. R. Marchbank, D. Ozkaya, M. Briceno de Gutierrez, A. Wagland, P. Collier and P. P. Wells , *Dalt. Trans.*, 2020, **49**, 232–240.

7 S. Lafuerza, J. García, G. Subías, J. Blasco and P. Glatzel, *Phys. Rev. B*, 2016, **93**, 31–33.

8 F. De Groot, G. Vankó and P. Glatzel, *J. Phys. Condens. Matter*, , DOI:10.1088/0953-8984/21/10/104207.

9 P. Glatzel and U. Bergmann, *Coord. Chem. Rev.*, 2005, **249**, 65–95.

10 P. Glatzel, T. C. Weng, K. Kvashnina, J. Swarbrick, M. Sikora, E. Gallo, N. Smolentsev and R. A. Mori, *J. Electron Spectros. Relat. Phenomena*, 2013, **188**, 17–25.

11 J. A. Rodriguez, J. C. Hanson and P. J. Chupas, *In Situ Characterization of Heterogeneous Catalysts*, Wiley, 2013.

12 E. K. Dann, E. K. Gibson, C. R. A. Catlow, V. Celorrio, P. Collier, T. Eralp, M. Amboage, C. Hardacre, C. Stere, A. Kroner, A. Raj, S. Rogers, A. Goguet and P. P. Wells, *J. Catal.*, 2019, **373**, 201–208.

13 L. Zhong, D. Chen and S. Zafeiratos, *Catal. Sci. Technol.*, 2019, **9**, 3851–3867.

14 F. W. Lytle, G. H. Via and J. H. Sinfelt, *J. Chem. Phys.*, 1977, **67**, 3831–3832.

15 K. Užarević, I. Halasz and T. Friščić, *J. Phys. Chem. Lett.*, 2015, **6**, 4129–4140.

16 I. Halasz, S. A, J. Kimber, P. J. Beldon, A. M. Belenguer, F. Adams, V. Honkimäki, R. C. Nightingale, R. E. Dinnebier and T. Friščić, *Nat. Protoc.*, 2013, **8**, 1718–1729.

17 T. Frišči, I. Halasz, P. J. Beldon and A. M. Belenguer, *Nat. Chem.*, 2012, **5**, 66–73.

18 S. Hayama, G. Duller, J. P. Sutter, M. Amboage, R. Boada, A. Freeman, L. Keenan, B. Nutter, L. Cahill, P. Leicester, B. Kemp, N. Rubies and S. Diaz-Moreno, *J. Synchrotron Radiat.*, 2018, **25**, 1556–1564.

19 S. Limandri, S. Ceppi, G. Tirao, G. Stutz, C. G. Sánchez and J. A. Riveros, *Chem. Phys.*, 2010, **367**, 93–98.

20 T. A. Tyson, Q. Qian, C.-C. Kao, J.-P. Rueff, F. M. F. De Groot, M. Croft, S.-W. Cheong, M. Greenblatt and M. A. Subramanian, *Phys. Rev. B*, 1999, **60**, 4665–4674.

21 H. K. Mao, J. Xu and P. M. Bell, *J. Geophys. Res.*, 1986, **91**, 4673.

22 X. Hong, M. Newville, V. B. Prakapenka, M. L. Rivers and S. R. Sutton, *Rev. Sci.*

Instrum., 2009, **80**, 073908.

23 M. C. Biesinger, B. P. Payne, A. P. Grosvenor, L. W. M. Lau, A. R. Gerson and R. S. C. Smart, *Appl. Surf. Sci.*, 2011, **257**, 2717–2730.

24 D. Rybicki, M. Sikora, J. Przewoznik, C. Kapusta and J. F. Mitchell, *Phys. Rev. B*, 2018, **97**, 1–8.

25 F. Farges, *Phys. Rev. B - Condens. Matter Mater. Phys.*, 2005, **71**, 1–14.

26 D. C. Radu, P. Glatzel, W. M. Heijboer, J. H. Bitter, B. M. Weckhuysen and F. M. F. de Groot, *Mn and Fe Ions and Oxo clusters in ZSM-5: Pushing the limits of X-ray Spectroscopy*, Elsevier B.V., 2007, **170**.

27 L. A. Isupova, G. M. Alikina, S. V. Tsybulya, A. N. Salanov, N. N. Boldyreva, E. S. Rusina, I. A. Ovsyannikova, V. A. Rogov, R. V. Bunina and V. A. Sadykov, *Catal. Today*, 2002, **75**, 305–315.

28 V. Cuartero, S. Lafuerza, M. Rovezzi, J. García, J. Blasco, G. Subías and E. Jiménez, *Phys. Rev. B*, 2016, **94**, 1–10.

29 A. Y. Ignatov, N. Ali and S. Khalid, *Phys. Rev. B - Condens. Matter Mater. Phys.*, 2001, **64**, 1–16.

30 F. M. F. De Groot, S. Huotari, R. J. Cava, T. Lorenz and M. Reuther, *arXiv:0802.2744*, 1–7.

31 R. Baran, L. Valentin, J. M. Krafft, T. Grzybek, P. Glatzel and S. Dzwigaj, *Phys. Chem. Chem. Phys.*, 2017, **19**, 13553–13561.

32 S. D. Gamblin and D. S. Urch, *J. Electron Spectros. Relat. Phenomena*, 2001, **113**, 179–192.

33 M. A. Beckwith, M. Roemelt, C. Duboc, T. Weng, U. Bergmann, P. Glatzel, F. Neese and S. Debeer, *Inorg. Chem.*, 2011, 8397–8409.

34 G. Peng, F. M. F. Degroot, K. Hamalainen, J. A. Moore, X. Wang, M. M. Grush, J. B. Hastings, D. P. Siddons, W. H. Armstrong, O. C. Mullins and S. P. Cramer, *J. Am. Chem. Soc.*, 1994, **116**, 2914–2920.

35 M. Bauer, *Phys. Chem. Chem. Phys.*, 2014, **16**, 13827–13837.

36 A. J. Atkins, M. Bauer and C. R. Jacob, *Phys. Chem. Chem. Phys.*, 2013, **15**, 8095–8105.

37 G. Smolentsev, A. V. Soldatov, J. Messinger, K. Merz, T. Weyhermüller, U. Bergmann, Y. Pushkar, J. Yano, V. K. Yachandra and P. Glatzel, *J. Am. Chem. Soc.*, 2009, **131**, 13161–13167.

38 R. Schlögl, *Springer Ser. Chem. Phys.*, 2004, **75**, 321–360.

39 Y. Syono and S. Akimoto, *J. Phys. Soc. Japan*, 1969, **26**, 993–999.

40 J. A. M. Van Roosmalen, P. van Vlaanderen and E. H. P. Cordfunke, *J. Solid State Chem.*, 1995, **114**, 516–523.

41 E. Boldyreva, *Chem. Soc. Rev.*, 2013, **42**, 7719–7738.

42 J. Kowalska and S. DeBeer, *Biochim. Biophys. Acta - Mol. Cell Res.*, 2015, **1853**, 1406–1415.

43 E. Gallo and P. Glatzel, *Adv. Mater.*, 2014, **26**, 7730–7746.

44 U. Bergmann, C. R. Horne, T. J. Collins, J. M. Workman and S. P. Cramer, *Chem. Phys. Lett.*, 1999, **302**, 119–124.

45 C. J. Pollock and S. DeBeer, *Acc. Chem. Res.*, 2015, **48**, 2967–2975.

46 C. J. Pollock, K. M. Lancaster, K. D. Finkelstein and S. Debeer, *Inorg. Chem.*, 2014, **53**, 10378–10385.

47 J. Singh, C. Lamberti and J. A. Van Bokhoven, *Chem. Soc. Rev.*, 2010, **39**, 4754–4766.

48 H. Najjar, J. F. Lamonier, O. Mentré, J. M. Giraudon and H. Batis, *Appl. Catal. B Environ.*, 2011, **106**, 149–159.

49 S. Royer, D. Duprez and S. Kaliaguine, *Catal. Today*, 2006, **112**, 99–102.

50 C. Escudero, P. Jiang, E. Pach, F. Borondics, M. W. West, A. Tuxen, M. Chintapalli, S. Carenco, J. Guo and M. Salmeron, *J. Synchrotron Radiat.*, 2013, **20**, 504–508.

51 N. H. Turner, *Anal. Chem.*, 1986, **58**, 153–165.

52 S. Jaiswar and K. D. Mandal, *J. Phys. Chem. C*, 2017, **121**, 19586–19601.

53 A. J. Nelson, J. G. Reynolds and J. W. Roos, *J. Vac. Sci. Technol. A Vacuum, Surfaces, Film.*, 2000, **18**, 1072–1076.

54 M. A. Stranick, *Surf. Sci. Spectra*, 1999, **6**, 31–38.

55 M. A. Stranick, *Surf. Sci. Spectra*, 1999, **6**, 39–46.

56 V. P. Santos, M. F. R. Pereira, J. J. M. Órfão and J. L. Figueiredo, *Appl. Catal. B Environ.*, 2010, **99**, 353–363.

57 D. J. Lam, B. W. Veal and D. E. Ellis, *Phys. Rev. B*, 1980, **22**, 5730–5739.

58 V. R. Galakhov, M. Demeter, S. Bartkowski, M. Neumann, N. A. Ovechkina, E. Z. Kurmaev, N. I. Lobachevskaya, Y. M. Mukovskii, J. Mitchell and D. L. Ederer, *Phys. Rev. B*, 2002, **65**, 1–4.

59 A. Staykov, H. Téllez, T. Akbay, J. Druce, T. Ishihara and J. Kilner, *Chem. Mater.*, 2015, **27**, 8273–8281.

60 T. A. Egerton, F. S. Stone and J. C. Vickerman, *J. Catal.*, 1974, **33**, 307–315.

61 F. Kapteijn, J. Rodriguez-Mirasol and J. A. Moulijn, *Appl. Catal. B Environ.*, 1996, **9**, 25–64.

62 R. Dudric, A. Vladescu, V. Rednic, M. Neumann, I. G. Deac and R. Tetean, *J. Mol. Struct.*, 2014, **1073**, 66–77.

63 T. S. Kharlamova, A. S. Matveev, A. V. Ishchenko, A. N. Salanov, S. V. Koshcheev, A. I. Boronin and V. A. Sadykov, *Kinet. Catal.*, 2014, **55**, 361–371.

64 D. F. Mullica, C. K. C. Lok, H. O. Perkins and V. Young, *Phys. Rev. B*, 1985, **31**, 4039–4042.

65 M. F. Sunding, K. Hadidi, S. Diplas, O. M. Løvvik, T. E. Norby and A. E. Gunnæs, *J. Electron Spectros. Relat. Phenomena*, 2011, **184**, 399–409.

66 A. Machocki, T. Ioannides, B. Stasinska, W. Gac, G. Avgouropoulos, D. Delimaris, W. Grzegorczyk and S. Pasieczna, *J. Catal.*, 2004, **227**, 282–296.

67 Y. Zhang-Steenwinkel, J. Beckers and A. Bliek, *Appl. Catal. A Gen.*, 2002, **235**, 79–92.

68 M. E. Rivas, C. E. Hori, J. L. G. Fierro, M. R. Goldwasser and A. Griboval-Constant, *J. Power Sources*, 2008, **184**, 265–275.

69 K. Jirátová, J. Mikulová, J. Klempa, T. Grygar, Z. Bastl and F. Kovanda, *Appl. Catal. A Gen.*, 2009, **361**, 106–116.

70 J. G. Kang, Y. Il Kim, D. Won Cho and Y. Sohn, *Mater. Sci. Semicond. Process.*, 2015, **40**, 737–743.

71 P. Fleming, R. A. Farrell, J. D. Holmes and M. A. Morris, *J. Am. Ceram. Soc.*, 2010, **93**, 1187–1194.

Chapter 5

Understanding the effect of different A-sites on the mechanochemical synthesis of manganite perovskites, $AMnO_3$

5.1 Introduction

Throughout this project an in-depth understanding of mechanochemistry has been explored as an alternative, novel preparation route for a $LaMnO_3$ catalyst. Previously, we have reported the advantages of performing advanced characterisation techniques such as X-ray absorption spectroscopy (XAS) on *ex situ* 'time-slices' throughout the mechanochemical synthesis, which allows for the analysis of both the amorphous and crystalline content; it does not rely on periodic ordering and, therefore, ideally suited to materials produced via ball milling.[1] XAS was able to highlight the ease at which La_2O_3 is able to disperse over Mn_2O_3, with noticeable changes visible in the La L_3 edge EXAFS data at the early stages of milling, previously not possible by lab-based X-ray diffraction (XRD). However, can we now start to apply this in-depth understanding of the $LaMnO_3$ mechanochemical synthesis to the preparation of different A-site manganite perovskites? By fully understanding the synthetic route, we can, in turn, begin to have a greater control over properties of the final milled materials.

In this chapter different A-site precursor oxides, Er_2O_3 and Y_2O_3, have been selected to understand and follow their mechanochemical synthesis to $ErMnO_3$ or $YMnO_3$. These manganite materials are well documented throughout the field of solid-state physics, where they are of great interest due to their ferroelectric and magnetic behaviour.[2] Both these perovskites can exist as two different polymorphs, hexagonal (*h*) and orthorhombic (*o*), with their formation highly dependent on the synthetic route chosen. Here, the hexagonal phase can be ascribed as layers of MnO_5 trigonal bipyramids, with the A cation positioned in between, coordinated to 7 oxygens (Figure 5.1.1A). Whereas, the orthorhombic structure consists of distorted MnO_6 octahedra's, 8-fold A ion coordination (Figure 5.1.1B).[2,3] Considering only the Er and Y ionic radii for calculating the Goldschmidt tolerance factor (discussed in section 1.3, Equation 1.3.1) to deduce the most stable geometry is insufficient

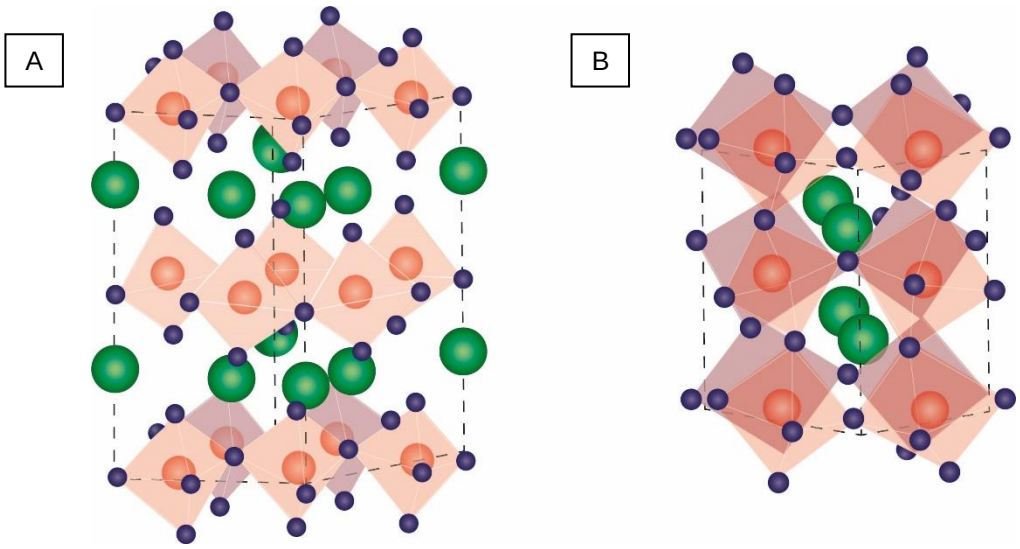

Figure 5.1.1: *Diagram to depicting* ***(A)*** *hexagonal and* ***(B)*** *orthorhombic structures for $AMnO_3$ species, where green is the large A cation, red is Mn and green is oxygen*

as a result of their comparable ionic radii, at 0.089 nm and 0.090 nm, respectively.[4] Yet, commonly it is the *h*-$AMnO_3$ phase that forms on crystallisation, with instability of the o-$AMnO_3$ structure suggested to originate from Jahn-Teller distortion of the Mn(III) ion, thus lowering the tolerance factor.[5]

Traditionally, single metal oxide precursors can be used to synthesise perovskites via the ceramic method, by annealing at elevated temperatures, 1100 – 1400 ˚C, for extended periods of time to form the $AMnO_3$ phase.[6,7] A sol-gel Pechini or citric acid synthetic route can be used for the preparation of these manganite perovskites from single metal nitrates, however, it requires a final high temperature calcination step (>850˚C), determined by the choice of A-site oxide.[3,8–11] Though lowering the overall temperature, this wet chemistry approach still requires the use of solvents, waste treatment, with multiple process culminating in an overall high energy input.

Recently, $ErMnO_3$ and $YMnO_3$ have been known to form via mechanochemistry from their respective single metal oxides precursors at room temperature. This alternative synthetic route has been found to synthesise the metastable *o*-$AMnO_3$ species at ambient conditions without the use of elevated pressures.[5,12,13] This literature, however, reports varying milling conditions in order to produce both $ErMnO_3$ and $YMnO_3$ perovskite phases, as well as for $LaMnO_3$.[14,15] It is generally considered that mechanochemical reactions are significantly different to thermal transformations, which is further confirmed by the formation of a different final geometric phase. However, with milling causing localised pressure and thermal conditions resulting from high impact collisions, temperature cannot be fully ignored.[16] Do the annealing temperatures of different perovskite materials translate directly to the mechanochemical synthesis?

In this work, once again, XAS has been utilised to provide a more in-depth understanding of these perovskite systems, alongside XRD, TEM and XPS studies. By

exploring the mechanochemical synthesis of different A-site manganite perovskites this work aims to further this area of mechanochemical synthesis catalysts and to expand the knowledge of the chemical steps involved in the process. In doing so, we hope to understand more of than just the unique chemistry associated with each precursor but to begin to build a genialised idea of the mechanochemical synthesised of manganite perovskites.

5.2 Material and methods

5.2.1 $AMnO_3$ Sample Preparation

The mechanochemical synthesis of both $ErMnO_3$ and $YMnO_3$ mixed metal oxides was conducted using manganese (III) oxide (Alfa Aesar, 98.0 %) with either erbium (III) oxide (Alfa Aesar 99.9%) or yttrium (III) oxide (Strem UK 99.99%) precursors. These samples were prepared using a Retsch 2–station Planetary Ball Mill, PM200 with 125 mL ZrO_2 grinding jars, at the Research complex, Harwell, UK. Measurements of Mn_2O_3 (2.10 g) and Er_2O_3 (2.94 g) starting materials were used in order to synthesise stoichiometric $ErMnO_3$ (5 g), with Mn_2O_3 (1.49 g) and Y_2O_3 (3.54 g) calculated for $YMnO_3$ (5 g). Experiments were either run with 5 mm or 10 mm yttria-stabilised zirconia (YTZ®) milling media, with the media weight ratio to the total precursor powder kept constant at of 10:1. The mill was operated at room temperature at 400 rpm for 6 hours. Note, that a separate jar was milled for each 'time-slice'.

$ErMnO_3$ and $YMnO_3$ were also prepared by the sol-gel Pechini method, comparatively to $LaMnO_3$ sol-gel synthesis (section 3.2.1).[17] Stoichiometric ratios of manganese (II) nitrate tetrahydrate (Alfa Aesar, 98 %) and either Erbium (III) nitrate hydrate (Strem UK, 99.9 %) or Yttrium (III) nitrate hexahydrate (Strem UK, 99.9 %) were used to form a gel. This material was then dried at 200 ^oC for 1 hour and further calcined at 700 ^oC for 4 hours with a ramp of 0.5 $^oC\ min^{-1}$. The subsequent powders were then heated at 800 ˚C, 900 ˚C or 1000 ˚C for 20 h to provide temperature studies for the formation of crystalline $AMnO_3$ phases.

5.2.2 Characterisation

Ex situ **X-ray diffraction (XRD)** patterns were collected as discussed in section 3.2.2.

For *in situ* heating experiments monitored by XRD, the diffraction data was collected using a Bruker D8 advanced with the sample contained within an Anton Paar XRK900 reaction chamber, at Johnson Matthey, Sonning Common, UK. Under an atmosphere of 20% O_2 in N_2 heat treatment was performed from 30 – 870 ˚C, with data collected every 20 ˚C. Phase identification was performed using Bruker DIFFRA.EVA V4.2 on the initial observation of crystalline material and on the final diffraction pattern. Peak fitting and refinement of appropriate .cifs to the data was performed using the Reitveld method on Bruker DIFFRA.TOPAS V4.2.

The **specific surface area analysis**, determined by the Brunauer-Emmett-Teller (BET) method, was performed by krypton adsorption, using a Quantachrome Autosorb iQ "E" at Johnson Matthey, Sonning, UK. Samples were initially heated to 523 K under vacuum for 90 min to remove any absorbed species on the surface before gas adsorption/desorption experiments began. The krypton adsorption/ desorption measurements were then performed at 77 K, achieved using liquid N_2, with relative pressure of P/P_0 = 0.175.

Transmission electron microscopy (TEM) samples were prepared as previously stated in section 3.2.2 by the Johnson Matthey analytical department. Using a JEM 2800 (Scanning) Transmission Electron Microscope the same instrumental conditions were applied: voltage (kV) 200; C2 aperture (um) 70 and 40.

X-ray Absorption Spectroscopy (XAS) measurements were conducted on the B18 Beamline, Diamond Light Source, UK. XAS measurements were performed at the Mn K-edge (6539 eV), Er L_3-edge (8358 eV) and Y K-edge (17038 eV) in transmission mode using QEXAFS setup with fast scanning Si(111) double crystal monochromator. All XAS spectra at the Mn K-edge, Er L_3-edge and Y K-edge were acquired with a time resolution of 20 min per spectrum (k_{max}= 15) averaged over 3 scans. Data processing was performed using IFEFFIT[18] with Horae package[19] (Athena and Artemis), with the amplitude reduction factor, S_0^2, derived using an appropriate reference spectra foil of known coordination numbers. The *ex situ* samples were prepared as 13 mm pressed pellets on homogenous mixing with cellulose, which allowed for an appropriate concentration.

5.2.3 Catalytic testing

Catalytic testing. N_2O decomposition (deN_2O) was performed on a Hiden CATLAB fixed-bed reactor as previously ascribed in section 3.2.3.

5.3 Results and discussion

5.3.1 The preparation of $AMnO_3$ (Er, Y) via mechanochemical synthesis

The same experimental procedure that was previously successful for the preparation of $LaMnO_3$ (section 3.2.1) was applied to both $ErMnO_3$ and $YMnO_3$, in order to attempt their mechanochemical synthesis.[1] XRD studies have initially been performed to assess the long-range structural changes at 'time-slices' during the milling of either Er_2O_3 or Y_2O_3 with Mn_2O_3 (Figure 5.3.1A and B, respectively).

XRD. For both materials clear structural alterations are observed on milling for just 1 h. The low intensity, broad peaks in the XRD indicates the formation of highly amorphous and disordered materials (Figure 5.1.1). On increasing the milling time to 6 h, the lack of diffraction peaks and presence of a low intensity broad 'halo' feature at 2θ = ~32˚ suggests the presence of fine crystallite sizes or highly amorphous material that lacks any long range order.[13,20] As a consequence Rietveld refinement could not be performed. These attributes are a common consequence during the mechanochemical synthesis of mixed metal oxide systems, whereby the chemical steps are suggested to proceed as: particle size reduction, amorphization, formation of new metaphases and then crystallisation.[21,22] The XRD data for both Er and Y A-site metal oxides suggests that even after 6 h of milling, using 5 mm milling media, there is insufficient mechanical energy for the evolution of a crystalline perovskite ($ErMnO_3$ and $YMnO_3$) phase. This differs considerably from the $LaMnO_3$ system, whereby after 2 h of milling perovskite Bragg peaks were first detected, with 100% of the crystalline content $LaMnO_3$ after 3 h.

Another clear alteration is that on milling under atmospheric conditions for both the Er and Y milled 'time-slices' there is no formation of their hydroxide state; $La(OH)_3$ was detected at time 0 h and at milling intervals during the mechanochemical synthesis of

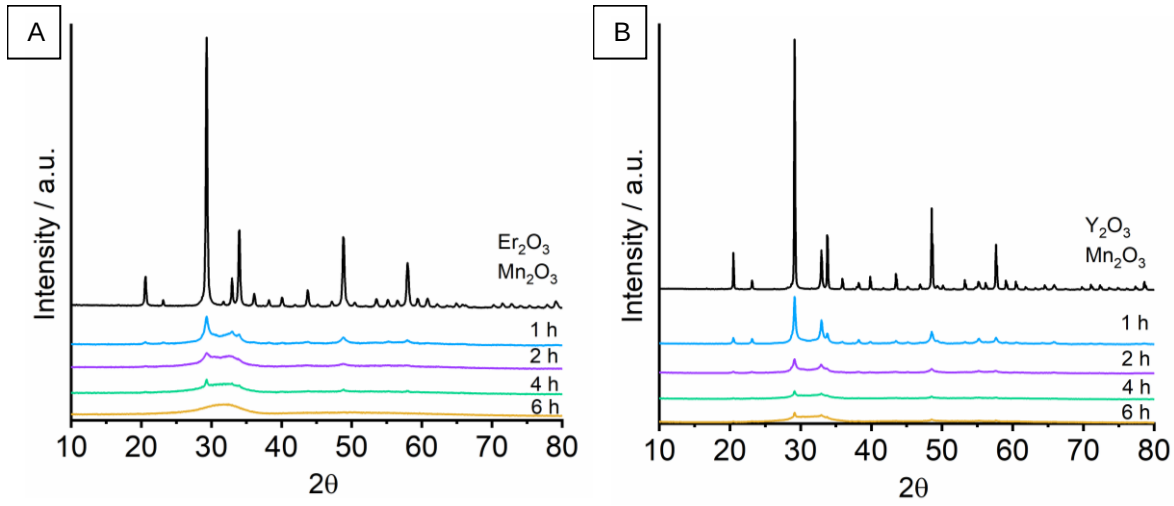

Figure 5.3.1: *XRD patterns after milling Mn_2O_3 with either* ***(A)*** *Er_2O_3 or* ***(B)*** *Y_2O_3 with 5mm milling media at 0, 2, 4 and 6 h 'time-slices'*

$LaMnO_3$ (section 3.3.1). This can be attributed to the large, diffuse radius of the La ion resulting in an overall low lattice energy (U) for the La_2O_3 species. With the XRD indicating that both Er_2O_3 and Y_2O_3 do not promote the absorption of moisture on exposure to air, it confirms they possess a greater lattice stability, or U, as a result of their lower ionic radii size.[4,23]

5.3.2 $AMnO_3$ sol-gel synthesis

In order to compare the milled materials to a crystalline reference perovskite sample, the analogous $AMnO_3$ (A=Er,Y) have been prepared by the Pechini sol-gel method.[17] After annealing the separate gel mixtures at 700 ˚C for 4 h (as performed for $LaMnO_3$) a variety of phases were detected by Rietveld refinement (Figure 5.3.2); Mn_2O_3, Er_2O_3 and *h*-$ErMnO_3$, and Y_2O_3 and *h*-$YMnO_3$. Only a maximum weight percentage of 51.2 wt% and 67.7 wt% was calculated as crystalline *h*-$ErMnO_3$ or *h*-$YMnO_3$, respectively.

Separate systematic heat treatments were then completed after the 700 ˚C calcination on the sol-gel materials at 800, 900 and 1000 ˚C (Figure 5.3.2). After heating to 800 and 900 ˚C an additional phase, AMn_2O_5, was detected for both Er and Y, causing an overall decrease in the wt% of $AMnO_3$. On increasing the temperature to 1000 ˚C, the AMn_2O_5 intermediate decomposes and a 100% *h*-$AMnO_3$ crystalline phase achieved; a 300 ˚C increase compared to $LaMnO_3$. This increase in temperature required to form the perovskite phase from Er and Y ions, compared to La, is dependent on the ionic radius size. Literature reports that a decrease in the ion radius for rare-earth metals is coupled with an increase in the required calcination temperature to achieve the perovskite phase.[2,24] Here, the ionic radii decrease in the order La (104 pm) > Y (90 pm) > Er (89 pm), corresponding well with the final annealing temperatures used on the sol-gel materials.[4] The presence of some *o*-$ErMnO_3$ could indicate a higher stability for the orthorhombic phase, in comparison to *o*-$YMnO_3$ species.

With both the sol-gel and mechanochemical synthesis routes unable to achieve $ErMnO_3$ and $YMnO_3$ phases under the same experimental conditions as for $LaMnO_3$, it can begin to suggest there are comparable underlying parameters that govern manganite perovskite formation. However, it is important to remember that mechanochemical reactions proceed via a different route to purely thermal treatments, *i.e.* by shear, stress, compression or friction, to produce metastable products.[16]

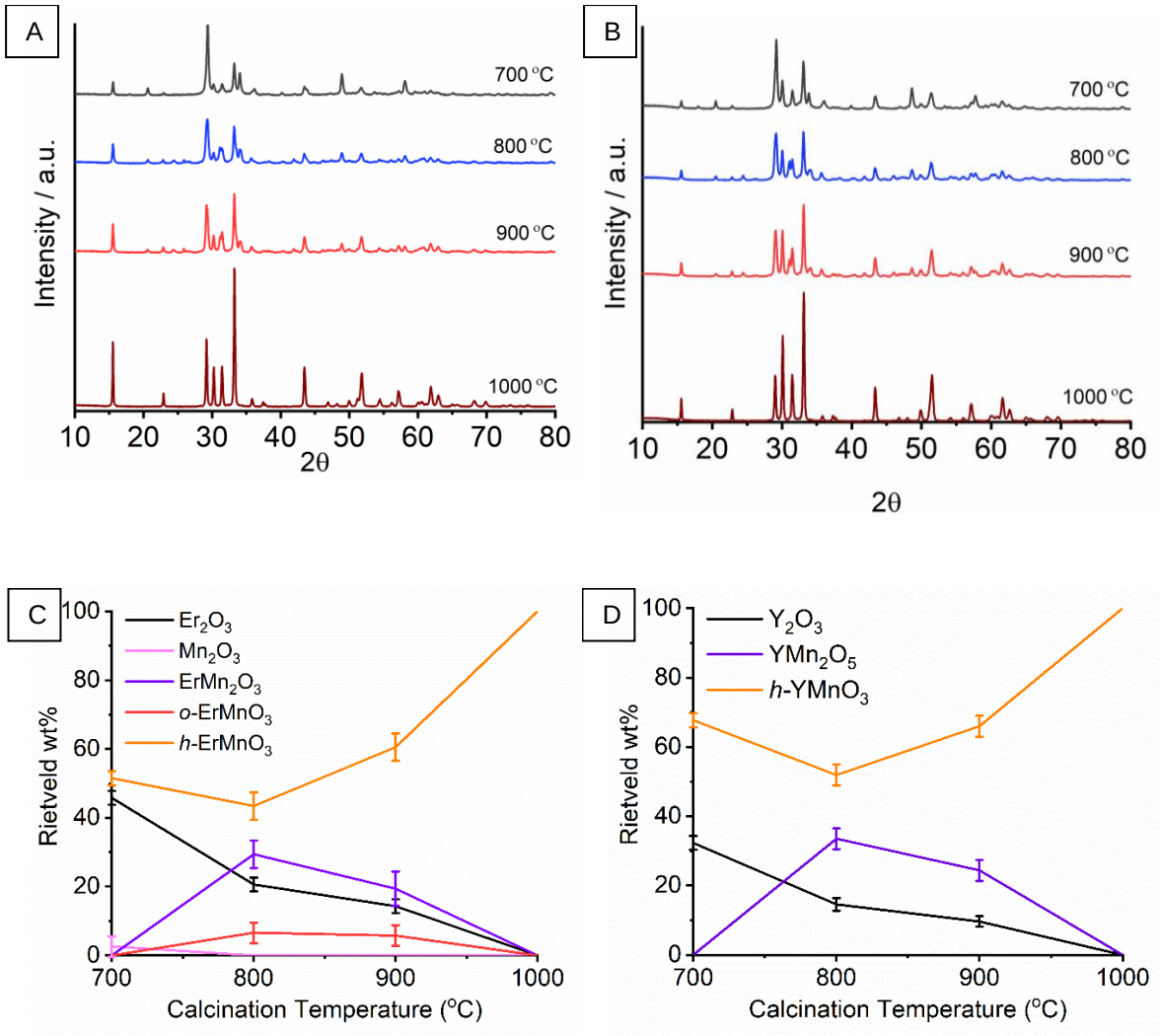

Figure 5.3.2: *XRD patterns for systematic heat treatments for sol-gel synthesised* ***(A)*** *$ErMnO_3$ and* ***(B)*** *$YMnO_3$ with their respective Rietveld wt%* ***(C)*** *$ErMnO_3$ and* ***(D)*** *$YMnO_3$*

5.3.3 *In situ* calcination of milled materials

To achieve a perovskite phase from the 5 mm media milled materials lab-based *in situ* XRD experiments have been performed on both $AMnO_3$ (A = Er and Y) 6 h milled samples (Figure 5.3.3A,C). On heating in a near ambient atmosphere crystalline material was first detected at 730 ˚C. Whilst a 100% of *o*-$ErMnO_3$ crystalline was detected at 730 and 870 ˚C, at 870 ˚C only 80.1% crystalline *o*-$YMnO_3$ was calculated by Rietveld refinement. In order to acquire a larger batch of material, a separate heat treatment was performed on the 6 h milled materials in a muffle furnace for 20 h at 800 ˚C. Here, XRD records 100% *o*-$ErMnO_3$ and 94.0 % *o*-$YMnO_3$ orthorhombic crystalline phases (Figure 5.3.4).

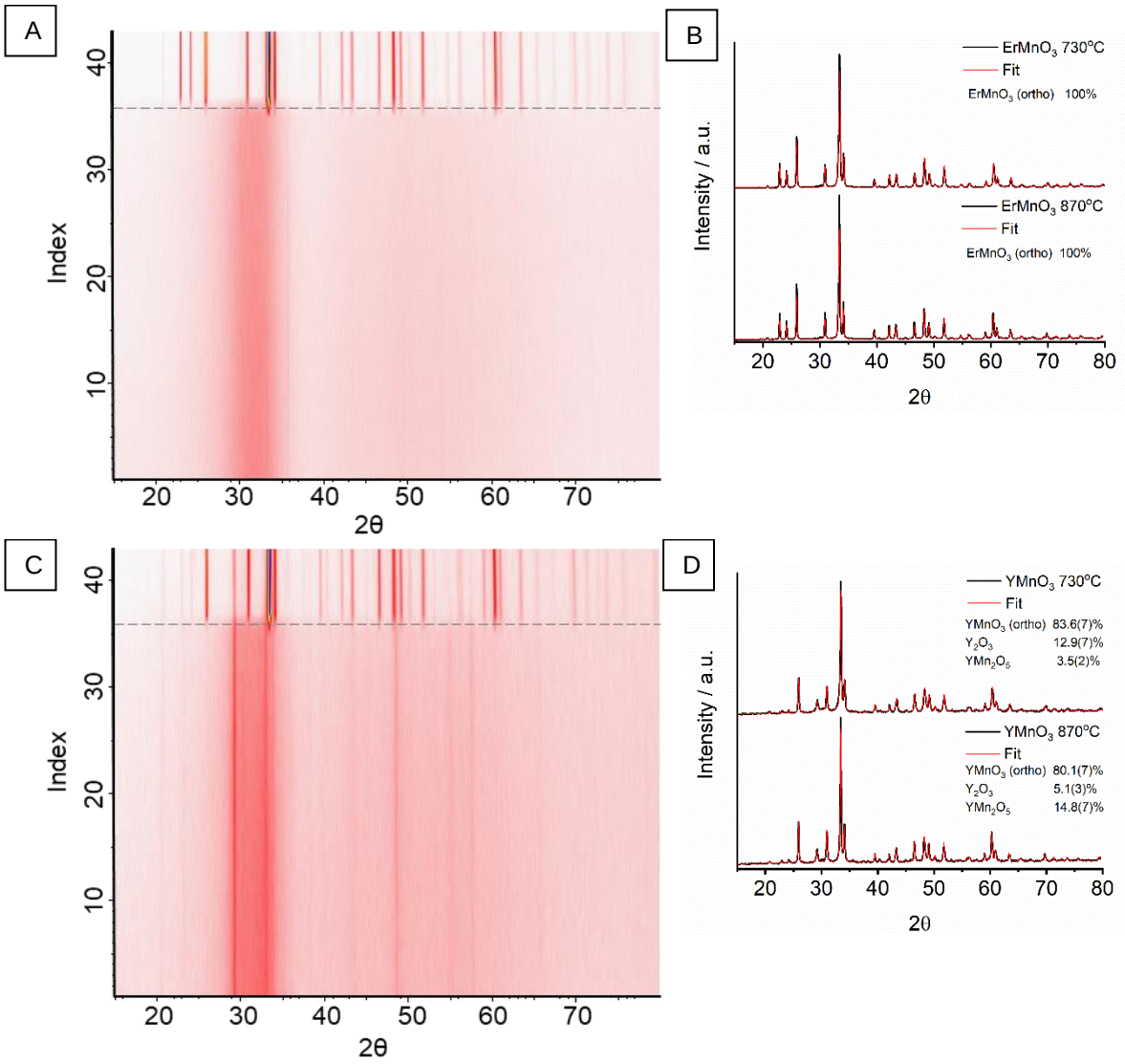

Figure 5.3.3: *In situ XRD patterns during increasing temperature every 20 ˚C from 30 – 870 ˚C for* ***(A)*** *$ErMnO_3$ and* ***(C)*** *$YMnO_3$ with respective Rietveld refinement performed after heating to 730 ˚C and final 870 ˚C at* ***(B)*** *and* ***(D)***

In section 5.3.2 it was shown that the ionic radii is directly linked to the final calcination temperature for sol-gel synthesised materials.[2] With Er and Y possessing comparable ionic radii, at 89 pm and 90 pm, respectively, it was reflected in both hexagonal perovskite species having the same annealing temperature. However, after calcining the milled material at 800 ˚C the diffraction patterns indicate that a higher temperature is required to reach 100% of crystalline *o*-$YMnO_3$. This, along with literature reporting an hexagonal perovskite crystallite as the thermodynamically stable product, and the orthorhombic phase as metastable, indicates an alternative chemical pathway occurs via mechanochemistry.[2] Traditionally extreme conditions, such as elevated pressures, are required to achieve the orthorhombic perovskite geometry for rare-earth metals with small ionic radii.[8,25,26] Whereas here, metastable *o*-$ErMnO_3$ and *o*-$YMnO_3$ perovskite phases have

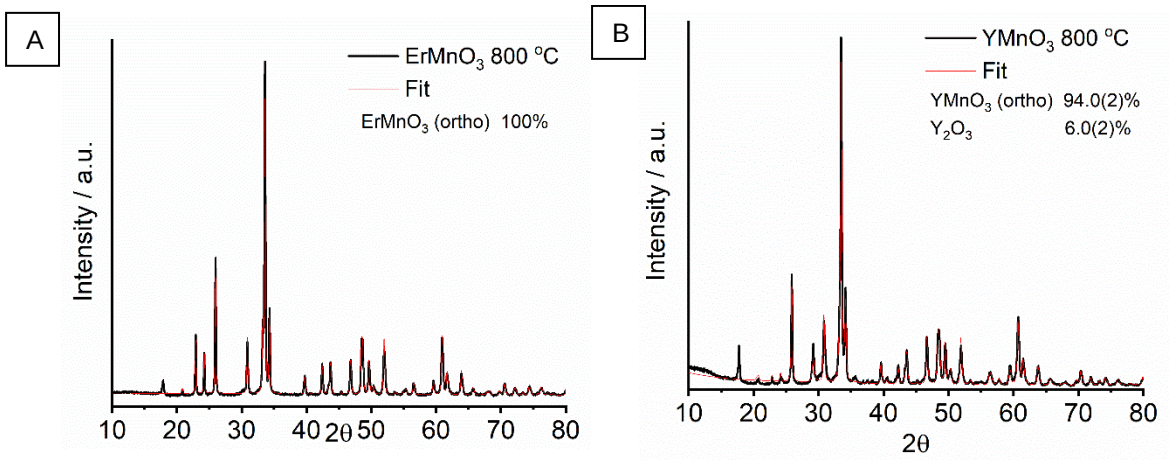

Figure 5.3.4: *XRD patterns after milling Mn_2O_3 with either* ***(A)*** *Er_2O_3 or* ***(B)*** *Y_2O_3 with 5mm milling media for 6 h with subsequent calcination at 800 ˚C for 20 h*

been synthesised by mechanochemistry from single metal oxide precursors, followed by a final high temperature calcination step. This indicates the high level of pressure applied to the powdered materials at the localised collision points on mechanical action for an orthorhombic geometry to form prior to heating. Previous attempts to replicate this pressure for the synthesis of $LaMnO_3$ from its single oxide precursors in a diamond anvil cell (DAC) were unsuccessful (section 4.3.1.4).[27] This allows us to deduce the importance of a pre-existing perovskite phase for the orthorhombic analogous species to form when applying pressure in the form of compression. Furthermore, by calcining the amorphous ball milled materials it has reduced the final annealing temperature by 300 ˚C; along with removing multiple process steps and the use of solvent to produce a more environmentally conscious process. These differences highlight that by changing the synthetic route it is possible to tailor materials to desired structures, which in turn can possess alternative properties that benefit specific applications.

5.3.4 X-ray absorption studies

In order to assess both the crystalline and amorphous content produced via ball milling *ex situ* XAS has been performed at the Mn K-edge and either the Er L_3-edge or Y K-edge on the milling 'time-slices'.

5.3.4.1 Understanding the mechanochemical synthesis of $ErMnO_3$

XANES spectra collected at the Er L_3-edge predominantly consists of a high intensity $2p \rightarrow 5d$ transition (Figure 5.3.5). For all samples the main edge position remains constant, indicating a Er(III) oxidation state throughout. The start and desired end points, Er_2O_3 and both *o*- and *h*-$ErMnO_3$, have first been assessed in order to better understand the ball milled 'time-slices'.

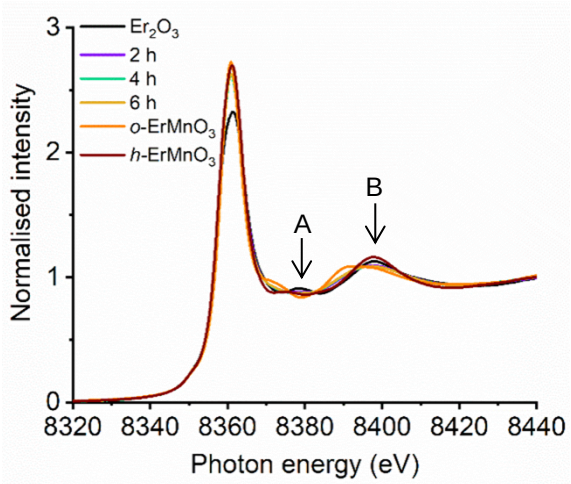

Figure 5.3.5: *Er L_3-edge XANES spectra at 'time-slices' during the mechanochemical synthesis of $ErMnO_3$ using 5 mm milling media*

Assessing the XANES spectra for Er_2O_3, it gives rise to the lowest intensity absorption peak maximum, attributed to a split in the 5*d* energy level.[28] Beyond this peak, features are observed at **(A)** 8378 eV and **(B)** 8399 eV, assigned to single and multiple scattering contributions and Er-O scattering, respectively.[29,30] These features indicate the central absorbing Er atom is positioned within a site of well-defined order; expected of a crystalline starting material.[29,30]

For both *h*- and *o*-$ErMnO_3$ the XANES spectra show an increase in the main peak height, with the number of density of states remaining consistent with the Er_2O_3 species it suggests a more degenerate 5*d* energy level (Figure 5.3.5). Whilst the *h*-$ErMnO_3$ spectrum follows a similar spectral profile to Er_2O_3, suggesting a comparable coordination environment, the *o*-$ErMnO_3$ shows significant variations. This confirms the vastly different electronic geometric arrangements surrounding the absorbing Er atom between hexagonal and orthorhombic perovskites.[28]

Observing the XANES spectra for the milled 'time-slices' (Figure 5.3.5), alterations can be seen after 2 h. No changes occur from 2 – 6 h of milling and have, therefore, been assessed collectively. As with both the $ErMnO_3$ reference species, an increase in the absorption peak maximum is achieved after 2 h of milling. This was previously linked to the formation of more equivalent 5*p* states, indicating a shift towards a perovskite-like electronic structure. Past the edge, features in the XANES spectra at 8370 eV and 8390 eV are consistent with those found for *o*-$ErMnO_3$. However, the low amplitude features, in comparison to the *o*-$ErMnO_3$ spectrum, indicate a lack of structural order, in agreement with the highly amorphous material detected by XRD (Figure 5.3.1).

To understand changes to the Mn environment during milling, XANES spectra have been collected at the Mn K-edge, which now corresponds to a dipole 1s → 4p transition (Figure 5.3.6).[27] An in-depth assessment of Mn K-edge XANES has been previously discussed in both Chapter 3 and 4, where it was highlighted that the pre-edge region provides valuable electronic information.[1,27] It was reported that local and non-local mixing

of Mn 3*d* and 4*p* orbitals can result in dipole allowed transitions before the edge; the electron is promoted to *p*-character when hybridised to Mn 3*d* orbitals. As a result, the intensity of these pre-features were found to be dependent on the most 'ideal' orbital mixing; with the strongest transition determined by (a) a short Mn-O bond length and (b) a linear Mn(4*p*)-O(2*p*)-Mn'(3*d*) bond angle.[31] Assessment of the XANES spectrum for the precursor material Mn_2O_3 was also discussed, where two low intensity peaks at **(1)** and **(2)** were assigned to different Mn(III) coordination sites; one with a regular octahedral geometry and the other possessing Jahn- Teller distortion.[27,32]

On first observation of the Mn K edge XANES for *o*-$ErMnO_3$, the main edge peak becomes sharper, with a greater intensity, indicating a higher degeneracy of *p*-states surrounding the central Mn ion (Figure 5.3.6). Furthermore, the feature observed at 6560 eV indicates the MnO_6 octahedron is surrounded by 8 Er atoms.[33] Within the pre-edge region two low intensity transitions are observed at 6536 eV and 6542 eV, suggesting less favourable hybridisation as a consequence of less extensive Mn–O–Mn interactions; this corresponds well with reports of the orthorhombic phase having high proportion of distortion.[3] The presence of two features could indicate an two Mn environments, with one effected by Jahn-teller distortion within the orthorhombic perovskite structure, previously seen within the Mn_2O_3 spectrum.

The Mn K-edge XANES spectra for the sol-gel synthesised *h*-$ErMnO_3$ shows a different spectral shape compared to the analogue orthorhombic perovskite (Figure 5.3.6). The first clear observation is the reduced amplitude of the main edge, along with an additional adsorption peak visible at 6565 eV; indicating the presence of two possible excited states. Though this twin feature is observed throughout literature for *h*-$ErMnO_3$ species, its origin at the Mn K-edge has not been sufficiently assessed.[34] One possible explanation can be suggested via work reported in literature by *Asokan et. al.* at the O K-

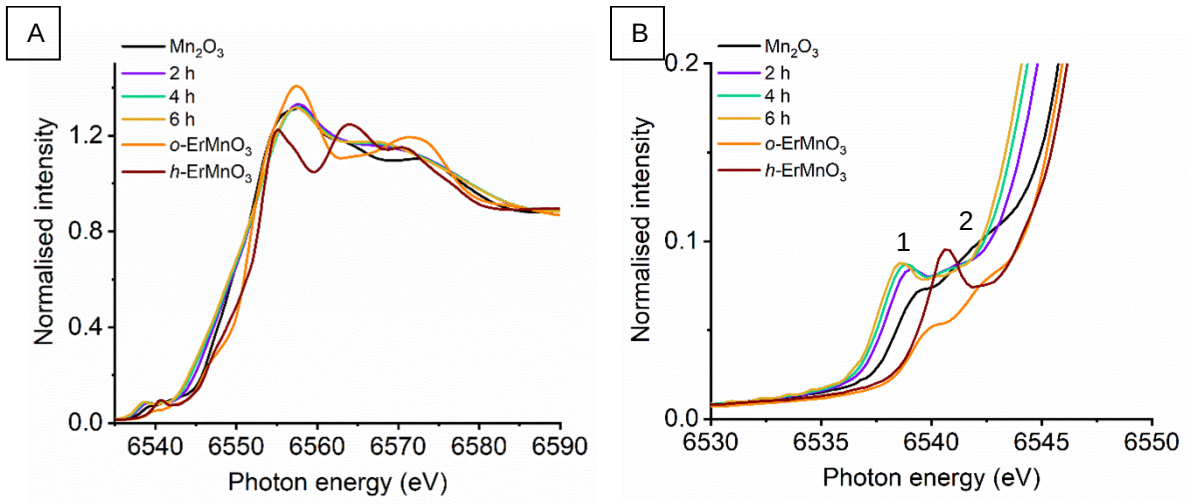

Figure 5.3.6: *Mn K-edge XANES spectra at 'time-slices' during the mechanochemical synthesis of $ErMnO_3$ using* ***(A)*** *5 mm milling media with corresponding* ***(B)*** *highlighted pre-edge*

edge XANES on manganite perovskites; assessment of the hexagonal electronic structure showed the unoccupied Mn 3$d_{x^2-y^2}$ orbital to strongly hybridise with the O 2*p* state.[2] However, research by *Ignatov et. al.* on $La_{1-x}Ca_xMnO_3$ reported that a feature 6 eV above the main edge, resulting from a multi-electron shake-up transition, and is therefore beyond the scope of a single electron model.[33] Within the pre-edge region a high intensity transition is observed at 6541 eV, which was previously demonstrated through HERFD-XANES of the sol-gel synthesised $LaMnO_3$, to consist of two overlapping transitions; one 1*s*→3*d* quadrupolar and one 1s →3*d*4*p* non-local excitation.[27,31] The high intensity of this feature suggests a greater degree of 3*d*4*p* mixing gained through either a shortening of the Mn-O bond length and/ or a more linear Mn-O-Mn' bond angle.[31]

Inspecting the XANES spectra for the milling 'time-slices' (Figure 5.3.6) at the Mn K-edge, immediate changes are observed at 2 h of milling, with no further alterations occurring on increasing the milling time, in parallel to the Er L_3-edge. Assessing the 2 – 6 h 'time-slices' together shows a shift to a lower energy of the rising edge, compared to Mn_2O_3. The evolution of the feature at 6570 eV suggests the presence of some scattering from the B-site cation, Er, indicative of a perovskite-like structure.[33] However, after milling for 6 h the low intensity features and clear alterations observed in comparison to the expected *o*-$ErMnO_3$ spectrum indicates a lack of structural order.

The pre-edge region has now been assessed in comparison to previous HERFD-XANES measurements of different Mn oxides (MnO_2, Mn_2O_3 and Mn_3O_4) and the reference $ErMnO_3$ materials (

Figure ***4.3.1***).[27] The shift to a lower energy for the transition at **(1)** to 6538 eV could indicate a proportion of Mn_3O_4 character, containing a mixed Mn (II/III) valency. The feature at **(1)** can be assigned to a tetrahedral coordinated Mn(II) transition resulting from a local 3*p*-4*d* hybridisation, with the peak at **(2)** 6542 eV ascribed as the Mn(III) centre.[32] It is, however, important to consider the difficulty in deducing oxidation states at the Mn K-edge without the use of high resolution techniques, such as HERFD-XANES. The pre-edge features of the milled 'time-slices' are not consistent to either *o*- or *h*-$ErMnO_3$ species, indicating a different electronic configuration has been formed on milling.

A linear combination fit (LCF) at both the Er L_3-edge and the Mn K-edge XANES region has been performed (Figure 5.3.7) using either Er_2O_3 or Mn_2O_3 and *o*-$ErMnO_3$ reference files (as previously assessed for $LaMnO_3$ in Figure 3.3.4). At both the Er L_3-edge and Mn K-edge the LCF shows an overall trend of the precursor materials steadily decreasing with a corresponding increase in $ErMnO_3$ species. Comparisons between the two edges suggest that the local electronic and geometric configurations surrounding the Er is more perovskite-like than the Mn environment.

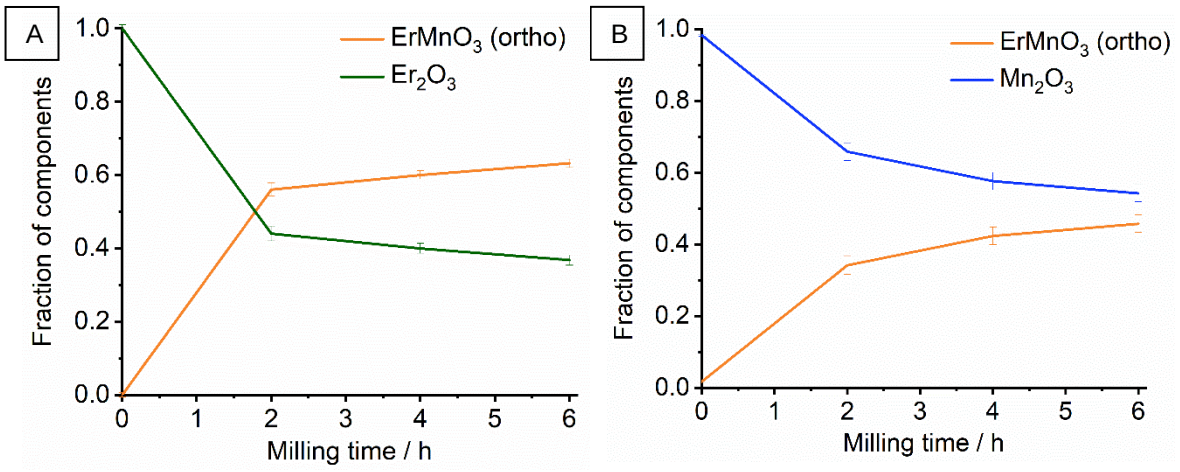

Figure 5.3.7: *Linear combination analysis at the* ***(A)*** *Er L_3-edge and* ***(B)*** *Mn K-edge of XANES spectra during 'time slices' during the mechanochemical synthesis of $ErMnO_3$ with 10 mm milling media, using Er_2O_3 or Mn_2O_3 and 6 h milled calcined $ErMnO_3$ as reference materials*

This further supports the previous insights within the $LaMnO_3$ system, where XAS indicated La dispersed over Mn_2O_3 in the initial stages of milling.[1] However, here the LCF highlights difficulties with the mechanical breaking down of Er_2O_3, and therefore less dispersion occurs compared to La A-site precursor. It is important to be aware that this analysis approach is limited due to the high proportion of unknown intermediates in the milled materials and therefore lack of appropriate reference materials; the LCF method is forced to produce an output equal to one, combining only the starting metal oxide and $ErMnO_3$.

EXAFS. In order to assess the local coordination geometry surrounding both Mn and Er with respect to milling time the EXAFS Fourier transform data for both Er L_3-edge and Mn K-edge of $ErMnO_3$ show highlighted regions for multiple coordination shells, corresponding to scattering paths calculated by FEFF (Figure 5.3.8). Appropriate fitting models have been calculated for the EXAFS Fourier transform data of reference materials, Er_2O_3 and both $ErMnO_3$ crystal phases (Table 5.3.4.1, Table 5.3.4.2 and Figure 5.3.9).

First assessing the EXAFS region at the Er L_3-edge (Table 5.3.4.1 and Figure 5.3.9A), the Fourier transform data for Er_2O_3 was well modelled to three scattering paths; one Er-O and two Er-Er. This simplified model is calculated effectively using a fixed CN of 6 for each scattering path to produce a simulated fit with good correlation to the experimental data, reflected in the R_{factor} of 0.02.

Next, a fitting model for *o*-$ErMnO_3$ was achieved by using multiple scattering paths, consisting of two Er-O, three Er-Mn and two Er-Er (Figure 5.3.9C). Within the first coordination shell the Mn-O scattering paths were reduced from four to two, at 2.29 Å and 2.57 Å, with the CN adjusted appropriately. As a consequence of the combination of scattering paths, an increase in the static disorder within the system is observed, which is reflected in the σ^2 parameter. Using a fixed oxygen CN of 8 produces good correlation to

the EXAFS data, reflected in the R_{factor}, indicative of the expected perovskite oxygen environment surrounding the central absorbing Er ion. Extending the fitting window to the second coordination shell, the model only requires two Er-Mn scattering paths, with calculated distances comparable to that of the crystalline structure, at 3.09 Å and 3.35 Å. However, on the addition of the third coordination shell difficulties arose in fitting the Er-Mn scattering path, with it deviating by 0.11 Å. This could be an indication that the scattering path has moved to oppose the Er-Er scatterer or as a result of alterations to the expected crystal structure for *o*-$ErMnO_3$ sample. Scattering paths at higher radial distances can often be challenging as a consequence of multiple overlapping contributions.

Preparing a fitting model for the EXAFS sol-gel *h*-$ErMnO_3$ data only required three scattering paths (Figure 5.3.9E). The three unique Er-O scattering distances identified in the crystalline structure was reduced to one Er-O path, with a CN of 7, to minimise parameters. The second and third coordination shells produced a good fit with the inclusion of Er-Mn and Er-Er scattering paths at 3.32 Å and 3.55 Å, respectively.

The low amplitude features observed for the milling 'time-slices' in the k^3-oscillations and EXAFS Fourier transform proved it was unsuitable for producing reliable fitting models. Instead visual comparisons of the EXAFS data, alongside the EXAFS fitting models of the

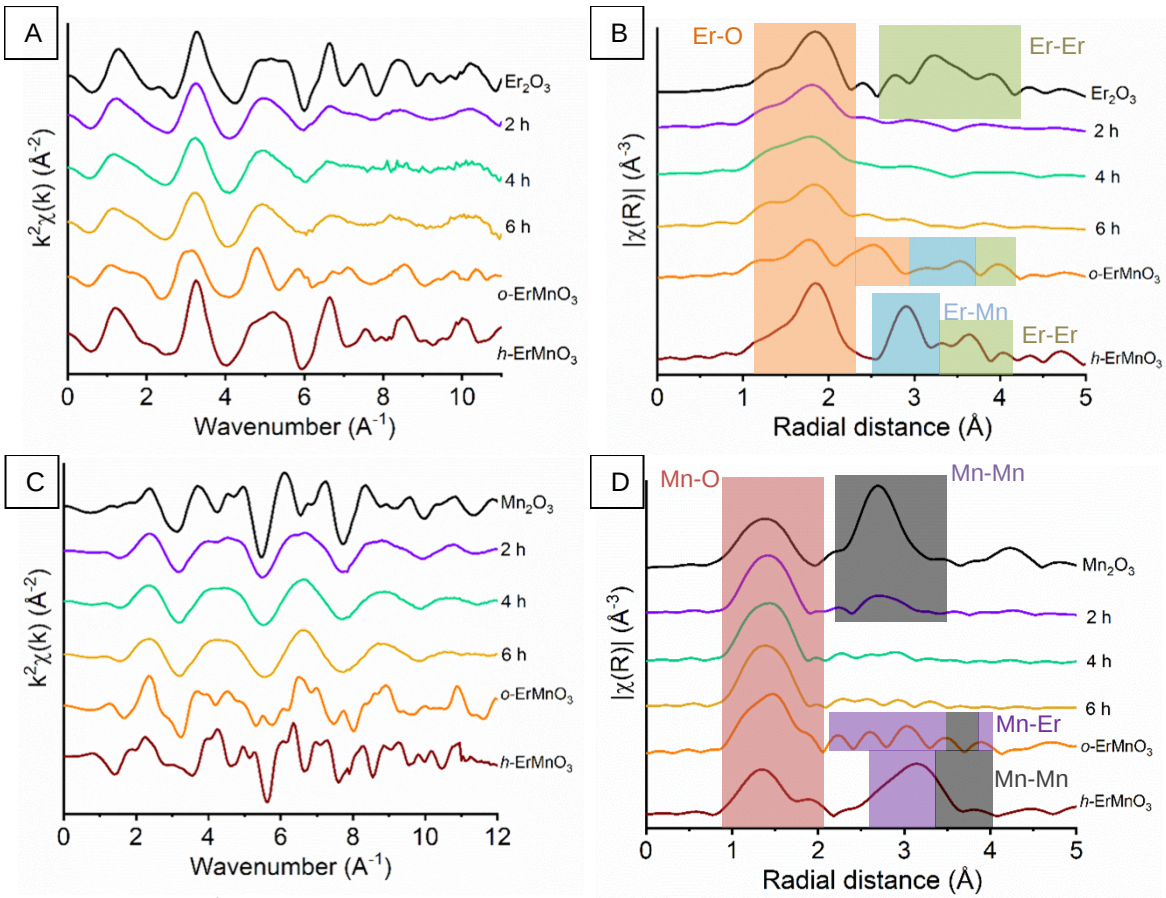

Figure 5.3.8: *k^3-weighted EXAFS oscillations at the **(A)** Er L_3-edge and its **(B)** respective nonphase-corrected Fourier transform and at the **(C)** Mn K-edge with respective **(D)** Fourier transform at 'time-slices' during the mechanochemical synthesis of $ErMnO_3$ with 5 mm milling media, with highlighted scattering paths*

reference materials, have been used to aid the assessment of the $ErMnO_3$ milled 'time-slices' (Figure 5.3.8).

After milling for 2 h significant alterations can be observed in the second coordination shell of the EXAFS Fourier transform, suggesting disruption to the extended Er-Er structure; previously indicated within the XANES region and by highly amorphous material detected by XRD. Increasing the milling time to 4 - 6 h no further changes are observed, resulting in a vastly different spectrum to the expected *o*-$ErMnO_3$ sample. Using comparisons in the k^3-oscillations between Er_2O_3 precursor and the desired *o*-$ErMnO_3$ sample, the feature at ~ 6 $Å^{-1}$ suggests the milling intermediates remain predominantly Er_2O_3 in character.

EXAFS modelling has now been performed at the Mn K-edge on the three reference materials, Mn_2O_3 and both $ErMnO_3$ crystal structures (Table 5.3.4.2 and Figure 5.3.9), equivalent to section 3.3.1. For full fitting information of the Mn_2O_3 spectrum (Figure 5.3.9B) see Chapter 3, section 3.3.1.

A suitable fitting model for *o*-$ErMnO_3$ was produced by using a simplified model of 6 paths (Figure 5.3.9D). Within the first coordination shell the number of Mn-O scattering paths was reduced from three to two. Here, the CN of both Mn-O scattering paths at 4 and 2 reflects the expected Jahn Teller distortion for the orthorhombic phase, with scattering lengths calculated at 1.90 Å and 2.23 Å, respectively. The second coordination shell was modelled effectively with two Mn-Er scattering paths, producing lengths consistent to the crystalline paths. A further two scattering paths, Mn-Mn and Mn-Er, were included at higher distances of 3.73 Å and 3.99 Å. These distances also reflect a significant divergence from the crystalline lengths observed at the Er L_3-edge, with a corresponding increase in the R_{factor}.

The sol-gel *h*-$ErMnO_3$ EXAFS data was suitably modelled using four scattering paths; two Mn-O, one Mn-Er and one Mn-Mn (Figure 5.3.9F). The Mn-O scattering paths at 1.85 Å and 2.02 Å show a much closer oxygen arrangement compared to that of *o*-$ErMnO_3$. This is also visible in the pre-features of the Mn K-edge XANES, where the higher intensity feature at 6541 eV observed in the *h*-$ErMnO_3$ pre-edge region has been reported to increase with decreasing Mn-O bond length.[32] The total oxygen CN of 5 confirms the expected monocapped MnO_5 structure present within hexagonal manganite perovskites.[2,35] Only the addition of two further scattering paths, simplified Mn-Er and Mn-Mn, were required to produce an appropriate fit to the experimental data.

Er L_3-edge

Table 5.3.4.1: *EXAFS fitting parameters for the Er L_3-edge for spectra collected on Er_2O_3, along with orthorhombic and hexagonal $ErMnO_3$. Fitting parameters: $S0_2$=0.8 as determined by the use of an Er foil standard; Fit range 3 < k>13, 1.2 <R > 4.0. [a]CN fixed to known structures and the number of scattering paths reduced in order to minimise fitting parameters*

Sample	Bond (Abs-Sc)	CN[a]	E_0 (eV)	σ^2	R / Å	R_{factor}
Er_2O_3 (Time 0)	Er-O1	6.0	2(1)	0.005(1)	2.26(1)	0.02
	Er-Er1	6.0		0.004(1)	3.52(1)	
	Er-Er2	6.0		0.005(1)	3.99(1)	
o-$ErMnO_3$	Er-O1	4.0	4(3)	0.006(2)	2.29(1)	0.03
	Er-O2	4.0		0.010(4)	2.57(3)	
	Er-Mn1	4.0		0.007(1)	3.09(1)	
	Er-Mn2	2.0		0.005(2)	3.35(2)	
	Er-Mn3	4.0		0.009(6)	3.76(5)	
	Er-Er1	2.0		0.005(2)	3.80(4)	
	Er-Er2	4.0		0.008(4)	4.04(4)	
h-$ErMnO_3$	Er-O1	7.0	3(1)	0.005(1)	2.28(1)	0.02
	Er-Mn1	3.0		0.004(1)	3.32(1)	
	Er-Er1	6.0		0.006(1)	3.55(1)	

Mn K-edge

Table 5.3.4.2: *EXAFS fitting parameters for the Mn K-edge for spectra collected on Mn_2O_3, along with orthorhombic and hexagonal $YMnO_3$. Fitting parameters: $S0_2$=0.7 as determined by the use of a Mn foil standard; Fit range 3 < k>14, 1.2 <R >3.85. [a]CN fixed to known structures and the number of scattering paths reduced in order to minimise fitting parameters*

Sample	Bond (Abs-Sc)	CN[a]	E_0 (eV)	σ^2	R / Å	R_{factor}
Mn_2O_3 (Time 0)	Mn-O1	4.0	-4(2)	0.005(1)	1.92(1)	0.02
	Mn-O2	2.0		0.011(7)	2.23(5)	
	Mn-Mn1	6.0		0.007(1)	3.11(2)	
	Mn-Mn2	6.0		0.013(3)	3.59(3)	
o-$ErMnO_3$	Mn-O1	4.0	-6(3)	0.003(1)	1.90(2)	0.04
	Mn-O2	2.0		0.007(3)	2.23(4)	
	Mn-Er1	4.0		0.007(2)	3.07(4)	
	Mn-Er2	2.0		0.003(2)	3.28(3)	
	Mn-Mn1	2.0		0.006(3)	3.73(6)	
	Mn-Er3	2.0		0.006(4)	3.99(7)	
h-$ErMnO_3$	Mn-O1	2.0	-1(2)	0.002(2)	1.85(2)	0.02
	Mn-O2	3.0		0.006(3)	2.02(3)	
	Mn-Er1	3.0		0.004(3)	3.38(4)	
	Mn-Mn1	6.0		0.004(2)	3.55(3)	

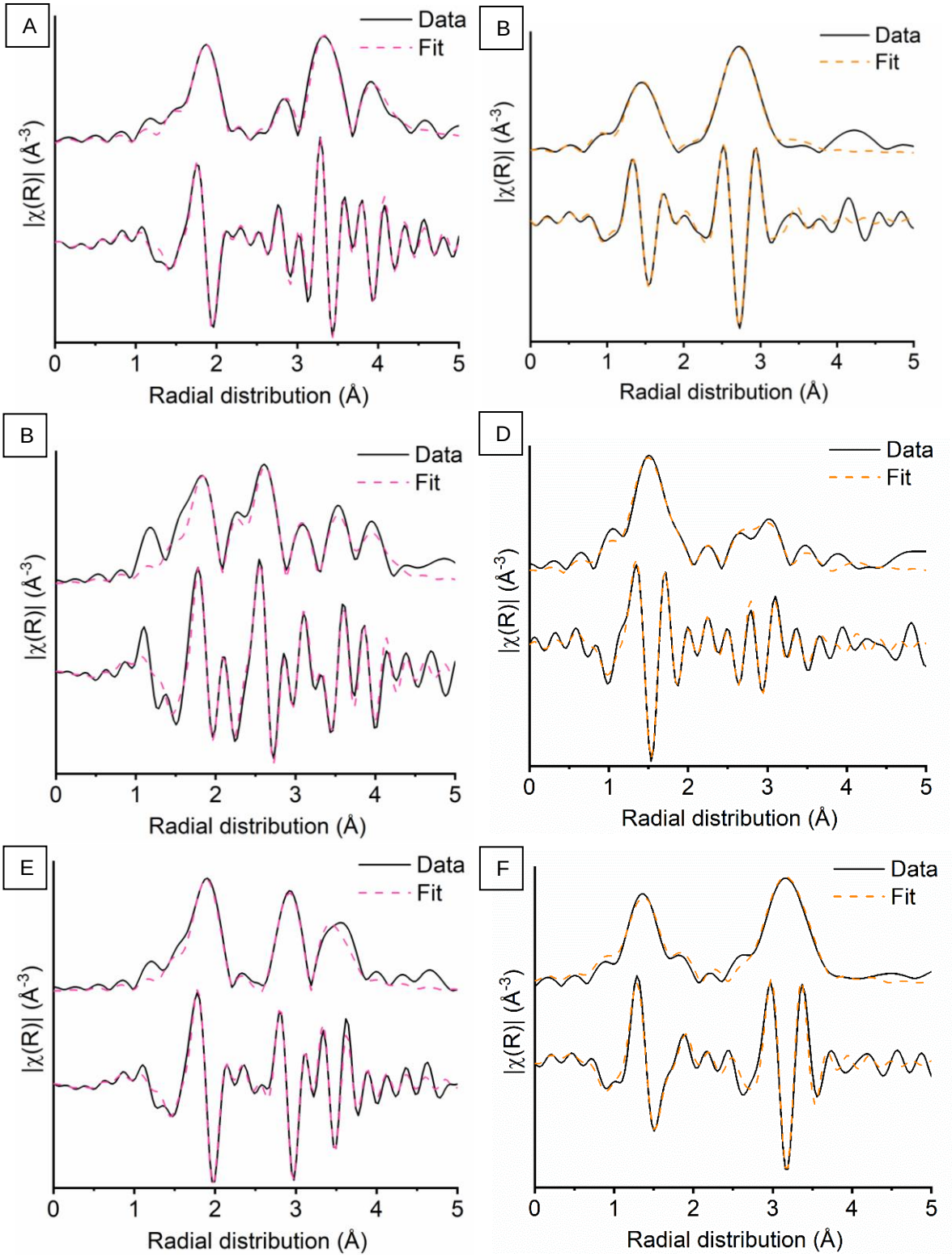

Figure 5.3.9: *Er L_3-edge (pink) and Mn K-edge (orange) EXAFS data of* ***(A)*** *Er_2O_3* ***(B)*** *Mn_2O_3* ***(C)*** *and* ***(D)*** *o-$ErMnO_3$ and* ***(E)*** *and* ***(F)*** *h-$ErMnO_3$ showing the magnitude and imaginary components of the k^3-weighted Fourier transform data and fits*

Visual observations have been completed for the milled 'time-slices' at the Mn K-edge in comparison to the reference materials, Mn_2O_3 and both *o*- and *h*-$ErMnO_3$ (Figure 5.3.8C, D). As with the Er L_3-edge, milling for 2 h shows a reduced amplitude within the second coordination shell, indicative of a decrease in the Mn-Mn scattering contribution. Further increasing the milling time to 4 and 6 h results in the absence of any structural features within this region. This indicates the formation of a highly disordered material, in agreement with observations at the Er L_3-edge (Figure 5.3.8A, B) and diffraction studies (Figure 5.3.1). Using comparisons in the k^3-oscillations between the Mn_2O_3 precursor and the desired *o*-$ErMnO_3$, the feature at ~ 9 Å for the 6 h milled sample indicates some character towards a perovskite-like structure. However, the lack of any defined oscillations, *i.e.* long-range structure, indicates it remains in a highly amorphous form.

By performing XAS studies at both Er L_3-edge and Mn K-edge on milling 'time-slices' for the synthesis of $ErMnO_3$ it is clear that there are difficulties in forming a perovskite via mechanochemistry under the same experimental conditions as for $LaMnO_3$. This indicates how changing just the A-site oxide starting material can significantly affect the evolution of the manganite perovskite phase.

5.3.4.2 Understanding the mechanochemical synthesis of $YMnO_3$

Performing XANES at the Y K-edge the spectra consists predominantly of a core 1*s* electron transition to unoccupied 5*p* density of states (Figure 5.3.10). The reference materials, Y_2O_3 and both *o*- and *h*-$YMnO_3$, were first assessed to allow for the interpretation of the XANES spectra for ball milled species.

Examining the Y_2O_3 XANES spectrum shows a double absorption peak, indicating that Y_2O_3 has a distorted octahedral coordination surrounding the central absorbing atom, with two Y environments, splitting the 5*p* level.[36,37]

The two crystalline phases, achieved by different synthetic routes, for the $YMnO_3$ perovskite have next been measured by XANES. The XANES spectrum for *h*-$YMnO_3$ also detects a double peak feature at the absorption maximum, similarly to the Y_2O_3. This indicates a comparable geometric coordination between the compounds; *h*-$YMnO_3$ possessing a doubly degenerate 5*p* level. In contrast the spectral line for the analogue orthorhombic perovskite shows a steeper single absorption peak with at a higher maximum. This indicates a more equivalent oxygen environment surrounding the central Y absorbing atom.

Using this assessment of the reference mixed metal oxide materials, insights into the milling 'time-slices' have now be performed. On milling for 2 h only a small shoulder of the double absorption peak from Y_2O_3 remains, with it completely absent after 4 h. No further change is observed with increasing the reaction time to 6 h. The XANES spectra for the

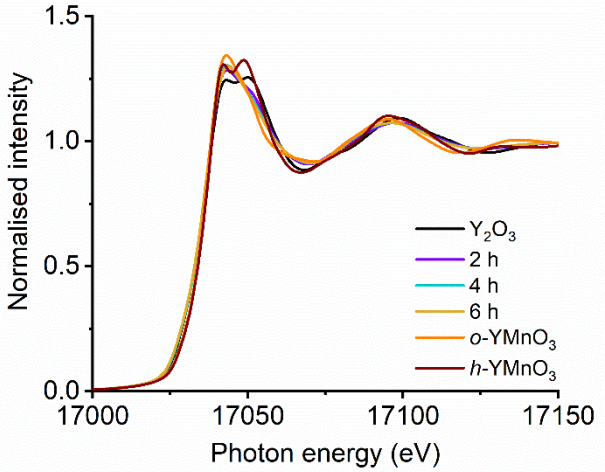

Figure 5.3.10: *Y K-edge XANES spectra at 'time-slices' during the mechanochemical synthesis of $YMnO_3$ using either 5 mm milling media*

milling 'time-slices' show comparable profiles to that of the crystalline *o*-$YMnO_3$, indicating a similar electronic and geometric arrangement, yet with a level of disorder.

XANES was performed at the Mn K-edge analogous to $ErMnO_3$ in section 5.3.4.1 for the $YMnO_3$ samples (Figure 5.3.11). A detailed description of the XANES region for Mn_2O_3 has previously been discussed in both Chapters 3 and 4.[27]

From first observations it is clear the *h*-$YMnO_3$ consists of a double peak at the main edge (Figure 5.3.11) along with comparable pre-edge features previously discussed at the Mn K-edge for *h*-$ErMnO_3$ (section 5.3.4.1). The spectrum measured for the *o*-$YMnO_3$ sample follows a different spectral profile to the sol-gel sample, despite possessing the same stoichiometry. Similarities can, once again, be observed to the Mn K-edge XANES spectrum of *o*-$ErMnO_3$ (Figure 5.3.6).

Assessing the ball milled 'time-slices' shows changes within the Mn K-edge spectra can be observed after milling for 2 h, with no changes detected from 4 – 6 h. The presence of one main edge peak indicates similarities with an orthorhombic crystalline structure, however, large differences occur within the pre-edge features. Assessing these pre-edge features shows similarities to the $ErMnO_3$ milled species (Figure 5.3.6). Here it was concluded the

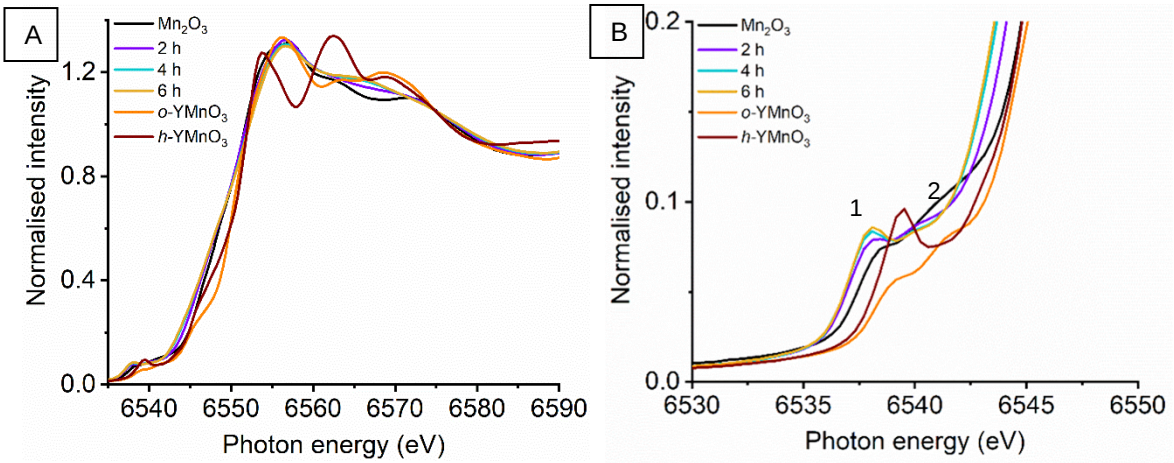

Figure 5.3.11: *Mn K-edge **(A)** XANES spectra at 'time-slices' during the mechanochemical synthesis of $YMnO_3$ using 5 mm milling media with **(B)** highlighted pre-edge*

transition at **(1)** is assigned to a tetrahedral coordinated Mn(II) transition resulting from a local 3*p*-4*d* hybridisation, with the peak at **(2)** 6542 eV ascribed as the Mn(III) centre.[32]

A LCF was performed, equivalent to the $ErMnO_3$ study (Figure 5.3.7), at both the Y and Mn K-edge XANES region (Figure 5.3.12). The LCF shows the steady decrease of the precursor fraction with increasing milling time at both the Mn and Y K-edge. Subsequently, an increase in the *o*-$YMnO_3$ phase is observed, with the Y environment indicating a more perovskite-like arrangement compared to Mn K-edge. However, the XANES spectra collected at both edges show that 6 h of milling is insufficient to reach a bulk perovskite phase. In comparison to the Er A-site analogous milling (Figure 5.3.7) changes are observed at both edges up to 4 h of milling, indicating a slower rate of formation for *o*-$YMnO_3$. This is in agreement with *in situ* XRD which required a higher temperature to reach *o*-$YMnO_3$ rather than *o*-$ErMnO_3$.

EXAFS Analysis. Figure 5.3.13 shows the EXAFS Fourier transform data for both Y K-edge and Mn K-edge for $YMnO_3$ with highlighted regions assigned to specific scattering paths. As before, the start and desired end point of the mechanochemical synthesis, *i.e.* Y_2O_3 or Mn_2O_3 with $YMnO_3$, were analysed to deconvolute structural changes as a consequence of milling (Table 5.3.4.3, Table 5.3.4.4, Figure 5.3.14).

At the Y K-edge the precursor Y_2O_3 spectrum was well modelled using 3 scattering paths; one Y-O and two Y-Y (Table 5.3.4.3, Figure 5.3.14A). Here, the metal oxide has a cubic bixbyite crystal structure, comparable to that of Er_2O_3, and therefore a possesses a similar fitting model (Table 5.3.4.3).[28] Both *o*-$YMnO_3$ (Figure 5.3.14B, E) and *h*-$YMnO_3$ (Figure 5.3.14C, F) EXAFS data were well modelled using equivalent $ErMnO_3$ models at both the Y and Mn K-edge. The fitting parameters showed that both A-site species produce materials with comparable structures when synthesised under the same conditions. One structural variation can be observed at the Mn K-edge, where the calculated model for the *o*-$YMnO_3$ species (Figure 5.3.14F) produces longer scattering distances for the majority of paths. This increase, specifically in the first coordination shell for the two Mn-O distances,

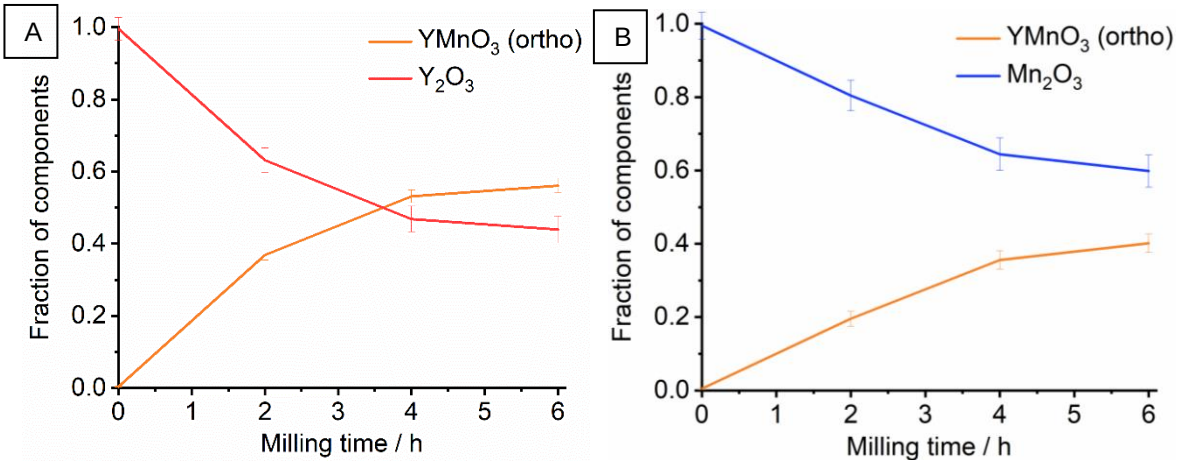

Figure 5.3.12: *Linear combination analysis at the* ***(A)*** *Y K-edge and* ***(B)*** *Mn K-edge of XANES spectra during 'time slices' during the mechanochemical synthesis of $YMnO_3$ with 5 mm milling media, using Y_2O_3 or Mn_2O_3 and 6 h milled calcined $YMnO_3$ as reference materials*

equates to a higher degree of Jahn-Teller distortion within the MnO_6 octahedron. This confirms *o*-$YMnO_3$ possess a less favourable geometric structure with a lower tolerance factor over *o*-$ErMnO_3$; corresponding well to the higher calcination temperature required to reach a pure crystalline *o*-$YMnO_3$ phase.

When assessing the milling 'time-slices' at both Y and Mn K-edges significant alterations can be observed within the second coordination shell after milling for 2 h (Figure 5.3.13). Here, a reduction in amplitude of both features, corresponding to Y-Y or Mn-Mn scattering, indicates disruption to the extended precursor structure. After milling for 4 h at the Y K-edge features assigned to perovskite character in both the EXAFS k^3-oscillations and Fourier transform remain absent, indicating that the Y_2O_3 precursor remains in a highly amorphous state, as suggested by XRD. Only on increasing milling time to 6 h at the Mn K-edge is Mn-Mn scattering no longer detected. However, similarities in the spectral profile for the k^3-oscillations of the Mn_2O_3 start and *o*-$YMnO_3$ end point make the assessment of milled species challenging.

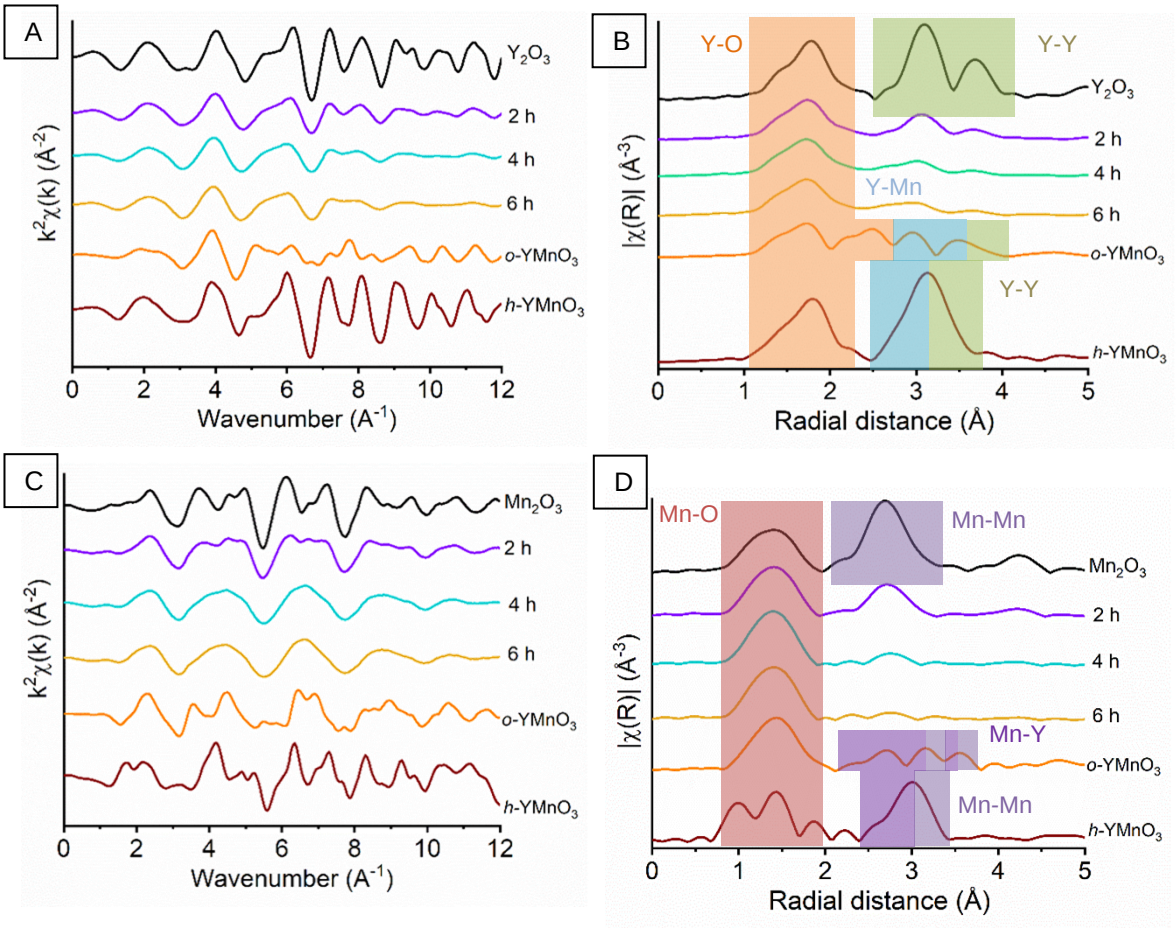

Figure 5.3.13: *k^3-weighted EXAFS oscillations at the **(A)** Y K-edge and its **(B)** respective nonphase-corrected Fourier transform and at the **(C)** Mn K-edge with corresponding **(D)** Fourier transform at 'time-slices' during the mechanochemical synthesis of $YMnO_3$ with 5 mm milling media, with highlighted scattering paths*

Y K-edge

Table 5.3.4.3: *EXAFS fitting parameters for the Y K-edge for spectra collected on Y_2O_3, along with orthorhombic and hexagonal $YMnO_3$. Fitting parameters: $S0_2$=1.0 as determined by the use of a Y foil standard; Fit range 3 < k>14, 1.2 <R > 4.0. [a]CN fixed to known structures and the number of scattering paths reduced in order to minimise fitting parameters*

Sample	Bond (Abs-Sc)	CN[a]	E_0 (eV)	σ^2	R / Å	R_{factor}
Y_2O_3 (Time 0)	Y-O1	6.0	-4(1)	0.005(1)	2.27(8)	0.04
	Y-Y1	6.0		0.005(1)	3.53(6)	
	Y-Y2	6.0		0.006(1)	4.00(1)	
6 h milled and calcined $YMnO_3$ (Orthorhombic)	Y-O1	4.0	1(2)	0.006(1)	2.29(1)	0.03
	Y-O2	4.0		0.012(1)	2.51(2)	
	Y-Mn1	2.0		0.005(1)	3.09(1)	
	Y-Mn2	4.0		0.008(2)	3.29(1)	
	Y-Mn3	2.0		0.003(1)	3.76(2)	
	Y-Y1	4.0		0.005(1)	3.79(2)	
Sol-gel $YMnO_3$ (Hexagonal)	Y-O1	7.0	-2(2)	0.005(1)	2.16(1)	0.02
	Y-Mn1	3.0		0.007(3)	3.33(2)	
	Y-Y1	6.0		0.004(1)	3.57(2)	
	Y-Mn2	3.0		0.003(2)	3.77(2)	

Mn K-edge

Table 5.3.4.4: *EXAFS fitting parameters for the Mn K-edge for spectra collected on Mn_2O_3, along with orthorhombic and hexagonal $YMnO_3$. Fitting parameters: $S0_2$=0.7 as determined by the use of a Mn foil standard; Fit range 3 < k>14, 1.2 <R >3.85. [a]CN fixed to known structures and the number of scattering paths reduced in order to minimise fitting parameters*

Sample	Bond (Abs-Sc)	CN[a]	E_0 (eV)	σ^2	R / Å	R_{factor}
Mn_2O_3 (Time 0)	Mn-O1	4.0	-6(2)	0.004(1)	1.92(1)	0.02
	Mn-O2	2.0		0.014(1)	2.22(5)	
	Mn-Mn1	6.0		0.006(1)	3.10(2)	
	Mn-Mn2	6.0		0.012(2)	3.57(3)	
o-$YMnO_3$	Mn-O1	4.0	-1(1)	0.004(1)	1.92(1)	0.02
	Mn-O3	2.0		0.008(3)	2.27(9)	
	Mn-Y2	4.0		0.008(1)	3.17(9)	
	Mn-Y3	2.0		0.004(1)	3.33(9)	
	Mn-Mn1	2.0		0.009(4)	3.80(3)	
	Mn-Y4	2.0		0.009(2)	3.90(2)	
	Mn-Mn2	4.0		0.014(4)	4.00(3)	
h-$YMnO_3$	Mn-O1	2	-5(1)	0.004(1)	1.85(1)	0.02
	Mn-O3	3		0.011(3)	1.99(1)	
	Mn-Y2	3		0.007(2)	3.29(2)	
	Mn-Mn1	6		0.008(1)	3.50(2)	

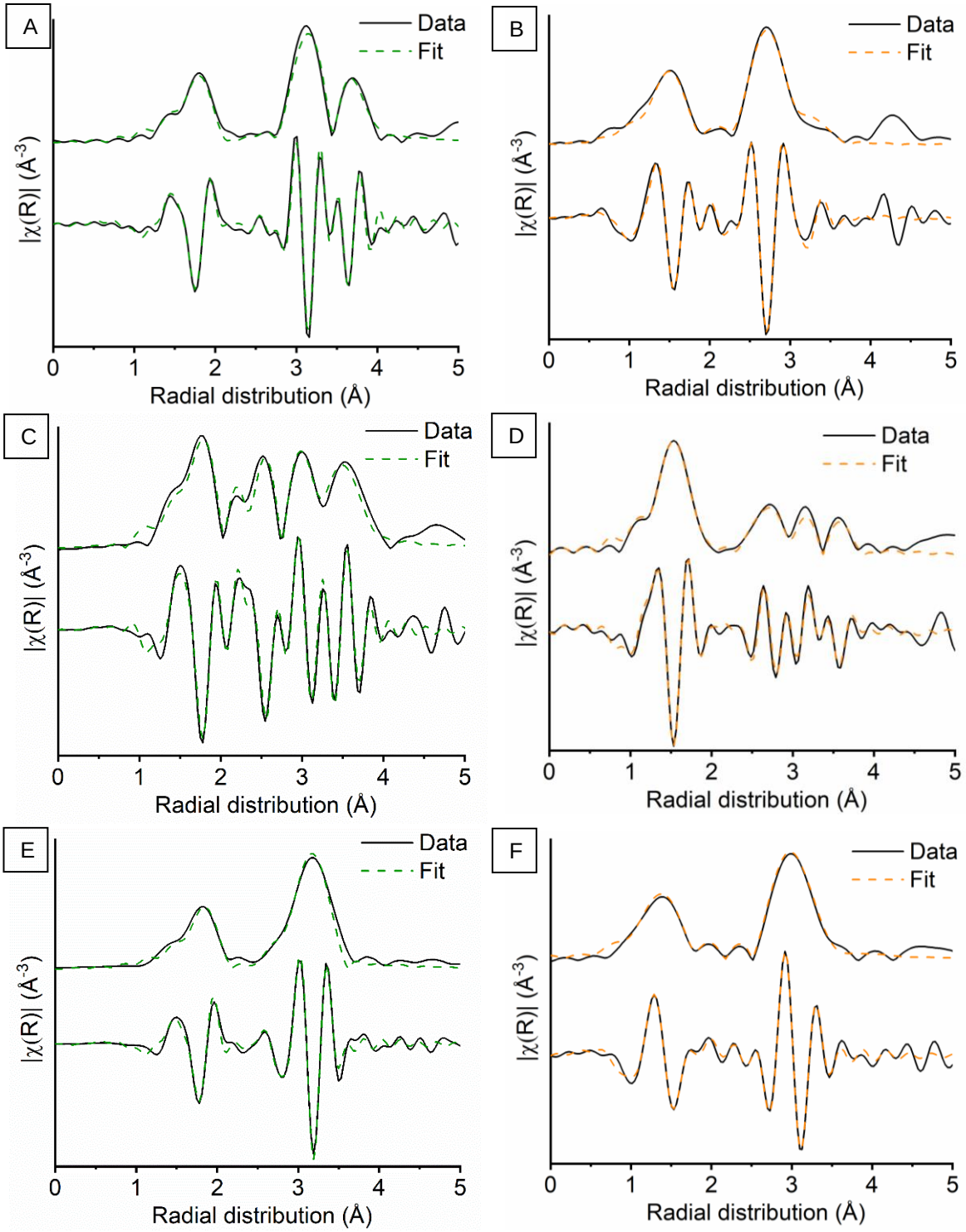

Figure 5.3.14: *Y K-edge (green) and Mn K-edge (orange) EXAFS data of* ***(A)*** *Y_2O_3* ***(B)*** *Mn_2O_3* ***(C)*** *and* ***(D)*** *o-$YMnO_3$ and* ***(E)*** *and* ***(F)*** *h-$YMnO_3$ showing the magnitude and imaginary components of the k^3-weighted Fourier transform data and fits*

5.3.5 Optimisation of the mechanochemical synthesis to achieve an $AMnO_3$ perovskite phase

Attempts to achieve a perovskite phase by ball milling alone, in the absence of a calcination step have now been performed by optimising the milling parameters. Subsequently, this will allow for the correlation between different A-site metal oxides and their evolution to the perovskite phase via mechanochemistry. Previous reports within literature for the mechanochemical synthesis of both $ErMnO_3$ and $YMnO_3$ perform milling using a greater milling media size than 5 mm. By using a larger media size it would be expected to increase the localised contact force experienced on the powders within the mill.[5,13] Therefore, whilst retaining a constant powder to media weight ratio, both Er_2O_3 or Y_2O_3 have been milled alongside Mn_2O_3 with 10 mm ZrO_2 media to induce the evolution of the manganite perovskite phase.

XRD. Initially the long-range structural changes have been assessed by XRD studies on 'time-slices' during the mechanochemical synthesis of $AMnO_3$ (A = Er, Y) (Figure 5.3.15). The first clear observation is that on milling low intensity Bragg peaks are detected within the diffraction pattern for both Er and Y A-site precursors (Figure 5.3.15A, B). On closer inspection of the milled 'time-slices' it is evident that a small proportion of crystalline material is present within the sample (Figure 5.3.15C, D). By performing Rietveld refinement after 2 h of milling on both A-sites 'time-slices', the perovskite phase can now be detected in its orthorhombic geometry.

For the Er_2O_3 and Mn_2O_3 milled 'time-slices', 100% of the crystalline content was calculated as *o*-$ErMnO_3$ from 2 – 6 h of milling (Figure 5.3.15E). When the milling time is increased to 6 h a decrease in amplitude of the diffraction peaks is observed. With comparable crystallite sizes calculated for *o*-$ErMnO_3$ at each 'time-slice', 7.2(3) - 7.5(3) Å, it indicates the $ErMnO_3$ 6 h sample has become more disordered with the extended milling time.

The XRD 'time-slices' corresponding to the milling of Mn_2O_3 with Y_2O_3 shows a reaction time of 6 h is required for 100% of the crystalline content to be *o*-$YMnO_3$ (Figure 5.3.15F). The longer milling time required for 100 % of the crystalline content to be associated as *o*-$YMnO_3$, compared to *o*-$ErMnO_3$, also reflects XRD and XAS studies in section 5.3.2 and 5.3.4; where a higher calcination temperature and slower breakdown of the precursor materials was observed during the synthesis of *o*-$YMnO_3$.

Crystalline *o*-$ErMnO_3$ and *o*-$YMnO_3$ have been successfully synthesised by mechanochemistry in ambient conditions, in the absence of a high temperature annealing step by altering just the milling media size. However, it is evident that a large proportion of amorphous material remains, which lab-based XRD is unsuitable to characterise. Therefore, XAS has been performed on the 10 mm milling media 'time-series' to provide further insights into the milled material.

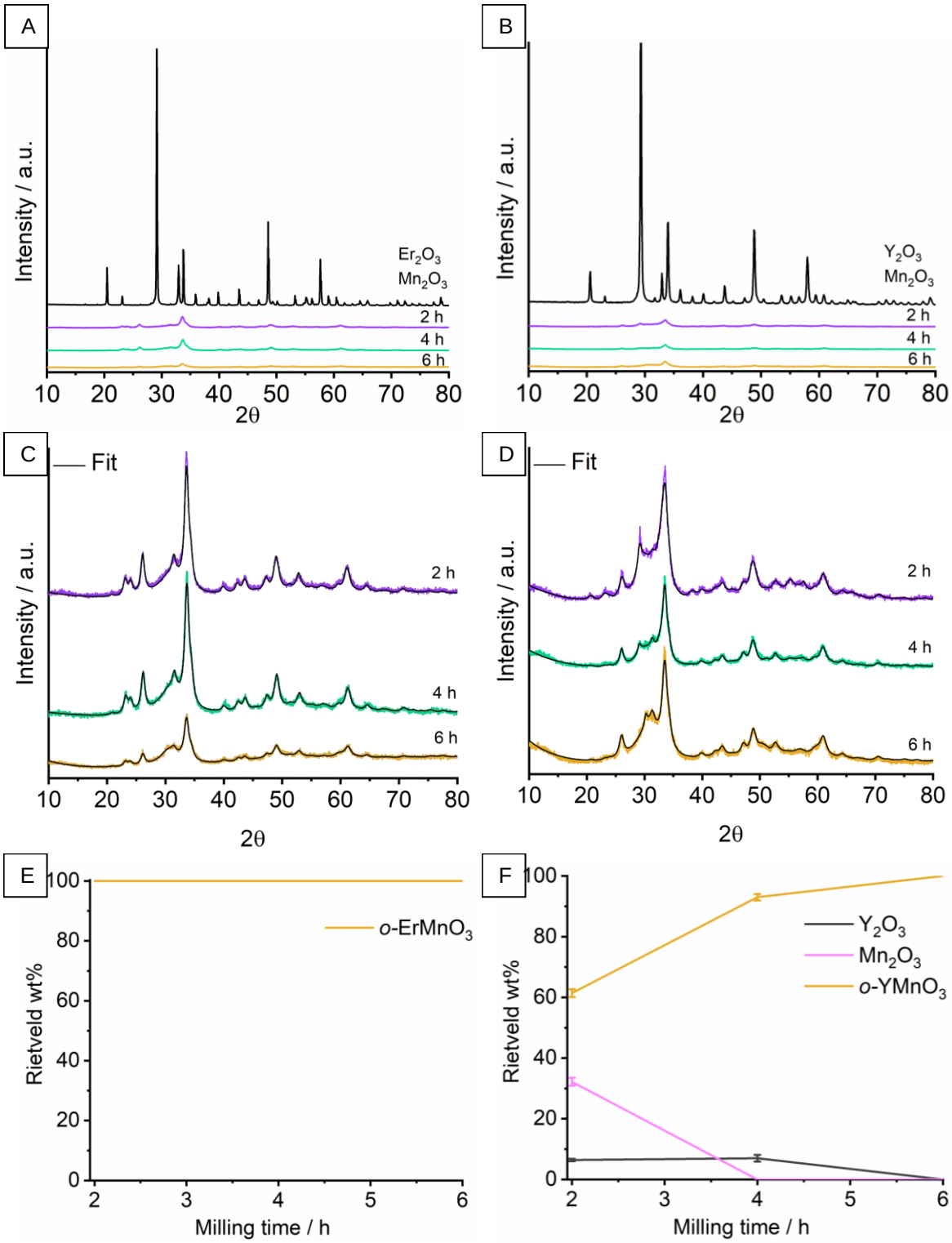

Figure 5.3.15: *XRD patterns after milling Mn_2O_3 with either* ***(A)*** *of Er_2O_3 or* ***(B)*** *of Y_2O_3 at 2, 4 and 6 h with 10 mm milling media with highlighted regions for the milled materials* ***(C)*** *$ErMnO_3$ and* ***(D)*** *$YMnO_3$ with respective wt% composition during milling* ***(E)*** *$ErMnO_3$ and* ***(F)*** *$YMnO_3$ calculated Rietveld refinement*

XANES. The A-site edge, Er L_3-edge and Y K-edge, XANES has first been assessed for the 10 mm milling media 'times-series' (Figure 5.3.16), with comparisons to the appropriate reference material, *o*-$ErMnO_3$ or *o*-$YMnO_3$ (section 5.3.4). Earlier time segments at 0.5 and 1 h have been added to investigate the transition at shorter milling times.

On the addition of 'time-slices' at earlier stages during the mechanochemical reaction, steady changes can be observed at both Er L_3-edge and Y K-edge up to 2 h of milling; highlighting the shift towards the orthorhombic electronic configuration. At both edges the XANES spectra indicate that just 0.5 h of milling was sufficient to cause alterations to the extended Er-Er or Y-Y structure. From 2- 6 h, as with the analogous 5 mm milled samples, no significant change can be observed within the XANES (Figure 5.3.5 and Figure 5.3.10). This suggests that the transfer of mechanical energy within the first 2 h is extremely important for phase transformations; corresponding well to findings within the $LaMnO_3$ system when milling under both atmospheric and inert milling environments (Chapter 3). Comparing both 5 mm and 10 mm 6 h milled samples indicates that the larger media size results in the spectra shifting towards the *o*-$AMnO_3$ structure. However, differences can still be observed between the milled and reference materials for either Er or Y coordination environments.

Assessing the XANES spectra collected at the Mn K-edge shows comparable spectra at 'time-slices' during the mechanochemical synthesis for *o*-$ErMnO_3$ and *o*-$YMnO_3$ (Figure 5.3.17). Both species show the steady progression of the feature at 6570 eV, indicating the inclusion of A-site into the perovskite lattice around the MnO_6 octahedron.[33] Comparisons between the reference spectra show the *o*-$ErMnO_3$ spectra to have a sharper, more intense absorption peak, signifying a more crystalline structure, compared to *o*-$YMnO_3$; corresponding well to previous assumptions on the higher level of disorder in the *o*-$YMnO_3$ phase.

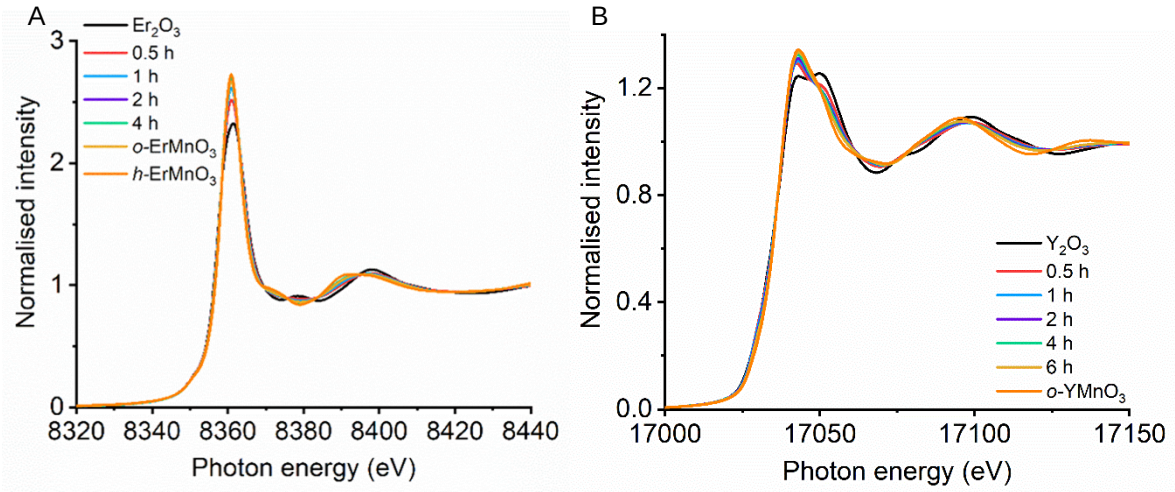

Figure 5.3.16: (A) *Er L_3-edge and* ***(B)*** *Y K-edge XANES spectra at 'time-slices' during the mechanochemical synthesis of $ErMnO_3$ or $YMnO_3$, respectively, using 10 mm milling media*

Small alterations within the pre-edge can be observed between both Er and Y 10 mm milled 'time-series', where the earlier 'time-slices' for *o*-$ErMnO_3$ indicate a slower transition to the 6 h sample. However, the final milled materials show similarities to one another in their pre-features, being comparable to the that of ball milled $LaMnO_3$.[27] Significant differences arise compared to the 5 mm milled 'time-series' (Figure 5.3.6 and Figure 5.3.11) where the position and intensity of the peak at **(1)** indicated Mn(II) character (section 5.3.4). Once again, large differences can still be observed between the final 10 mm milled and reference *o*-$AMnO_3$ materials; indicating that performing milling experiments with 10 mm media is still insufficient for a perovskite-like phase to form.

A LCF has been performed in conjunction with previous calculations (section 5.3.4) at the Er L_3-edge or Y K-edge alongside the Mn K-edge XANES region. All spectra show an overall trend of precursor materials steadily decreasing with a corresponding increase in *o*-$AMnO_3$ perovskite phase (Figure 5.3.18). With increasing the milling media size to 10 mm, the LCF indicates a closer electronic arrangement towards the desired perovskite phase.

Assessing both spectra for the $ErMnO_3$ 'time-series' shows little change occurs within the XANES region after 2 h of milling, indicating the importance of early stage reactions. At the Mn K-edge, the 6 h sample shows a significant decrease in the perovskite

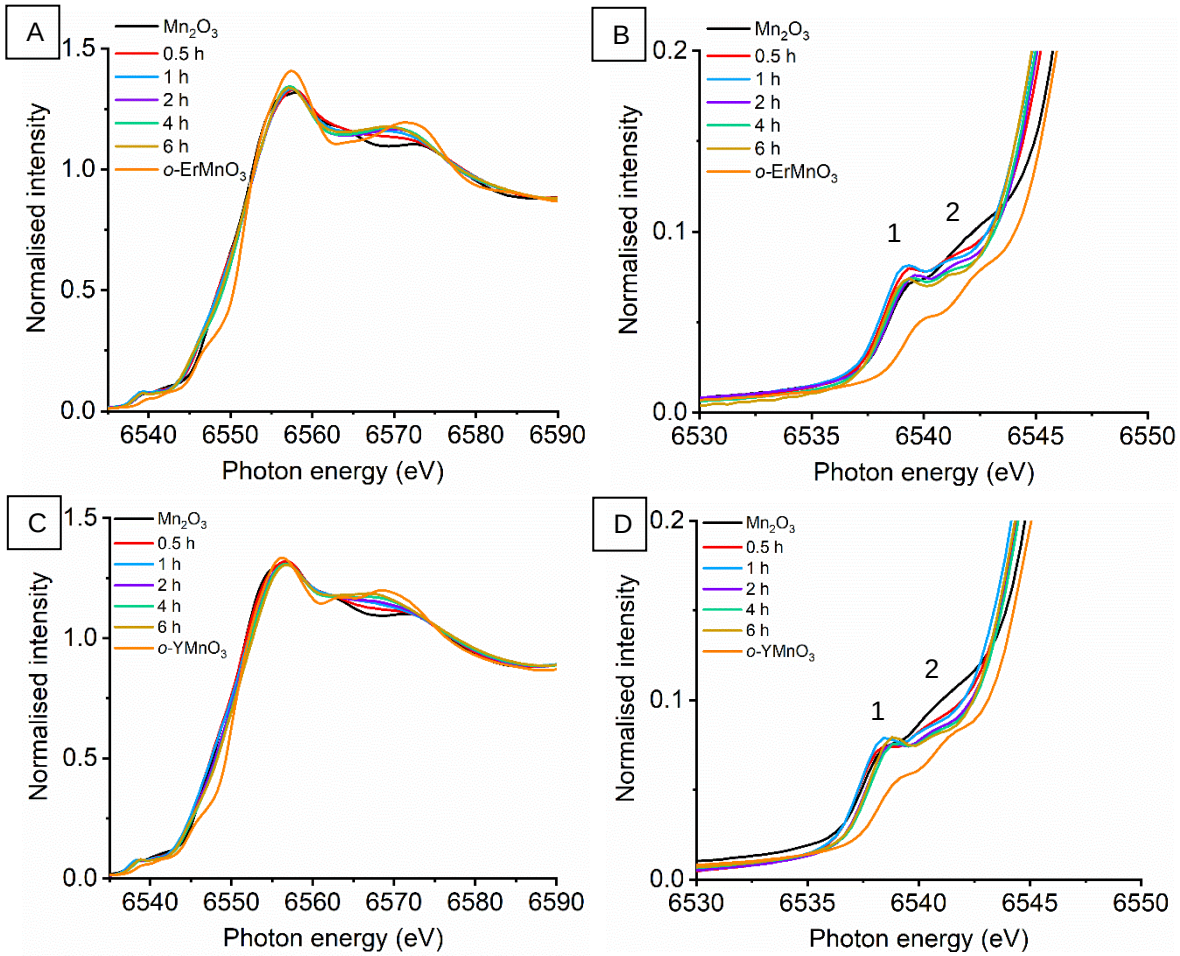

Figure 5.3.17: *Mn K-edge XANES spectra at 'time-slices' during the mechanochemical synthesis of* ***(A)*** *$ErMnO_3$ with* ***(B)*** *highlighted pre-region and* ***(C)*** *$YMnO_3$ with* ***(D)*** *highlighted pre-region using 10 mm milling media*

fraction. Linking this with the decrease in intensity of Bragg peaks for this sample (Figure 5.3.15C) could indicate amorphous Mn_2O_3 or perovskite degradation has occurred on extensive milling.

The LCF spectra at both Y and Mn K-edge also show the largest proportion of change occurs within the first stages of milling, 0 – 1 h. Unlike the LCF for 5 mm media milled $YMnO_3$ (Figure 5.3.12A) and both the $ErMnO_3$ (Figure 5.3.7A and Figure 5.3.18A) 'time-series', the data does not plateau with increasing milling time. This can be an indication that further changes towards the perovskite phase could be observed on increasing the milling time further. Similarly, to the $ErMnO_3$ sample, the higher decrease in the Y_2O_3 fraction could indicate the importance of the A-site precursor for evolution of the perovskite phase.

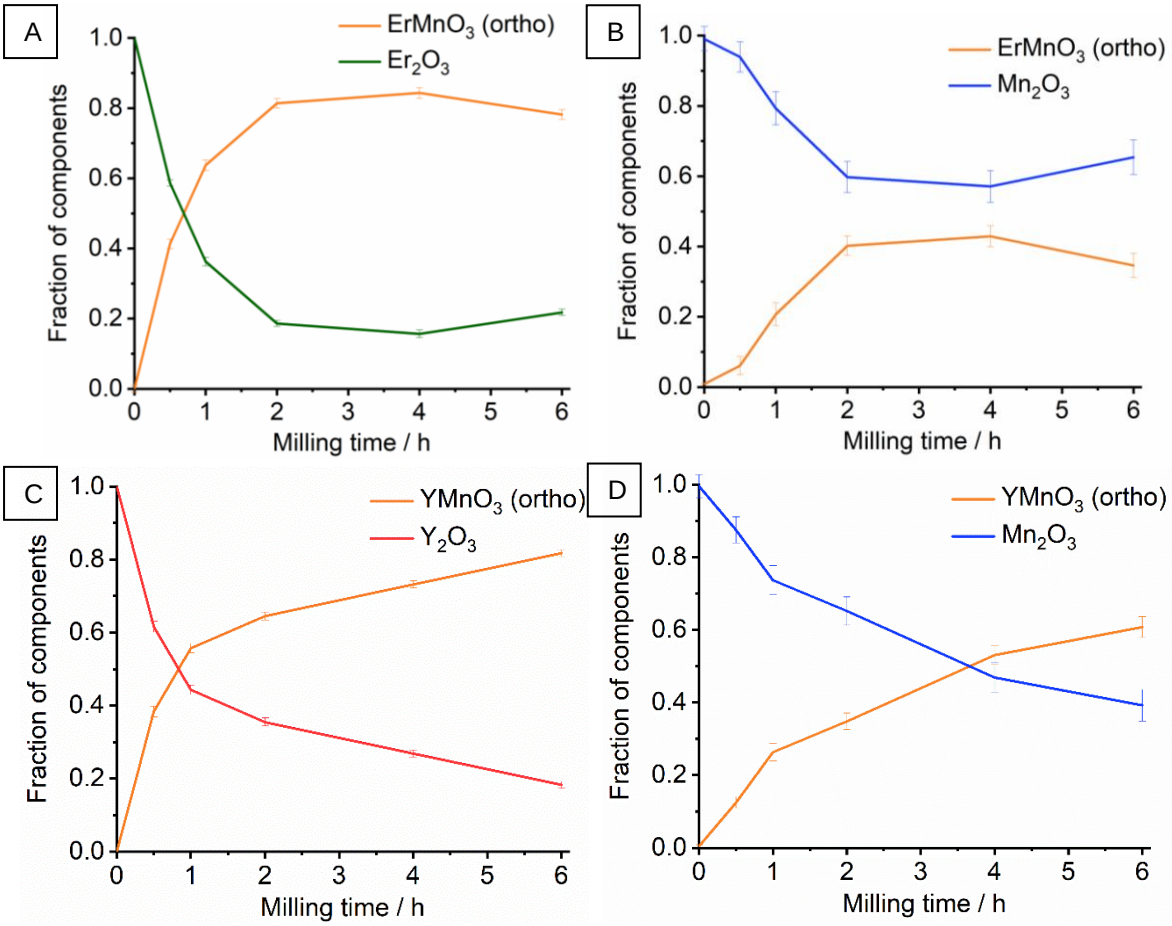

Figure 5.3.18: *Linear combination analysis for XANES 'time slices' during the mechanochemical synthesis with 10 mm media for $ErMnO_3$ at the* ***(A)*** *Er L_3-edge and* ***(B)*** *Mn K-edge compared to $YMnO_3$ at the* ***(C)*** *Y K-edge and* ***(D)*** *Mn K-edge*

EXAFS. The local coordination geometry surrounding both Er/Mn and Y/Mn absorption centres has now been assessed by investigating the EXAFS region with respect to the milling time. Once again, attempts to produce fitting models of the 10 mm milled 'time-slices' proved challenging due to the small amplitude features as a result of the low structural order of the materials. Therefore, comparisons have been performed to the previous reference material EXAFS models (section 5.3.4).

First assessing the A-site edge, Er L_3-edge and Y K-edge (Figure 5.3.19), immediate changes can be observed on milling for just 30 min, in agreement with observations in the XANES region. Similarly, with the 5 mm media milled 'time-series' significant alterations in the second coordination shell of the EXAFS Fourier transform indicates lower CN of Er-Er or Y-Y scattering paths. At the Er L_3-edge after 2 h of milling subtle features in both the k^3-oscillations and Fourier transform, at 5.8 $Å^{-1}$ and 2.5 Å respectively, can be indicative of a perovskite-like structure. However, at the Y K-edge, though a feature at ~2.5 Å is visible in the Fourier transform from 2 – 6 h, observations within the k^3-oscillations suggest that even after 6 h milling the spectrum is more consistent with Y_2O_3.

EXAFS measurements performed at the Mn K-edge during the mechanochemical synthesis of both $YMnO_3$ and $ErMnO_3$ (Figure 5.3.20) show the reduction in Mn-Mn

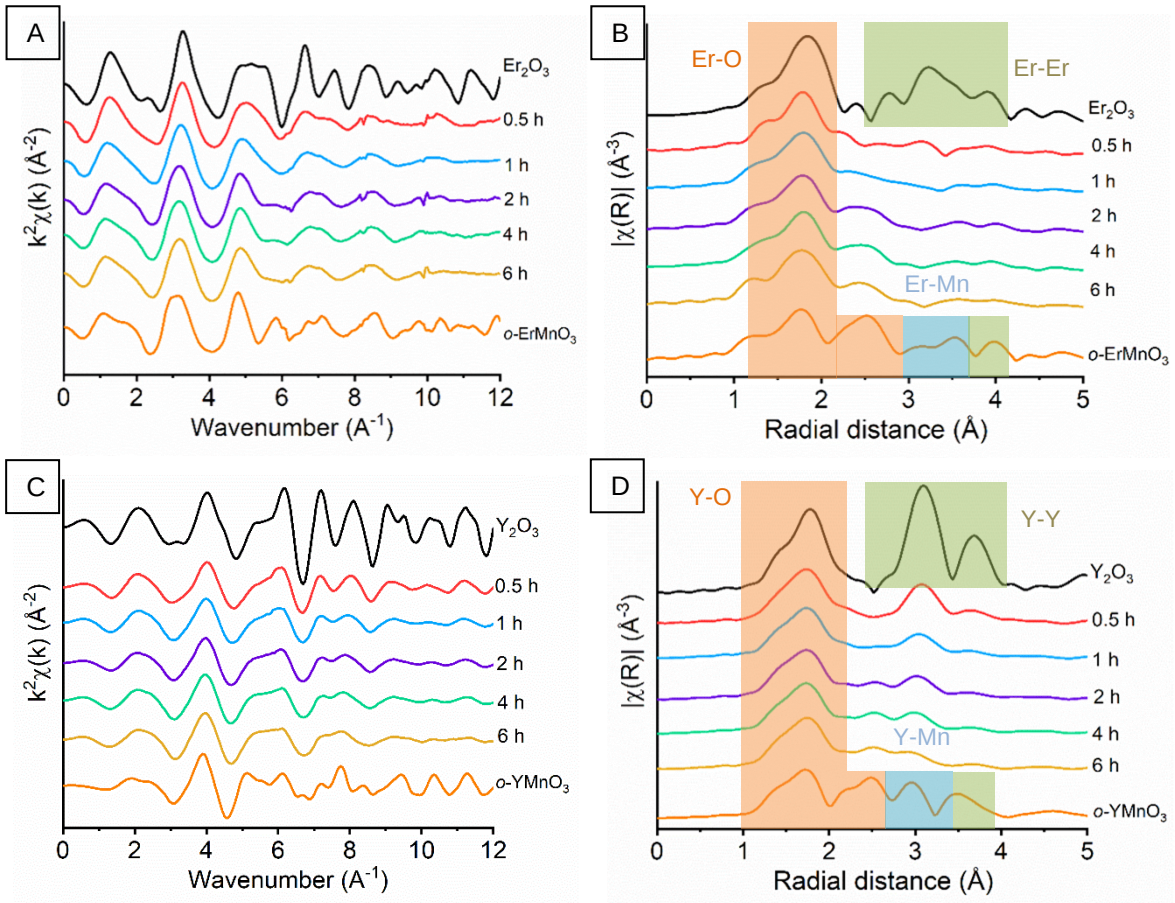

Figure 5.3.19: *k^3-weighted EXAFS oscillations at the **(A)** Er L_3-edge and its **(B)** respective nonphase-corrected Fourier transform and at the **(C)** Y K-edge with respective **(D)** Fourier transform at 'time-slices' during the mechanochemical synthesis of either $ErMnO_3$ or $YMnO_3$ with 10 mm milling media, with highlighted scattering paths*

coordination. This is more pronounced for the Er milled 'time-series', where the Fourier transform indicates no extended Mn-Mn scattering after 2 h. Assessing the Er L_3-edge k^3-oscillations for the feature at ~7 Å, which produces a unique oscillation for both the single metal oxide and the calcined perovskite, the 2 – 6 h milled species suggest some similarities to *o*-$ErMnO_3$. For the Y milled 'time-series' the amplitude of the feature corresponding to Mn-Mn scattering is only absent after 6 h of milling. With observations at the Y K-edge k^3-oscillations difficult due to similar fluctuations between the Mn_2O_3 and *o*-$YMnO_3$ reference materials it is challenging to deduce the phase of the milling intermediates.

These visual comparisons at both the A-site edges and Mn K-edge EXAFS indicates the breakdown of the A-site extended structure at earlier milling times than for Mn-Mn. This supports previous reports of the A-site dispersing over bulk Mn in the initial stages of milling (Chapter 3). However, these visual comparisons show that $YMnO_3$ is even more challenging to synthesis via mechanochemistry by comparison to $ErMnO_3$, and $LaMnO_3$. Furthermore, both EXAFS regions indicate that predominantly disordered and amorphous materials still remain after 6 h of milling, even after performing mechanochemistry with 10 mm milling media. Whilst XANES spectra show comparable profiles to that of the desired $AMnO_3$ reference structure, within the EXAFS region large differences can still be observed. This

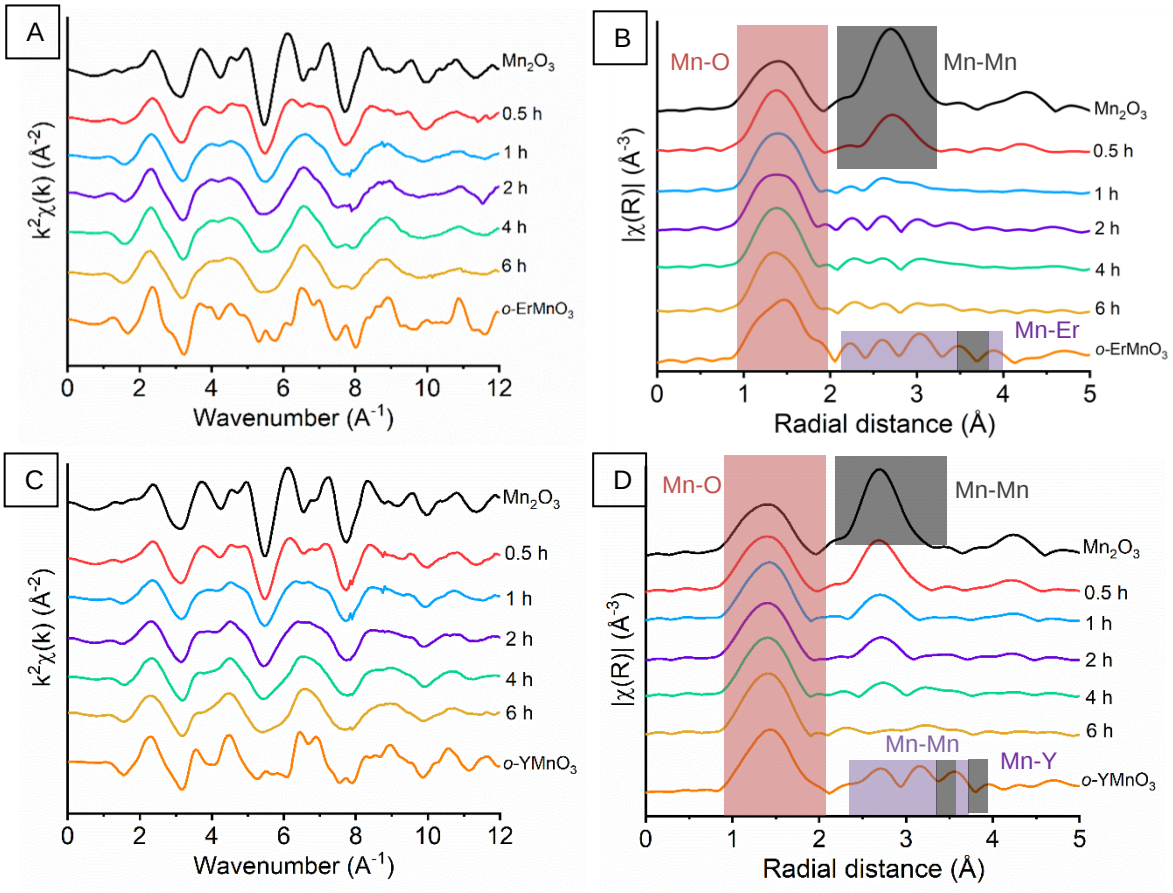

Figure 5.3.20: *Mn K-edge k^3 weighted EXAFS oscillations at 'time-slices' during the mechanochemical synthesis of* ***(A)*** *$ErMnO_3$ and its* ***(B)*** *respective nonphase-corrected Fourier transform, compared to* ***(C)*** *$YMnO_3$ with corresponding* ***(D)*** *Fourier transform with 10 mm milling media, with highlighted scattering paths*

indicates that changes to the electronic and geometric configuration of the first coordination shell occur readily, with difficulties arising in forming the extended perovskite structure.

5.3.6 Understanding the catalytic properties and behaviour of differently synthesised $AMnO_3$ materials

Equivalent to activity testing performed in Chapter 3, section 3.3.4, the decomposition of N_2O (deN_2O) has been conducted in order to understand how the synthetic route affects the activity of the $AMnO_3$ materials (Figure 5.3.21). First assessing the initial light-off curves (Figure 5.3.21A, B) both the *h*-$AMnO_3$ and *o*-$AMnO_3$ catalysts possess the better catalytic activity of all materials tested, beginning at ~350 ˚C with 100 % conversion achieved ~575 – 600 ˚C. On reproducibility no clear distinction in T_{50} is observed between the two phases Figure 5.3.21C,D). In contrast to previous deN_2O studies on $LaMnO_3$, the ball milled $AMnO_3$ materials here show no pronounced early on-set conversion at lower temperatures. The $YMnO_3$ 5 mm milled catalyst reproduced some improved activity from 350 – 450 ˚C,

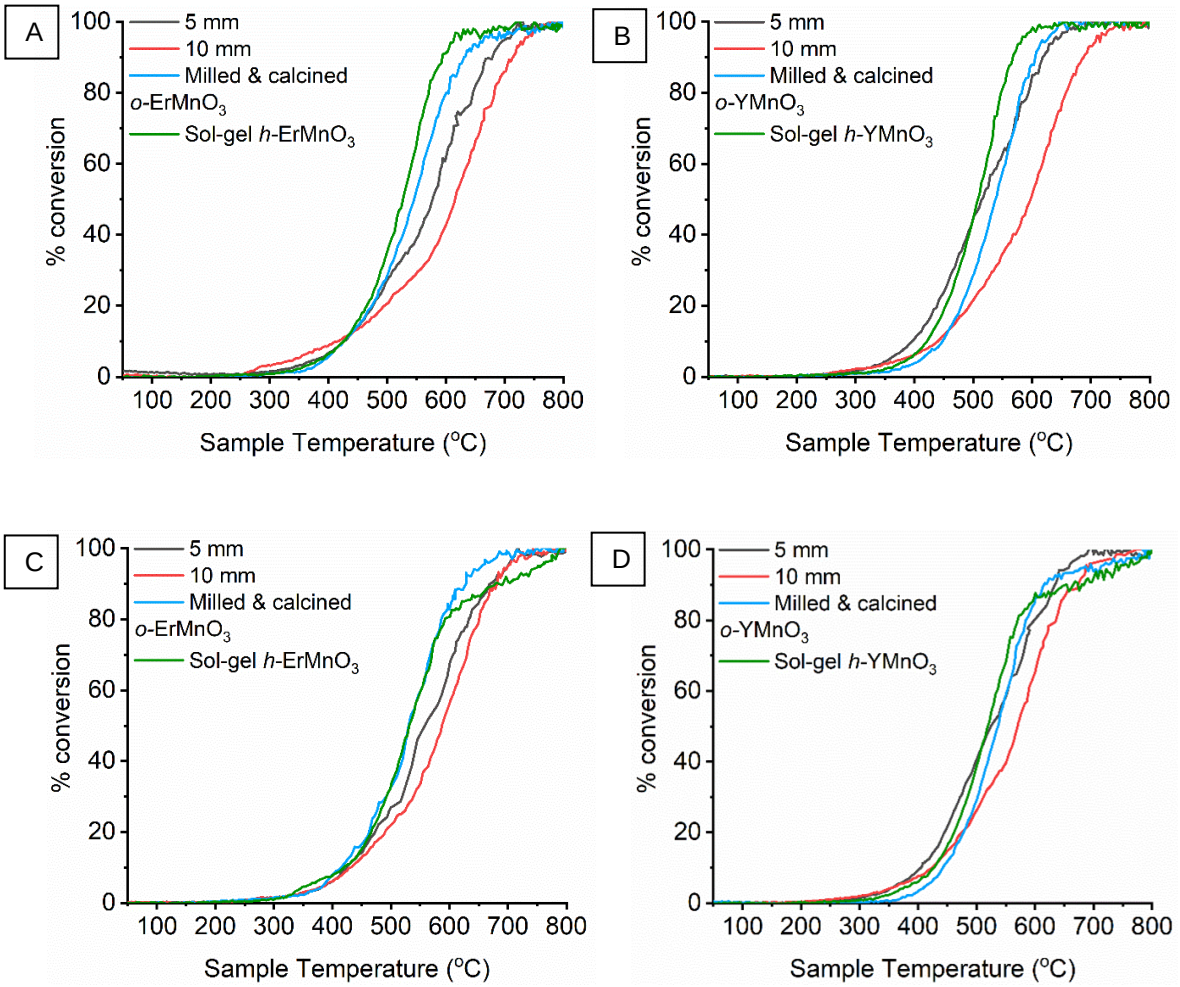

Figure 5.3.21: *Light-off curves for the percentage conversion of deN_2O to N_2 over differently synthesised* ***(A)*** *$ErMnO_3$ and* ***(B)*** *$YMnO_3$ catalysts, with corresponding reproducibility testing* ***(C)***, ***(D)***

however, is at a much lower degree than previously observed for the ball milled $LaMnO_3$. Whilst the $ErMnO_3$ 10 mm milled material does show some early on-set conversion, it was not reproduceable. The assessment by XRD and XAS of the 5 mm and 10 mm milled bulk structures detected highly amorphous species with no extended perovskite structure. This can suggest the importance of the perovskite phase, rather than homogeneous mixture of precursor powders, for effective deN_2O. Further observations of the light-off curves show a much higher T_{50} value for 10 mm ball milled species, which could result from the larger media size increase sintering at the surface. However, with all catalysts possessing comparable surface areas, 1.6 - 3.8 $m^2\ g^{-1}$, further of surface a properties and morphology must also be considered with previous XPS and TEM studies on $LaMnO_3$.

XPS studies have been performed and analysed at the Mn 2*p*, O 1*s* and either Er 4*d* or Y 3*d* regions for the differently synthesised $ErMnO_3$ and $YMnO_3$, in conjunction with Chapter 3 (section 3.3.3). First assessing the XPS Mn 2*p* region from 670 – 630 eV (Figure 5.3.22), curve fitting on all $AMnO_3$ samples was successfully performed with the use of one peak for each Mn $2p_{1/2}$ and Mn $2p_{3/2}$ features, indicating a single valency.[38] Both Mn $2p_{1/2}$ and Mn $2p_{3/2}$ peak positions for all $AMnO_3$ samples are detected within range of 641.5 and 643.2 eV, respectively, reported in literature for a Mn(III) oxidation state (Table 5.3.6.1 and Table 5.3.6.2).[39] The small deviations observed for both 5 mm and 10 mm A-sites ball species is not significant enough to indicate Mn(IV) behaviour, in agreement with the symmetrical curve fitted peaks.[40] With no significant alterations at the Mn catalytic active site between the differently synthesised $AMnO_3$ it stresses the importance of understanding changes to O 1*s* and A-site XPS regions.

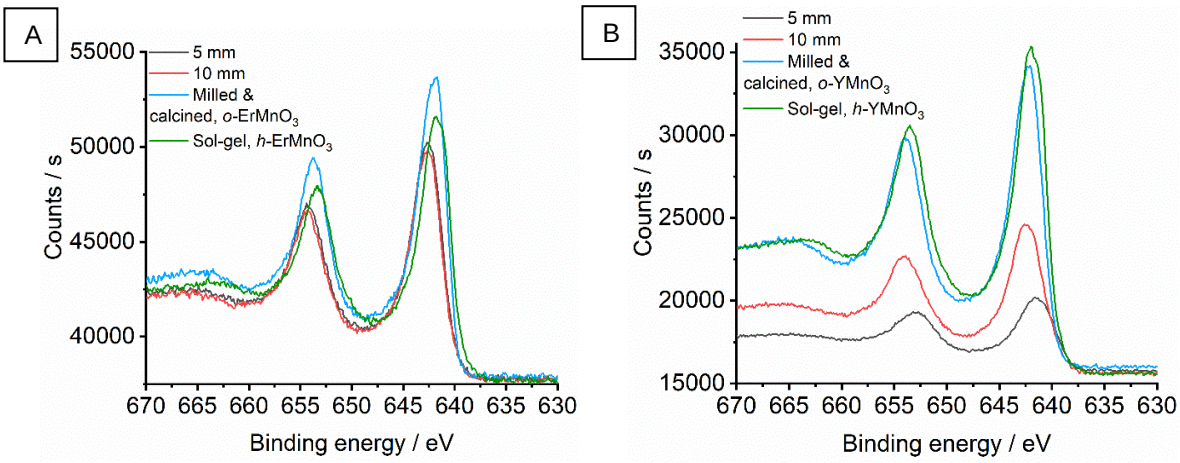

Figure 5.3.22: *XPS spectra in the Mn 2p region for differently synthesised* ***(A)*** *$ErMnO_3$ and* ***(B)*** *$YMnO_3$ catalysts*

***Table 5.3.6.1**: XPS deconvoluted peak positions and areas for differently synthesised $ErMnO_3$ catalysts at O 1s, Mn 2p and Er 4d regions*

Region	Sample	Peak 1	Peak 2
O 1*s*	**5 mm**	530.1, 63367, 68.9 %	532.5, 28654, 31.1 %
	10 mm	530.2, 67565, 68. 9%	532.5, 30573, 31.1 %
	Milled & calcined *o*-$ErMnO_3$	529.8, 64740, 72.6 %	531.8, 24466, 27.4 %
	Sol-gel *h*-$ErMnO_3$	529.4, 56427, 76.0 %	531.8, 17790, 24.0 %
Mn 2*p*	**5 mm**	642.7	654.2
	10 mm	642.6	654.1
	Milled & calcined *o*-$ErMnO_3$	642.1	653.7
	Sol-gel *h*-$ErMnO_3$	641.8	653.3
Er 4*d*	**5 mm**	167.8	
	10 mm	167.4	
	Milled & calcined *o*-$ErMnO_3$	167.8	170
	Sol-gel *h*-$ErMnO_3$	167.4	

***Table 5.3.6.2:** XPS deconvoluted peak positions and areas for differently synthesised $YMnO_3$ catalysts at O 1s, Mn 2p and Y 3d regions*

Region	Sample	Peak 1	Peak 2	Peak 3
O 1*s*	**5 mm**	529.9, 20382, 65.3%	532.3, 10810, 34.7%	
	10 mm	529.5, 12693, 100%	-	
	Milled & calcined *o*-$YMnO_3$	529.8, 29010, 70.4%	532.2, 12211, 29.6%	
	Sol-gel, *h*-$YMnO_3$	529.5, 27224, 75.0%	531.8, 9090, 25.0%	
Mn 2*p*	**5 mm**	641.9	653.4	
	10 mm	642.2	653.8	
	Milled & calcined *o*-$YMnO_3$	642.3	653.8	
	Sol-gel, *h*-$YMnO_3$	641.9	653.4	
Y 3*d*	**5 mm**	155	157.2	159.3
	10 mm	155.2	157.5	159.6
	Milled & calcined *o*-$YMnO_3$	156.1	157.5	159.4
	Sol-gel, *h*-$YMnO_3$	154.5	156.5	158.5

The O 1*s* region was next deconvoluted by curve fitting to produce two distinct features at 529.5 – 530.0 eV and 531.8 - 532.3 eV, with the exception of $YMnO_3$ 10 mm (Figure 5.3.23). The lowest energy binding peak is ascribed to lattice-type oxygens, O_2^{2-}, with the additional feature assigned to adsorbed species on the surface, O^{2-}, O^- or OH^-.[41–43] It is these adsorbed species that act to compensate for lattice oxygen vacancies, and thus can be used as a qualitative measure for surface vacancies (with all materials possessing comparable surface areas of 1.6 - 3.8 $m^2\ g^{-1}$) .[43] For a full description see Chapter 3 (section 3.3.3) and Chapter 4.[1,27]

On first observations of the O 1s XPS region, both *h*-$AMnO_3$ and *o*-$AMnO_3$ reference catalysts record much greater intensity for the peak assigned to lattice-type oxygens compared to that of absorbed species (Table 5.3.6.1 and Table 5.3.6.2). This is expected is to arise from their high temperature synthesise forming a more ordered sub-oxygen lattice and causing sintering of surface sites.[44] Most significantly, the ball milled catalysts report a higher percentage of absorbed species at the surface. However, this does not correspond to an earlier on-set conversion of N_2O as it did for $LaMnO_3$, indicating these ball milled $ErMnO_3$ and $YMnO_3$ catalysts have different factors dominating their activity.

Measurements at both the Er 4*d* and Y 3*d* confirm the sesquioxide phase is present at the surface, rather than their analogous hydroxide (Figure 5.3.24).[45,46] Both sol-gel synthesised $AMnO_3$ Er 4*d* and Y 3*d* spectra show a slight shift in the peak position binding energy, indicating how the change in hexagonal A-site coordination to oxygen is also present at the surface, in agreement with the O1*s* region.

Previous work on $LaMnO_3$ showed that when the A-site La 3*d* XPS region detected -OH type species, which when combined with an increase in oxygen vacancies at the surface produced an earlier on-set production of N_2 from N_2O a lower temperature.[1] With the ball milled $AMnO_3$ samples possessing an increase in oxygen vacancies but no A-site hydroxide species, it could indicate the importance of the presence of -OH for low temperature deN_2O conversion.

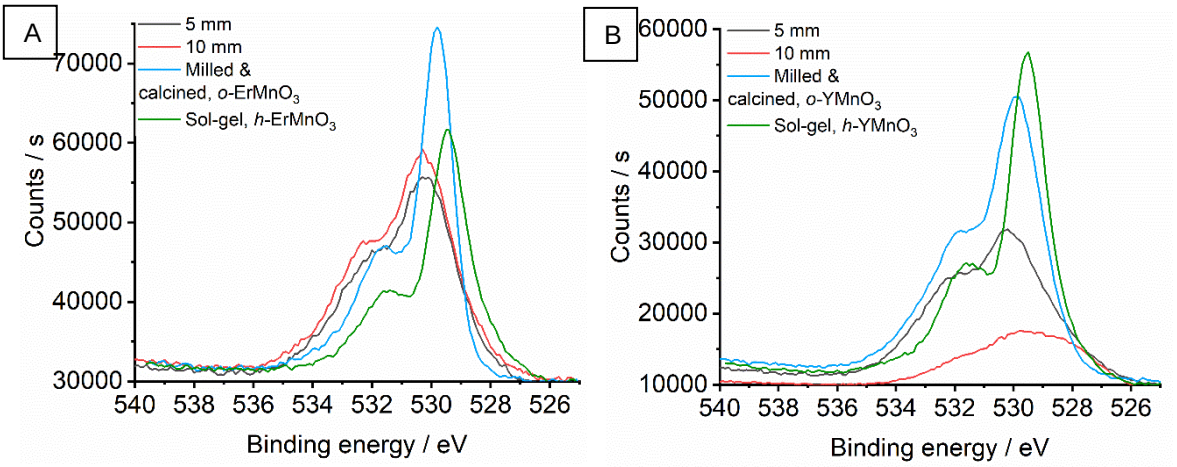

Figure 5.3.23: *XPS spectra at the O 1s region for differently synthesised* ***(A)*** *$ErMnO_3$ and* ***(B)*** *$YMnO_3$ catalysts*

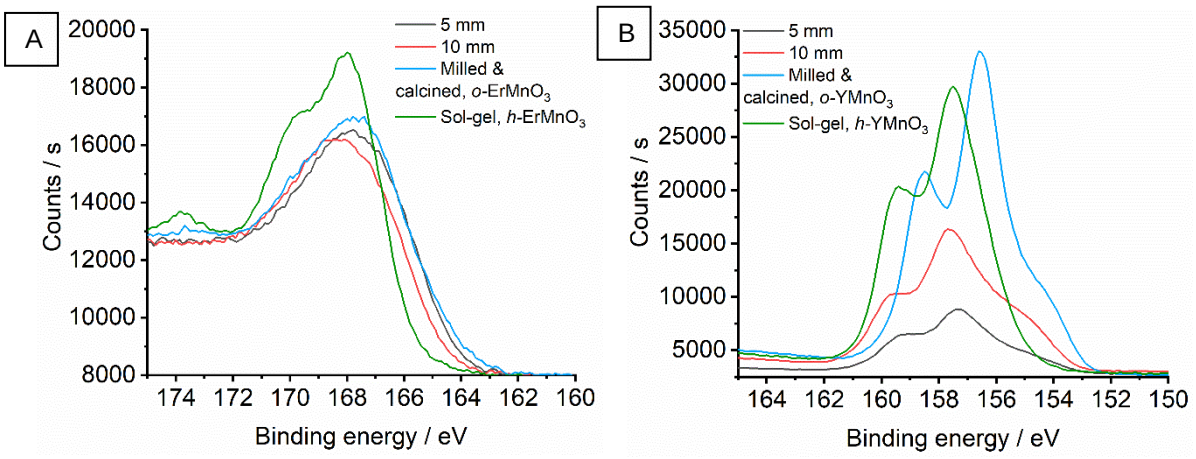

Figure 5.3.24: *XPS spectra for the differently synthesised $AMnO_3$ catalysts at* ***(A)*** *the Er 4d region for $ErMnO_3$ and* ***(B)*** *the Y 3d for $YMnO_3$*

In order to investigate how changes to the A-site effect the topological structure of the different manganite perovskite catalysts, the morphology and elemental mapping has been examined by TEM. Figure 5.3.25 and Figure 5.3.26 shows both Er and Y 5mm and 10 mm milled ball milled materials to have comparable agglomerated structures. On calcination of the 5 mm milled species, *o*-$AMnO_3$ (Figure 5.3.25C and Figure 5.3.26C), the image shows signs of a more defined structure, however, remains largely agglomerated. Preparation of the perovskite by sol-gel, *h*-$AMnO_3$, shows a completely alterative 'honey-comb' cage-like structure, consisting of larger particle sizes (Figure 5.3.25D and Figure 5.3.26D).[17] Though TEM detects vastly different morphologies for these two $AMnO_3$ phases, the light-off curves for deN_2O (Figure 5.3.21) show comparable catalytic behaviour indicating the importance of a combination of factors such as surface defects and vacancies.

Bright field (BF)-TEM imaging was then performed to achieve high magnification resolution images (Figure 5.3.27 and Figure 5.3.28). All ball milled $AMnO_3$ samples indicate predominantly amorphous material. In comparison to the 5 mm Er A-site species (Figure 5.3.27A), the 10 mm catalyst (Figure 5.3.27B), observed an increase in the number of crystallites in the matrix, in agreement with XRD studies. The 5 mm Y A-site sample (Figure 5.3.28A), showed a higher proportion of crystal structures than the analogous Er species (Figure 5.3.27A), however, XAS studies indicate the sample remains in its precursor-like phase. After calcination of the 5 mm catalyst, *o*-$AMnO_3$ images (Figure 5.3.27C and Figure 5.3.28C) detected a more crystalline sample, with the Y A-site producing a highly strained and defected structure. This corresponds well to EXAFS analysis, where a higher degree of structural distortion was modelled in comparison to *o*-$ErMnO_3$. The sol-gel *h*-$AMnO_3$ (Figure 5.3.27D and Figure 5.3.28D) produces vastly different, highly uniform

microstructures in contrast to the ball milled materials, however, an amorphous phase is still suggested to surround the exterior of the particles.

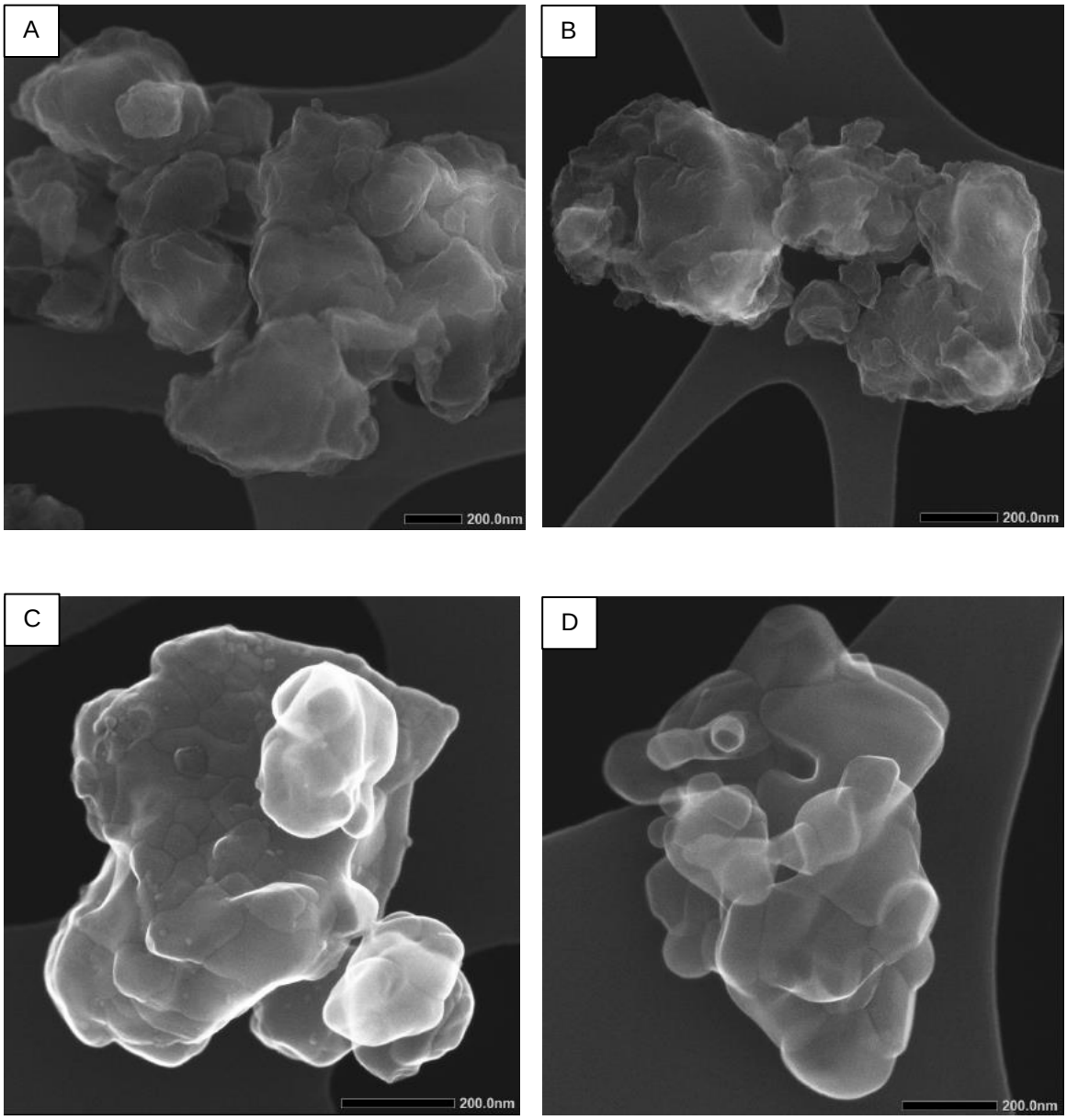

Figure 5.3.25: *SE images for A-site Er, showing the morphological changes between* ***(A)*** *5 mm* ***(B)*** *10 mm milled compared to reference* ***(C)*** *o-$ErMnO_3$ milled and calcined and* ***(D)*** *h-$ErMnO_3$ sol-gel*

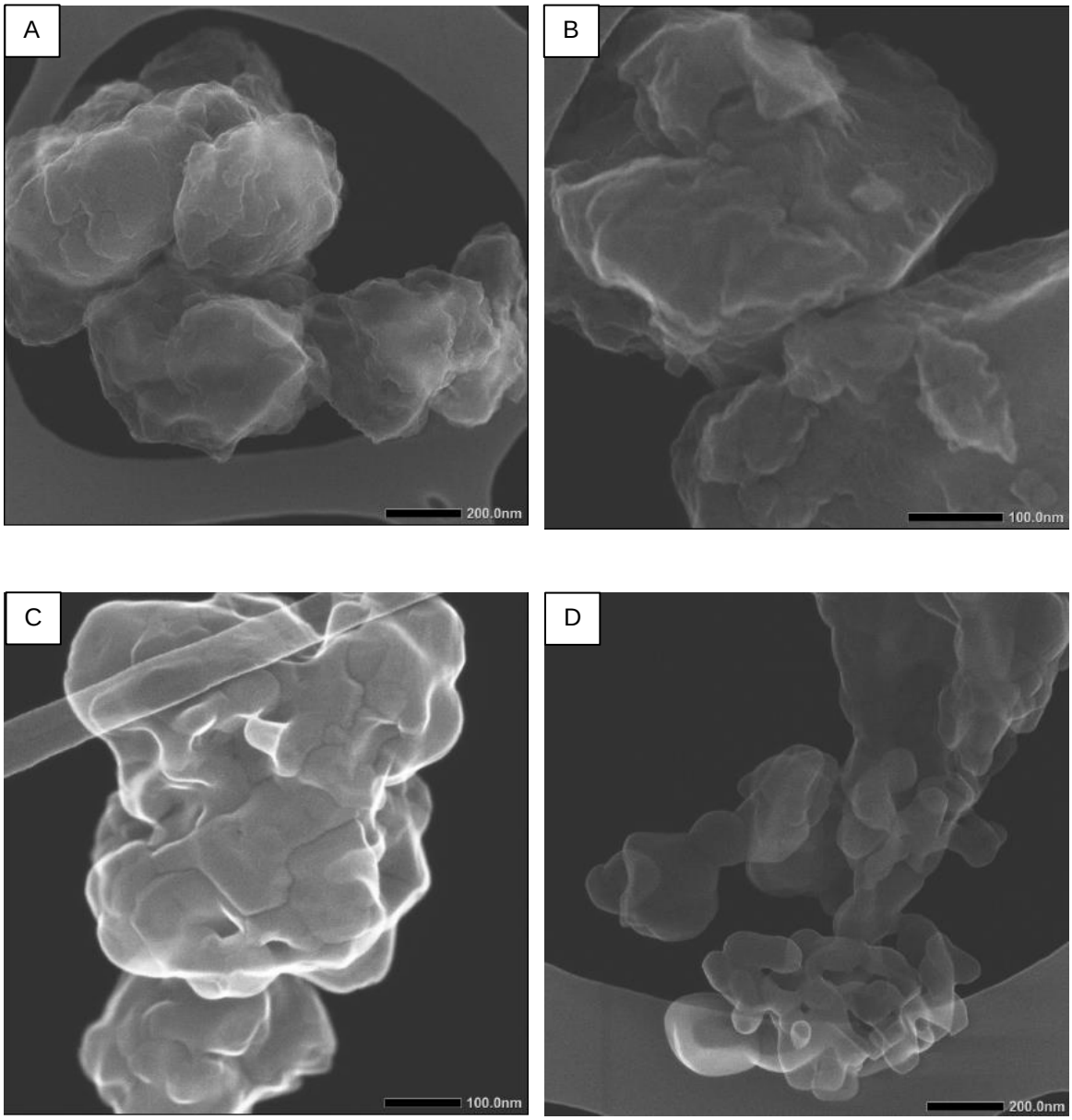

Figure 5.3.26: *SE images for A-site Y, showing the morphological changes between* ***(A)*** *5 mm* ***(B)*** *10 mm milled compared to reference* ***(C)*** *o-$YMnO_3$ milled and calcined and* ***(D)*** *h-$YMnO_3$ sol-gel*

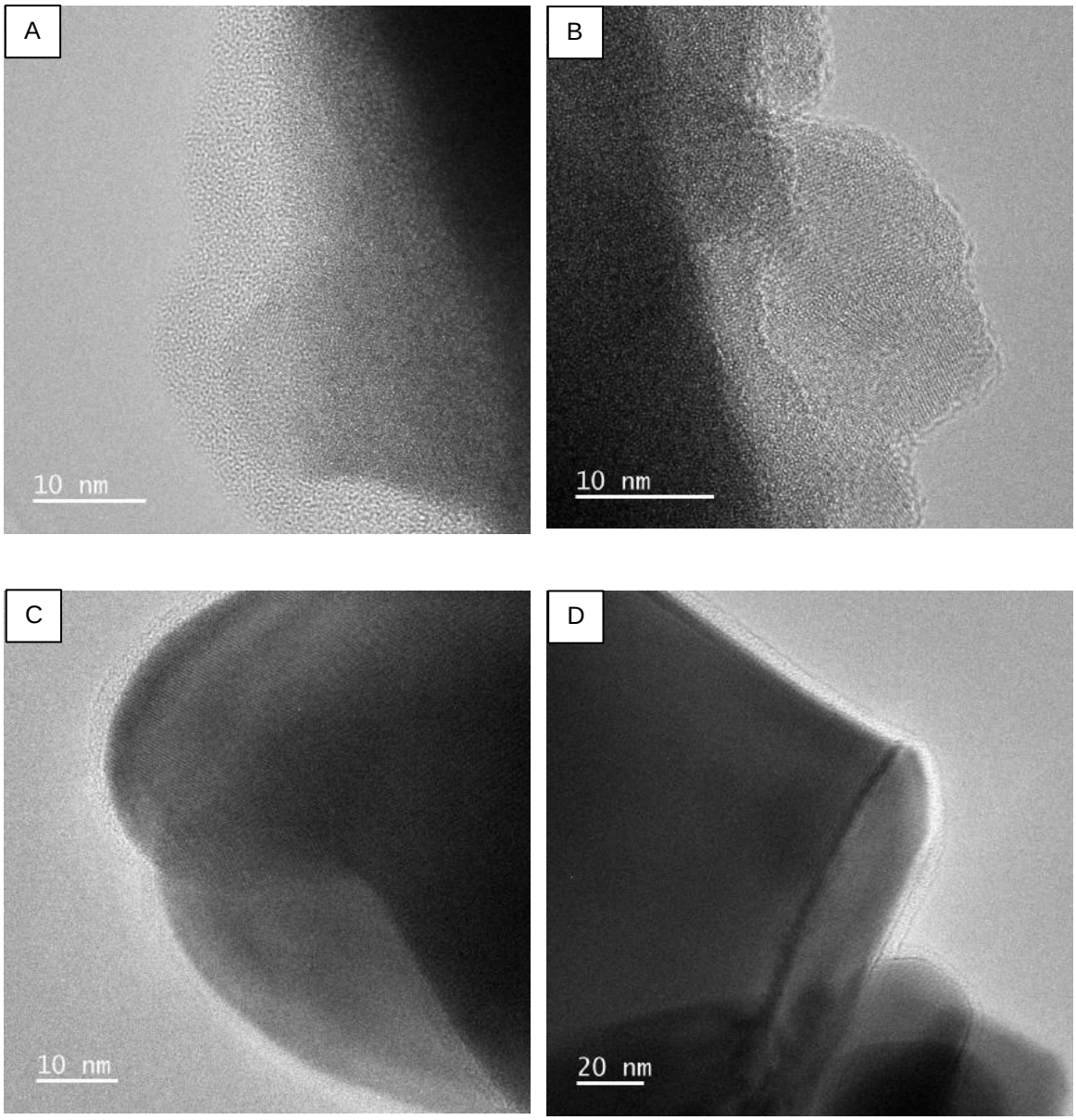

Figure 5.3.27: *BF-TEM images for A-site Er, showing the morphological changes between* ***(A)*** *5 mm* ***(B)*** *10 mm milled compared to reference* ***(C)*** *o-$ErMnO_3$ milled and calcined and* ***(D)*** *h-$ErMnO_3$ sol-gel*

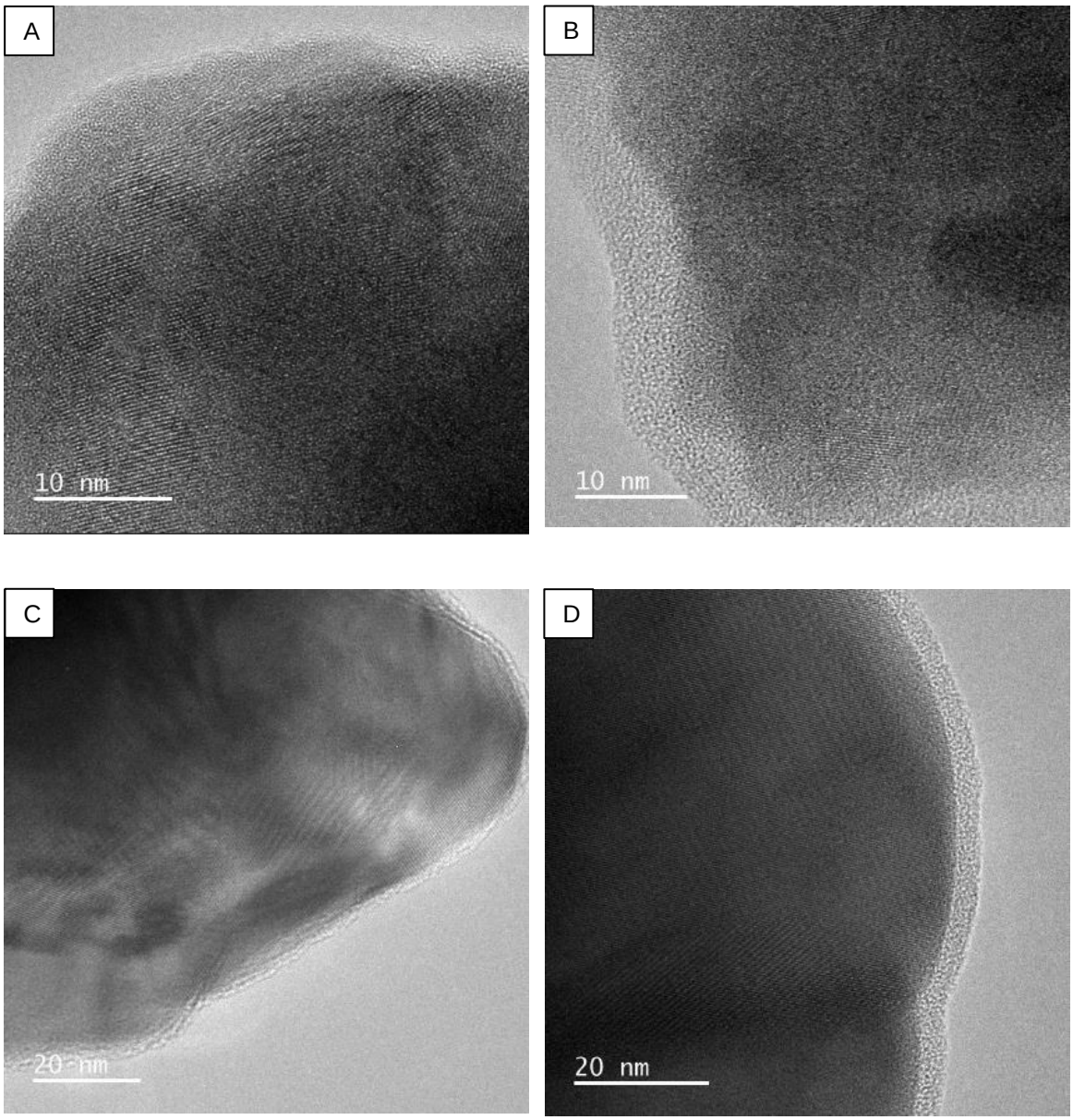

Figure 5.3.28: *BF-TEM images for A-site Er, showing the morphological changes between* ***(A)*** *5 mm* ***(B)*** *10 mm milled compared to reference* ***(C)*** *o-$YMnO_3$ milled and calcined and* ***(D)*** *h-$YMnO_3$ sol-gel*

Performing compositional analysis on a TEM by X-ray emission in scanning mode, elemental mapping images have been produced consisting of Mn (red), A-site, Er or Y (green), oxygen (white) and Zr (blue) (Figure 5.3.29 and Figure 5.3.30). The first clear observation for all milled $AMnO_3$ species, including the reference *o*-$AMnO_3$, is the addition of Zr contamination. For the 5 mm and 10 mm milled catalysts (Figure 5.3.29A,B and Figure 5.3.30A,B) the Zr is suggested to be trapped in the Mn A-site matrix, whereas on calcination of the 5 mm sample the Zr is excluded from the *o*-$AMnO_3$ crystals (Figure 5.3.29C and Figure 5.3.30C). The calculated at% indicates the 10 mm milled species to have a higher proportion of Zr at ~ 10%, in comparison to the 5 mm, at < 4 %. This is an unfortunate characteristic of increasing the impact energy with 10 mm milling media, to result in additional degradation of the milling media and jars. In turn, this could be a detrimental

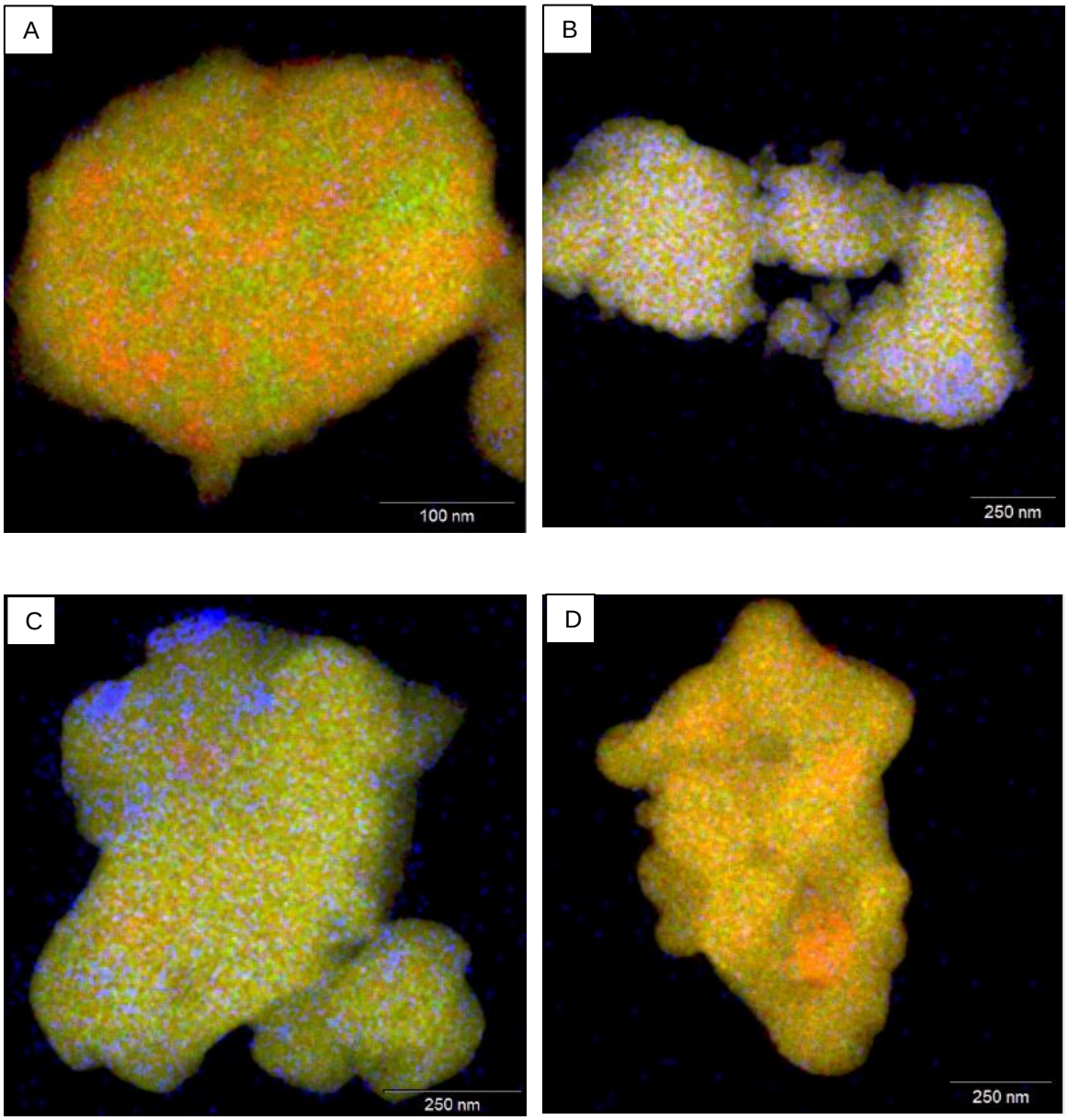

Figure 5.3.29: *Compositional analysis by EDX in scanning mode for A-site Y, showing the morphological changes between* ***(A)*** *5 mm* ***(B)*** *10 mm milled $ErMnO_3$ compared to reference* ***(C)*** *milled and calcined, o-$ErMnO_3$ and* ***(D)*** *h-$ErMnO_3$ sol-gel*

effect to the catalytic activity of the 10 mm $AMnO_3$ catalysts for deN_2O. Further assessment of the elemental maps suggests a high degree of inhomogeneity of all samples, even including the sol-gel prepared *h*-$AMnO_3$. For all samples prepared with a Y A-site oxide (Figure 5.3.30) the mapping images show a high proportion of the A- site at the surface, compared to the analogous Er materials.

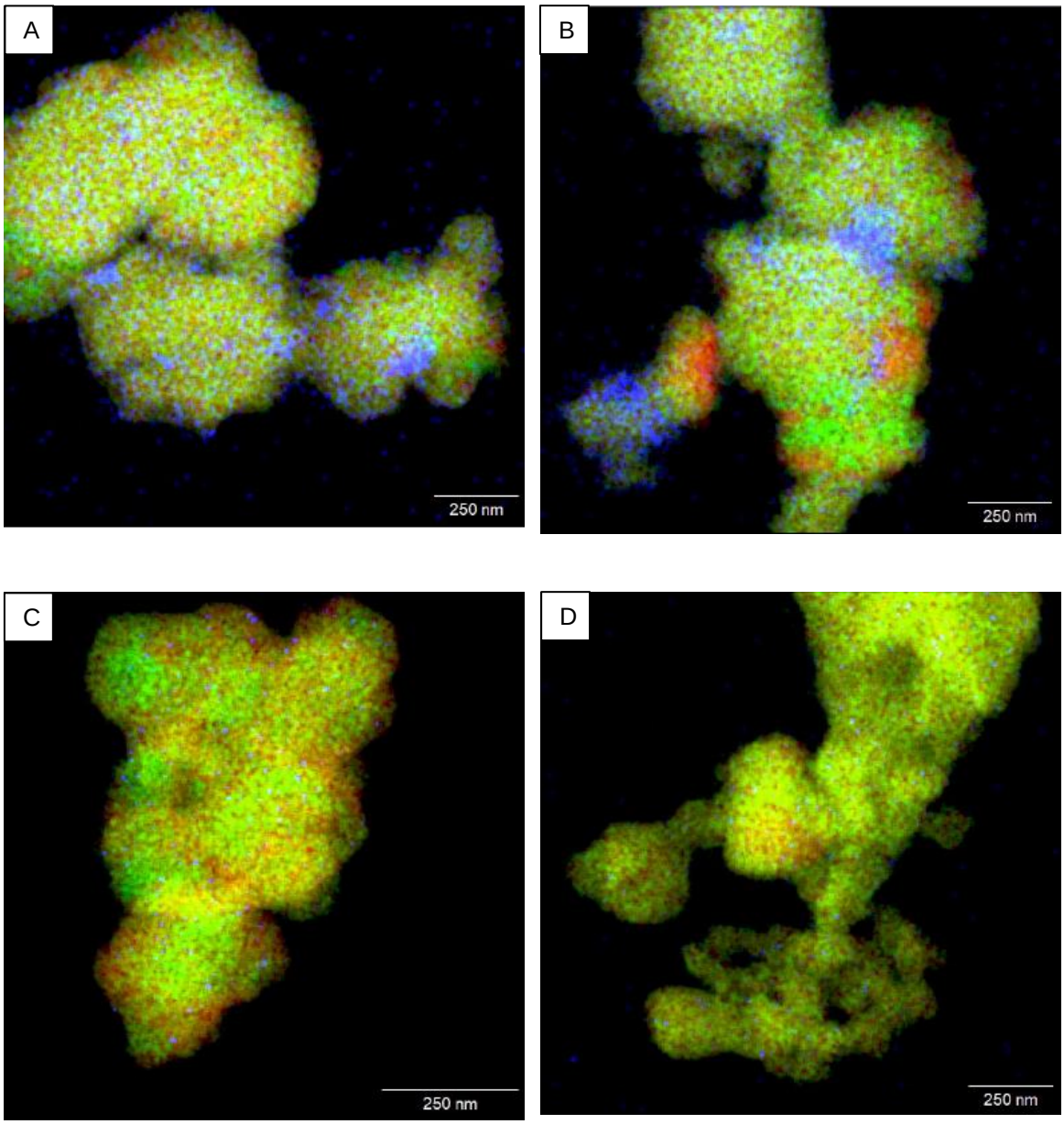

Figure 5.3.30: *Compositional analysis by EDX in scanning mode for A-site Y, showing the morphological changes between* ***(A)*** *5 mm* ***(B)*** *10 mm milled $YMnO_3$ compared to reference* ***(C)*** *milled and calcined, o-$YMnO_3$ and* ***(D)*** *h-$YMnO_3$ sol-gel*

Assessing the deN_2O light-off curves for the ball milled $AMnO_3$ catalysts (Figure 5.3.21) no change in activity is observed at higher temperatures. Previously, two regions in the light-off curve was observed for ball milled $LaMnO_3$ (section 3.3.4), due to the formation of a highly crystalline perovskite phase. These ball milled $AMnO_3$ catalysts are, however, still expected to undergo a phase transformation as a consequence of the elevated temperatures. To assess this structural change, XRD and XAS studies have been completed on the post deN_2O samples.

Figure 5.3.31 and Figure 5.3.32 show XRD studies measured before and after deN_2O for the differently synthesised $ErMnO_3$ and $YMnO_3$ catalysts, respectively. For the 5 mm and 10 mm ball milled $AMnO_3$ materials a high degree of crystalline orthorhombic phase is detected after catalytic testing. Most significantly, the milled and calcined *o*-$AMnO_3$ catalyst for both Er and Y A-sites (Figure 5.3.31C and Figure 5.3.32C) undergoes a phase transformation from orthorhombic to hexagonal; in agreement that the hexagonal phase is the thermodynamically stable species. No change is observed in the long range structure after deN_2O for the sol-gel synthesised *h*-$AMnO_3$ (Figure 5.3.31D and Figure 5.3.32D).

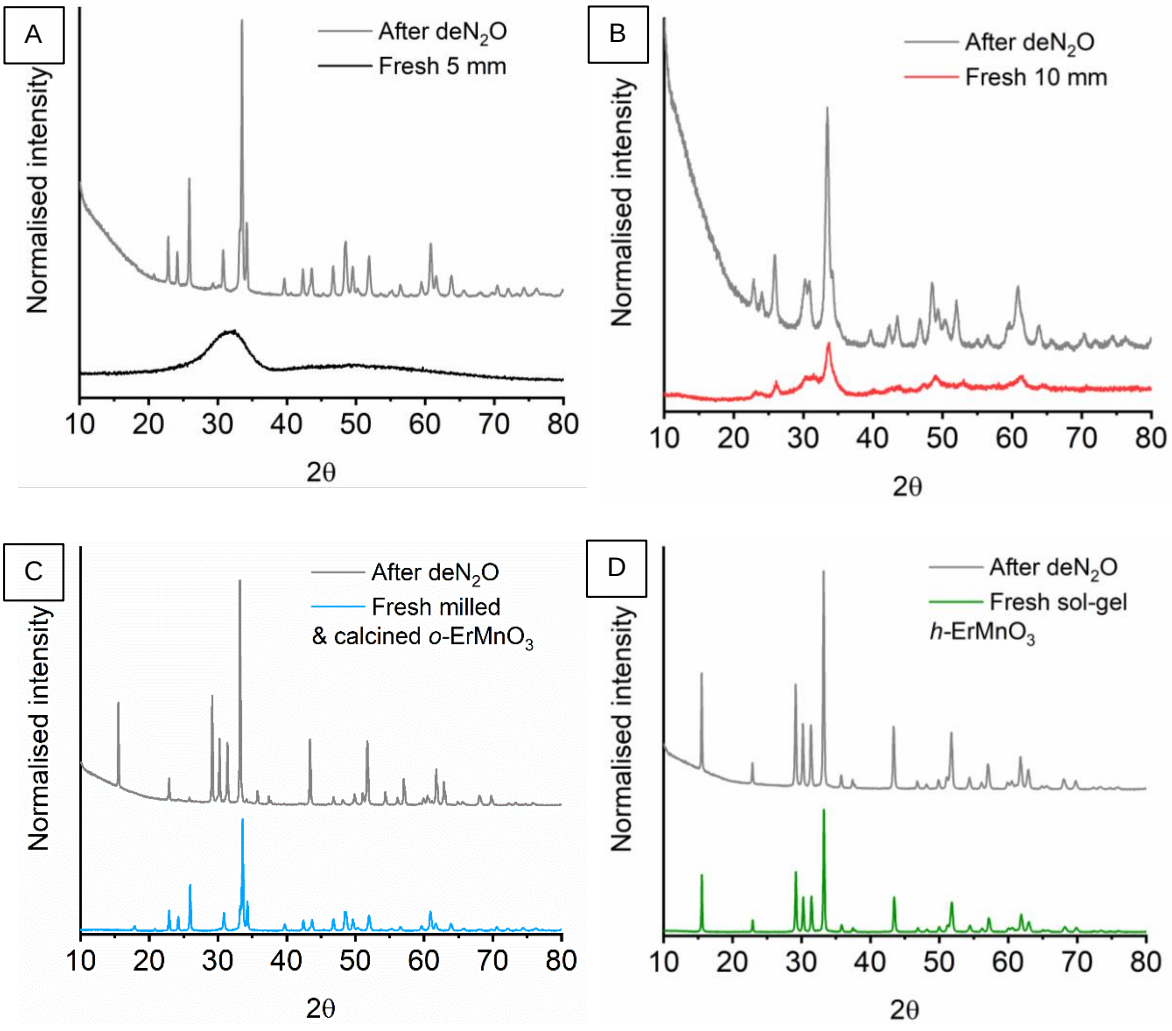

Figure 5.3.31: *Comparison of XRD patterns of differently synthesised $ErMnO_3$ catalysts before and after deN_2O studies*

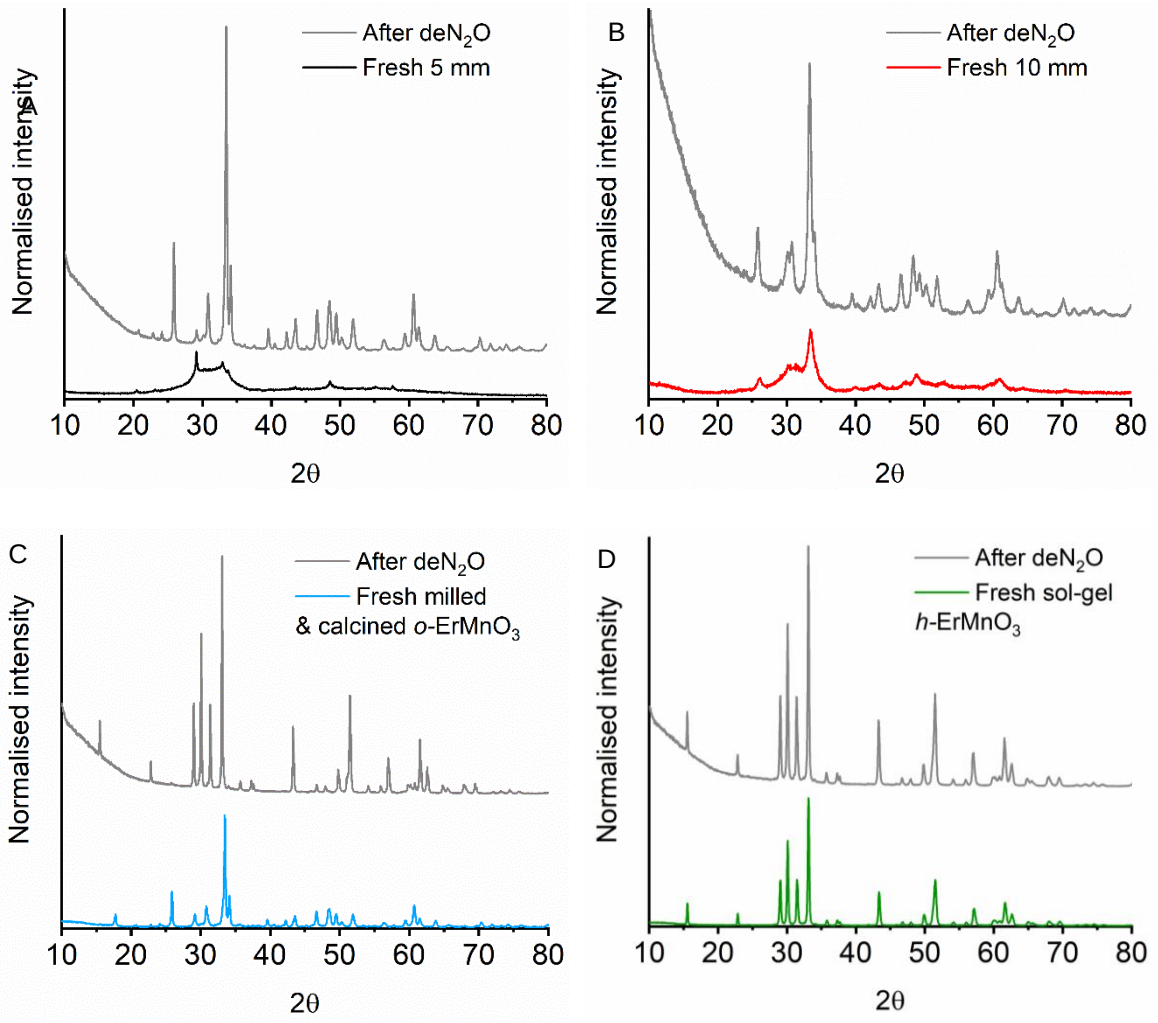

Figure 5.3.32: *Comparison of XRD patterns of differently synthesised $YMnO_3$ catalysts before and after deN_2O studies*

X-ray absorption studies have been performed to understand how the average bulk structure is altered after completing deN_2O. First assessing the Er L_3-edge and Y K-edge XANES spectra (Figure 5.3.33) it is clear the milled and calcined catalyst now possesses the same geometric and electronic configuration as *h*-$AMnO_3$, confirming a phase transformation to hexagonal. Both 5 mm and 10 mm ball milled $AMnO_3$ at the A-site edge follow the same spectral profile as for the *o*-$AMnO_3$. These observations are also reflected in the Mn K-edge XANES (Figure 5.3.34). Issues occurred when measuring the 5 mm sample at the Y K-edge, however, the spectrum is expected to match that of the 10 mm and *o*-$AMnO_3$ species.

The EXAFS k^3-oscillations and respective Fourier transforms at either A-site edge (Er or Y) (Figure 5.3.35) and the Mn K-edge (Figure 5.3.36) suggest the formation of a more ordered material after deN_2O has been performed. EXAFS analysis was performed for both $ErMnO_3$ (Table 5.3.6.3,

Table ***5.3.6.4***, Figure 5.3.37), and $YMnO_3$ K-edge (Table 5.3.6.5, Table 5.3.6.6, Figure 5.3.38), analogous to section 5.3.4. The simulated EXAFS models confirmed $AMnO_3$ 5 mm and 10 mm to possess orthorhombic structures, with the sol-gel and milled and calcined having a hexagonal geometry. The data was modelled with close comparisons to the expected crystalline structures.

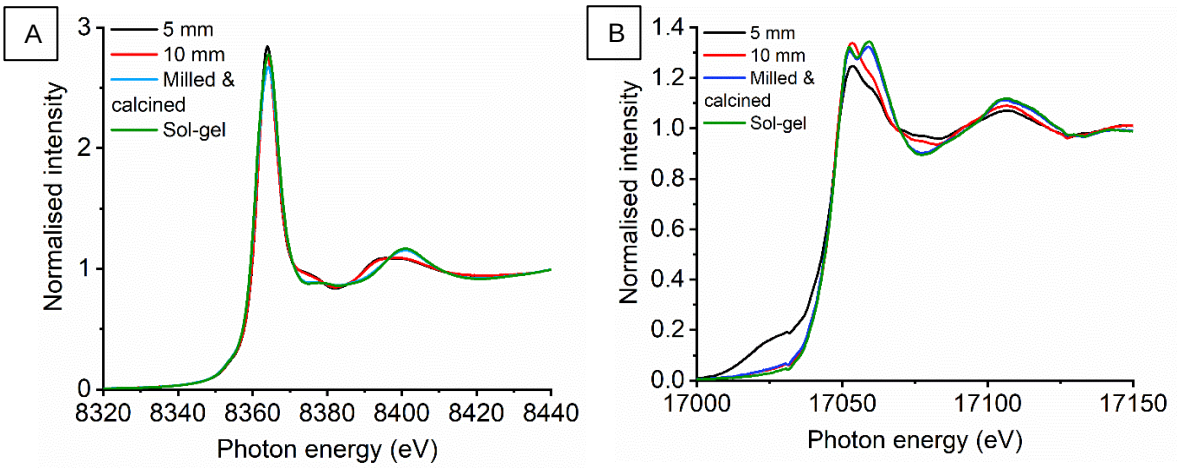

Figure 5.3.33: (A) *Er L_3-edge and* ***(B)*** *Y K-edge XANES patterns of differently synthesised $YMnO_3$ catalysts before and after deN_2O studies*

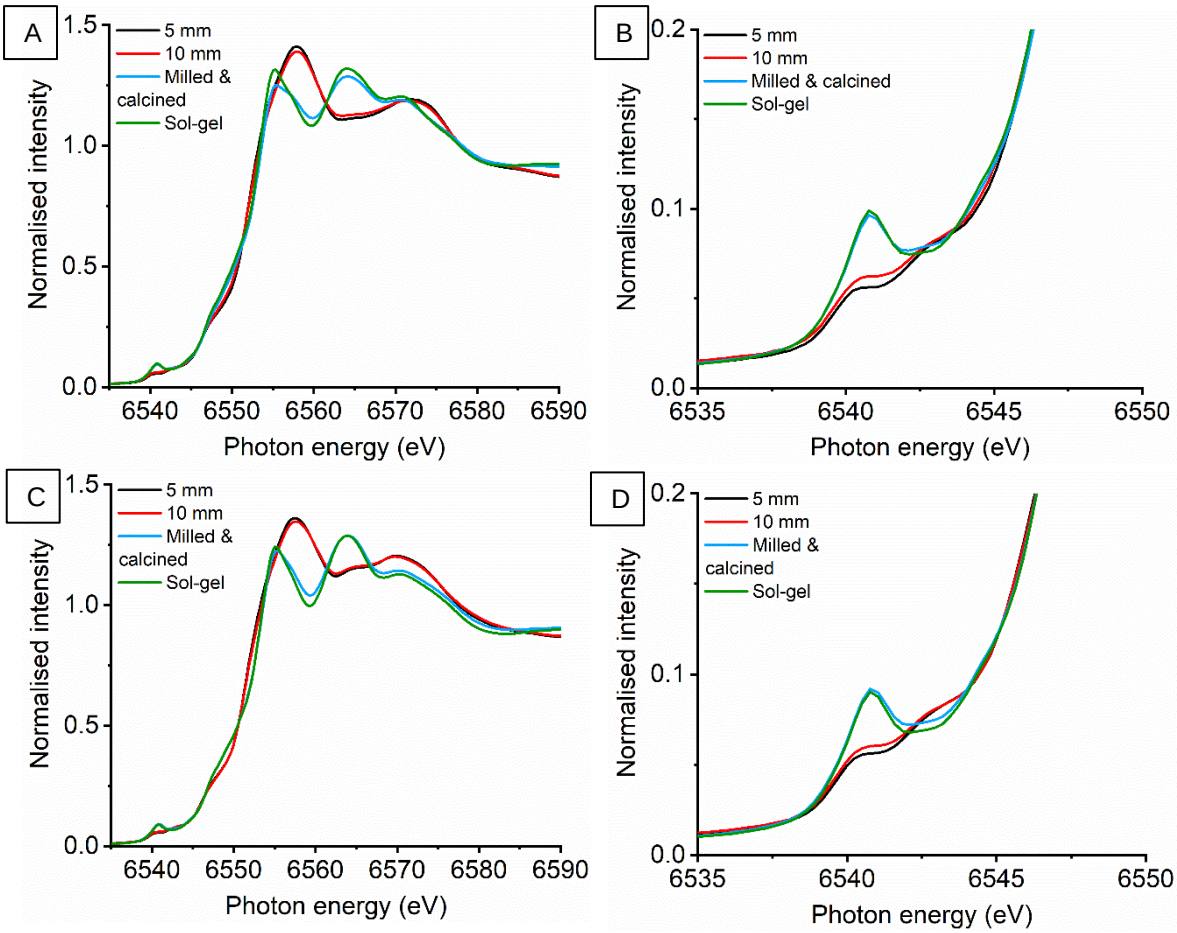

Figure 5.3.34: *Mn K-edge XANES for* ***(A)*** *$ErMnO_3$ and* ***(B)*** *highlighted pre-edge region compared to* ***(C)*** *$YMnO_3$ and* ***(D)*** *highlighted pre-edge region after deN_2O studies*

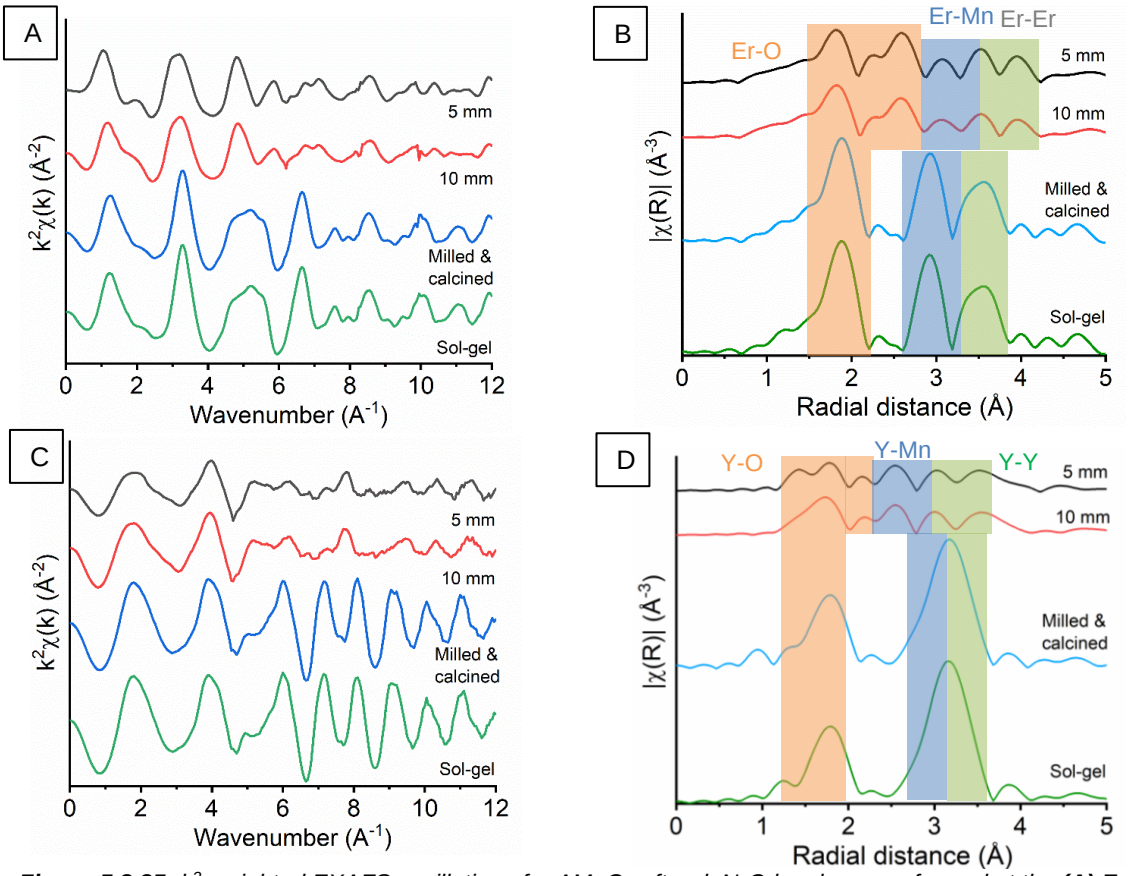

Figure 5.3.35: *k^3-weighted EXAFS oscillations for $AMnO_3$ after deN_2O has been performed at the* ***(A)*** *Er L_3-edge and its* ***(B)*** *respective Fourier transform and at the* ***(C)*** *Y K-edge with respective* ***(D)*** *Fourier transform*

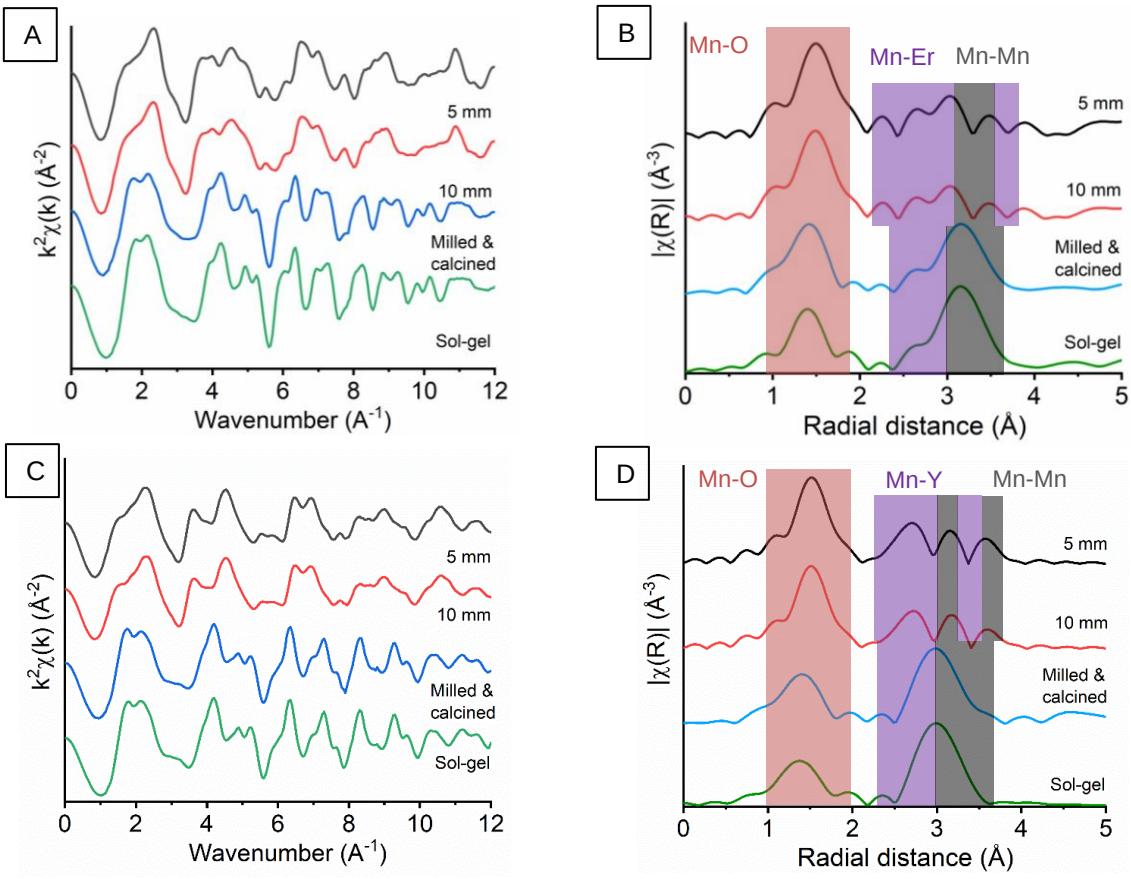

Figure 5.3.36: *Mn K-edge k^3-weighted EXAFS oscillations $AMnO_3$ after deN_2O has been performed for* ***(A)*** *$ErMnO_3$ and* ***(B)*** *respective Fourier transform and for* ***(C)*** *$YMnO_3$ and* ***(D)*** *respective Fourier transform*

Table 5.3.6.3: *EXAFS fitting parameters for the Er L_3-edge for spectra collected on o- and h-$ErMnO_3$. Fitting parameters: $S0^2$=0.8 as determined by the use of an Er foil standard; Fit range 3 < k>13, 1.2 <R > 4.0. [a]CN fixed to known structures and the number of scattering paths reduced in order to minimise fitting parameters*

$ErMnO_3$ Sample	Bond (Abs-Sc)	[a]CN	E_0 (eV)	σ^2	R / Å	R_{factor}
Sol-gel *h*-$ErMnO_3$	Er-O1	7	2(1)	0.005(1)	2.28(1)	0.027
	Er-Mn1	3		0.003(1)	3.32(1)	
	Er-Er1	6		0.006(1)	3.53(1)	
Milled & calcined *h*-$ErMnO_3$	Er-O1	7	2(1)	0.005(1)	2.28(1)	0.026
	Er-Mn1	3		0.004(1)	3.32(1)	
	Er-Er1	6		0.006(1)	3.54(1)	
5mm *o*-$ErMnO_3$	Er-O1	4	1(2)	0.005(1)	2.25(2)	0.42
	Er-O2	4		0.015(8)	2.46(4)	
	Er-Mn1	4		0.009(2)	3.08(2)	
	Er-Mn2	2		0.006(2)	3.30(3)	
	Er-Er1	4		0.007(3)	3.84(3)	
	Er-Er2	2		0.003(2)	4.01(4)	
10 mm *o*-$ErMnO_3$	Er-O1	4	1(2)	0.005(2)	2.25(2)	0.035
	Er-O2	4		0.014(7)	2.47(4)	
	Er-Mn1	4		0.007(2)	3.08(2)	
	Er-Mn2	2		0.006(3)	3.27(4)	
	Er-Er1	4		0.005(3)	3.84(3)	
	Er-Er2	2		0.003(2)	4.02(4)	

Table 5.3.6.4: *EXAFS fitting parameters for the Mn K-edge for spectra collected on o- and h-$ErMnO_3$. Fitting parameters: $S0^2$=0.7 as determined by the use of a Mn foil standard; Fit range 3 < k>14, 1.2 <R >3.85. [a]CN fixed to known structures and the number of scattering paths reduced in order to minimise fitting parameters*

$ErMnO_3$ Sample	Bond (Abs-Sc)	[a]CN	E_0 (eV)	σ^2	R / Å	R_{factor}
Sol-gel *h*-$ErMnO_3$	Mn-O1	2	-1(2)	0.002(2)	1.88(2)	0.017
	Mn-O2	3		0.007(3)	2.05(2)	
	Mn-Er1	3		0.006(3)	3.23(3)	
	Mn-Mn1	6		0.005(1)	3.62(1)	
Milled & calcined *h*-$ErMnO_3$	Mn-O1	2	-4(2)	0.003(2)	1.87(2)	0.24
	Mn-O2	3		0.012(5)	2.00(2)	
	Mn-Er21	3		0.005(2)	3.35(2)	
	Mn-Mn1	6		0.007(2)	3.53(1)	
5mm *o*-$ErMnO_3$	Mn-O1	4	-7(3)	0.003(1)	1.91(1)	0.027
	Mn-O2	2		0.007(5)	2.23(3)	
	Mn-Er1	4		0.011(4)	3.09(3)	
	Mn-Er2	2		0.003(2)	3.31(3)	
	Mn-Mn1	2		0.006(5)	3.75(4)	
10mm *o*-$ErMnO_3$	Mn-O1	4	-7(3)	0.004(1)	1.90(1)	0.035
	Mn-O2	2		0.011(5)	2.24(4)	
	Mn-Er1	4		0.012(4)	3.08(3)	
	Mn-Er2	2		0.004(2)	3.31(3)	
	Mn-Mn1	2		0.007(4)	3.76(4)	

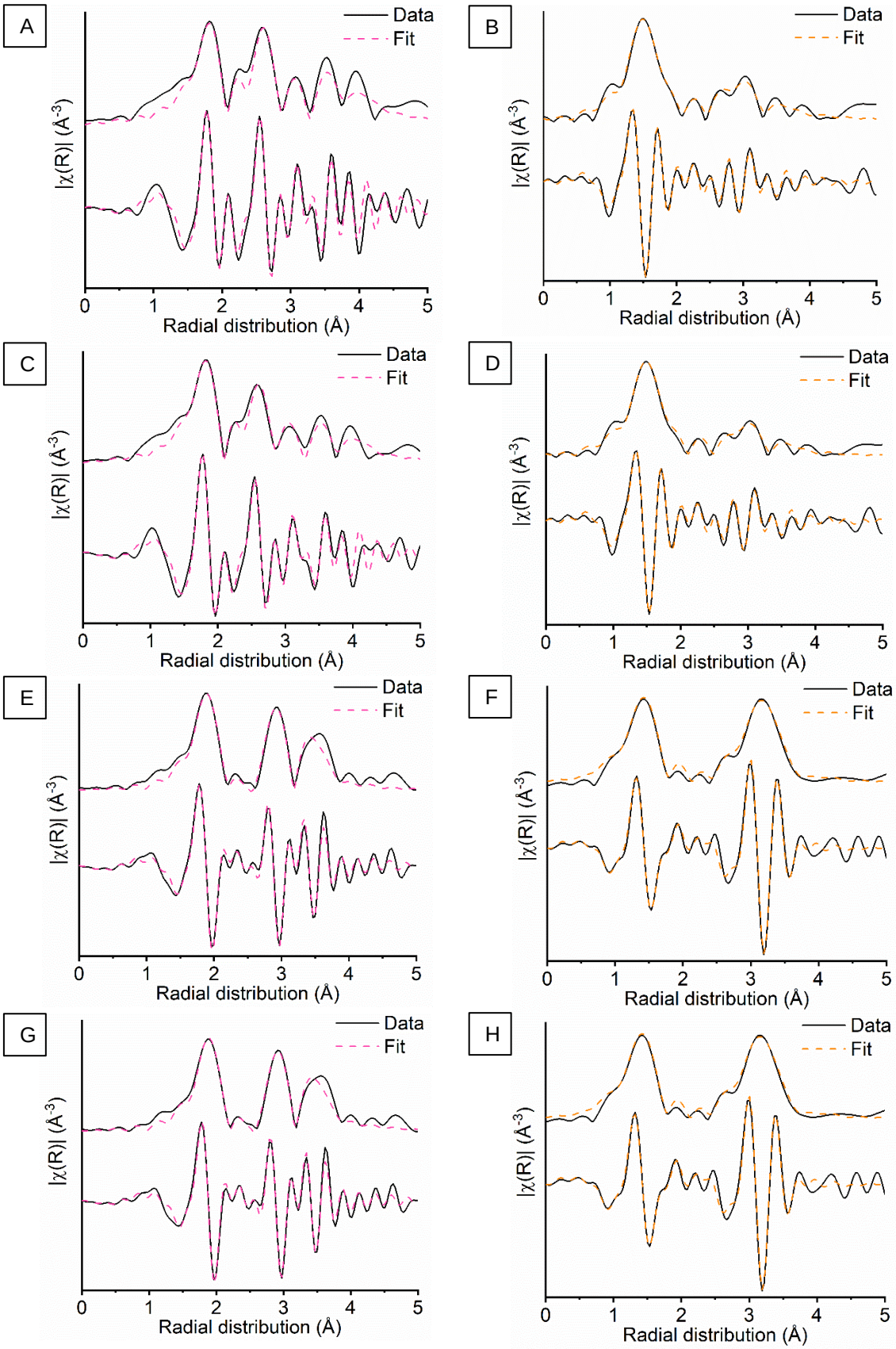

Figure 5.3.37: *Er L_3-edge (pink) and Mn K-edge (orange) EXAFS data* ***(A)*** *and* ***(B)*** *6 h milled with 5 mm media,* ***(C)*** *and* ***(D)*** *10 mm media,* ***(E)*** *and* ***(F)*** *milled and calcined $ErMnO_3$ and* ***(G)*** *and* ***(H)*** *sol-gel h-$ErMnO_3$ showing the magnitude and imaginary components of the k^3-weighted Fourier transform data and fits*

Table 5.3.6.5: *EXAFS fitting parameters for the Y K-edge for spectra collected on o- and h-$YMnO_3$ after deN_2O. Fitting parameters: $S0_2$=1.0 as determined by the use of a Y foil standard; Fit range 3 < k>14, 1.2 <R > 4.0. [a]CN fixed to known structures and the number of scattering paths reduced in order to minimise fitting parameters*

$YMnO_3$ Sample	Bond (Abs-Sc)	[a]CN	E_0 (eV)	σ^2	R / Å	R_{factor}
Sol-gel *h*-$YMnO_3$	Y-O1	7	-3(2)	0.006(1)	2.30(1)	0.019
	Y-Mn1	3		0.005(3)	3.33(2)	
	Y-Y1	6		0.004(1)	3.57(2)	
	Y-Mn2	3		0.003(3)	3.76(3)	
Milled & calcined *h*-$YMnO_3$	Y-O1	7	-4(2)	0.006(1)	2.29(1)	0.010
	Y-Mn1	3		0.007(3)	3.33(2)	
	Y-Y1	6		0.005(1)	3.57(3)	
	Y-Mn2	3		0.004(3)	3.73(4)	
5mm *o*-$YMnO_3$	Y-O1	4	-3(2)	0.008(2)	2.30(3)	0.060
	Y-O2	4		0.014(6)	2.54(4)	
	Y-Mn1	4		0.011(2)	3.13(3)	
	Y-Mn2	2		0.006(2)	3.33(3)	
	Y-Mn4	4		0.003(2)	3.76(6)	
	Y-Y1	2		0.005(1)	3.78(4)	
10mm *o*-$YMnO_3$	Y-O1	4	-3(2)	0.005(1)	2.28(2)	0.044
	Y-O2	4		0.012(4)	2.50(4)	
	Y-Mn1	4		0.011(2)	3.12(3)	
	Y-Mn2	2		0.005(2)	3.32(2)	
	Y-Mn4	4		0.003(2)	3.73(5)	
	Y-Y1	2		0.006(1)	3.77(4)	

Table 5.3.6.6: *EXAFS fitting parameters for the Mn K-edge for spectra collected on o- and h-$YMnO_3$. Fitting parameters: $S0^2$=0.7 as determined by the use of a Mn foil standard; Fit range 3 < k>14, 1.2 <R >3.85. [a]CN fixed to known structures and the number of scattering paths reduced in order to minimise fitting parameters*

$YMnO_3$ Sample	Bond (Abs-Sc)	[a]CN	E_0 (eV)	σ2	R / Å	R_{factor}
Sol-gel *h*-$YMnO_3$	Mn-O1	4	-3(2)	0.003(2)	1.85(2)	0.017
	Mn-O3	2		0.008(4)	2.02(2)	
	Mn-Y2	6		0.005(2)	3.33(2)	
	Mn-Mn1	6		0.007(1)	3.54(1)	
Milled & calcined *h*-$YMnO_3$	Mn-O1	4	-4(2)	0.004(2)	1.87(2)	0.010
	Mn-O3	2		0.012(6)	2.01(3)	
	Mn-Y2	6		0.005(2)	3.33(2)	
	Mn-Mn1	6		0.009(2)	3.53(3)	
5mm *o*-$YMnO_3$	Mn-O1	4	-4(2)	0.003(1)	1.92(1)	0.060
	Mn-O3	2		0.007(4)	2.23(2)	
	Mn-Y2	4		0.008(2)	3.08(1)	
	Mn-Y3	2		0.005(3)	3.28(2)	
	Mn-Mn1	2		0.006(2)	3.77(5)	
	Mn-Y4	2		0.005(2)	3.84(4)	
	Mn-Mn2	4		0.013(3)	3.90(4)	
10mm *o*-$YMnO_3$	Mn-O1	4	-3(2)	0.003(1)	1.91(1)	0.022
	Mn-O3	2		0.008(3)	2.23(2)	
	Mn-Y2	4		0.009(2)	3.08(2)	
	Mn-Y3	2		0.005(2)	3.32(2)	
	Mn-Mn1	2		0.008(5)	3.76(8)	
	Mn-Y4	2		0.007(3)	3.84(5)	
	Mn-Mn2	4		0.013(5)	3.91(7)	

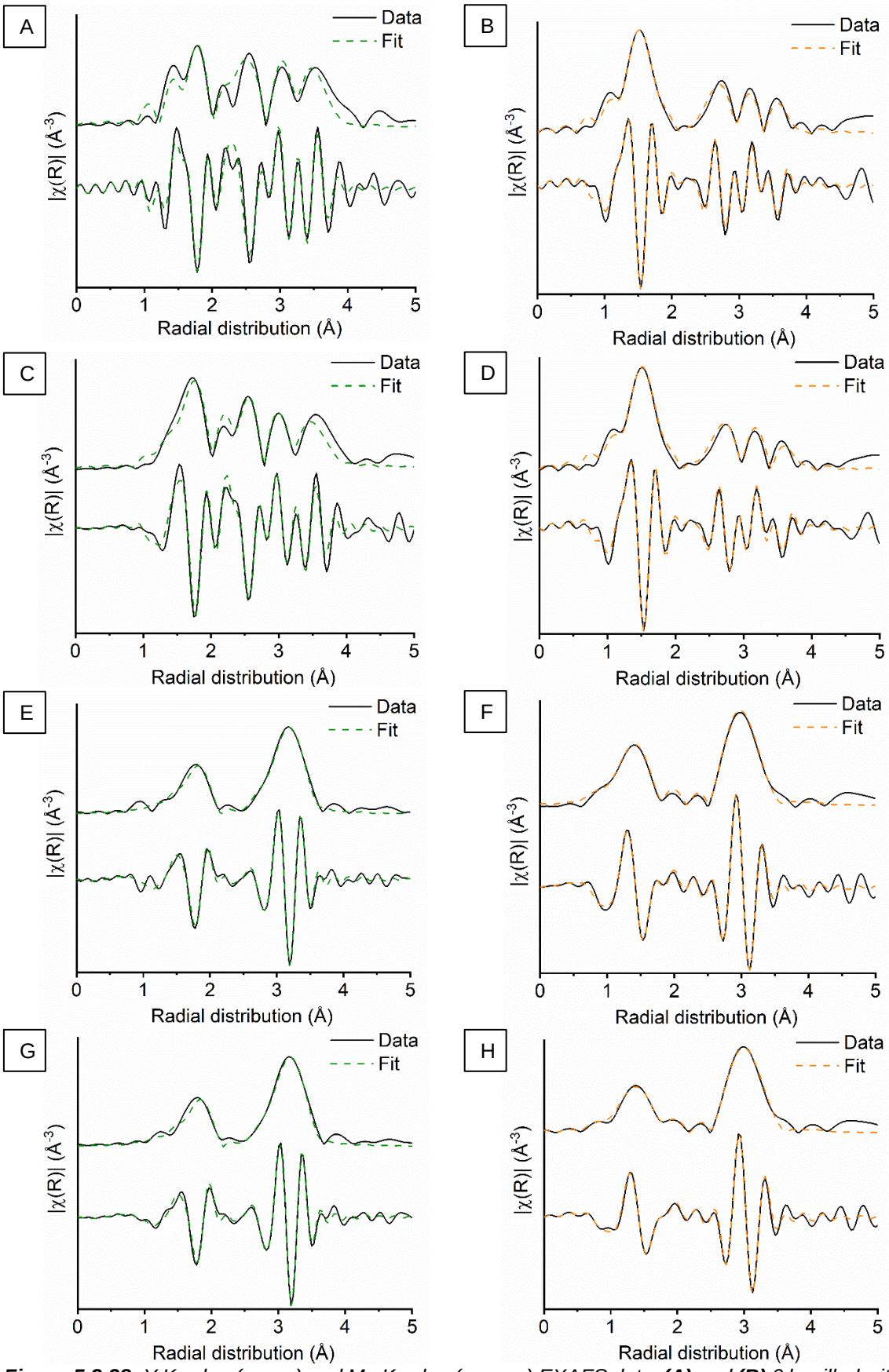

Figure 5.3.38: *Y K-edge (green) and Mn K-edge (orange) EXAFS data* ***(A)*** *and* ***(B)*** *6 h milled with 5 mm media,* ***(C)*** *and* ***(D)*** *10 mm media,* ***(E)*** *and* ***(F)*** *milled and calcined $ErMnO_3$ and* ***(G)*** *and* ***(H)*** *sol-gel h-$YMnO_3$ showing the magnitude and imaginary components of the k^3-weighted Fourier transform data and fits*

To understand how these phase transformations effect the catalytic recyclability, an additional deN_2O cycle was performed on the used catalysts (Figure 5.3.39). Both Er and Y A-site materials show comparable deN_2O conversion. The sol-gel synthesised *h*-$AMnO_3$ remains comparable to the first deN_2O performance run, with the milled and calcined showing a small decrease. This thermal stability is expected to arise from the high temperatures used in both preparation routes. Though both the sol-gel and milled and calcined catalyst now possess the same hexagonal structure, there is a clear distinction between their light-off curves, which could result from their different morphologies. The ball milled samples show the biggest decrease in catalytic activity, with a reduction of ~50 ˚C in the T_{50} for both 5 mm and 10 mm milled $AMnO_3$. Significantly the 10 mm catalyst shows the lowest catalytic activity, even whilst having comparable bulk structure to the 5 mm after the first catalytic cycle. This suggests further investigations into how surface properties change with respect deN_2O should be explored as well.

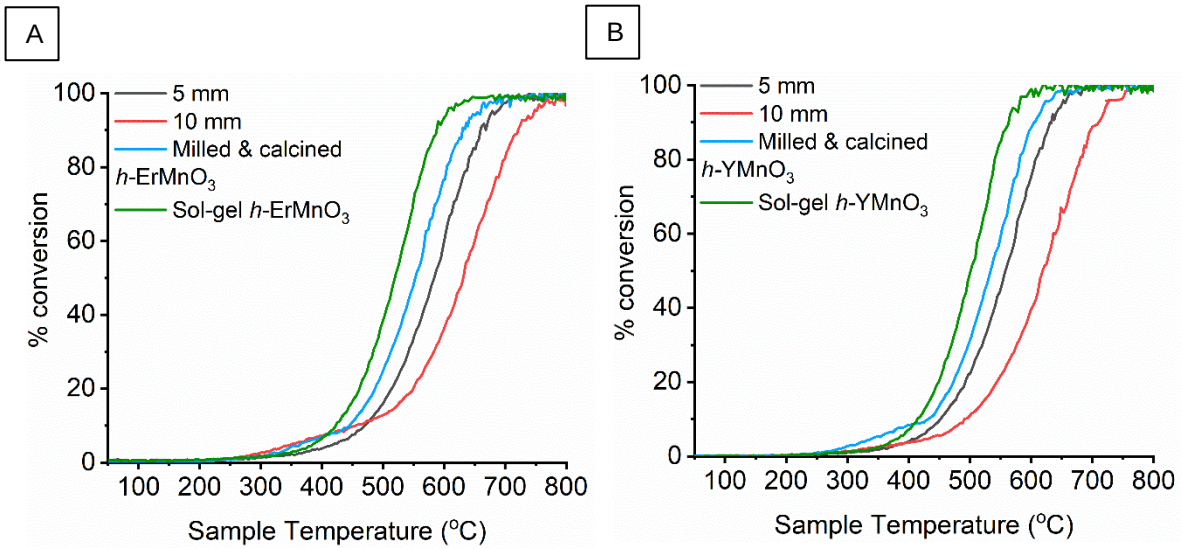

Figure 5.3.39: *Light-off curves for the percentage conversion of deN_2O to N_2 over differently synthesised* ***(A)*** *$ErMnO_3$ and* ***(B)*** *$YMnO_3$ catalysts was performed on the used catalysts to produce cycle 2 data*

5.4 Conclusions

Attempts to synthesis $ErMnO_3$ and $YMnO_3$ by mechanochemistry and sol-gel synthesise were unsuccessful under the same experimental conditions as $LaMnO_3$. For the sol-gel synthesis, the smaller A-site ionic radii of Er/Y, compared to La, required a higher final thermal temperature, in accordance to the Goldschmidt tolerance factor. Calcining the amorphous 5 mm ball milled material resulted in an $AMnO_3$ phase, reducing the final annealing temperature by 300 ˚C compared to the sol-gel synthesis; along with removing multiple process steps and the use of solvent to produce a more environmentally friendly process. Furthermore, by optimising the milling process to use a larger media size some crystalline perovskite was detected, indicating that a greater impact energy was required. However, this increase in media size unfortunately resulted a high percentage of Zr contamination from the milling equipment in final material, detected by TEM-EDX, which could be linked to the decrease in deN_2O activity for the 10 mmm catalysts.

However, we must take care when drawing comparisons between the required mechanical and thermal energies as these different synthetic routes proceed via alterative pathways to produce different perovskite phases; orthorhombic (metastable) and hexagonal (thermodynamically stable), respectively. This is further highlighted with the milling of the Y A-site system, which requires a greater reaction time for 100 % of its crystalline content to be *o*-$YMnO_3$. It is observed by XAS and TEM that this orthorhombic structure has a higher degree of Jahn-Teller distortion in comparison to *o*-$ErMnO_3$, thus further lowering its overall stability.

Further XAS studies highlighted how complex and complicated the milled materials were. The lack of any overall long-range order for the ball milled species, indicating that highly disordered species remained even after milling for 6 h with 10 mm milling media. This made it challenging to extract definite structural information. However, this could be an exciting opportunity for future work to perform multivariate component analysis in order to identify the intermediate phases throughout milling by analysis of the initial components (later discussed in Chapter 7).[47] However, by performing XAS at both A- and B-site edges here it was possible to signify that the initial stages of milling, 0-2 h, is extremely important for the evolution of new phases. Comparisons between the 5 mm and 10 mm milled materials showed the greatest proportion of change occurred from 0-2 h, with increasing the milling duration having little effect. This suggests that the required activation energy for perovskites, supplied by the transfer of mechanical energy, is dependent on the impact energy rather than increased number of collisions.

Performing deN_2O catalytic reactions shows the ball milled catalysts to have no improved activity over their sol-gel equivalents. Though XPS reported a higher percentage of surface oxygen vacancies for the ball milled catalysts, their lower catalytic performance could be an indication of the importance of an extended perovskite-like structure or

presence of hydroxide ions at the A-site. With an increase in the number of surface vacancies no longer comparable to an earlier on-set conversion of deN_2O, as previously observed for $LaMnO_3$, it could signify the important role of A-site hygroscopy. This can be linked to the rate determining step for deN_2O, which is the desorption of O_2 from the surface. Further investigation is required to understand the catalytic pathway for these materials.

Post deN_2O *ex situ* characterisation showed crystallisation to the orthorhombic phase for the ball milled species, which in turn reduced their performance on a second cycle of deN_2O. activity. Interestingly the *o*-$ErMnO_3$ reference material transformed to a hexagonal phase as a result of the elevated temperatures during deN_2O, further confirming the thermal stability of *h*-$AMnO_3$. With the sol-gel and newly hexagonal milled and calcined species having differing light-off curves it indicates the importance in morphology.

These differences highlight that by changing the synthetic route it is possible to tailor materials to desired structures, which in turn can possess alternative properties that benefit specific applications. However, this chapter also shows the challenges arising through preparing materials via mechanochemistry, as even these similar mixed metal oxide materials require specific optimisation.

5.5 References

1 R. H. Blackmore, M. E. Rivas, T. E. Erden, T. D. Tran, H. R. Marchbank, D. Ozkaya, M. Briceno de Gutierrez, A. Wagland, P. Collier and P. P. Wells , *Dalt. Trans.*, 2020, **49**, 232–240.

2 K. Asokan, C. L. Dong, C. W. Bao, H. M. Tsai, J. W. Chiou, C. L. Chang, W. F. Pong, P. Duran, C. Moure and O. Peña, *Solid State Commun.*, 2005, **134**, 821–826.

3 K. Bergum, H. Okamoto, H. Fjellvåg, T. Grande, M.-A. Einarsrud and S. M. Selbach, *Dalt. Trans.*, 2011, **40**, 7583.

4 Y. Yokogawa, M. Yoshimura and S. Somiya, *J. Mater. Sci. Lett.*, 1991, **10**, 509–511.

5 A. Moure, T. Hungría, A. Castro, J. Galy, O. Peña, J. Tartaj and C. Moure, *Chem. Mater.*, 2010, **22**, 2908–2915.

6 O. Fedorova, G. Kozhina and S. Uporov, *J. Alloys Compd.*, 2018, **740**, 677–686.

7 M. H. Harunsani, J. Li, Y. B. Qin, H. T. Tian, J. Q. Li, H. X. Yang and R. I. Walton, *Appl. Phys. Lett.*, 2015, **107**, 1–6.

8 K. Uusi-Esko, J. Malm, N. Imamura, H. Yamauchi and M. Karppinen, *Mater. Chem. Phys.*, 2008, **112**, 1029–1034.

9 X. Y. Xie, J. N. Yang, L. L. Yu, J. Y. Min, D. D. Sun, P. S. Tang and H. F. Chen, *IOP Conf. Ser. Mater. Sci. Eng.*, 2018, **362**, 1–6.

10 B. Raneesh, A. Saha, D. Das and N. Kalarikkal, *J. Alloys Compd.*, 2013, **551**, 654–659.

11 S. Ishiwata, Y. Tokunaga, Y. Taguchi and Y. Tokura, *J. Am. Chem. Soc.*, 2011, **133**, 13818–13820.

12 A. Moure, T. Hungría, A. Castro, J. Galy, O. Peña, I. Martínez, J. Tartaj and C. Moure, *Ceram. Int.*, 2012, **38**, 1507–1513.

13 M. Počuča-Nešić, Z. Marinković Stanojević, Z. Branković, P. Cotič, S. Bernik, M. S. Góes, B. A. Marinković, J. A. Varela and G. Branković, *J. Alloys Compd.*, 2013, **552**, 451–456.

14 Q. Zhang and F. Saito, *J. Alloys Compd.*, 2000, **297**, 99–103.

15 A. M. Bolarín, F. Sánchez, A. Ponce and E. E. Martínez, *Mater. Sci. Eng. A*, 2007, **454**–**455**, 69–74.

16 E. Boldyreva, *Chem. Soc. Rev.*, 2013, **42**, 7719–7738.

17 L. A. Isupova, G. M. Alikina, S. V. Tsybulya, A. N. Salanov, N. N. Boldyreva, E. S. Rusina, I. A. Ovsyannikova, V. A. Rogov, R. V. Bunina and V. A. Sadykov, *Catal. Today*, 2002, **75**, 305–315.

18 M. Newville, *J. Synchrotron Radiat.*, 2001, **8**, 322–324.

19 B. Ravel and M. Newville, *J. Synchrotron Radiat.*, 2005, **12**, 537–541.

20 S. Kaliaguine, A. Van Neste, V. Szabo, J. E. Gallot, M. Bassir and R. Muzychuk, *Appl. Catal. A Gen.*, 2001, **209**, 345–358.

21 I. J. Lin and S. Nadiv, *Mater. Sci. Eng.*, 1979, **39**, 193–209.

22 V. V. Boldyrev and E. G. Avvakumov, *Thermochim. Acta*, 1971, **40**, 847.

23 Y. Zhao, *Materials (Basel).*, 2012, **5**, 1413–1438.

24 D. Y. Cho, J. Y. Kim, B. G. Park, K. J. Rho, J. H. Park, H. J. Noh, B. J. Kim, S. J. Oh, H. M. Park, J. S. Ahn, H. Ishibashi, S. W. Cheong, J. H. Lee, P. Murugavel, T. W. Noh, A. Tanaka and T. Jo, *Phys. Rev. Lett.*, 2007, **98**, 1–4.

25 S. C. Haw, J. M. Lee, S. A. Chen, K. T. Lu, F. C. Chou, N. Hiraoka, H. Ishii, K. D. Tsuei, C. H. Lee and J. M. Chen, *J. Phys. Soc. Japan*, 2013, **82**, 3–6.

26 H. Chen, T. Yu, P. Gao, J. Bai, J. Tao, T. A. Tyson, L. Wang and R. Lalancette, *Inorg. Chem.*, 2013, **52**, 9692–9697.

27 R. H. Blackmore, M. E. Rivas, G. F. Tierney, K. M. H. Mohammed, D. Decarolis, S. Hayama, F. Venturini, G. Held, R. Arrigo, M. Amboage, P. Hellier, E. Lynch, M. Amri, M. Casavola, T. Eralp Erden, P. Collier and P. P. Wells, *Phys. Chem. Chem. Phys.*, 2020, **22**, 18774–18787.

28 Y. Mao, J. Bargar, M. Toney and J. P. Chang, *J. Appl. Phys.*, 2008, **103**, 94316.

29 C. Mignotte, *Appl. Surf. Sci.*, 2004, **226**, 355–370.

30 C. Mignotte, *J. Non. Cryst. Solids*, 2001, **291**, 56–77.

31 V. Cuartero, S. Lafuerza, M. Rovezzi, J. García, J. Blasco, G. Subías and E. Jiménez, *Phys. Rev. B*, 2016, **94**, 1–10.

32 F. Farges, *Phys. Rev. B - Condens. Matter Mater. Phys.*, 2005, **71**, 1–14.

33 A. Y. Ignatov, N. Ali and S. Khalid, *Phys. Rev. B - Condens. Matter Mater. Phys.*, 2001, **64**, 1–16.

34 K. Asokan, Y. S. Chen, C. W. Pao, H. M. Tsai, C. W. O. Lee, C. H. Lin, H. C. Hsueh, D. C. Ling, W. F. Pong, J. W. Chiou, M. H. Tsai, O. Pea and C. Moure, *Appl. Phys. Lett.*, 2009, **95**, 3–6.

35 S. Mukherjee, H. Ganegoda, A. Kumar, S. Pal, C. U. Segre and D. D. Sarma, *Inorg. Chem.*, 2018, **57**, 9012–9019.

36 M. Malvestuto, R. Carboni, F. Boscherini, F. D'Acapito, S. Spiga, M. Fanciulli, A. Dimoulas, G. Vellianitis and G. Mavrou, *Phys. Rev. B - Condens. Matter Mater. Phys.*, 2005, **71**, 1–8.

37 F. Jollet, C. Noguera, N. Thromat, M. Gautier and J. P. Duraud, *Phys. Rev. B*, 1990, **42**, 7587–7595.

38 S. Jaiswar and K. D. Mandal, *J. Phys. Chem. C*, 2017, **121**, 19586–19601.

39 M. A. Stranick, *Surf. Sci. Spectra*, 1999, **6**, 39–46.

40 M. A. Stranick, *Surf. Sci. Spectra*, 1999, **6**, 31–38.

41 K. Jirátová, J. Mikulová, J. Klempa, T. Grygar, Z. Bastl and F. Kovanda, *Appl. Catal. A Gen.*, 2009, **361**, 106–116.

42 V. P. Santos, M. F. R. Pereira, J. J. M. Órfão and J. L. Figueiredo, *Appl. Catal. B Environ.*, 2010, **99**, 353–363.

43 A. Machocki, T. Ioannides, B. Stasinska, W. Gac, G. Avgouropoulos, D. Delimaris, W. Grzegorczyk and S. Pasieczna, *J. Catal.*, 2004, **227**, 282–296.

44 P. Granger, V. I. Parvulescu, S. Kaliaguine and W. Prellier, in *Perovskites and Related Mixed Oxides Concepts and Applications*, eds. P. Granger, V. Parvulescu, S. Kaliaguine and W. Prellier, Wiley-VCH, 2015, pp. 3–23.

45 X. Wang, Y. F. Jiang, Y. N. Liu and A. W. Xu, *New J. Chem.*, 2018, **42**, 19901–

19907.

46 K. M. Cole, D. W. Kirk and S. J. Thorpe, *Surf. Sci. Spectra*, 2020, **27**, 024010.

47 A. Voronov, A. Urakawa, W. van Beek, N. E. Tsakoumis, H. Emerich and M. Rønning, *Anal. Chim. Acta*, 2014, **840**, 20–27.

Chapter 6

Understanding the effect of La doping on supported Au nanoparticles by milling and its catalytic properties

6.1 Introduction

The use of supported metal nanoparticles (NP) is well established within heterogeneous catalysis.[1] Depositing nanoscale metals on a high surface area supports has resulted in the formation of highly efficient catalysts that are widely utilised for many industrial processes today. This is includes: three-way catalysts for automotive exhaust emission control, Pd-TiO_2/Rh-Al_2O_3-La_2O_3[2], for the water-gas shift reaction to produce hydrogen, Pt/CeO_2[3] and for catalysing selective hydrogenation of alkenes, Pd/C[4]. The catalytic activity of metal supported NPs is reported throughout literature to be highly dependent on particle size, shape and structure along with the choice of support and its subsequent interaction with the chosen metal.[5] However, NP catalysts are disadvantaged by their high metal cost and ability to deactivate under operating conditions, by either poisoning or sintering of the particles.[6] This has led to continued research within this area and for the development of next generation catalysts.

A large array of research has focused solely on the optimisation of supported NP catalyst synthesis. Traditional preparation routes, such as impregnation and precipitation struggle to allow for accurate control of the final material properties, with the use of subsequent thermal treatments resulting in NP agglomeration.[7] However, using sol-immobilisation it is possible to tune the NP size and dispersion by either changing the polymer to metal ratio, the choice of solvent or temperature of the colloidal solution.[8,9] Still, using this solvent based preparation routes requires multiple reaction steps, precise temperature control and stringent waste treatment procedures, all at a high energy and environmental cost.

Mechanochemical synthesis is a versatile, simple and solvent-free synthetic route, that is not commonly reported within NP research. This synthetic route generally produces particles on the micro-size scale, rather than the nano, with literature predominantly focusing on preparation of the metal oxide support, such as Al_2O_3. Within the last decade

only a few publications have attempted the combination of metal NP research with mechanochemistry. Rak *et. al.* were able to produce highly monodisperse metal NPs in lignin, however, it wasn't until 2019 when Schreyer *et al.* reported the bottom-down approach of macroscopic metal powders onto a variety of metal oxide supports.[10,11] Schreyer *et al.* also detected a phase transformation for the Al_2O_3 support, from α to γ-Al_2O_3. The formation of this metastable γ-Al_2O_3 phase further indicates a high potential for catalysis. Though no significant improvement of activity was detected for the ball milled catalysis towards CO conversion over impregnation or co-precipitation techniques, it provides a clear opportunity to explore mechanochemistry in NP supported catalyst research.

Traditionally considered as catalytically benign, research into gold catalysts has significantly increased over the past 30 years thanks to work published by Bond *et. al.*[12], Haruta *et. al.*[13] and Hutchings *et. al.* showing dispersed Au NP, over the bulk metal, possess excellent catalytic activity. Haruta *et. al* first reported NP Au to have high activity towards CO oxidation at low temperatures. The high selectivity and tunability of Au loading makes it a highly accessible and promising catalyst. Today Au supported catalysts have shown large commercial potential, and are now being used for hydrochlorination of acetylene for the production of a vinyl chloride monomer (VCM), a chemical intermediate of polyvinyl chloride (PVC).[14]

However, there is limited understanding of the catalytic steps occurring at these low temperatures that result in an improved activity, and there is often debate around identifying the active site, $Au^{\delta+}$ or Au(I/III).[3,15] Further difficulties arise as the Au NPs are highly dependent on the specific reaction conditions and the nature of the support used. Currently there is not enough evidence to decipher whether it is Au in its cationic state or in gold clusters that results in the enhanced catalytic activity.[16] It has been observed that the cationic form of Au is highly unstable during high temperatures and oxidising conditions.[17]

Recent reports on the stabilisation of cationic forms of Au(I) or Au(III) have shown promising catalytic activity, along with the indication that La is able to stabilise these species.[18–20] However, these reports on La_2O_3 supported Au NPs also produce contradictory hypotheses towards the nature of the Au active site and the mechanism for CO oxidation remains elusive. Fierro-Gonzalez *et. al.* and Goguet *et. al.* reported high stability of the cationic Au(III) species throughout CO oxidation and calcination procedures, respectively,[18,20] whereas, Mihaylov *et. al.* initially detected Au(0) NPs, which under reaction conditions were oxidised by CO_2 to form $Au^{\delta+}$ in order to facilitate CO oxidation.[21,22]

Previously, work on the preparation of $LaMnO_3$ by ball milling showed that La could be easily 'activated' through the physical action of grinding La_2O_3 with a pestle and mortar in the presence of another precursor material.[23] Herein, this work attempts to establish if this 'activation' of La can be utilised as a promoter for 0.5wt% Au/Al_2O_3 catalysts alongside

the effect of ball milling on Au supported NP. This provides a clear opportunity for research within this area utilising a combination of advanced characterisation and mechanochemical synthesis.

6.2 Materials and methods

6.2.1 Material synthesis

La-Au/Al_2O_3 Synthesis. The 0.5wt% Au/Al_2O_3 were prepared by impregnation, supplied by Johnson Matthey, Sonning Common, UK. To investigate the effect of La dispersion over 0.5wt% Au/Al_2O_3 four samples were prepared:

1. 0.5wt% Au/Al_2O_3 = Au/Al_2O_3
2. 0.5wt% Au/Al_2O_3 milled for 30 min = Au/Al_2O_3_milled
3. 2wt% La and 0.5wt% Au/Al_2O_3 mixed with a pestle and mortar = La_Au/Al_2O_3_mixed
4. 2wt% La and 0.5wt% Au/Al_2O_3 milled for 30 min = La_Au/Al_2O_3_milled

Milling was performed for samples **2** and **4**, using a Retsch 2–station Planetary Ball Mill, PM200 with 125 mL ZrO_2 grinding jars, at the Research complex, Harwell, UK. La_2O_3 was initially heated at 500 ˚C for 12 h to ensure an oxide starting phase. For samples **2** and **4**, 0.5wt% Au/Al_2O_3 (5 g) or a La_2O_3 (0.15 g) and 0.5wt% Au/Al_2O_3 (5 g) mixture, respectively, were placed in the milling jar, on top of the media and then sealed with a lid. Experiments were run with 5 mm yttria-stabilised zirconia (YTZ®) milling media, with a media weight ratio to the total precursor powder of 10:1. The mill operated at room temperature at 100 rpm for 30 min. Note, that a separate jar was milled for sample **2** and **4**. Sample **3** was prepared using the same stoichiometric measurements as for sample **4**, but grinded by hand in a 50 mL agar pestle and mortar for 10 min.

6.2.2 Characterisation

X-ray diffraction (XRD) patterns were collected on a Bruker AXS D8 diffractometer (Johnson Matthey, Sonning Common, UK) with Cu $K\alpha$ radiation over a range of 2θ = 10 - 130° with 0.044° step size.

X-ray absorption spectroscopy (XAS) measurements were performed at the B18 Beamline, Diamond Light Source. XAS measurements were performed at the Au L_3-edge (11920 eV) and La L_3-edge (5483 eV) in transmission mode using QEXAFS setup with fast scanning Si(111) double crystal monochromator. All XAS spectra were acquired concurrently with the appropriate foil placed between I_t and I_{ref}. Au L_3-edge XAS spectra were acquired with a time resolution of 5 min per spectrum (k_{max}= 16) averaged over 3 scans. La L_3-edge XAS spectra were acquired with a time resolution of 5 min per spectrum

(k_{max}= 10) averaged over 3 scans. Data processing was performed using IFEFFIT[24] with Horae package[25] (Athena and Artemis). The amplitude reduction factor, S_0^2 was derived using EXAFS analysis of appropriate reference spectra foil of known coordination numbers.

X-ray photoelectron spectroscopy (XPS) was carried out with a Thermo Escalab 250. The radiation used was monochromatised aluminium Kα radiation with a 650 μm spot size. Charge compensation was provided by the in-lens electron flood gun at a 2 eV setting and the "401" unit for "zero energy" argon ions. Energy scales were corrected to the Al 2*p* signal (74.5 eV) to compensate for charging effects. Sensitivity factors after Scofield were used in quantification, which was measured and analysed by Johnson Matthey, Sonning Common, UK

Transmission electron microscopy (TEM) samples were prepared as previously stated in section 3.2.2 by the Johnson Matthey analytical department. Using a JEM 2800 (Scanning) Transmission Electron Microscope the same instrumental conditions were applied: voltage (kV) 200; C2 aperture (um) 70 and 40.

Brunauer-Emmett-Teller (BET) surface area analysis was performed on the different Au/Al_2O_3 catalysts using nitrogen adsorption on a Quantachrome Autosorb iQ “E” at Johnson Matthey, Sonning Common, UK. Samples (~10 – 25 mg) were initially heated to 573 K with a ramp of 10 ˚C min^{-1} under a vacuum for 4 h to remove any absorbed species on the surface before gas adsorption/desorption experiments began. The nitrogen adsorption/ desorption measurements were then performed at 77 K, achieved using liquid N_2, with relative pressure of P/P^0 = 0.1.

Transmission infrared (IR) spectroscopy. CO chemisorption was performed using an is10 Nicolet spectrometer with a deuterated triglycine sulfate (DTGS) detector. Samples (~20 – 25 mg) were pressed into a self-supporting 13 mm^2 pellet and mounted into a sealed Harrick transmission cell. The cell was purged for 30 min under a He gas flow of 30 ml min^{-1} before a background spectrum was collected. Pulses of 10% CO / He were introduced into the cell at 10 ml min^{-1}, along with 20 ml min^{-1} of He, at 30 s intervals until no change was observed in the CO bands, *i.e.* once full saturation of the surface occurred. The IR spectra were recorded from 40 – 4500 cm^{-1} with a resolution of 4 cm^{-1} and an accumulation of 64 scans after purging the cell until free CO gas was no longer detected. Background subtraction was performed using the OMNIC software package, allowing for spectral observations of CO absorption bands.

6.2.3 Catalytic activity testing

CO oxidation was carried out in a Hiden CATLAB fixed-bed quartz reactor in the temperature range of 40 – 250 ^oC with a ramp of 5 ^oC min^{-1}. The different Au/Al_2O_3 samples were pressed and sieved into a 125 – 250 μM pellet faction. The reaction was performed over 100 mg of sample at a total flow of 17.5 mL min^{-1} with GHSV = 41,000 h^{-1}, composed

of 10% CO/He, 5 mL min^{-1}, with an excess flow of 20% O_2/He, 12.5 mL min^{-1}. A pre-treatment was performed on the catalysts under 17.5 mL min^{-1} of He up to 150 ˚C to remove any surface species before CO oxidation. The composition of exhaust gases was measured using a Hiden QGA mass spectrometer for He (*m/e* = 4), CO (*m/e* = 28, 12), CO_2 (*m/e* = 44), O_2 (*m/e* = 32).

6.3 Results & Discussion

6.3.1 XRD

XRD was first performed to assess how La doping and milling affects the long-range structure of different Au/Al_2O_3 catalysts. Initial observations show the diffraction patterns for all Au/Al_2O_3 samples contain broad, low intensity peaks indicative of small particle size and/or amorphous content (Figure 6.3.1). No Bragg peaks corresponding to Au are visible within the XRD of all four samples, resulting from extremely small particle sizes and low metal loading. The average Au crystallite size can therefore not be determined by XRD. Assessing the Au/Al_2O_3 and Au/Al_2O_3 milled catalysts, XRD identifies an α-Al_2O_3 phase.[26] On the addition of La precursor, by both mixing and milling, the peaks associated with $La(OH)_3$ are now observed. Both milled species, Au/Al_2O_3 milled and $La\text{-}Au/Al_2O_3$ milled, detected a subtle decrease in peak intensity on milling, suggesting some amorphisation. This is a common consequence of mechanochemistry. Literature reports it is possible to form a α-Al_2O_3 phase on milling of γ-Al_2O_3.[26,27] A phase transformation has not occurred in this case as a result of the low energy milling conditions used, in order to reduce the opportunity of Au NP agglomeration.

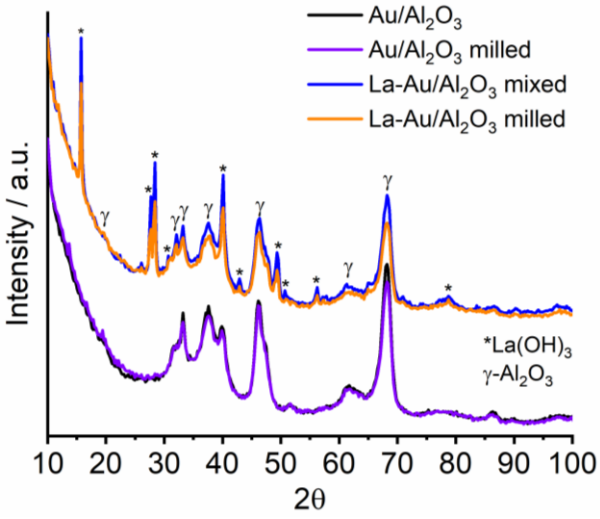

Figure 6.3.1: *XRD patterns of different Au/Al_2O_3 catalysts*

6.3.2 TEM

TEM imaging was performed on the different Au/Al_2O_3 catalysts to assess how changes with respect to La doping and/or milling effects the morphology, Au dispersion and Au average particle size; previously not possible by XRD. ***Figure 6.3.2*** shows representative TEM images of the Au particles distributed about the alumina support for all four Au/Al_2O_3 catalysts. No clear morphological alterations are observed on milling (Figure 6.3.2B, D).

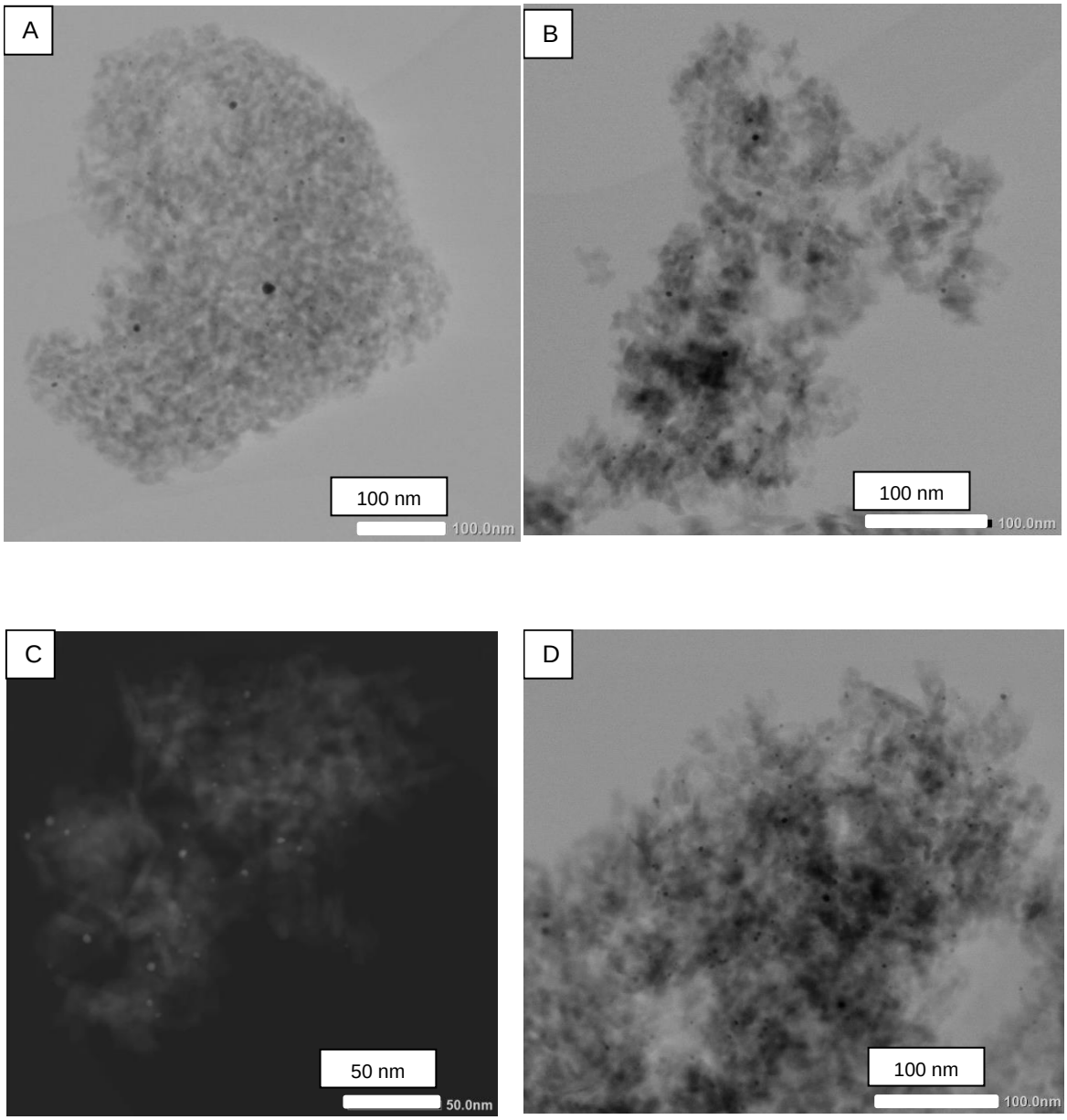

Figure 6.3.2: *Representative TEM HAADF images of* ***(A)*** *$AuAl_2O_3$,* ***(B)*** *$AuAl_2O_3$ milled,* ***(C)*** *La-$AuAl_2O_3$ mixed and* ***(D)*** *La-$AuAl_2O_3$ milled catalysts*

Samples doped with La show large particles of La for both mixed and milled materials (***Figure 6.3.2***C, D), confirmed by elemental mapping (Figure 6.3.3). However, on milling Au/Al_2O_3 with La_2O_3, the La precursor began to show signs of distribution into the oxide support.

The average Au particle diameter histograms for the different Au/Al_2O_3 catalysts are shown in Figure 6.3.4. Calculating the average Au particle size across a minimum of 115 particles showed that ball milling of Au/Al_2O_3 decreased the particle size, from 5.1 ± 3.6 nm to 3.8 ± 0.9 nm. Both La-Au/Al_2O_3 mixed and La-Au/Al_2O_3 milled samples also estimated a reduction in average particle size compared to Au/Al_2O_3 of 3.6 ± 2.0 nm and 4.2 ± 1.5 nm, respectively. The energy transferred to the powdered material via mechanical action of the

mill would be expected to destabilise the small Au NP, resulting in agglomeration and an increase in average NP size. Large errors are, however, recorded for the initial Au/Al_2O_3 material. It is also important to note that this is only a small sample area and is not fully representative of the overall bulk composition.

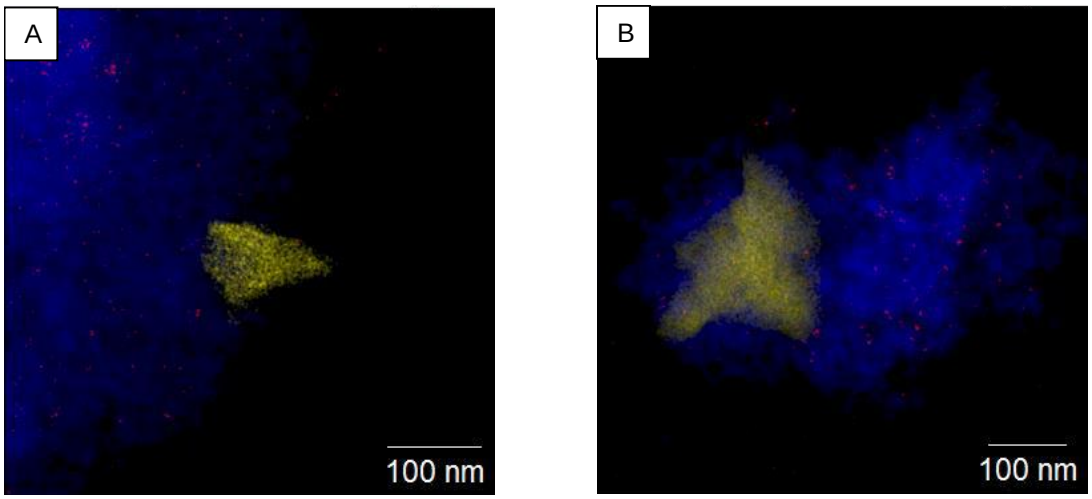

Figure 6.3.3: *TEM EDX imagine of* ***(A)*** *La-$AuAl_2O_3$ mixed and* ***(B)*** *La-$AuAl_2O_3$ milled catalysts, showing the distribution of La (yellow) compared to Au (red) and Al (blue)*

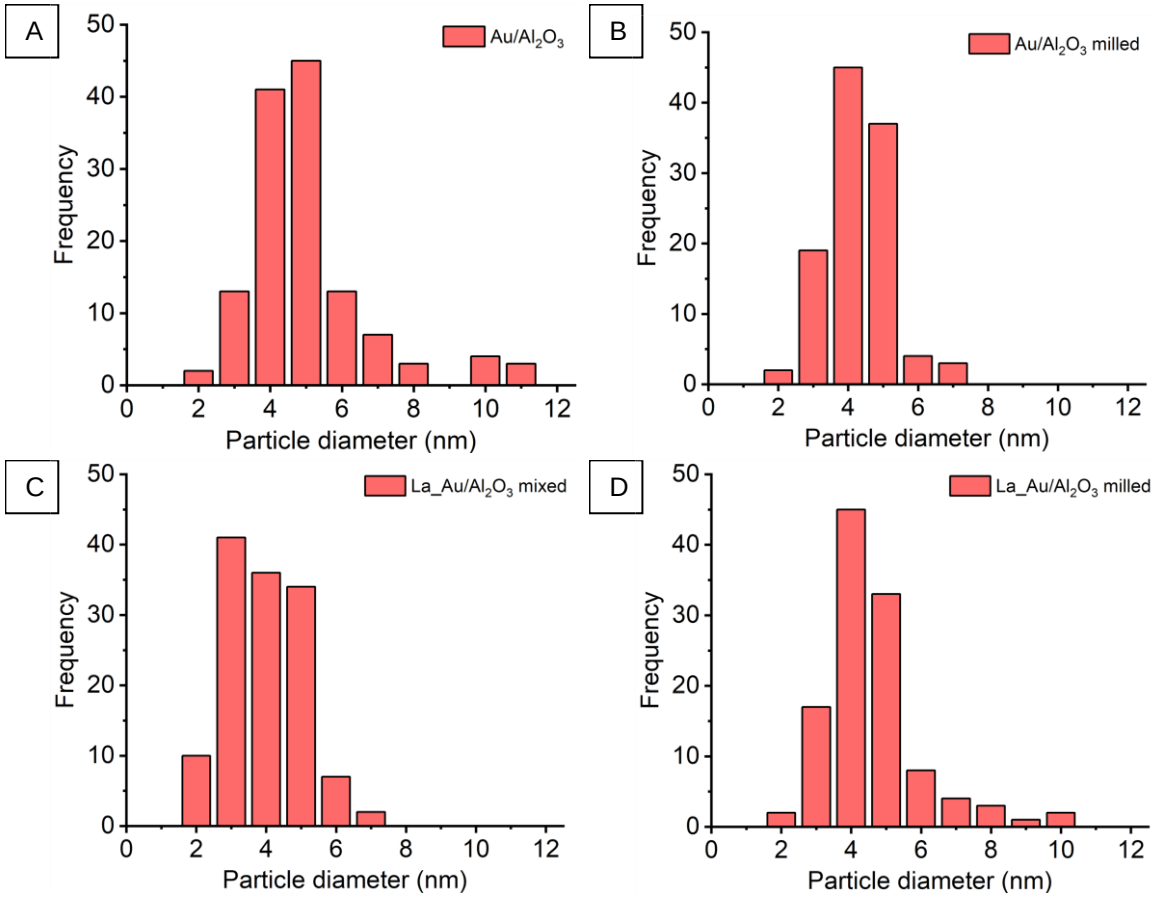

Figure 6.3.4: *Au particle diameter histograms of* ***(A)*** *$AuAl_2O_3$,* ***(B)*** *$AuAl_2O_3$ milled,* ***(C)*** *La-$AuAl_2O_3$ mixed and* ***(D)*** *La-$AuAl_2O_3$ milled catalysts*

6.3.3 XAS

To understand the Au and La local coordination environments, independent of periodic ordering, XAS has been performed at both Au and La L_3-edges. Previously, XAS of $LaMnO_3$ has shown that measuring two edges, Mn K-edge and La L_3-edge, on the same sample provided unique perspectives, crucial for understanding the structures of milled materials.[23]

XANES measured at the Au L_3-edge (***Figure 6.3.5***) corresponds to a $2p \rightarrow 5d$ transition. For all Au/Al_2O_3 samples the XANES spectra is indicative of a metallic Au^0 species. With Au^0 possessing a completely full $5d$ orbital, $5d^{10}6s^1$, the main absorption edge at 11920 eV is expected to occur as a result of hybridisation and the formation of a $5d^{10-\delta}6s^{1+\delta}$ state.[28] No change is observed on milling or with the addition of La.

No alterations are observed at the La L_3-edge XANES (***Figure 6.3.6***) and respective EXAFS Fourier transform between the $La\text{-}Au/Al_2O_3$ mixed and $La\text{-}Au/Al_2O_3$ milled catalysts. This suggests La has remained in its bulk form, with no significant dispersion within Au/Al_2O_3. Therefore, no overall association of Au with La for either the mixed or milled $La\text{-}Au/Al_2O_3$ samples has occurred.

Assessing the EXAFS at the Au L_3-edge to produce fitting models is a powerful tool in determining the coordination number (CN) and average particle size of Au NPs. The calculated particle size values are representative of the whole sample, in contrast to the previous TEM studies. Figure 6.3.7 shows the magnitude and imaginary components of the k^2-weighted Fourier transform data and simulated fits, with corresponding fitting parameters in Table 6.3.3.1.

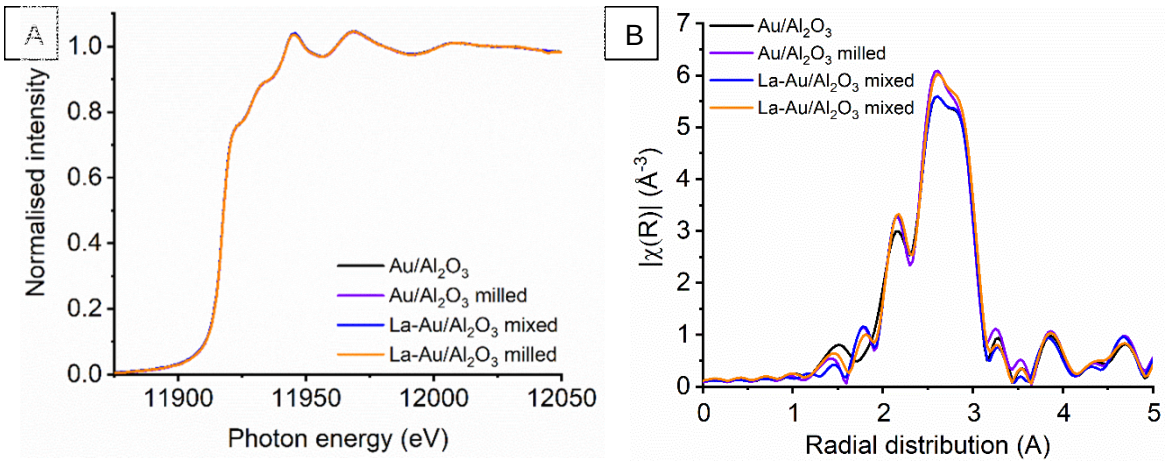

Figure 6.3.5: *XAS performed at the Au L_3-edge on Au/Al_2O_3 catalyst that has been milled/mixed in the presence of $La(OH)_3$ showing* ***(A)*** *XANES and* ***(B)*** *non-phase corrected Fourier transform*

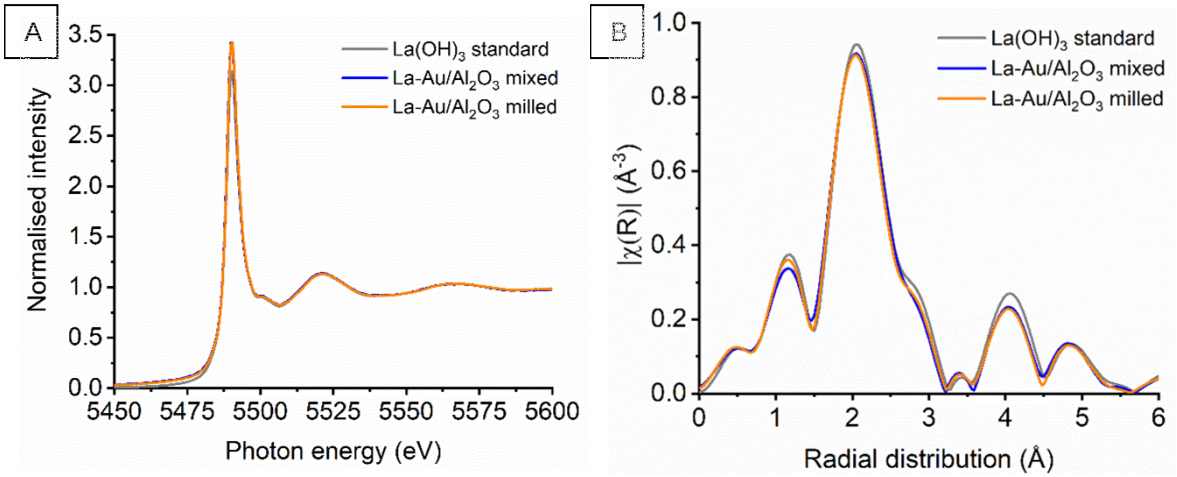

Figure 6.3.6: *XAS performed at the La L_3-edge on La-Au/Al_2O_3 mixed and milled samples compared to a $La(OH)_3$ standard showing* ***(A)*** *XANES and* ***(B)*** *non-phase corrected Fourier transform*

All Au/Al_2O_3 catalysts show a high amplitude feature within the first coordination shell, assigned to Au-Au scattering at 2.83 – 2.84 Å. This feature corresponds to a calculated Au-Au CN of 10.1 – 10.8 by EXAFS fitting (Table 6.3.3.1.). These values are lower than that recorded for bulk Au, which is reported to have a CN of 12 and Au-Au bond length of 2.88 Å.[29] A reduced in Au-Au scattering distance and CN calculated for the different Au/Al_2O_3 catalysts is expected to result from a decrease in particle size.[30] As NPs have a high surface to volume ratio, on decreasing size they possess a higher fraction of uncoordinated surface Au atoms, and thus decreases the overall Au-Au CN.[31]

Using this first shell CN, the average Au NP diameter size was determined using the method reported by Beale *et. al.*[32] Previously, the low metal loading and small Au NP sizes meant it was not possible to detect them by lab-based XRD (Figure 6.3.1). To perform this model on the Au/Al_2O_3 samples, it was first required to assume that all Au NP were spherical, under 3 nm in size and in a face centred cubic (FCC) arrangement. The average Au particle diameter calculated by EXAFS shows variations and smaller particle sizes in comparison to those observed by TEM analysis. Here, the initial, unaltered, Au/Al_2O_3 catalyst has the smallest average Au NP diameter, 2.1 nm. Milling Au/Al_2O_3 results in an increase of 0.3 nm. On the addition of La by mixing and milling an average Au NP size of 2.8 nm and 3.0 nm, respectively was calculated, indicating dispersed Au was less stable on the oxide support. By performing both TEM and EXAFS particle size analysis can produce complementary information. While TEM uses a small representative sampling size, EXAFS size takes into consideration the entirety of the sample. Furthermore, the electron beam within TEM can often destabilise the NP, resulting in agglomeration on particles. It would therefore be expected for TEM studies to suggest a larger average particle diameter.

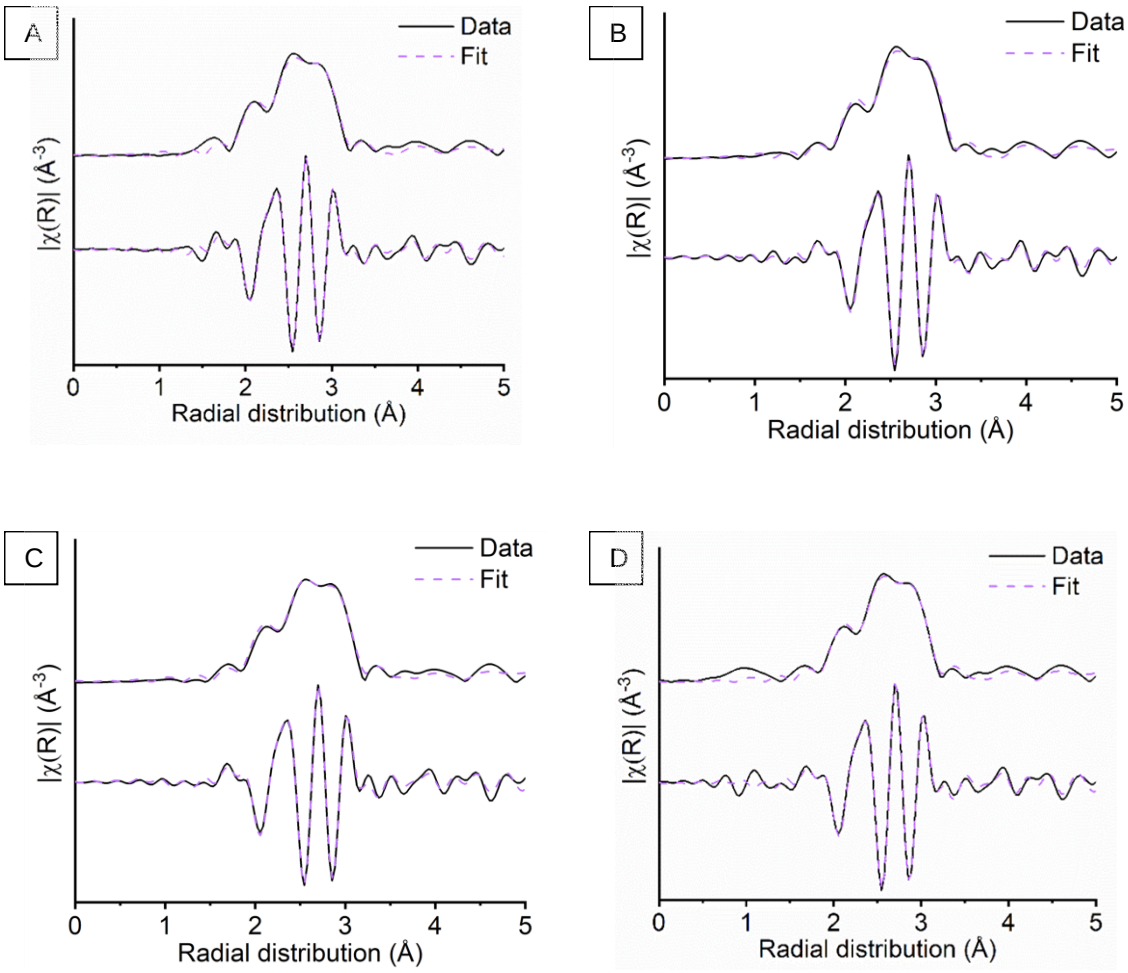

Figure 6.3.7: *Au L_3-edge EXAFS fitting data of* ***(A)*** *$AuAl_2O_3$,* ***(B)*** *$AuAl_2O_3$ milled,* ***(C)*** *La-$AuAl_2O_3$ mixed and* ***(D)*** *La-$AuAl_2O_3$ milled catalysts, showing the magnitude and imaginary components of the k^2-weighted Fourier transform data and simulated fits*

Table 6.3.3.1: *EXAFS fitting parameters at the Au L_3-edge for different Au/Al_2O_3 catalysts. Fitting parameters: $S_0^2 = 0.8$ as determined by the use of an Au foil standard; Fit range $3 < k > 13$, $1.4 < R > 5.0$.*

Sample	Bond (Abs-Sc)	CN	E_0 (eV)	σ^2	R / Å	R_{factor}	Average Au diameter / nm
Au/Al_2O_3	Au-Au1	10.1(8)	4(1)	0.009(1)	2.83(5)	0.02	2.1
	Au-Au2	0.8(9)		0.006(5)	4.04(3)		
	Au-Au3	4.7(7)		0.015(8)	4.95(3)		
Au/Al_2O_3 milled	Au-Au1	10.4(9)	4(1)	0.010(1)	2.83(1)	0.02	2.4
	Au-Au2	0.8(8)		0.004(4)	4.05(3)		
	Au-Au3	6.3(7)		0.011(8)	4.95(4)		
La-Au/Al_2O_3 mixed	Au-Au1	10.7(9)	4(1)	0.010(1)	2.83(4)	0.02	2.8
	Au-Au2	1.1(5)		0.008(9)	4.03(4)		
	Au-Au3	4.9(6)		0.011(8)	4.95(4)		
La-Au/Al_2O_3 milled	Au-Au1	10.8(9)	4(1)	0.009(1)	2.84(1)	0.02	3.0
	Au-Au2	1.3(9)		0.007(8)	4.04(4)		
	Au-Au3	7.1(7)		0.012(8)	4.96(4)		

6.3.4 XPS

XPS has been performed to understand how the surface composition of the Au/Al_2O_3 catalyst changes with respect to milling and the addition of La. The surface atomic percentage ratios are shown in Table 6.3.4.1. It is clearly observed that no change occurs to the alumina support on milling or the addition of La at the surface for all four Au/Al_2O_3 catalysts. Furthermore, there is no significant change between the Au/Al_2O_3 and Au/Al_2O_3 milled samples. After the addition of La to Au/Al_2O_3, a higher proportion of La is detected on the surface for the mixed sample, over the milled analogue. This suggests that on simple mixing by a pestle and mortar the La precursor remains at the surface of Au/Al_2O_3. However, on milling the La-Au/Al_2O_3 a reduction of the Al:La ratio indicates La is further dispersed and/or incorporated in the alumina support. It is important to note that a proportion of La, along with Au/Al_2O_3, could have remained inside the milling jar and therefore there is a lower proportion of La to total sample size. The surface composition of milled La-Au/Al_2O_3 also shows an increase in the amount of Al:Au ratio compared to all four catalysts.

Table 6.3.4.1: *Surface atomic percentage ratios of the different Au/Al_2O_3 and La catalysts*

Ratio	Au/Al_2O_3	Au/Al_2O_3 milled	La-Au/Al_2O_3 mixed	La-Au/Al_2O_3 milled
O:Al	1.6	1.6	1.6	1.6
Al:Au	1102	1091.3	1092.7	815.0
Al:La	-	-	91.1	271.7

The change in the La can be observed within the La 3*d* XPS region (Figure 6.3.8) where a reduced signal is detected for the milled sample, in comparison to the mixed. The peak at 833 eV is assigned to inorganic contamination remaining from the preparation method of Au/Al_2O_3.

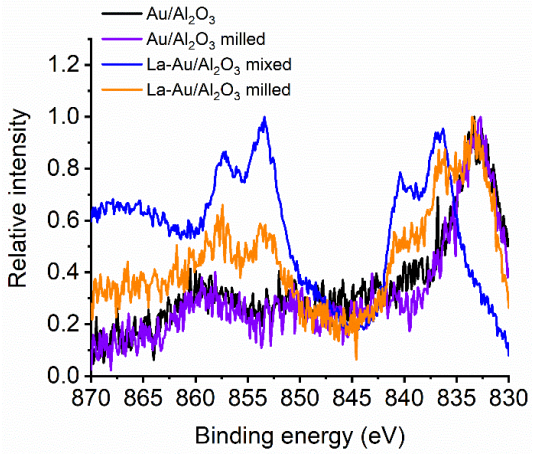

Figure 6.3.8: *XPS spectra within the La 3d region of different Au/Al_2O_3 catalyst*

Assessing the Au 4*f* and Al 2*p* XPS regions (Figure 6.3.9) shows no changes between the different Au/Al_2O_3 samples. The binding energy of the Au $4f_{7/2}$ region is indicative of pure metallic Au^0 surface species, in agreement with bulk analysis by Au L_3-edge XAS (Figure 6.3.5).[33]

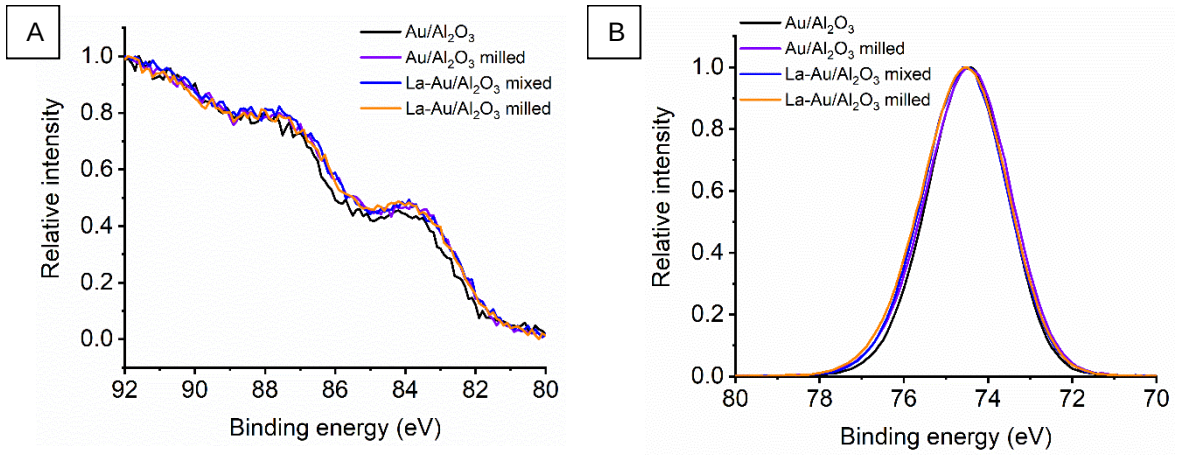

Figure 6.3.9: (A) *Au 4f and* ***(B)*** *Al 2p XPS regions for the different Au/Al_2O_3 catalysts*

6.3.5 Transmission IR

To assess the available Au surface sites, CO chemisorption studies were performed by transmission IR (Figure 6.3.10). The only significant absorption band observed within the spectra for Au/Al_2O_3 is detected at ~ 1900 cm^{-1}. This broad absorption band is extremely difficult to assign, with only clusters of $Au_5(CO)$ reported in literature within range of this wavenumber.[34] Broad CO adsorption bands result from the dipole coupling effect between neighbouring CO molecules; when CO coverage is large, the dipoles between CO

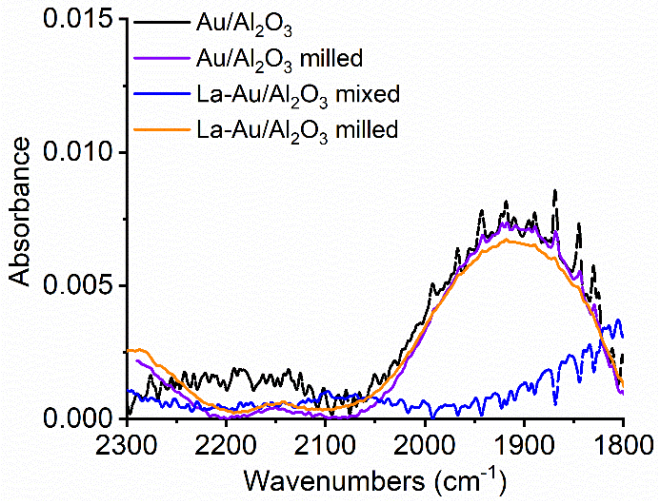

Figure 6.3.10: *Transmission IR spectra for CO absorption studies of different Au/Al_2O_3 catalysts*

molecules couple, increasing the width of the adsorption band. This indicates that large clusters of Au particles are present at the surface of Al_2O_3 for all catalysts.[9] The height of the absorption peak is often considered a quantitative assessment of the number of Au available sites, whilst maintaining the same sample weight. It is clear that La-Au/Al_2O_3 mixed catalyst has an extremely low number of Au surface sites. This indicates that the high proportion of La detected at the surface by XPS (Table 6.3.4.1) inhibits the chemisorption of CO onto Au sites at the surface.

6.3.6 Catalytic studies

CO oxidation experiments were carried out on all Au/Al_2O_3 catalysts to evaluate how the change in Au-supported NPs, induced by milling and/or La, affects their catalytic activity. Surface area analysis was performed by BET method to show that all catalysts had comparable values, 136 – 144 $m^2\,g^{-1}$.

Assessing the CO oxidation light-off curve (Figure 6.3.11) the first clear observation is that the initial Au/Al_2O_3 catalyst has the greatest activity. Milling of Au/Al_2O_3 significantly increases the T_{50} to 103.4 °C. However, on milling Au/Al_2O_3 with La the T_{50} is reduced to 85.2 °C. No significant alterations are observed in the *ex situ* characterisation for the La-Au/Al_2O_3 catalysts, indicating that doping with La has resulted in a beneficial interaction with Au during CO oxidation, compared to the Au/Al_2O_3 milled sample. A drastic decrease in activity is detected for the La-Au/Al_2O_3 mixed sample, producing a T_{50} of 142.0 °C. Observations by transmission IR showed that La mixed with Au/Al_2O_3 strongly reduced the available surface Au sites, thus inhibiting the CO oxidation activity. By simply mixing La with Au/Al_2O_3 by hand in a pestle and mortar the La can be observed to target and associate itself with the Au NPs. Though this effectively extinguishes the catalytic activity, the La dispersion has extremely high potential for low energy mechanochemical synthesis.

It is clear there is pronounced interaction between La and Au, which modifies the catalytic behaviour. Whilst within this study the investigation into milling and doping with La did not improve the catalytic activity, it provides further insights into how La behaves in the presence of metal oxides. With an initial zerovalent Au oxidation state detected by both XAS and XPS before CO oxidation takes place, it raises an interesting point when trying to deduce the active Au species.[20] Literature reported a pure La_2O_3 support stabilised Au(III) state, before and during CO oxidation. With this not the case here, it can be an indication that $Au^{\delta+}$ sites are generated under reaction conditions from the zerovalent Au nanoclusters.[21] This requires future work into *in situ* techniques, such as XAS or IR.

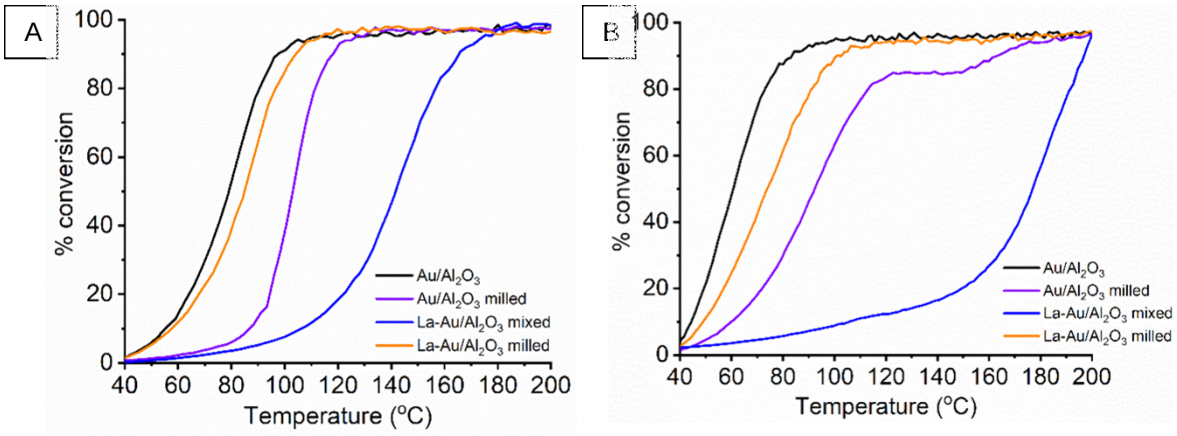

Figure 6.3.11: (A) *Light-off curve showing the percentage conversion of CO to CO_2 by Au/Al_2O_3 and its milled analogue and in the presence of La compared to it* ***(B)*** *reproducibility*

6.3.7 Post CO oxidation characterisation

Previous work has highlighted how catalytic reactions, performed at elevated temperatures, have significantly affected the structure of the catalyst. Therefore, *ex situ* characterisation by XRD and XAS has been conducted to understand the longevity of the different Au/Al_2O_3 catalysts. Furthermore, this can provide mechanistic insights into the catalytic reaction due to detected structural changes after CO oxidation.

XRD studies performed after CO oxidation (Figure 6.3.12) show a decrease in peak intensity, alongside broadening of the baseline for all four Au/Al_2O_3 catalysts. This indicates an increased proportion of disordered amorphous content, in comparison to the XRD measurements prior to the catalytic run (Figure 6.3.1). This can suggest that the metal oxide support, Al_2O_3, considered throughout literature as inert, has become amorphous and undergoes a form of structural rearrangement on performing CO oxidation. Both Au/Al_2O_3 and its milled analogous follow comparable diffraction patterns. Small variations are observed between the $La\text{-}Au/Al_2O_3$ mixed and milled catalysts. The differences observed in

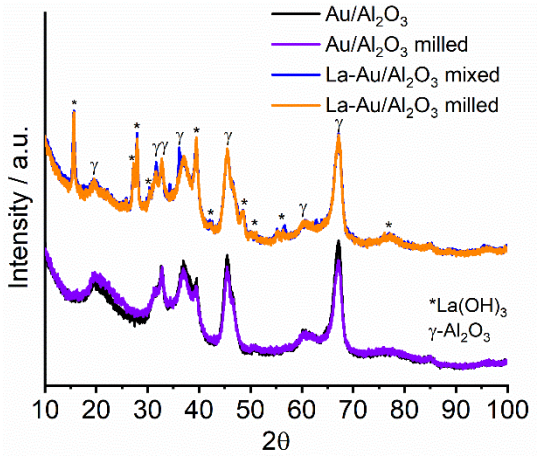

Figure 6.3.12 *XRD patterns of different Au/Al_2O_3 catalysts after CO oxidation*

the XRD for the La-Au/Al_2O_3 mixed material are challenging to interpret due to the low signal-to-noise intensity without the use of phase identification and refinement software; not accessible as a result of COVID restrictions.

To analyse both the amorphous and crystalline material, XAS studies have been performed at both the Au and La L_3-edge (Figure 6.3.13 and Figure 6.3.14). The Au L_3-edge XANES spectra for all Au/Al_2O_3 catalysts show similarities in the Au oxidation state compared to the fresh catalyst measurements (Figure 6.3.13); a zerovalent Au state remains. Changes in the amplitude of the main absorption peak at the La L_3-edge indicates that the La environment has become more crystalline after CO oxidation has be performed.

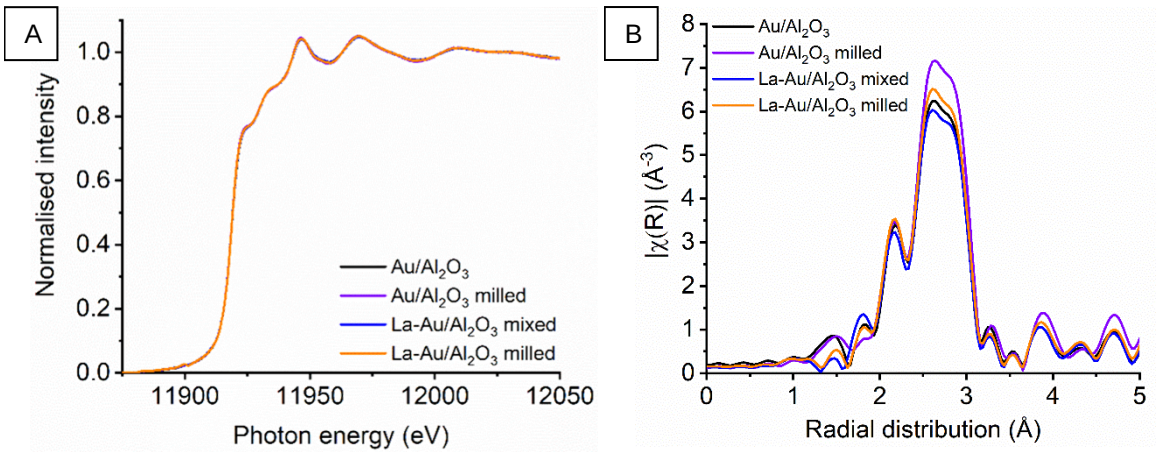

Figure 6.3.13: *XAS performed at the Au L_3-edge on Au/Al_2O_3 catalyst that has been milled/mixed in the presence of La(OH)$_3$ showing* ***(A)*** *XANES and* ***(B)*** *non-phase corrected Fourier transform*

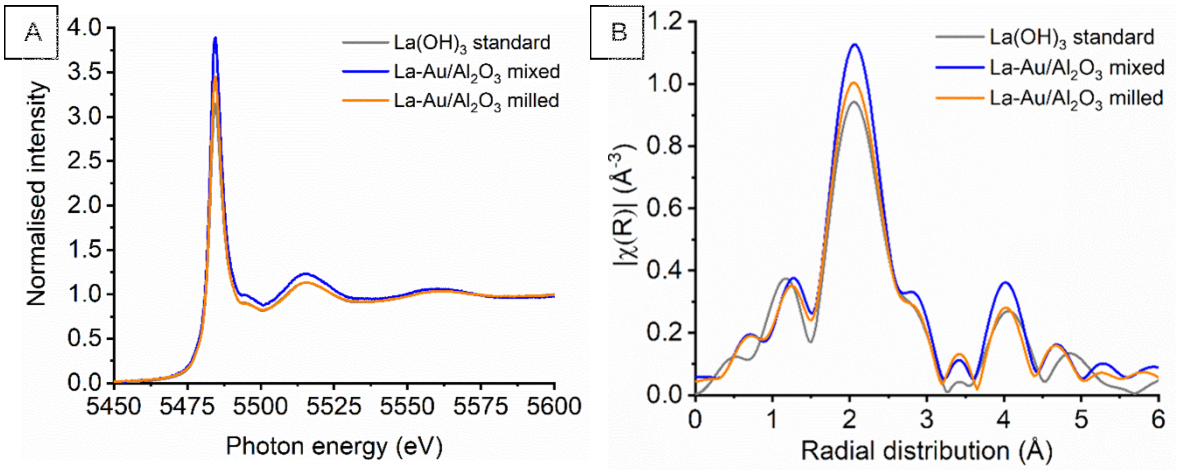

Figure 6.3.14: *XAS performed at the La L_3-edge on La-Au/Al_2O_3 mixed and milled samples compared to a La(OH)$_3$ standard showing* ***(A)*** *XANES and* ***(B)*** *non-phase corrected Fourier transform*

Performing EXAFS analysis on the different Au/Al_2O_3 catalysts after CO oxidation (Figure 6.3.15) shows changes to the Au coordination have occurred. Assessing the fitting parameters of the simulated EXAFS models (Table 6.3.7.1), an increase in the CN for the first scattering shell is observed for all catalysts, except the $La\text{-}Au/Al_2O_3$ mixed. This is further reflected in the average Au NP diameter, using the Beale *et. al.* formula.[32] The $La\text{-}Au/Al_2O_3$ mixed sample is the only catalyst that remains constant and does not increase in size at 2.8 Å; indicating the La interaction with Au prevented particle agglomeration on increasing the temperature.[32] Both milled catalysts, Au/Al_2O_3 milled and $La\text{-}Au/Al_2O_3$ milled, report the greatest increase in first shell Au-Au CN to 11.0 and 11.3, respectively. This large increase causes their average Au particle diameter to increase above 3 nm, making them unsuitable to be used within the equation.

Large errors were produced for the Au-Au CN within the first coordination shell, which in turn can affect the calculated particle size. To further assess this change in Au NP size as a result of CO oxidation, the spectra prior and post catalysis have been subtracted to show the difference (Figure 6.3.16); the smallest change is an indication of the catalyst

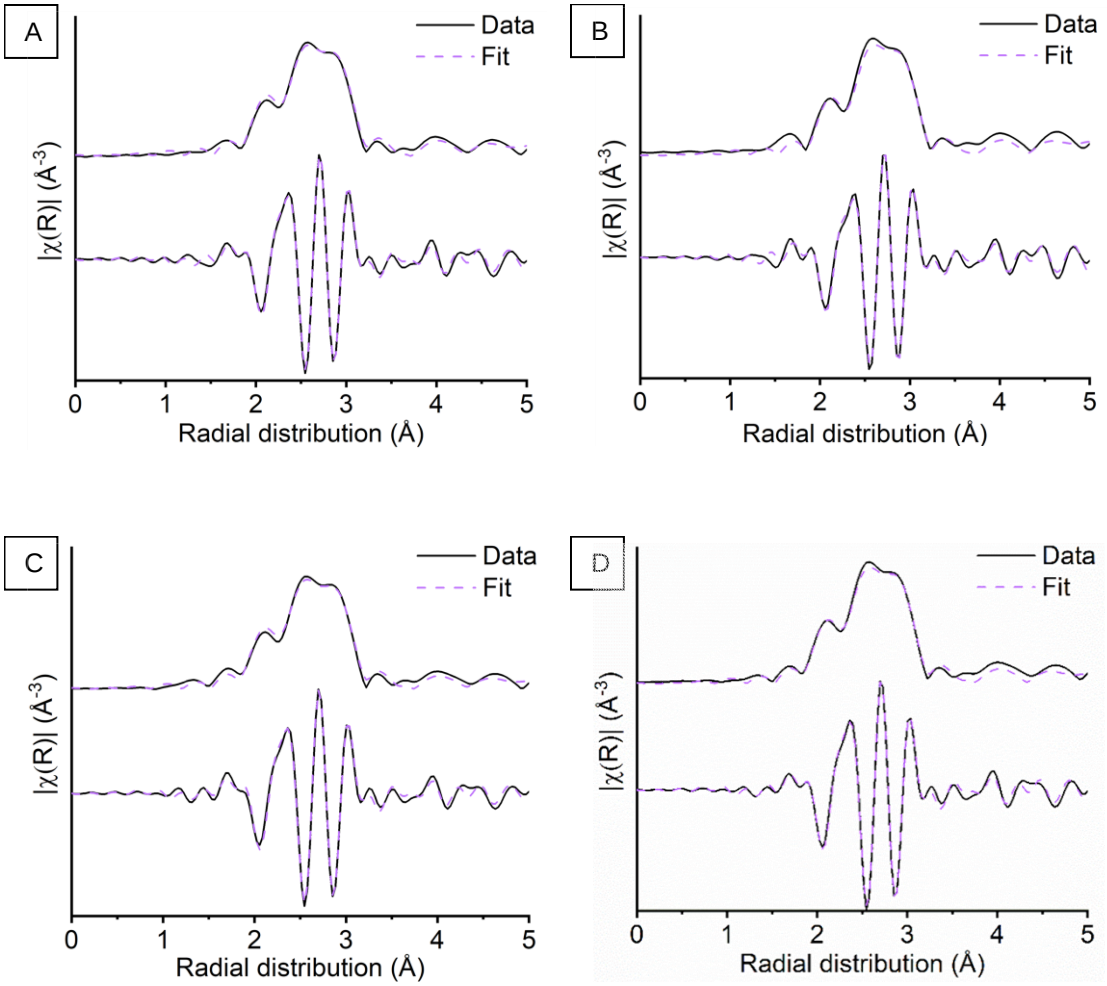

Figure 6.3.15 *Au L_3-edge EXAFS fitting models on data after CO oxidation of* ***(A)*** *$AuAl_2O_3$,* ***(B)*** *$AuAl_2O_3$ milled,* ***(C)*** *$La\text{-}AuAl_2O_3$ mixed and* ***(D)*** *$La\text{-}AuAl_2O_3$ milled catalysts, showing the magnitude and imaginary components of the k^2-weighted Fourier transform data and simulated fits*

with the most stable Au NP size. First assessing the effect milling has on Au/Al_2O_3 post reaction (Figure 6.3.16A), features at 11920 eV and 11943 eV show a large variation between the spectra, compared to the initial Au/Al_2O_3 catalyst. This indicates that a change has occurred on milling to destabilise the interface between Al_2O_3 and surface Au. On performing CO oxidation, the increase in temperature then allows for an increase in Au mobilisation to result in agglomeration. However, it is observed in Figure 6.3.16B that on milling in the presence of La, less aggregation has occurred after CO oxidation suggesting La is stabilising the surface Au under milling conditions. Further comparisons between the catalysts (Figure 6.3.16C, D) show the La-Au/Al_2O_3 mixed material shows the greatest Au NP size stabilisation after CO oxidation. This supports the calculated for NP sizes by EXAFS analysis before and after catalysis performed on the different Au/Al_2O_3 materials; in the presence of La, doped by either mixing or milling, an interaction with Au has stabilised the Au to prevented particle agglomeration on increasing the temperature.

Table 6.3.7.1: *EXAFS fitting parameters at the Au L_3-edge for different Au/Al_2O_3 catalysts after CO oxidation has been performed. Fitting parameters: S_0^2 = 0.8 as determined by the use of an Au foil standard; Fit range 3 < k>13, 1.4 <R >5.0.*

Post CO Oxidation	Bond (Abs-Sc)	CN	E_0 (eV)	σ^2	R / Å	R_{factor}	Average Au diameter / nm
Au/Al_2O_3	Au-Au1	10.7(9)	4(1)	0.009(1)	2.84(1)	0.02	2.8
	Au-Au2	1.3(9)		0.006(8)	4.06(3)		
	Au-Au3	6.9(7)		0.012(8)	4.97(4)		
Au/Al_2O_3 milled	Au-Au1	11(1)	5(1)	0.009(1)	2.85(1)	0.02	3.4
	Au-Au2	1.8(5)		0.006(6)	4.06(3)		
	Au-Au3	9.6(8)		0.011(6)	4.98(3)		
La-$AuAl_2O_3$ mixed	Au-Au1	10.7(9)	4(1)	0.009(1)	2.84(1)	0.02	2.8
	Au-Au2	1.2(5)		0.007(9)	4.06(4)		
	Au-Au3	5.7(7)		0.011(9)	4.96(4)		
La-$AuAl_2O_3$ milled	Au-Au1	11.3(1)	4(1)	0.009(1)	2.84(1)	0.02	4.4
	Au-Au2	1.8(3)		0.008(7)	4.05(3)		
	Au-Au3	7.5(8)		0.012(7)	4.96(3)		

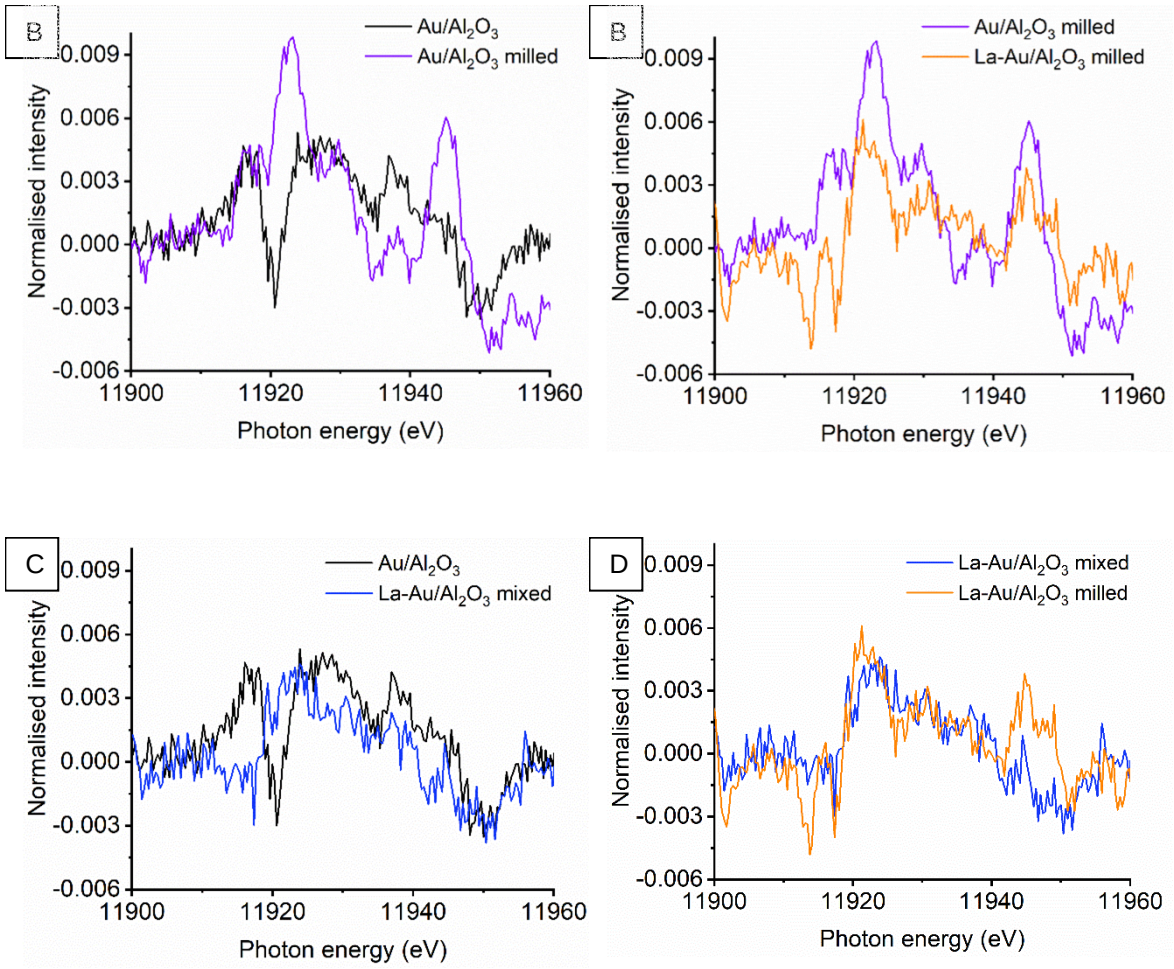

Figure 6.3.16: *Comparison of Au L_3-edge XANES subtracted spectra before and after CO oxidation for* ***(A)*** *Au/Al_2O_3 and Au/Al_2O_3 milled,* ***(B)*** *Au/Al_2O_3 milled and La-Au/Al_2O_3 milled* ***(C)*** *Au/Al_2O_3 and La-Au/Al_2O_3 mixed and* ***(D)*** *Au/Al_2O_3 and Au/Al_2O_3 milled*

6.4 Conclusions

This work has further explored the role of a La precursor within ball milling by investigating its interaction with Au-supported NPs. It was not possible to detect a cationic Au(III) species by *ex situ* characterisation of La doped Au/Al_2O_3 by mechanochemical action, with Au L_3-edge XANES indicating an average Au(0) state. However, this work has been successful in further exploring how La acts on activation at low mechanical energies *i.e.* with a pestle and mortar. Simply mixing by hand, a high proportion of La was detected at the surface by XPS, to associate itself with available Au sites by IR. This, in turn, dramatically reduced the catalytic activity towards CO oxidation. However, with no obvious change was observed in the bulk Au or La structures by XAS and XRD, it raises an interesting point at what interaction is occurring between the La and Au particles. This could be a result of the large particle sizes forming a bulk environment average or the possibility La and Au are indirectly bound to one another. After performing CO oxidation, the average Au particle size for the $La\text{-}Au/Al_2O_3$ mixed catalyst remained constant at 2.8 Å. This indicates La possesses a stabilising ability for Au NPs, preventing agglomeration, previously remarked on in literature for Au/La_2O_3 systems.[18]

By milling, even at a 100 rpm for 30 min, the association between La-Au is indicated to be significantly reduced. However, this $La\text{-}Au/Al_2O_3$ milled catalyst observed a dramatically decreased T_{50} value in comparison to the equivalent Au/Al_2O_3 milled material. This could once again indicate stabilisation of the Au environment on milling, however, large NP increases were calculated for both species after CO oxidation.

Ex situ XRD performed after CO oxidation also indicated a significant decrease in crystallinity for the Al_2O_3 support for all of the Au/Al_2O_3 catalysts. With both Al_2O_3 and La_2O_3 considered as inert supports which do not possess redox capabilities it questions their involvement within CO oxidation. However, without further assessment of the Al coordination it can be challenging to understand.

Though these initial investigations into the stabilisation of cationic Au NP detected only Au(0) species and a loss of catalytic activity, the addition of La by low energy mechanochemistry not only shows scope towards the stability of Au NP size but further potential into the use of La by mechanical grinding. Future work would be to further investigate the Au active species by *in situ* CO oxidation and the how the La associates itself on Au NPs.

6.5 References

1 Z. Li, S. Ji, Y. Liu, X. Cao, S. Tian, Y. Chen, Z. Niu and Y. Li, *Chem. Rev.*, 2020, **120**, 623–682.

2 US, 4992405, *US Pat.*, 1991 –' THREE-WAY CATALYST FOR AUTOMOTIVE EMISSION CONTROL AND METHOD OF MAKING THE CATALYST'

3 Q. Fu, H. Saltsburg and M. Flytzani-Stephanopoulos, *Science*, 2003, **301**, 935–938.

4 A. Al-Ammar and G. Webb, *J. Chem. Soc., Faraday Trans.*, 1978, **74**, 657–664.

5 M. C. Kung, R. J. Davis and H. H. Kung, *J. Phys. Chem. C*, 2007, **111**, 11767–11775.

6 T. W. Hansen, A. T. Delariva, S. R. Challa and A. K. Datye, *Acc. Chem. Res.*, 2013, **46**, 1720–1730.

7 S. Carrettin, P. McMorn, P. Johnston, K. Griffin, C. J. Kiely and G. J. Hutchings, *Phys. Chem. Chem. Phys.*, 2003, **5**, 1329–1336.

8 N. Dimitratos, A. Villa, L. Prati, C. Hammond, C. E. Chan-Thaw, J. Cookson and P. T. Bishop, *Appl. Catal. A Gen.*, 2016, **514**, 267–275.

9 S. M. Rogers, C. R. A. Catlow, C. E. Chan-Thaw, D. Gianolio, E. K. Gibson, A. L. Gould, N. Jian, A. J. Logsdail, R. E. Palmer, L. Prati, N. Dimitratos, A. Villa and P. P. Wells, *ACS Catal.*, 2015, **5**, 4377–4384.

10 H. Schreyer, R. Eckert, S. Immohr, J. de Bellis, M. Felderhoff and F. Schüth, *Angew. Chemie - Int. Ed.*, 2019, **58**, 11262–11265.

11 M. J. Rak, T. Friščić and A. Moores, *Faraday Discuss.*, 2014, **170**, 155–167.

12 G. C. Bond, P. A. Sermon, G. Webb, D. A. Buchanan and P. B. Wells, *J. Chem. Soc. Chem. Commun.*, 1973, **13**, 444–445.

13 M. Haruta, T. Kobayashi, H. Sano and N. Yamada, *Chem. Lett.*, 1987, **16**, 405-408.

14 P. Johnston, N. Carthey and G. J. Hutchings, *J. Am. Chem. Soc.*, 2015, **137**, 14548–14557.

15 D. Tibiletti, A. Amieiro-Fonseca, R. Burch, Y. Chen, J. M. Fisher, A. Goguet, C. Hardacre, P. Hu and D. Thompsett, *J. Phys. Chem. B*, 2005, **109**, 22553–22559.

16 J. C. Fierro-Gonzalez and B. C. Gates, *Chem. Soc. Rev.*, 2008, **37**, 2127–2134.

17 J. A. Van Bokhoven, C. Louis, J. T. Miller, M. Tromp, O. V. Safonova and P. Glatzel, *Angew. Chemie - Int. Ed.*, 2006, **45**, 4651–4654.

18 A. Goguet, M. Ace, Y. Saih, J. Sa, J. Kavanagh and C. Hardacre, *Chem. Commun.*, 2009, **32**, 4889–4891.

19 J. Sá, M. Ace, J. J. Delgado, A. Goguet, C. Hardacre and K. Morgan, *ChemCatChem*, 2011, **3**, 394–398.

20 J. C. Fierro-Gonzalez, V. A. Bhirud and B. C. Gates, *Chem. Commun.*, 2005, **42**, 5275–5277.

21 M. Mihaylov, E. Ivanova, Y. Hao, K. Hadjiivanov, H. Knözinger and B. C. Gates, *J. Phys. Chem. C*, 2008, **112**, 18973–18983.

22 M. Mihaylov, E. Ivanova, Y. Hao, K. Hadjiivanov, B. C. Gates and H. Knözinger, *Chem. Commun.*, 2008, **2**, 175–177.

23 R. H. Blackmore, M. E. Rivas, T. E. Erden, T. D. Tran, H. R. Marchbank, D.

Ozkaya, M. Briceno de Gutierrez, A. Wagland, P. Collier and P. P. Wells, Dalt. Trans., 2020, **49**, 232–240.

24 M. Newville, *J. Synchrotron Radiat.*, 2001, **8**, 322–324.

25 B. Ravel and M. Newville, *J. Synchrotron Radiat.*, 2005, **12**, 537–541.

26 S. R. Chauruka, A. Hassanpour, R. Brydson, K. J. Roberts, M. Ghadiri and H. Stitt, *Chem. Eng. Sci.*, 2015, **134**, 774–783.

27 P. A. Zielinski, R. Schulz, S. Kaliaguine and A. Van Neste, *J. Mater. Res.*, 1993, **8**, 2985–2992.

28 M. Giorgetti, G. Aquilanti, B. Ballarin, M. Berrettoni, M. C. Cassani, S. Fazzini, D. Nanni and D. Tonelli, *Anal. Chem.*, 2016, **88**, 6873–6880.

29 J. T. Miller, A. J. Kropf, Y. Zha, J. R. Regalbuto, L. Delannoy, C. Louis, E. Bus and J. A. van Bokhoven, *J. Catal.*, 2006, **240**, 222–234.

30 W. Szczerba, H. Riesemeier and A. F. Thünemann, *Anal. Bioanal. Chem.*, 2010, **398**, 1967–1972.

31 G. F. Tierney, D. Decarolis, N. Abdullah, S. M. Rogers, S. Hayama, M. Briceno De Gutierrez, A. Villa, C. R. A. Catlow, P. Collier, N. Dimitratos and P. P. Wells, *Nanoscale Adv.*, 2019, **1**, 2546–2552.

32 A. M. Beale and B. M. Weckhuysen, *Phys. Chem. Chem. Phys.*, 2010, **12**, 5503–5513.

33 M. P. Casaletto, A. Longo, A. Martorana, A. Prestianni and A. M. Venezia, Surf. Interface Anal., 2006, **38,** 215–218.

34 L. Jiang and Q. Xu, *J. Phys. Chem. A*, 2005, **109**, 1026–1032.

35 A. Voronov, A. Urakawa, W. van Beek, N. E. Tsakoumis, H. Emerich and M. Rønning, *Anal. Chim. Acta*, 2014, **840**, 20–27.

36 M. Bauer, *Phys. Chem. Chem. Phys.*, 2014, **16**, 13827–13837.

37 F. Schüßler, E. A. Pidko, R. Kolvenbach, C. Sievers, E. J. M. Hensen, R. A. Van Santen and J. A. Lercher, *J. Phys. Chem. C*, 2011, **115**, 21763–21776.

Chapter 7

Conclusions and future work

The work within this thesis has sought to extensively understand the mechanochemical synthesis of manganite perovskites, along with La doped Au/Al_2O_3. Changing the synthetic route has had a profound effect on the final metal properties making the milled materials suitable for catalytic applications. It was, therefore, vital to understand the process by which perovskites formed via milling and the structural properties that benefited their catalytic activity. In order to do so a huge variety of both *ex situ* and *in situ,* lab-based and synchrotron characterisation techniques, such as XRD, XAS, HERFD-XANES, XES, TEM and XPS were explored. The implications surrounding monitoring of mechanochemical synthesis has often required the use of iterative and systematic optimisation of milling conditions for each individual system. The research presented here begins to initiate the discussion surrounding building generalised mechanochemical rules, for the correlation of milling parameters to desired characteristics. In doing so, it can aid the rational design of new catalyst technologies.

The work throughout this thesis repeatedly highlights the structural complexity and heterogeneity of the milled perovskite materials. Though we were able to provide new insights, this work faced multiple challenges in extracting precise conclusions. A huge variety of characterisation methods were required, and even after the use of advanced techniques many questions still remain. These advanced methods are hallmarked within literature, and rightly so, but their limitations are often not discussed and in doing so can result in their use in inappropriate situations.

For example, performing XRD was initially essential to identify the crystalline phases. In Chapter 5 it was reported how mechanochemistry produced a metastable orthorhombic perovskite phase, as opposed to the thermally stable hexagonal analogue by sol-gel synthesis. However, XRD is not suitable to detect the amorphous content, which is also produced during the mechanochemical synthesis. This is where XAS was successful; it is element specific and does not rely on periodic ordering. Its use within Chapter 3 was highly advantageous for providing new insights into the chemical steps occurring during milling for $LaMnO_3$ to evolve. However, this technique also comes with its limitations. The milled materials consisted of a mixture of both amorphous and crystalline phases. With XAS

providing an average bulk structure of the overall sample composition, clear gaps remained not only remained regarding the chemical and phase transformations occurring under milling conditions but also in variations occurring at the surface. On top of this, the EXAFS structure model is restricted by assumptions on the choice of an appropriate reference material, as intermediate species remain unknown.

To overcome the tendency of traditional Mn K-edge XANES having broadened and smeared features in the spectra, Mn K-edge HERFD-XANES measurements were performed in Chapter 4. This was successful in producing highly resolved spectra, suitable for assigning pre-edge transitions to further understand the electronic configuration. However, work within the past 15 years has shown it is no longer viable to take the position of the absorption edge in XANES spectra as a direct reflection of the absorbing element oxidation state. Therefore, an alternative method, $K\beta_{1,3}$ XES, is commonly regarded to provide suitable information via the fingerprint method on oxidation state, independent of the surrounding geometry and ligand environment. Chapter 4 noted limitations within this technique, not commonly discussed in literature. Even before assessing oxidation states of the milled materials, the reference Mn_2O_3 and $LaMnO_3$ metal oxides, which possess the same central Mn(III) ion, detected different Mn $K\beta_{1,3}$ positions. This strongly indicates the care which researchers must take when choosing appropriate reference materials and making oxidation state assumptions. It emphasises the continued innovation required, even within these advanced characterisation techniques.

Strategies to attain more information on the mechanochemical synthesis were approached in Chapter 4 by performing *in situ* experiments; with a vibrational ball mill and high pressure DAC. The incredible achievement of being able to monitor the milling of MOFs real-time was a significant finding within the mechanochemical field, was only achieved 8 years ago. The modified step-up, however, was not suitable for the mixed metal oxide system, emphasising the need for a high energy planetary ball mill to provide higher impact energies. This was further reflected in the high pressure DAC experiments. However, the high risk of the perforated diamond windows breaking limited the measurements, and without the ability of the cell to perform temperature ramps, further mechanochemical effects could not be explored. It would be interesting to explore these techniques for La-Au/$A_{l2}O_3$ discussed in Chapter 6; where significant alterations occurred at much lower mechanical energies. However, this work indicates the increasing development of equipment capabilities required to replicate the mechanical action and energy transfer of a planetary ball mill, if at all possible.

To overcome the challenges of unknown phases and *in situ* monitoring, a solution would be to perform multivariate component analysis. Multivariant curve resolution (MCR) has been shown to extract component spectra without the use of reference spectra.[1] This numerical approach removes the need for prior knowledge or assumptions on the

intermediate states to blindly separate spectral components, benefiting over traditional linear combination fitting. By using a least squares refinement method of both the component concentration and spectral profiles, MCR can be used within this work effectively to identify the phases throughout milling. However, MCR presents its own limitations. This approach requires a large volume of data sets, which when generating one at a time is tedious. Yet, it shows exciting scope towards understanding the milling intermediates. Future theoretical calculations can then be performed to help resolve the components identified by MCR. For example, the work within Chapter 4 was able to assign the pre-edge transitions for Mn K-edge HERFD-XANES. However, DFT can provide complimentary information that adhere specifically towards HERFD-XANES; as HERFD-XANES follows the transition of one electron, it removes the need to consider multiplet structures, core-hole potential and multiple-electron excitations, making the calculations more accessible.[2] However, it requires a dedicated analyst, not always readily available. Furthermore, it is prudent to weigh up the large amount of work involved with how much extra information it truly provides.

When correlating the surface properties to the catalyst activity, XAS cannot be applied in the same way for perovskite materials as for supported metal NPs, as their catalytic active site is also often dispersed throughout the bulk. With all the $AMnO_3$ catalysts recording extremely low surface areas, the structural variations at the surface, observed by XPS and high resolution TEM, are not expected to be reflected in the average bulk structure. Therefore, to understand how surface properties affect the catalytic activity deN_2O experiments were performed on the newly commissioned B07 beamline, VerSoX, at DLS. This beamline allows for XPS to be performed under a gaseous sample environment, allowing for *in situ* monitoring of catalytic reactions. Chapter 4 showed how this technique provided valuable information on how the ball milled $LaMnO_3$ facilitated N_2O adsorption at RT for improved activity at low temperatures. However, its description of 'near ambient' conditions, with a pressure of 10 mBar, is significantly different to the operating conditions experienced in the fixed bed microreactor. Furthermore, whilst the ball milled perovskites show potential towards catalysis - are they actually possible commercial catalysts? The ball milled materials undergo a phase transformation at elevated temperatures, losing their beneficial properties. However, this work does show scope to perform deN_2O at low temperatures. Future investigations can seek to understand how presence of a low concentrations of water or after a pre-treatment to saturate the surface was hydroxyls affects deN_2O.

Though many complexities occurred surrounding the assessment of the milling procedure and resulting materials throughout this thesis, significant progress has been made towards the formation of a generalised understanding of mechanochemistry. Systematic work to compare the mechanochemical synthesis of different A-site materials in

Chapter 5 showed the ease at which the perovskite formed was not only correlated to the precursor properties but to the stability of the final state. With Y_2O_3 and Er_2O_3 A-site starting materials having similar properties, it was the degree of Jahn-Teller distortion that determined the rate of perovskite formation. However, the high variety of milling conditions, equipment and specific materials used within the mechanochemical field shows the continued research required to achieve generalised rules. The work presented in Chapters 3, 5 and 6 indicates how milling conditions, such as atmosphere, media size, precursors and expected final material properties, commonly are required to be tuned for each specific system. Increasing amounts of work are, however, still required into investigating how the different milling parameters correspond to one another, *i.e.* can increasing the rotation speed of the mill equal the impact energy achieved on increasing media size increase? It would also be interesting to investigate further the effects of milling atmospheres, such as O_2 and moisture, on perovskite formation. Based on Chapter 3, it would be expected an oxygen milling environment would be beneficial for perovskite formation.

It is also important to consider the behaviour of the powders within the mill under mechanical action. For example, the La precursor exhibits the ability to readily disperse over Mn_2O_3 at low mechanical energies, increasing the rate of perovskite phase formation. Chapter 6 continued to understand this behaviour by applying low mechanical stress to dope pre-synthesised Au/Al_2O_3 with La. By simply mixing by hand, the La precursor was observed to associate itself with the available Au surface sites. Though, this came at huge detriment to its catalytic behaviour towards CO oxidation it shows La high affinity for dispersion under mild mechanochemical conditions. With initial e*x situ* characterisation only able to detect Au(0) species, it leads into further work towards investigating the oxidation state of the active site during CO oxidation and to understand the interaction between Au and La. However, most significantly the work shows exciting potential for use of milling La within different systems, minimising the use of solvents and multiple process steps. For example, it presents opportunities to easily disperse La into metal organic framework (MOFs) or zeolite structures. Cationic La(III) has been shown to stabilise the zeolite cage by the formation of multinuclear cations of La OH-bridge clusters, however, to perform the ion exchange a large array of process and high temperature steps were required.[3] Furthermore, continuing the research into supported metal NPs as a new field for mechanochemistry shows exciting opportunities, towards both the stability of the support and the metal NPs.

7.1 References

1 A. Voronov, A. Urakawa, W. van Beek, N. E. Tsakoumis, H. Emerich and M. Rønning, *Anal. Chim. Acta*, 2014, **840**, 20–27.

2 M. Bauer, *Phys. Chem. Chem. Phys.*, 2014, **16**, 13827–13837.

3 F. Schüßler, E. A. Pidko, R. Kolvenbach, C. Sievers, E. J. M. Hensen, R. A. Van Santen and J. A. Lercher, *J. Phys. Chem. C*, 2011, **115**, 21763–21776.